Investigation of Physiological Solutions of Metalloproteins in a High-Repetition Rate Picosecond X-ray Absorption Experiment

THÈSE N^{O} 5249 (2011)

PRÉSENTÉE LE 14 DÉCEMBRE 2011

À LA FACULTÉ DES SCIENCES DE BASE
LABORATOIRE DE SPECTROSCOPIE ULTRARAPIDE
PROGRAMME DOCTORAL EN PHYSIQUE

ÉCOLE POLYTECHNIQUE FÉDÉRALE DE LAUSANNE

POUR L'OBTENTION DU GRADE DE DOCTEUR ÈS SCIENCES

PAR

Frederico ALVES LIMA

acceptée sur proposition du jury:

Prof. R. Houdré, président du jury
Prof. M. Chergui, directeur de thèse
Prof. S. Della Longa, rapporteur
Prof. P. Leiman, rapporteur
Prof. M. Négrerie, rapporteur

ÉCOLE POLYTECHNIQUE
FÉDÉRALE DE LAUSANNE

Suisse
2011

"On ne voit bien qu'avec le coeur. L'essentiel est invisible pour les yeux"

Antoine de Saint-Exupéry

Contents

Summary

Over the last decade, ultrafast time-resolved X-ray absorption spectroscopy (XAS) has evolved to be now a mature and well-established experimental technique, giving extremely detailed information about the local geometrical and electronic structure in the early stages of a chemical reaction or biological process. Electronic structure changes are the fundamental driving forces triggering structural modifications in many chemical and biological reactions. Ultrafast time-resolved XAS is an ideal experimental technique to probe these changes in "real time" during the course of a chemical reaction, a biological function or a physical process. Ideally, the observation of ultrafast processes is made in conditions as close as possible as the natural ones, *i.e.*, biological processes in physiological media (instead of crystals or frozen films). In this sense XAS offers unique capabilities, since it can be applied to any kind of system.

In this thesis we successfully implemented a new scheme for measuring time-resolved XAS spectra with picosecond temporal resolution at MHz repetition rate. The increase in the data acquisition repetition rate provided an increase in the signal-to-noise (S/N) of a factor of > 20 compared to previous experiments in the kHz regime. To assess the improvements in this new data acquisition methodology, we used the light-induced spin transition in aqueous solutions of $[Fe(bpy)_3]^{2+}$ to benchmark our experiments. This system has been well-characterized by both ultrafast laser and x-ray time-resolved spectroscopies. The expected gain in data quality was confirmed, which allowed the recording of subtle changes in the pre-edge region of the XAS spectrum, reflecting the different electronic structure of $[Fe(bpy)_3]^{2+}$ upon the spin transition.

We also present the investigation of the electronic and geometric structures of a series of metalloproteins (Myoglobin) in physiological solutions by means of X-ray absorption spectroscopy. To our knowledge, this is the first study of the structure of the different forms of Myoglobin in physiological media using XAS. The analysis of the XANES region of the spectrum using full-multiple scattering (FMS) formalism revealed that the iron-nitrogen bond length in the porphyrins ring converged to a common value of about 2 Å, in contrast to the wide variation found in the crystallographic structures. Porphyrins are known to be very rigid structures due to the big number of carbon-carbon double bounds, supporting our conclusion. The relative geometry of the ligands with respect to the heme is reported for the whole series of Myoglobins investigated. In addition, time-resolved XAS has been measured for two types of Myoglobin, Carboxy-Myoglobin (MbCO) and (Nitrosyl-Myoglobin) MbNO. It has been shown that, as expected from

previous studies, the transient structure of photo-excited MbCO resembles that of the deligated ferrous Myoglobin (deoxyMb). On the other hand, the transient structure of photo-excited MbNO at 50 ps deviates slightly from that of deoxyMb. The analysis of the transient XANES indicates that the NO molecule moves 2.88 Å away from the heme, staying closer to the iron atom than in the case of photo-excited MbCO. The NO geminate recombination time with the heme was also measured in "real time", and it has been found to occur in 216 ± 24 ps. This is the first direct measurement, *i.e.* sensitive to structural changes, of this geminate recombination time.

KEYWORDS: *X-ray absorption spectroscopy, Ultrafast Time-resolved X-ray absorption spectroscopy, High repetition rate, Proteins, Myoglobin, Physiological solutions, Picosecond X-ray Pulses, Synchrotron Radiation, Pump-probe spectroscopy*

Zusammenfassung

In der letzten Dekade hat sich zeitaufgelöste Röntgenabsorptionsspektroskopie (XAS) zu einer ausgereiften und gut etablierten experimentellen Technik entwickelt, welche überaus detaillierte Information über die lokale geometrische und elektronische Struktur im Frühstadium einer chemischen Reaktion oder eines biologischen Prozesses liefert. Änderungen der elektronischen Struktur sind die fundamentalen, treibenden Kräfte welche strukturelle Modifikationen in vielen chemischen und biologischen Reaktionen induzieren. Ultraschnelle zeitaufgelöste XAS ist eine ideale experimentelle Technik um diese Änderungen während dem Ablauf einer chemischen Reaktion, einer biologischen Funktion, oder einem physikalischen Prozess in Echtzeit zu sondieren. Idealerweise werden ultraschnelle Prozesse unter natürlichen experimentellen Bedingungen gemessen, sowie beispielsweise biologische Prozesse in physiologischen Medien (anstelle von Kristallen oder gefrorenen Schichten). In diesem Sinn bietet XAS einzigartige Möglichkeiten, da sie für allerlei Systeme anwendbar ist.

In dieser Arbeit haben wir erfolgreich ein neues Schema implementiert, welches erlaubt, zeitaufgelöste XAS mit Picosekundenzeitauflösung und MHz-Repetitionsraten zu messen. Die Zunahme in der Repetitionsrate der Datenakquisition hat, verglichen mit vorangehenden Experimenten im kHz-Bereich, zu einem um einen Faktor > 20 erhöhten Signal-Rausch-Verhältnis (S/N) geführt. Um die Verbesserungen aufgrund dieser neuen Datenakquisitionsmethode bemessen zu können, haben wir den lichtinduzierten Spincrossover Effekt in wässrigen Lösungen von $[Fe(bpy)_3]^{2+}$ betrachtet. Dieses System wurde bereits sowohl durch ultraschnelle Laser- wie auch zeitaufgelöste Röntgenspektroskopien ausführlich charakterisiert. Die erwartete Zunahme der Datenqualität wurde bestätigt, was uns erlaubt hat, subtile Änderungen in der Region der Vorkante des XAS Spektrums zu messen, welche die durch den Spin-crossover Effekt veränderte elektronische Struktur reflektieren.

Wir präsentieren auch die Untersuchung der elektronischen und geometrischen Struktur einer Reihe von Metalloproteinen (Myoglobin) in physiologischen Lösungen mit Hilfe der Röntgenabsorptionsspektroskopie. Soweit uns bekannt ist, handelt es sich hierbei um die erste Studie der Struktur von verschiedenen Formen von Myoglobin in physiologischen Medien mittels XAS. Die Analyse der XANES Region des Spektrums basierend auf dem Full-Multiple Scattering (FMS) Formalismus hat enthüllt, dass die Eisen-Stickstoff Bindungslänge im Porphyrinring gegen einen gemeinsamen Wert von ungefähr 2 Å konvergiert, was im Gegensatz steht zur breiten Variation, welche in kristallographis-

chen Strukturen vorliegt. Aufgrund ihrer hohen Zahl an Doppelbindungen sind Porphyrine als sehr steife Strukturen bekannt, was unsere Schlussfolgerung unterstützt. Die relative Geometrie der Liganden zum Häm ist für die ganze Serie der untersuchten Myoglobine aufgelistet. Zusätzlich haben wir zeitaufgelöste XAS für zwei Typen von Myoglobin, nämlich MbCO und MbNO gemessen. Wie aus vorangehenden Studien erwartet, wurde gezeigt, dass die Übergangsstruktur von lichtangeregtem MbCO derjenigen von unligiertem Eisen(II)-Myoglobin (deoxyMb) ähnelt. Andererseits weicht die Übergangsstruktur von lichtangeregtem MbNO nach 50 ps leicht von derjenigen von deoxyMb ab. Die Analyse der transienten XANES deutet darauf hin, dass sich das NO-Molekül vom Häm zu 2.88 Åwegbewegt und näher beim Eisenatom bleibt als im Fall von lichtangeregtem MbCO. Die Zeitdauer für die paarweise Rekombination (dont know of any better / official word describing geminate) von NO mit dem Häm wurde ebenfalls in Echtzeit gemessen und mit 216 ± 24 ps bemessen. Dies ist die erste direkte Messung dieser Paar-Rekombinationszeit, welche sensitiv auf strukturelle Änderungen ist.

SCHLÜSSELWÖRTER: *Röntgenabsorptionsspektroskopie, Ultraschnelle zeitaufgelöste Röntgenabsorptionsspektroskopie, Hohe Repetitionsrate, Proteine, Myoglobin, Physiologische Lösungen, Picosekunden-Röntgenpulse, Synchrotronstrahlung, Pump-Sonden Spektroskopie*

Resumé

Au cours de la dernière décennie, la spectroscopie d'absorption des rayons X (XAS) résolue en temps s'est développée pour devenir une technique expérimentale aboutie et bien établie. Elle permet d'obtenir des informations très détaillées sur les structures électroniques et géométriques locales lors des étapes initiales de réactions chimiques ou de processus biologiques. Les changements de structure électronique constituent la force motrice à l'origine de modifications structurelles dans beaucoup de réactions chimiques et biologiques. La spectroscopie d'absorption des rayons X ultrarapide est une technique expérimentale idéale pour sonder ces changements «en temps réel» au cours d'une réaction chimique, d'une fonction biologique ou d'un processus physique. Idéalement, l'observation de ces processus ultrarapides doit se faire dans des conditions aussi proches que possible de celles *in vivo*, c'est-à-dire dans un milieu physiologique à température ambiante (et non sous forme cristallisée ou de films à basse température). Dans ce sens, la technique XAS offre des possibilités uniques, car elle peut s'appliquer à n'importe quel système.

Au cours de ce travail, un nouveau montage permettant l'acquisition de spectres XAS résolus en temps avec une résolution temporelle picoseconde et un taux de répétition de l'ordre du MHz a été implémenté avec succès. L'élévation du taux de répétition de l'acquisition des données a permis d'améliorer le rapport signal sur bruit (S/N) d'un facteur > 20 comparé à des expériences ultérieures effectuées dans le régime kHz. Afin d'évaluer les améliorations dues à cette nouvelle méthode d'acquisition des données, nous avons utilisé la transition de spin photo induite du $[Fe(bpy)_3]^{2+}$ en solution aqueuse comme référence pour notre expérience. En effet ce système a déjà été caractérisé de manière détaillé par des mesures de spectroscopie laser et rayons X ultrarapide. Le gain attendu en termes de qualité des données s'est confirmé. Cela nous a permis d'enregistrer de subtiles changements dans la région du seuil du spectre XAS, traduisant la différence de structure électronique du $[Fe(bpy)_3]^{2+}$ lors de la transition de spin.

L'étude des structures électronique et géométrique d'une série d'hémoprotéines (myoglobine) en solution physiologique, à l'aide de la spectroscopie d'absorption des rayons X, est aussi présentée. A notre connaissance, ceci est la première étude structurelle des différentes formes de myoglobine en milieu physiologique, utilisant la technique XAS. L'analyse de la région XANES du spectre, utilisant le formalisme de la diffusion multiple (FMS), a révélé que la distance de liaison entre les atomes de fer et d'azote du cycle de la porphyrine est d'environ 2 Å, résultats clairement différent des valeurs divergentes

obtenu à partir de structures cristallographiques. Les porphyrines sont reconnues pour leur structure très rigide due au grand nombre de doubles liaisons carbone-carbone, corroborant notre conclusion. La géométrie du ligand relative à l'hème est présentée pour la série entière de myoglobines étudiées. De plus, le XAS résolu en temps a été mesuré pour deux formes de myoglobine, la carboxy myoglobine (MbCO) et la nitrosyl-myoglobine (MbNO). Les résultats ont démontré que, comme attendu par des études précédentes, la structure transitoire de la MbCO photo excitée ressemble à celle de la myoglobine ferreuse déliée (deoxyMb). En outre, la structure transitoire à 50 ps de la MbNO photo excitée dévie légèrement de celle de la deoxyMb. L'analyse des données XANES transitoires indique que la molécule de NO s'éloigne de 2.88 Åde l'hème, restant plus proche de l'atome de fer que dans le cas de la MbCO photo excitée. La recombinaison géminée du NO avec l'hème a pu aussi être suivie «en temps réel», celle-ci se déroulant en 216 ± 24 ps. Ceci est la première mesure directe, c'est-à-dire sensible aux changements structurels, du temps de recombinaison géminée.

MOTS-CLÉS: *Spectroscopie d'absorption des rayons X, Spectroscopie ultrarapide, Haut taux de répétition, Protéines, Myoglobine, Solutions physiologiques, Pulses de rayons X picoseconde, Rayonnement synchrotron, Spectroscopie pompe-sonde.*

Riassunto

Durante l'ultimo decennio la spettroscopia di assorbimento a raggi X ultra-veloce risolta nel tempo (XAS) si é evoluta fino a diventare l'attuale consolidata e affermata tecnica sperimentale, capace di fornire informazioni estremamente dettagliate sulla geometria locale e sulla struttura elettronica nei primi istanti di una reazione chimica o di un prcesso biologico. I cambiamenti nella struttura elettronica sono alla base delle modifiche che hanno luogo in molte reazioni chimiche e biologiche. La spettroscopia a raggi X ultra-veloce risolta nel tempo é una tecnica sperimentale ideale per indagare questi cambiamenti in "tempo reale" durante il corso di una reazione chimica, di una funzione biologica o di un processo fisico. Idealmente, infatti, l'osservazione dei processi ultraveloci dovrebbe essere effettuata in condizioni più vicine possibili a quelle naturali cioé i processi biologici dovrebbero essere studiati in mezzi fisiologici (invece di cristalli o pellicole congelate). In questo senso, la spettroscopia XAS è unica nel suo genere, in quanto può essere applicata a qualunque tipo di sistema.

In questa tesi abbiamo implementato con successo un nuovo schema per misurare la spettroscopia di assorbimento a raggi X risolta nel tempo con una risoluzione del picosecondo nel rateo di ripetizione del MHz. L'aumento nel rateo di ripetizione nell'acquisizione dei dati ha portato all'incremento nel rapporto segnale/rumore di un fattore superiore a 20 in confronto agli esperimenti effettuati nel regime del kHz. Per verificare i miglioramenti ottenuti grazie a questa nuova metodologia per l'acquisizione dei dati, abbiamo usato la transizione di spin indotta dalla luce nelle soluzioni acquose di $[Fe(bpy)_3]^{2+}$, punto di riferimento dei nostri esperimenti. Tale sistema é stato infatti ampiamente caratterizzato sia dalla spettroscopia con laser ultra-veloce che da quella a raggi X risolta nel tempo. Il guadagno atteso nella qualità dei dati é stato confermato, permettendo così l'osservazione di sottili cambiamenti nella regione delle spettro XAS prima del picco: tali variazioni riflettono la diversa struttura elettronica di $[Fe(bpy)_3]^{2+}$ in presenza di una transizione di spin.

Presentiamo anche lo studio delle strutture elettroniche e geometriche di una serie di metalloproteine (Mioglobina) in soluzioni fisiologiche, effettuato tramite la spettroscopia di assorbimento a raggi X. Per quanto ci é dato sapere, questo é il primo studio della struttura di diverse forme di Mioglobina in un mezzo fisiologico, effettuato usando la spettroscopia XAS. L'analisi della regione XANES dello spettro, effettuata usando il formalismo della diffusione multipla completa, ha rivelato che la lunghezza del legame ferro-azoto nell'anello porfirinico converge a un valore comune di circa 2 Å , al contrario

delle ampie variazioni trovate nelle strutture cristallografiche: il fatto che le porfirine siano notoriamente strutture molto rigide a causa dei numerosi doppi legami carbonio-carbonio supporta a pieno la nostra conclusione. La geometria dei ligandi relativa al gruppo eme é descritta per l'intera serie di Mioglobine studiate. Inoltre, lo spettro XAS a tempo risolto é stato misurato per due tipi di Mioglobina, MbCO e MbNO. Abbiamo mostrato che, come atteso da studi precedenti, la struttura transiente della proteina MbCO fotoeccitata assomiglia a quella della Mioglobina ferrosa non legata (deossiMb). Al contrario, la struttura del MbNO fotoeccitato a 50 ps devia leggermente da quella della della deossimioglobina. L'analisi del transiente XANES indica che la molecola NO si allontana di 2.88 Å dal gruppo eme, stando più vicina all'atomo di ferro che nel caso della proteina MbCO fotoeccitata. Anche il tempo di ricombinazione del geminato NO con l'eme é stato misurato in "tempo reale" ed é risultato avvenire in 216 ± 24 ps: questa é la prima misura diretta (cioé sensibile ai cambi di struttura) del tempo di ricombinazione di tale geminato.

KEYWORDS: *Spettroscopia di assorbimento a raggi X, Spettroscopia di assorbimento a raggi X ultra-veloce risolta nel tempo, Alto rateo di ripetizione, Proteine, Mioglobina, Soluzioni fisiologiche, Impulsi a raggi X nel dominio temporale del picosecondo, Radiazione di Sincrotrone, Spettroscopia Pump-probe*

"The diversity of the phenomena of nature is so great, and the treasures hidden in the heavens so rich, precisely in order that the human mind shall never be lacking in fresh nourishment."

Johannes Kepler

1 Shining Light into Biology

Over many years the curiosity of mankind has been the driving force for new discoveries that have changed the way we live and interact with the world. From cosmological length scales to elementary particles, we have been looking for a complete description of the universe we live in. The understanding of many complex processes in nature have greatly influenced almost all aspects of modern human society.

Biological molecules represent a typical example of the complexity of fundamental processes working in conjunction, resulting in a very interesting fact: *life*. These biological molecules fall in a special category when trying to apply a methodology to try to understand how they function. They are too small to be completely described by classical theories, yet too big to be accurately described by quantum mechanics. The search for an appropriate theory that can account for the behaviour of biological molecules is an ongoing task for many scientists. In contrast with the enormous amount of different functions played by proteins is the small amount of fundamental pieces composing them. Only twenty different structures are combined to form as many as 100 000 different proteins, which are responsible for executing and controlling all the biological functions in living organisms [1].

It can be said that if proteins were were rigid, static structures no life could exist [2]. Numerous experiments have shown that ligand and substrate binding, partner recognition, control of transport processes, catalysis and in general, regulation of activity demand flexible structures capable of movement. The static view given by the crystallographic structure provides information of an ensemble of states of the macromolecule, and although this information is valuable, it can be misleading when trying to understand how certain biological processes occur. Understanding the general rules which govern the prevailing structure of a protein in its natural state and defining an appropriate theoretical framework capable of describing its dynamic behaviour is one of the main goals for modern structural biology. In this sense, this has become a multidisciplinary topic, involving physicists, chemists, computer scientists and mathematicians. The combination of experimental tools and theoretical treatments each of these specialists can provide helps in broadening the knowledge about the correlation between structure and

function in biological systems. The next frontier of structural biology is the elucidation of the structure of different proteins at atomic resolution, over the whole timescales of relevance to biology. It is clear that experimental tools that provide information about movement of the atoms, *i.e.* the dynamics, are needed in order to have a full picture of how the protein functions.

Myoglobin (Mb) is an extremely compact heme protein consisting of a single polypeptide chain of 153 amino acid residues. It is found primarily in cardiac and red skeletal muscles, functioning mainly in the storage of oxygen and facilitates the transport of oxygen to the mitochondria [3]. Myoglobin is particularly abundant in diving mammals including the whale, seal, and porpoise. Sperm whale Myoglobin in the ferric form was the first protein for which the complete three-dimensional crystal structure was determined. A breakthrough analysis of the x-ray diffraction pattern was carried out by John Kendrew and co-workers in England in the late 1950's [4]. The investigation of the Mb atomic structure as given by Kendrew *et al.* immediately indicated that there was no obvious channel for the diffusion of oxygen in and out of the protein, thus some mobility of the protein was presumed to be essential for the diffusion process of ligands to the active site. In 1984, Mills *et al.* [5] performed the first ever time-resolved X-ray absorption spectroscopy (XAS) to study the CO recombination to Carboxy-Myoglobin (MbCO) after laser photolysis with μs temporal resolution. They developed a scheme using a synchronized Nd:YAG laser to photolyze the MbCO in a flowing sample solution and probed the changes in the XAS spectrum. After this remarkable experiment, many more time-resolved structural techniques have been applied to the study of photo-excited MbCO [6–17]. This has culminated with the beautiful work of Srajer *et al.* [10] who used nanosecond time-resolved crystallography to study the structure of the protein after photo-dissociation. However, it took a great deal of additional work and several important technical developments [18] to achieve the necessary quality in the diffraction data to allow a direct interpretation in terms of the conformational changes of the protein due to photo-dissociation [11–15]. This wealth of information available about Mb structure and dynamics, however, has not been able to provide a complete and detailed description of its function.

At first glance, Mb can be regarded as a very simple system with a well determined function: store oxygen. However, over the last 20 years the understanding of the functional role of Mb has increased considerably [19]. The concept that Mb serves only to store oxygen, though oversimplified, is correct. It is based on the studies of the physiology of diving mammals, which revealed a ten-fold higher Mb concentration in their muscles than in humans. One of the functions of Mb, which is often neglected, is its contribution in facilitating molecular oxygen diffusion from capillaries to mitochondria [19]. Transgenic Mb-deficient mice were reported to behave normally, but presented an increased density of capillaries so as to compensate for the lack of Mb and the reduction in the effective diffusion path length [20]. More recently, another relevant function of Mb has been proposed: to act a scavenger of NO in muscles, protecting cellular respiration [21, 22]. This NO scavenger effect in Oxy-Myoglobin (MbO_2) is speculated to prevent

inhibition of respiration in the skeletal and cardiac muscle, which would avoid a vicious cycle in the respiration process, leading to death. Myoglobin can be said to represent a paradigm of complexity. As a biological system it is simple enough to present very fundamental biochemical processes to be used as test-case for new theoretical and experimental frameworks, yet complicated to the level that many of these processes are yet to be fully understood. In this sense, Mb is often referred to as the *hydrogen atom of biochemistry* [23]. One very interesting an useful property of Mb is its photo-sensitivity and the ability to photo-induce efficient ligand detachment [3, 24]. This fact has been extensively used by scientists to perform a controlled photo-excitation of Mb and study the resulting effects, including electronic and geometrical changes, ligand rebinding dynamics, changes on affinity and its dependence in external parameters like temperature and pressure.

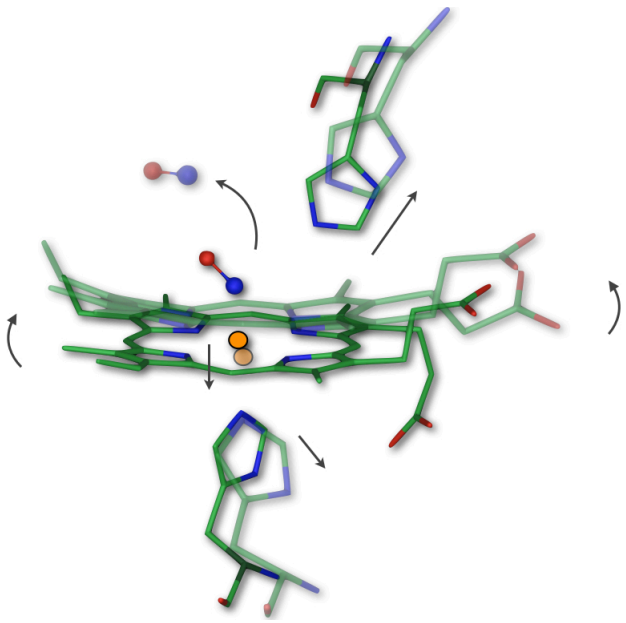

Figure 1.1.: Illustrative picture of the movement around the active center of Myoglobin upon photo-excitation. The ligand moves far from the heme, the iron moves out of the porphyrin plane and the heme domes around it. The position of the proximal and distal histidines are also affected by the ligand movement.

Most of the structural studies of Mb have been performed using crystals, including both the steady-state and photo-excited structures [6–16, 25–29]. This raises a question about the fundamental properties of the protein in crystals and how they are related to its properties in solution. It has generally been assumed that the structures of proteins in crystals and in solution are the same, because the lattice forces are small [24]. In order to investigate this hypothesis, a complete investigation under both sets of conditions is necessary. Some preliminary experiments [24] suggest that the geminate reactions of hemoglobin with O_2 and CO are very similar in solution and in crystals. Even though this is an encouraging experimental verification, many more comparisons between function

in crystals and in solution are required to ensure that the correlations observed are valid independent of the protein. Such a study is not found in the scientific literature, which motivates us to choose to study the structural properties of Mb in conditions as close as possible to those it encounters in its natural physiological environment.

In the XAS spectrum, the low-energy region close to the absorption edge is sensitive to chemical bonding of the valence orbitals, *i.e.* orbital occupancies, oxidation state, charge transfer, orbital hybridization, bonding and backbonding contributions and so on. [30, 31]. It is also extremely sensitive to the structural details of the absorbing site (overall symmetry, distances and angles), though these details are not easily obtained. On the other hand, the high-energy region of the spectrum provides more direct information about bond distances and coordination numbers, *i.e.*, the structural geometry as a whole. Extending the XAS technique to include the time domain as a parameter allows the study of ultrafast photo-induced processes like intramolecular electron transfer, molecular spin transitions, chemical bond formation and many others [32–38]. In particular, the study of biologically relevant processes using XAS includes the investigation of the photo-detachment of CO in Carboxy-Myoglobin [25–29].

Time-resolved XAS have been extensively applied to a broad range of systems in the fields of biology, chemistry, physics and materials science. Complete reviews are given by Bressler and Chergui [32–34] and Chen [38], showing the main advances in ultrafast time-resolved XAS in the last 10 years and emphasizing the primary breakthroughs. Many of the scientific problems tackled by time-resolved XAS were performed in liquids, which is the natural environment in which many relevant chemical and biological processes occur. These studies greatly profit from the XAS local sensitivity and the ability to investigate, in real time, both the geometrical structure and the electronic structural modifications underlying the geometry rearrangement. With the aim of studying ultrafast processes in proteins in natural conditions, we have implemented a new scheme for ultrafast time-resolved XAS experiments, increasing the data acquisition repetition rate by a factor of 500. This way, the laser and x-ray repetition rates are better matched, allowing significant improvements in data quality, along with decreased acquisition times. A comparison with previous experiments [39, 40] reveals an increase of about 20 times in the signal-to-noise (S/N) ratio. This new scheme has made possible the measurement of subtle changes in the pre-edge region of the XAS spectrum of $[Fe(bpy)_3]^{2+}$, which was the test case system used to benchmark our new setup. We then focused on the study of several different forms of Mb in physiological solutions. We revised the steady-state XAS spectra of these species, analysing the XANES region. The time-resolved XAS of MbCO and MbNO (Nytrosyl-Myoglobin) were also investigated.

Thesis outline

Chapter 2 introduces some important aspects of transition metal complexes and their relation with the structure and function of proteins. A short review of hemeproteins and its importance to life are given. Some relevant aspects of the electronic and geomet-

rical structure and the connection with the dynamics of ligand detachment are briefly discussed. Chapter 3 gives an introduction to the x-ray absorption process and the theoretical framework necessary for the analysis of the steady-state and transient XAS spectra. A description of the experimental apparatus used to measure steady-state XAS spectra is given in Chapter 4, which also describes in detail the setup implemented to perform time-resolved XAS measurements at a high repetition rate (MHz). In Chapter 5 the results of the benchmark experiments of the new high repetition rate scheme for ultrafast time-resolved XAS experiments are presented, together with the analysis of the spectral features in the pre-edge region. A detailed investigation of the steady-state XAS of several Mb forms in physiological solutions is presented in Chapter 6, together with the study of the time-resolved XAS of MbNO. The main conclusions are given in Chapter 7, together with an outlook and future perspectives for the type of studies presented here.

"Few scientists acquainted with the chemistry of biological systems at the molecular level can avoid being inspired."

Donald J. Cram

2

Transition metal complexes and heme proteins

This chapter introduces some important aspects of transition metal complex photochemistry and the involvement of the d electrons in forming bonds with ligand molecules. In this thesis, two particular examples of transition metal complexes have been investigated, one representing a general class of spin-transition systems - $[Fe(pby)_3]^{2+}$ - and one model system of metallo-proteins - Myoglobin (Mb). We will briefly introduce the class of heme proteins and stress its importance to biology and life. Following, a short description of the structure of Mb is given and the implications on the ligand binding/release. The Chapter finishes with a review of the recent XAS studies of Mb.

2.1 Importance of d electrons on transition metal complexes

Transition metal complexes represent an important class of coordination chemistry [41] compounds and have been extensively studied as molecular model systems for complex interactions involving electronic, spin and structural degrees of freedom in catalysis, material synthesis, photochemistry and biology [41, 42]. Most of the times, these molecules consist of a central transition metal bound to another group of organic molecules called *ligands*.

Complexes formed by transition metal ions usually contain a well-defined number of ligands. The number of ligand atoms forming bonds with the metal is often referred to as the *coordination number*. The chemical reactivity of a certain complex depend mainly on the electronic properties of the system [43]. One of the main characteristic features of transition metal complexes is the presence of unpaired d electrons. These electrons are involved in molecular boding and are the ones determining the complex chemistry of transition metal complexes [44, 45]. Additionally, the presence of ligands lowers the spherical symmetry around the transition metal and breaks the energy degeneracy of the atomic d levels [41]. An illustration of the 5 atomic d orbitals is shown in Figure 2.1.

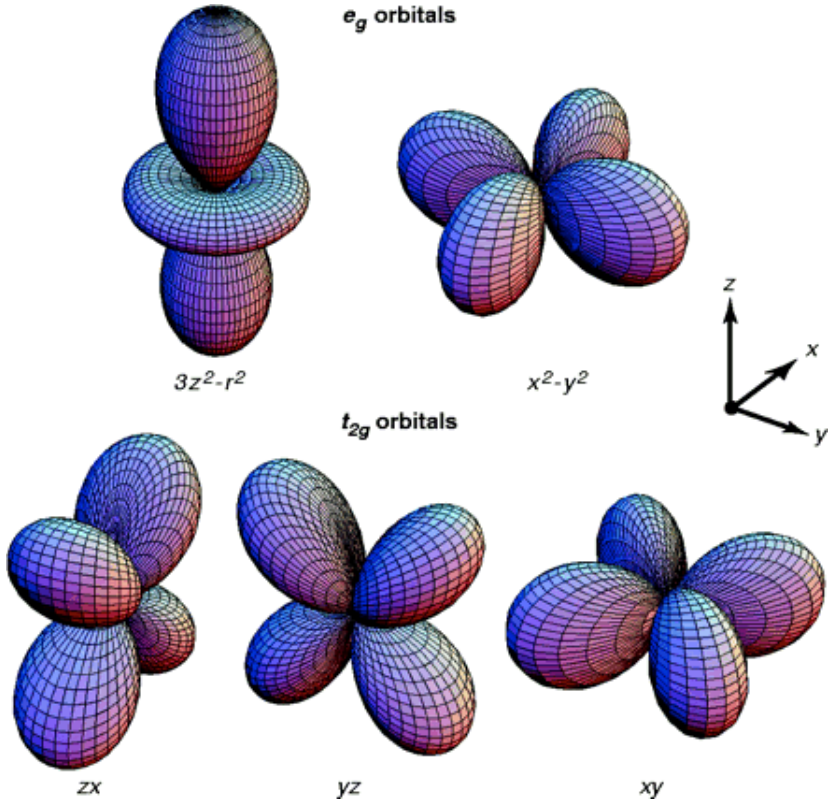

Figure 2.1.: Representation of the 5 different forms of d orbitals in transition metal complexes. Reproduced from Ref. [46]

The electronic density associated with these orbitals are represented by the lobes. Three of the five orbitals are degenerate, and in a Cartesian coordinate system, are oriented between the axes. They are named as d_{xy}, d_{yz} and d_{zx}. The other two orbitals, d_{z^2} and $d_{x^2-y^2}$, are oriented along the axes. In an octahedral geometry, the energy splitting of the d-levels groups the five d-orbitals into two bands, which are called t_{2g} and e_g. The orbitals constituting the t_{2g} level are those oriented in-between the Cartesian axes, *i.e.*, d_{xy}, d_{yz} and d_{zx}. On the other hand, the e_g level is constituted by the orbitals aligned along the axes, d_{z^2} and $d_{x^2-y^2}$. The difference in energy between the t_{2g} and e_g levels is called *ligand-field splitting* and is denoted by Δ or 10Dq. An illustration of the splitting of the d-orbitals is shown in Figure 2.2. The geometrical structure of a transition metal complex strongly depends on the electronic configuration. The bond length between the metal and the ligands, as well as its relative strength, is reflected by the occupation of bonding and anti-bonding orbitals.

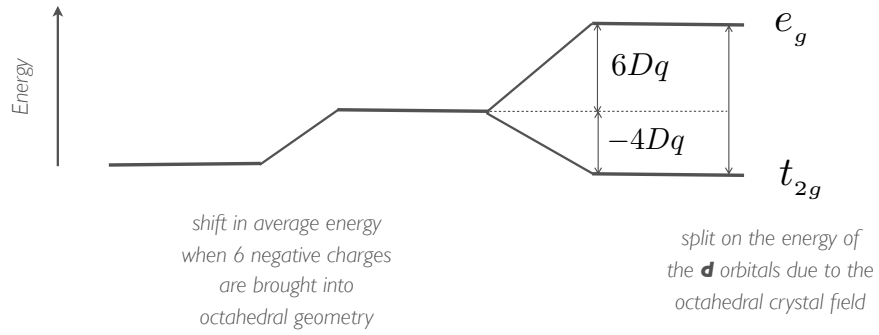

Figure 2.2.: Illustration of the energy splitting of the d orbitals in a transition metal complex with octahedral symmetry.

2.2 Heme proteins and its importance to biology and life

Proteins perform most of the work in living systems. Between one quarter and one third of all known proteins are metalloproteins, *i.e.* proteins that contains a metal ion either as a single atom or as part of a cluster [47]. Among the fundamental biological processes in which metalloproteins participate as the main actor are electron storage and transfer, di-oxygen binding, storage and activation, and subtract transport, catalysis and activation. Much of this activity has to do with the properties of the metals inside those proteins. An understanding of protein function with predictive power will advance fields from biology to medicine and bioengineering. The road to such an understanding requires detailed studies of simple protein models that provide a deep understanding of the fundamental processes occurring when they function.

Myoglobin (Mb) is a good candidate for the endeavor of understanding protein function. Mb is an extremely compact heme protein found primarily in cardiac and skeletal muscles, and as such, it can be obtained in relatively large quantities and represents a

rather simple structure. Although the textbook role of Mb is only the storage of dioxygen, it has long been known to react with a wide variety of small molecules [3]. The suggestion that the physiological role of Mb may be multifaceted comes from many observations in biochemistry, *e.g.* NO and CO are intimately involved in the regulation of cellular function, H_2O_2, O_2^- and $ONOO^-$ are decisive to oxidative damage and perhaps regulation of tissue, and it is present at high concentrations in muscles [48]. Indeed, many other biological functions have been associate with Mb. It may facilitate oxygen diffusion, mediate oxidative phosphorylation, protect against oxidative damage, and inactivate enzymes. Mb also may increase the effectiveness of NO as a signalling molecule by enhancing the NO concentration gradients [48, 49]. Another crucial role attributed to Mb is the ability to act as NO scavenger in heart and skeletal muscle [21, 22, 50]. The reaction cycle of Myoglobin with respect to the interaction with NO and O_2 is illustrated in Figure 2.3. Mb in its unligated ferrous form (deoxyMb) reversibly binds O_2 to yield Oxy-Myoglobin (MbO_2) which is long known to facilitate the transport of oxygen from the periphery of the cell into the mitochondria for use in respiration. MbO_2 reacts irreversibly with NO yielding nitrite and unligated ferric Myoglobin (metMb), so that free NO molecules that otherwise might inhibit Cytochrome-c oxidize are neutralized. The cycle continues with metMb being reduced to deoxyMb, which also binds to free NO molecules.

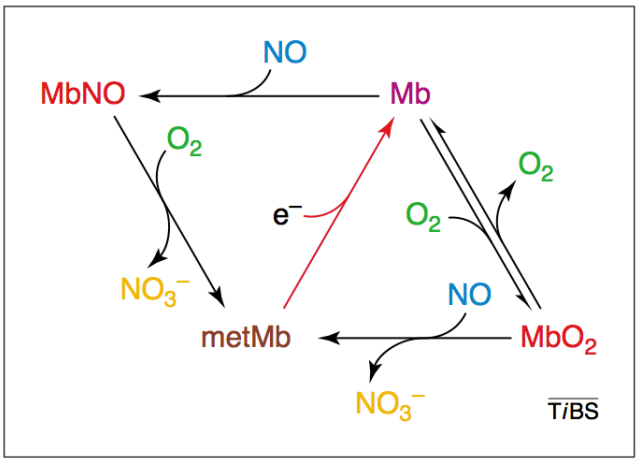

Figure 2.3.: The reaction cycle of Myoglobin with O_2 and NO. Taken from Ref. [22]

Other heme proteins have recently been discovered, indicating that the complete function these proteins have for life are far to be understood. Particularly exciting is the recent discovery of a new heme protein in the nervous system of vertebrates, Neuroglobin (Ngb) [51]. The physiological role of Ngb is still debated, although recent studies have proposed that Ngb is involved in neuroprotection, as the recovery from stroke in experimental animals is enhanced by over-expression of this protein [51–53]. Recent studies on the structure of this protein using XAS and molecular dynamics [29, 54] reveals an interesting new world of protein dynamics to be explored by structural sensitive time-resolved

techniques, *e.g.* time-resolved XAS, XES and RIXS.

2.2.1. Myoglobin structure

Myoglobin is hailed to be the first protein to be seen at atomic resolution. Breakthrough x-ray analysis of myoglobin was carried out by J. Kendrew and co-workers in England, back in the end of the 1950's [4]. A very complex x-ray diffraction pattern, with nearly 25,000 reflections was resolved via a fourier transform computer analysis in three stages. The structure of Mb is illustrated in Figure 2.4. The main aspects of the structure are shown, the α-helices in green and the heme group in the active center in blue. The ligand is shown as the two yellow spheres. The heme is embedded inside the protein, without direct contact to the surrounding solvent. An investigation of the structure reveals the absence of an obvious channel through which ligand migration between the active site and the solvent could happen during biological function [55]. Moreover, analysis of the structure of globular proteins revealed that internal packing defects result in the formation of cavities, which are known as the Xenon cavities [56, 57]. The structure of metMb equilibrated with Xe at 7 atm at room temperature showed the presence of four binding sites [58]. The presence of these holes inside the protein have been connected to the ligand migration and docking [13, 59]. This has caught the attention of many scientists interested in investigating how does the structure of Mb controls its function. Conformational fluctuations in proteins have been used to explain the diffusion of small

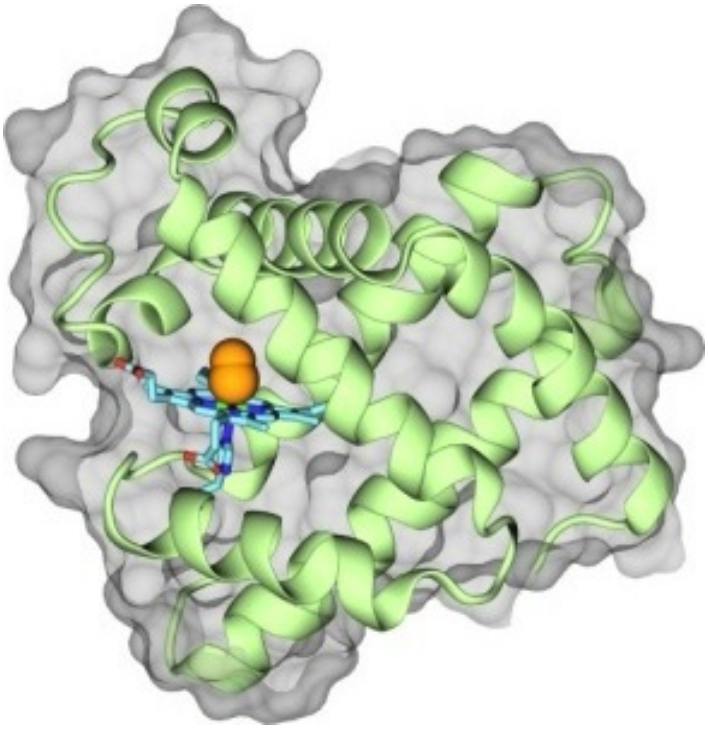

Figure 2.4.: Three-dimentional representation of the geometrical structure of Myoglobin. Reproduced from Ref. [60]

ligands through the protein matrix [2]. The link between structure, function and now dynamics was established.

2.2.2. Myoglobin structural dynamics

Ultrafast laser spectroscopy has provided a wealth of novel information about the structural dynamics of Myoglobin. [2, 61]. The photo-dissociation of the ligand has been used to mimic the protein function of ligand diffusion. However, this photo-activation process is not natural, but due to the high quantum yield associated [62, 63] it has been used in a controlled way to synchronize the ligand dissociation and study the subsequent dynamics of the protein [2, 62, 64]. The early photo-physical processes involve two excited states, which decay in a few hundred fs and a few ps, respectively [64]. The dynamics of geminate recombination after ligand photo-dissociation have been studied in the ps time scale, so as to indirectly probe the resulting protein structural rearrangement. In Carboxy-Myoglobin (MbCO), multiple time-dependent energy barriers affect the motion of the CO molecule within the protein matrix, resulting in a non-exponential time dependence of the ligand detachment. The ligand dissociation process in MbCO can be represented by a simplified three-state scheme

$$MbCO \rightarrow Mb* \rightarrow Mb \tag{2.1}$$

in which MbCO is the starting point of the protein (ground-state), Mb is the final state in which the CO molecule is in the solvent outside the protein, and Mb* represent all the intermediate states when the CO molecule is in the protein matrix.

Many photo-crystallography studies with ps-ns time resolution have shown that after photolysis, major structural rearrangements take place [11–15, 55]. These include the displacement of the iron in the heme towards the proximal histidine (His93) and side chain movements to reach a conformation similar to deoxyMb. All these movements are fully developed within 3 ns, and the protein only reaches back its initial state after ms [65]. Concomitant with the structural changes in the heme site, docking of the CO ligand in one of the Xe cavities is observed

2.2.3. XAS studies of Myoglobin

The experimental methodology and data analysis procedure for XAS started to gain momentum at the time when the rapidly expanding horizons in biochemistry started to propose some important structural questions. Luckily, at the same time synthetic models for metalloprotein active sites (metallo-porphyrins) became available, providing valuable insight into the structure of these metalloproteins [30]. An interesting example is the use of porphyrin compounds to investigate hemoglobin cooperativity, immediately after their structure was determined.

The study of the structure of metallo-proteins profit enormously from the advances in

x-ray-based techniques. Crystallography and especially XAS have been used regularly for metallo-protein characterization [66]. The local symmetry in the porphyrin ring structure of Mb results in relatively strong modulations in the fine-structure of the XAS spectrum. Many contributions are observed, not only from the the N atoms in the pyrrole rings and axial ligands (proximal and distal histidines), but also from distant shells of carbon atoms making the porphyrin [30]. Unfortunately, when questions about the doming of the porphyrin arise, the analysis of the spectrum is dubious, and have led to surprisingly different interpretations of the data [67].

One problem that affects the structural determination of proteins is the radiation damage. Free radicals are produced when x-rays strike biological samples. Although direct photo-reaction of biological metal centres may occur, the more important damage mechanism is reaction with migrating free radicals and hydrated electrons. Measurable photo-reduction of Cytochrome c has been reported [30], and even exploited experimentally to induce lysis of MbCO [27]. The opposite effect, photo-oxidation of a reduced protein has not been reported [30]. The physics of x-ray radiation damage have been discussed extensively [30, 68–71]. In a first approximation it does not appear to be an insurmountable problem for biochemical XAS studies as long as appropriate precautions are taken. These may include the use of low temperature (most common of all), frequent sample changes, radical traps, or excessive reductant use. However, in crystallographic studies, radiation damage can be a serious problem [68–75]. A recurrent debate in the literature about radiation damage involves whether or not there are dose-rate effects at cryo-temperatures. No definite answer seems to exist, the best approach is to keep the x-ray dose as low as possible and, if possible, exchange the sample regularly and monitor its properties (UV-Vis spectrum) in the course of the experiment.

The Mb structure has been extensively investigated by means of XAS over the last years, notably by groups in Rome, L'Aquila and Frascati, all in Italy. Studies involving crystallography are more widespread, remarkable examples involve the study of the CO photo-dissociation in MbCO [11–15]. Interestingly, these studies have been always performed using crystals. Even when the use of protein solutions in XAS experiments is reported, an investigation of the experimental description indicates that the spectra were collected at 20 K [76]. Even though no influence of x-ray damage has been reported in the XAS studies, it cannot be completely neglected. On the other hand, using flowing liquids eliminates this problem. The deposited x-ray dose on each molecule is minimized and it is given time to disperse the free-radicals. However, no study of the structure of Mb in solution was found in the literature.

2.3 Conclusions

Metallo-proteins are extremely important in biological function. Myoglobin, specifically, has been proved to be responsible for many different ones, from the simple storage of di-oxygen in muscles to aid in cellular signalling. As a model system for scientists, it

represents the ideal system. It is simple enough to allow the study of very fundamental processes, but complicated to a level that the investigations are not boring.

Myoglobin exist in the ferric (Fe^{3+}) or the ferrous (Fe^{2+}) states, both having some biological role. The fluctuations in the conformational state of Mb lead to the concept of *energy landscape*, which states that the protein is not a static structure. Several simultaneous conformational substates exist and are directly connected to the functional role of the protein.

Myoglobin has been investigated for more than 100 years. Nevertheless, a complete understanding of its functions and the connections between structure and dynamics have not been reached. We hope to provide one more contribution to the study of this magnificent system by using XAS under physiological conditions. This way, our results should provide a more realistic picture of the local structure, because of the use of liquid solutions in an environment close to the natural one.

"The fundamental laws necessary for the mathematical treatment of a large part of physics and the whole of chemistry are thus completely known, and the difficulty lies only in the fact that application of these laws leads to equations that are too complex to be solved."

Paul Dirac

3

X-ray absorption spectroscopy: theory and data analysis

This chapter introduces the x-ray absorption process and gives a quantitative description of x-ray absorption spectroscopy (XAS) to support the analysis of the XAS experiments of $[Fe^{II}(bpy)_3]^{2+}$ and Myoglobin, given on Chapters 5 and 6, respectively. It starts in Section 3.1 with a brief description of the physical phenomena involved in the x-ray absorption process. In Section 3.3 a short review of the theoretical framework used to explain the x-ray absorption spectroscopy in terms of Full Multiple Scattering (FMS) theory is given. Two examples of the computer codes used for calculations of XAS spectra are given, with emphasis on the different approaches for interpreting XAS spectra, *i.e.*, simulation and fit. The `FEFF9` and `MXAN` computer codes that are used for the XANES calculations/fits in Chapters 5 and 6 are described in Sections 3.3.5 and 3.3.6, respectively.

3.1 X-ray interaction with matter

X-rays were first observed by Wilhem Conrad Röntgen in 1895 when performing experiments with a high-voltage discharge tube in a darkened room [77]. The name given to this new type of radiation was inspired on the unknown nature of the radiation emitted by those discharge tubes, and it is now known they are electromagnetic radiation with wavelength in the range of an Ångstrom (1Å= 10^{-10}m). Since their discovery x-rays have become an invaluable tool for the study of the structure and properties of matter. The constant advances in both the theoretical understanding of the interaction of x-rays with matter and in the expertise of how to exploit them experimentally, have been used by many different branches of science, from the fundamental properties of the surface of monoatomic crystals, to more complex systems such as the three-dimensional structure of DNA and biologically-relevant proteins.

Being an electromagnetic wave, x-rays shows waveparticle duality, which is described by the well-known relation between quantized energy and wavelength:

$$E = h\nu = hc/\lambda_{ph} \tag{3.1}$$

with E being the energy of the photon, h is Planck's constant, c is the speed of light, and ν and λ_{ph} are the frequency and wavelength of the wave. The wave-particle character is also a phenomenon observed with electrons. We often speak of the *de Broglie* wavelength λ_{el} (and momentum p_{el}) of an electron, given by:

$$\lambda_{el} = h/p_{el} \tag{3.2}$$

The kinetic energy of an electron is related to its *de Broglie* wavelength by eq. 3.1 (also known as the *Einstein relation*) and is given by:

$$E_{el} = h^2/2m_{el}\lambda_{el}^2 \tag{3.3}$$

where m_{el} is the electron mass.

Several kinds of interactions of x-rays with matter can occur, the most relevant ones are absorption and scattering. At very high energies (greater than 1.022 MeV[a]) production of electron-positron pairs becomes possible. This process is, however, negligible at typical energies used for x-ray absorption spectroscopy, *i.e.,* up to several tens of keV. [31]

X-ray scattering events occur when x-ray photons, after interaction with matter, are deflected from their original direction of propagation. Elastic (Thomson) scattering happens when a photon with specific frequency ω and momentum $\vec{k}$ impinges on a sample, interacts with the electrons, and a photon of the same frequency but different momentum direction ($\vec{k}$) is emitted. From a classical point of view, an incident electromagnetic wave

[a] The pair production cross-section only becomes significant for gamma rays with energies above $2mc^2$ = 1.02 MeV

causes the electrons bound to an atom to oscillate back and forth, and these electrons generate their own secondary wave field that has the same frequency as the incident wave. Inelastic scattering differs from elastic scattering in that the frequency of the emitted photon is not the same as the incident photon; it is generally of lower frequency, *i.e.*, lower energy. The energy difference between the scattered and incident photon is transferred to the sample, generally by inducing electronic transitions.

An x-ray photon is absorbed by an atom and the excess energy is transferred to an electron, which is expelled from the atom, leaving it ionized. The process is known as *photoelectric absorption* and will be explain in detail in Section 3.3. Two dominant processes occur subsequent to the absorption of an x-ray photon and the ejection of a photoelectron: x-ray fluorescence and Auger electron emission.

In x-ray fluorescence, all the excess energy remaining in the atom, after relaxation of an electron from a shell further out to the hole left behind by the photoelectron emission, is carried away by an x-ray photon. In contrast, Auger electron emission is a nonradiative process, in which the excess energy is carried away by a second electron being ejected. Auger-electron emission and x-ray fluorescence are competitive processes [77, 78]. The rate of spontaneous fluorescence is proportional to the third power of the energy difference between the upper and lower states.

3.2 Origin and description of the x-ray absorption effect

The absorbing power of a material is given by the absorption coefficient μ, which describes the attenuation in the intensity of an incident x-ray beam passing through a medium. Formally, μdz is the attenuation of the beam through an infinitesimal amount of sample dz as illustrated on figure 3.1. The x-ray intensity I_T after such path is, therefore:

$$-dI_T = I_T(z)\mu dz \tag{3.4}$$

which can be solved by simple integration, leading to the *Lambert-Beer law*:

$$I_T(z) = I_0 e^{-\mu z} \tag{3.5}$$

where I_0 is the incoming x-ray intensity.

The absorption coefficient μ depends on the types of atoms constituting the medium, how they are distributed, the nature of their bonding, magnetism, the light polarization and the wavelength of the x-rays. By measuring the incoming and transmitted x-ray intensities, and knowing the exact sample thickness d, the absorption coefficient can be experimentally determined using $\mu = \ln(I/I_0)/d$.

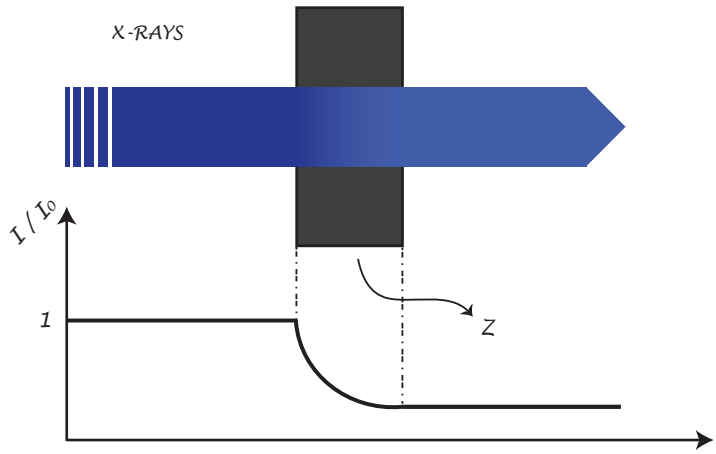

Figure 3.1.: Illustration of the attenuation of an x-ray beam passing through matter due to absorption. The attenuation follows an inverse exponential curve as given by equation 3.5.

3.2.1. Absorption coefficients and cross-sections

The absorption coefficient is essentially an indication of the electron density in the material. Consequently, if a particular substance can assume different geometric forms, and therefore have different densities, μ will be different accordingly. Likewise, compounds that are chemically distinct but contain the same number of electrons per formula unit and have similar densities will have similar absorption properties - except close to an *absorption edge*, where the absorption coefficient increases abruptly due to the absorption of radiation. A manifestation of this effect is evident in the case of Myoglobin with different ligands and/or oxidation state and will be further explored in chapter 6.

One can, equivalently, describe the x-ray absorption effect using a more detailed parameter than μ; namely the *atomic absorption cross-section* of the element σ_a. The relationship between σ_a and μ is given by:

$$\begin{aligned} \mu = \rho_a \, \sigma_a &= \left(\frac{\rho_m N_A}{A} \right) \sigma_a \\ &= c_{mol} N_A \sigma_a \end{aligned} \tag{3.6}$$

where ρ_a, N_A, ρ_m, A and c_{mol} are the atomic number density, Avogadro's number, the mass density, the atomic mass and the molar concentration, respectively. The absorption cross-section has units of area [b] and a useful unit, the *Barn* is often used. One Barn is defined as 10^{-28} m^2 and is approximately the cross sectional area of a uranium nucleus.

The absorption coefficient μ is element-specific and has a strong dependency on the x-ray energy. An example is shown in figure 3.2 for the element gold, together with

[b] The absorption cross-section can, equivalently, be given as the mass absorption cross-section, which has units of area per mass. The relation between them is $\sigma_a[cm^2 g^{-1}] = N_A/A \, \sigma_a[cm^2] = \mu/\rho_m$.

the elastic (Thomson) and inelastic (Compton) scattering contributions [79, 80] This example illustrates the dependency of the absorption cross-section on the x-ray energy (varying approximately as E^{-3}) and the presence of some discontinuities at specific energies. These discontinuities occur at energies for which an x-ray photon has sufficient energy to eject an electron from a core electronic orbital to the continuum, which gives rise to a sudden increase of the absorption cross-section. The presence of these *absorption edges* is the fundamental phenomenon exploited in an X-ray absorption spectroscopy (XAS) experiment, which will be discussed in details in the following sections.

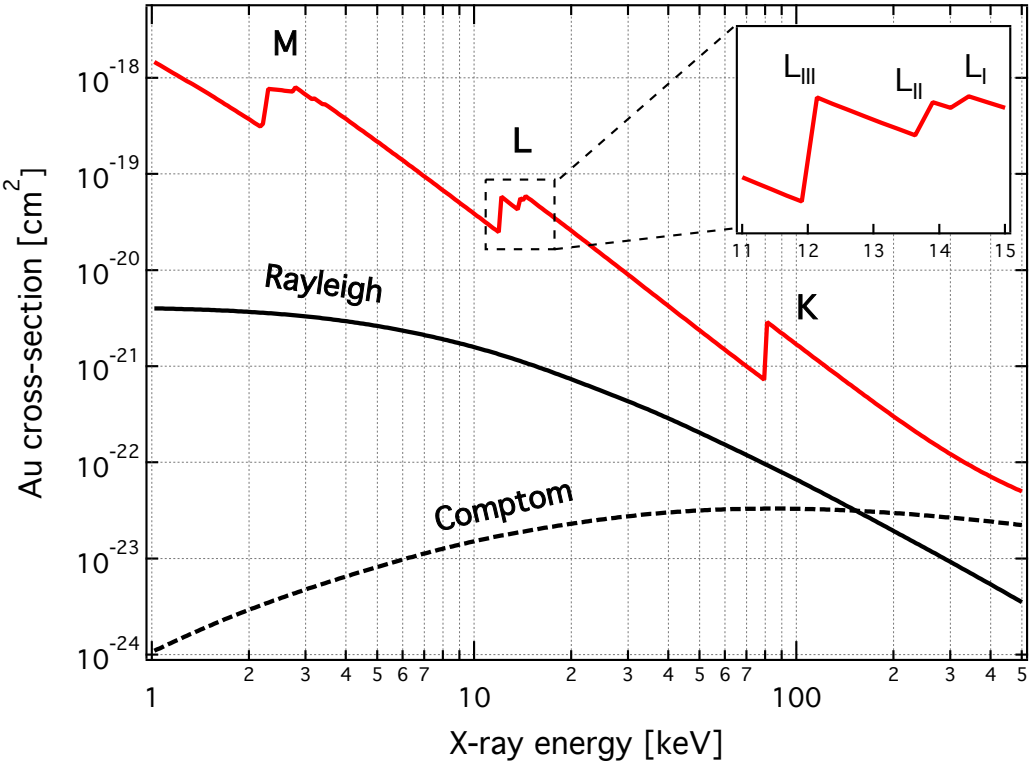

Figure 3.2.: Dependence of the x-ray absorption (red) and scattering (black) cross-sections with energy for the element gold (obtained using the XOP program [79, 80]). The inset zooms into the energy region around 12 keV where the L-edges occur. The nomenclature used to label the different absorption edges is explained on Section 3.2.2.

3.2.2. Absorption edges

As mentioned on the previous section, for a given element the absorption coefficient μ varies approximately as the inverse of the third power of the photon energy. It is also strongly dependent on the atomic number of the element, varying approximately as Z^4. This trend is interrupted by steplike increases in the absorption cross-section at specific energies. The element-specific energies of the discontinuous jumps in μ are called *ab-*

sorption edges. An x-ray absorption edge occurs when the energy of the x-ray photon interacting with the material is sufficient to excite a core-level electron into one unoccupied level above the Fermi energy E_F, the excess energy usually being used to create a photoelectron. This process is known as *photoelectric absorption*. The transitions are usually to a (quasi)-continuum level above the ionization potential (IP), but in the case the electron is promoted to a valence orbital the transition is said to be *bound-bound*. In Chapters 5 and 6 it will be shown that bound-bound transitions play a significant role on XAS of third-row transition metals.

Quantum mechanics states that in a many-electron atom, the electrons occupy a series of discrete atomic levels or orbitals whose wavefunctions and eigenvalues are solutions to the *Schrödinger equation*. Each of these levels is characterized by a series of *quantum numbers*, specifying the state in which the atom is said to be. The levels are classified according to their principal quantum number n, being labelled as K for $n = 1$, L for $n = 2$, M for $n = 3$, ... Constraints on the allowable quantum numbers, together with the *Pauli* exclusion principle, dictate limits on the number of electrons in each shell. In a purely Coulomb field each level has a degeneracy $2n^2$ so that it can contain $2n^2$. In a multi-electron atom however, apart of the Coulomb field of the nucleus, each electron also feels the field generated by the other electrons. The effect is that the degeneracy is lifted into subshells, depending on the quantum numbers, which are then labelled as $(nl_j)^{2j+1}$. The quantum numbers are the principal n, the orbital l, the magnetic m and the spin s. $2j + 1$ represents the multiplicity of a given orbital, quantifying how many unpaired electrons (with different spin) can occupy the same orbital. An externally applied non-central electric field will split even further the subshell, depending on the magnetic quantum number m. Likewise, the presence of an magnetic field will lift the spin degeneracy according to s.

In the Sommerfeld notation the absorption edges are labelled in order of increasing energy. For example the K-edge corresponds to an absorption from the $(1s)^2$ level; whereas the L_I-, L_{II}- and L_{III}-edges arise from absorption from the $(2s)^2$, $(2p_{1/2})^2$ and $(2p_{3/2})^4$, respectively. A scheme of the atomic energy levels and the nomenclature used to label the x-ray absorption edges of the elements is shown on Figure 3.3. The specific energies at which the absorption edges occur are unique to each type of atom, serving as fingerprint of the atomic species present in a material. The absorption cross-section for a certain atomic species has a distinct dependence on the photon energy [81, 82], as shown on Figure 3.2 for the element gold. Far from the absorption edges it is approximately proportional to E^{-3}, where E is the photon energy.

The intensity of the transition is governed by the quantum mechanical laws, given by the transition matrix elements $\langle f \,|\, \mathbb{H} \,|\, i \rangle$ [83], on which $|i\rangle$, $\langle f|$ are the initial and final electronic states and $\mathbb{H}$ is the interaction Hamiltonian. Dipole-mediated transitions are dominant in the case of XAS (see section 3.3), the interaction being given by the dipole operator in the position form $\hat{\epsilon} \cdot \vec{r'}$ [84]. Ignoring the spin, the dipole selection rules are: $\Delta l = \pm 1$, $\Delta m = 0, \pm 1$. Later, it will be shown that the intensities of transitions to final

states can be interpreted by using the connection between the absorption cross-section and the final state l-projected density of states (l-DOS).

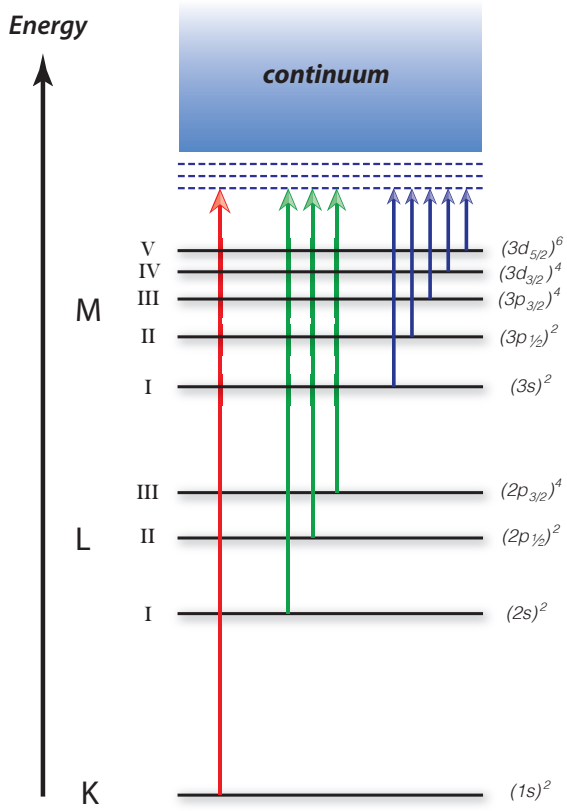

Figure 3.3.: Schematic drawing of the atomic energy levels and the nomenclature used to label the x-ray absorption edges. Transitions occur to empty levels above the Fermi level, according to the dipole selection rules. (Redrawn and adapted from reference [81])

3.2.3. X-ray absorption fine structure

X-ray absorption spectra of molecules or solids present several characteristic features. There are strong fluctuations in intensity around the absorption edge, as well as small-amplitude (typically a few percent) variations at higher energies. These features are absent in isolated atoms such as noble gases on the gas phase, indicating that their occurrence is due to the presence of neighbouring atoms, either altering the electronic structure of the absorber or by scattering/interference effects on the outgoing photoelectron wave created after the absorption effect. They are known as the *X-ray absorption fine structure* (XAFS), containing detailed electronic and geometrical information of the material. XAFS is a very important experimental technique for many branches of science.

Typically the XAFS spectrum is divided in two different regions, according to the energy of the photoelectron and the information content provided. The X-ray absorption near-edge structure (XANES) refers to the energy region lying just above the absorption edge. The lowest-energy XANES signal actually occurs *below* the absorption edge, and are referred to as *bound-bound* or *pre-edge transitions*. They are strongly influenced by the symmetry and local environment around the absorbing atom. The XANES signal is caused by transitions to bound states and the (quasi)continuum just above the ionization threshold and, as such, it reflects mainly the electronic configuration of the material and also the symmetry around the absorbing atom. The low kinetic energy of the photoectrons in the XANES region results on large scattering amplitudes, increasing the occurrence of multiple-scattering events. Because the XANES region is strongly influenced by the symmetry of the local environment around the absorbing atom, many different structural and electronic effects interact and contribute to the signal. These effects, combined with the fact that several approximations are needed for its theoretical description, makes the quantitative interpretation of the XANES spectrum a challenge. Fits of the XANES spectrum to geometrical and electronic properties of the material under study are rather exceptional, *e.g.* via the MXAN [85–87] and FitIT [88]) codes. Recent advances in the theory of XANES, including better models for the potentials and losses are becoming reality [89–91], leading to a better description of the XANES region and leading the way towards a complete *ab initio* description of the entire XAFS spectra. On the other hand, the Extendend x-ray absorption fine structure (EXAFS) refers to the oscillations in the x-ray absorption coefficient starting at approximately 50 eV above an absorption edge and extending up to several hundred eV. In the EXAFS region, the energy of the photoelectrons is such that their mean-free paths is on the order of a few Angstroms, meaning that it mainly probes the immediate neighbourhood of the absorbing atom. Single-scattering events dominate the EXAFS signal, although multiple-scattering also plays a role on the signal. Therefore, it is a local probe, yielding information about the geometrical structure around specific sites. An example of a XAFS spectrum of a biological system in solution (nitrosyl-Myoglobin) is shown in Figure 3.4.

The XAFS spectrum is generally defined as the normalized, oscillatory part of the x-ray absorption coefficient above a certain absorption edge. It is given by:

$$\chi(E) = \frac{\mu(E) - \mu_0(E)}{\mu_0(E)} \tag{3.7}$$

where $\mu_0(E)$ is the smoothly varying atomic-like background, arising from absorption of the absorbing atom in the presence of its neighbours, but without any scatter effect from them. It is often said to be the background due to an "embedded atom" since it comes from the sole contribution of the absorber embedded in a potential generated by its neighbours. Conventionally, χ is defined with respect to the photolectron wavevector k_{el}, *i.e.*, a transformation from the absolute energy space to the relative k-space is done. The photoelectron kinetic energy is given by the difference between the incident x-ray photon energy E and the energy E_0 needed to expel the electron from its core level.

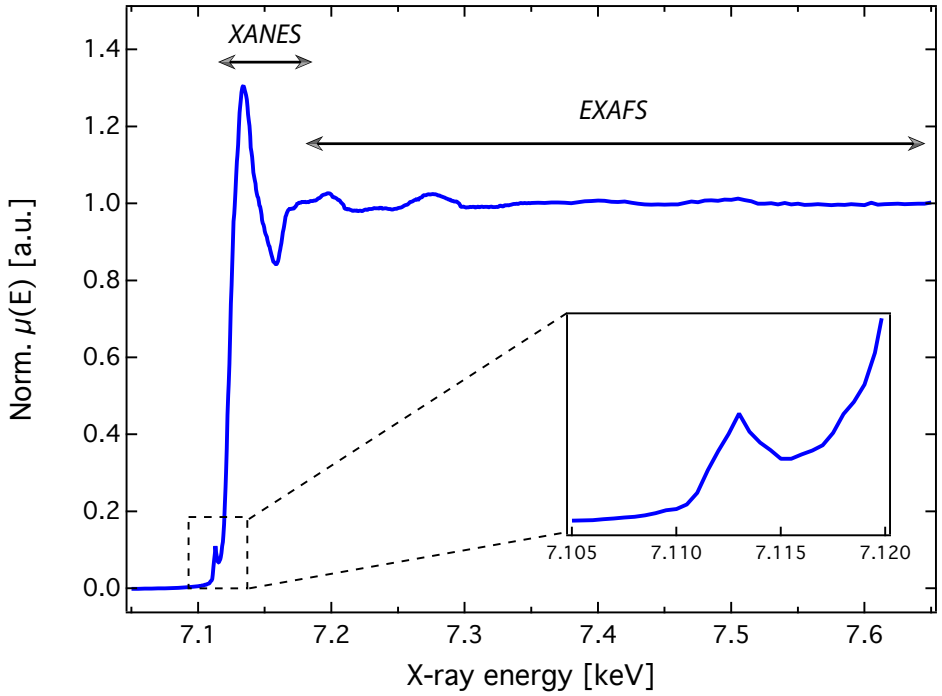

Figure 3.4.: XAS spectrum of a protein (nitosyl-Myoglobin, MbNO) in physiological conditions illustrating the two regions: the low-energy XANES region up to ~ 50 eV above the absorption edge and the high-energy EXAFS region (> 50 eV from the absorption edge). The spectrum has been normalized as described in Section 3.3.4. The inset shows a zoom of the pre-edge region showing the bound-bound transition.

Using Equations 3.2 and 3.3 it is possible to transform from E- to k-space, and the photoelectron wave vector is given by:

$$k_{el} = \sqrt{\frac{2m_{el}}{\hbar^2}(E - E_0)} \tag{3.8}$$

From here on, the subscript $_{el}$ used to identify the photoelectron will be omitted. In cases where confusion may arise, the proper distinction will be made.

3.2.4. Relaxation processes after x-ray absorption

The interaction of x-rays with matter is done via either *absorption* or *scattering* of a photon. In the case of x-ray absorption, a photon is absorbed by the atom and a photoelectron is then created. The excited atom is then in an unstable state and will relax back to its ground-state. The relaxation can happen though several mechanisms, giving rise to fluorescence x-rays, Auger electrons or secondary electrons [81, 82]. These relaxation processes are shown schematically in Figure 3.5.

Radiative decay

The filling of an inner shell vacancy (core hole) by an outer shell electron after the absorption of an x-ray photon, produces *x-ray fluorescence* (Figure 3.5c), whose energy is equal to the difference in energy between the two shells. The nomenclature for the x-ray fluorescence lines is somewhat more complex than that for absorption and is covered extensively in the literature [77, 92]. The reason being that x-ray fluorescence involves two bound orbitals, contrary to only one in the case of absorption. The K- series involves transitions where the electron relaxes to the K- (or $1s$) state. Likewise, fluorescence L-lines have L-states ($n = 2$) as the final destination in the electronic relaxation process, and so on. Within each series, the transition with smallest energy difference between the levels involved is labeled α, with the successive lines denoted β, γ, etc as the energy difference increases. The fluorescence lines are actually further split due to the spin-orbit interaction, and are labelled with suffixes 1, 2 and so on.

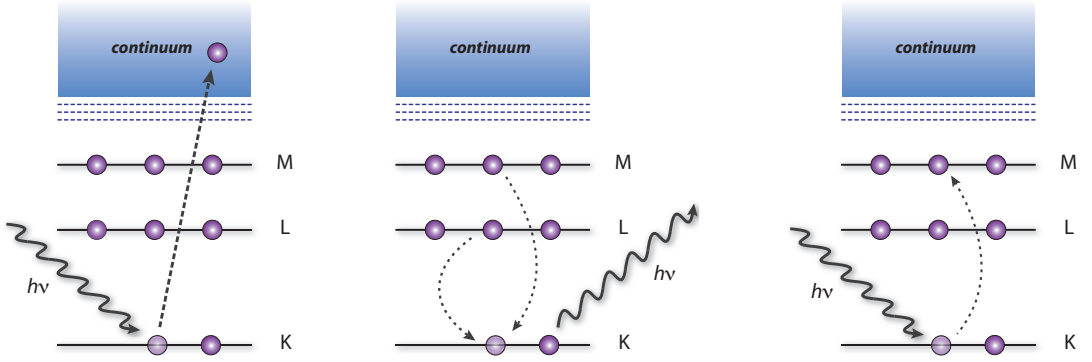

(a) Photoionization (b) X-ray emission (c) Bound-bound transition

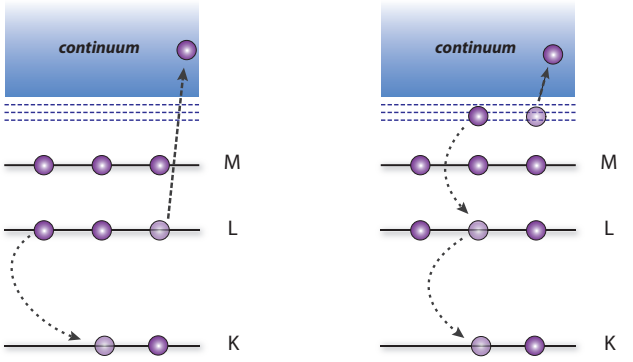

(d) Auger decay (e) Secondary electron decay

Figure 3.5.: Schematics of the energy level diagrams of atomic excitation and relaxation processes. For clarity only the the three lowest shells are shown. (Redrawn and adapted from reference [81]).

The fluorescence yield (or radiative probability) ϵ_f is defined as the ratio of the emitted x-rays to the number of primary vacancies created. The ϵ_f function increases monotonically with the atomic number Z, and is larger for K than for L and subsequent emissions. The measured x-ray fluorescence intensity I_F is proportional to the incoming x-ray intensity I_0, the fluorescence yield ϵ_f, the absorption coefficient $\mu(E)$ and fractional solid angle of detection $\Omega/4\pi$. X-ray fluorescence or, more generally *x-ray emission* can also be used to obtain electronic information about the material under study. It exhibits chemical sensitivity if the instrumental energy resolution is on the same order of the lifetime broadenings [93]. Non-resonant x-ray emission spectroscopy (XES) provides information on occupied electron orbitals in the valence shell. The experiment is done by tuning the incident energy to an absorption edge and observing the specific x-ray emission lines. Figure 3.6 gives an example of a XES spectrum of an aqueous solution of $FeCl_2$, showing the $K\alpha_1$ and $K\alpha_2$ emission lines of iron.

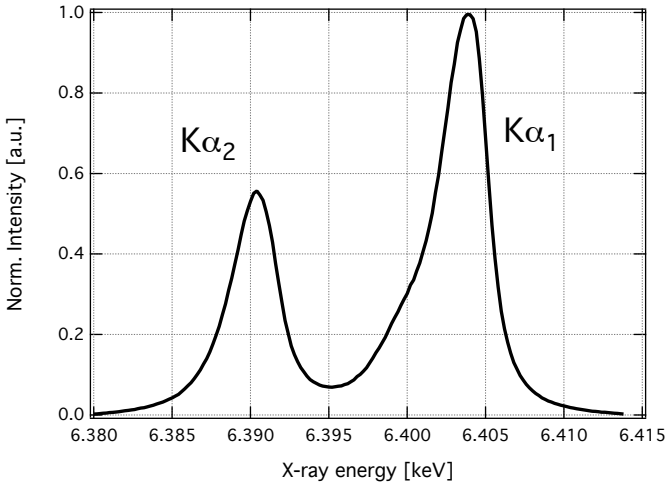

Figure 3.6.: XES spectrum of $FeCl_2$ in aqueous solution. The spectrum has been normalized to the peak value of the stronger emission line ($K\alpha$).

Non-radiative decay

As stated previously, after the absorption of an x-ray photon the atom is in an excited, unstable state. Apart of x-ray fluorescence, one major de-excitation process is the *Auger effect*. Auger emission (Figure 3.5d) is a radiationless, three-electron process occurring when an outer shell electron relaxes to the core-hole produced by the ejection of a photoelectron and the excess energy is channelled into the ejection of another electron [77]. Another non-radiative process is the production of secondary electrons (Figure 3.5e). The production of secondary electrons is a multi-step process in which emitted fluorescence x-ray photons or Auger electrons eject electrons from the outer shells as they leave the atom. The total yield of the non-radiative processes ϵ_n is given by the complement of the (radiative) fluorescence yield ϵ_f, *i.e.*, $\epsilon_n = 1 - \epsilon_f$. The relative yields

depend on the atomic number Z [77, 78, 82]

3.2.5. Broadening

XAS spectra are intrinsically affected by core-hole lifetime broadening, which gives a finite energy width to energy levels. An atom with a core hole is in an excited, unstable state, and it has a finite lifetime because electrons in higher energy states rapidly make transitions to fill the core hole, either emitting fluorescence radiation or undergoing non-radiative decay as explained previously. The *Heisenberg uncertainty relation* implies that the finite lifetime τ produces an uncertainty (broadening) of the energy given by $\Delta E \approx \hbar/\tau$. The core-hole width ΔE increases with the atomic number Z [31], *e.g.*, going from 1 eV for vanadium ($Z = 23$) up to more than 50 eV for gold ($Z = 79$) in the case of K-shell absorption [78, 94]. The limitation imposed by the core-hole lifetime can be overcome by dispersing the x-ray emission and detecting it with a better resolution than the natural line width, so that subtle details around the edge of the XAS spectra can be investigated. This technique is known as High energy resolution fluorescence detection (HERFD) and will not be covered on this thesis. The theory and technical apparatus are extensively covered on the literature [95, 96].

The photoelectron propagates and interacts with the gas of other electrons in the material as a quasiparticle, with a behaviour that differs from that of a free electron. These many-body effects, such as plasmon excitations, electron-hole pairs and scattering destroy the coherence of the photoelectron wave, resulting on a finite life time which finally leads to an additional broadening of the XAS spectrum [84]. This effect enters the theory of XAS by the use of a complex, energy-dependent *self-energy* $\Sigma(E)$, which is connected to the *mean-free path* of the photoelectron in the system. The importance of the self-energy will be clear on Section 3.3 during the discussing of the XAS theory and the multiple scattering effects.

3.3 Theory of X-ray Absorption Spectroscopy

Although the fine structure present in the XAS spectra has been known since the early 1920's, it has not been satisfactorily described before the early 1970's [30]. The structural information contained on the XAS fine structure was not completely recognized until the the work of Stern, Lytle and Sayers in 1971 [30, 97–99] relating the structural parameters with a Fourier transform of the spectrum.

The x-ray absorption coefficient $\mu(E)$ is proportional to the transition probability of the photoelectric event. According to Fermi's Golden Rule the transition probability is a function of the initial-state and final-state wave functions [100]:

$$\mu(E) \propto |\left\langle f \left| \mathbb{H}' \right| i \right\rangle|^2 \delta(E_f - E_i - \hbar\omega) \tag{3.9}$$

in which the initial and final electronic states are represented by $|i\rangle$ and $\langle f|$, respectively;

$\mathbb{H}'$ represents the interaction Hamiltonian between the x-rays' electromagnetic field and the electrons, and the delta function δ guarantees energy conservation.

The initial state is the localized core level, whereas the final state is that of the ejected photoelectron represented as an outgoing spherical wave originating from the absorbing atom. This outgoing wave is backscattered by nearby atoms producing an incoming (photoelectron) wave at the absorption site. The initial outgoing photoelectron then interferes with the backscattered waves, modulating the matrix element $\langle f | \mathbb{H}' | i \rangle$ that controls the strength of the transition. The modulations in μ arise from the constructive and destructive interference of the photoelectron waves as the x-ray photon energy is varied. The amplitude and frequency of those modulations depends on the type of atom absorbing the x-rays, its electronic structure, the bonding characteristics with the neighbours, and on the geometry in general.

Figure 3.7 shows a pictorial illustration of the process of scattering events in an XAFS process and the consequent interference caused on the photoelectron wave. If the photoelectron scatters off a neighbouring atom only once, the event is said to be a single scattering (SS); whereas multiple scattering (MS) occurs if the wave scatters off twice or multiple times before returning to the absorbing atom.

In an effective *one-electron picture*, after an x-ray absorption event, the excited photoelectron behaves as a *quasiparticle* as it traverses the solid or molecule, moving in an effective complex-valued *optical potential* (V). The XAFS can thus be seen as a pure quantum mechanical problem of solving a one-particle Schrödinger-like equation and finding the photoelectron wavefunctions and eigenvalues. An optical potential, however, introduces losses, which are needed to calculate not only the phase shifts and scattering of the photoelectron wave, but also the damping occurring as it travels through the material. The Schrödinger-like, one-particle Dyson equation for the photoelectron final-state wavefunction ψ_f is then:

$$\mathbb{H}'\psi_f = \left(\frac{p^2}{2m} + V_c' + \Sigma(E) \right) \psi_f = E\psi_f \tag{3.10}$$

where $\mathbb{H}'$ is the (non-Hermitian [c]) final state Hamiltonian, V_c' is the final state Coulomb potential and $\Sigma(E)$ is the photoelectron *self-energy*. The functional form of $\Sigma(E)$ depends on the particular approximation used, and is currently the main bottleneck in the accuracy of the calculations of XANES spectra, as will be shown on Chapter 6. Here and elsewhere a prime is used to denote final-state quantities calculated in the presence of a screened core hole.

[c] The non-Hermiticity implies the eigenvalues are complex, which are responsible for the finite lifetime of the final state.

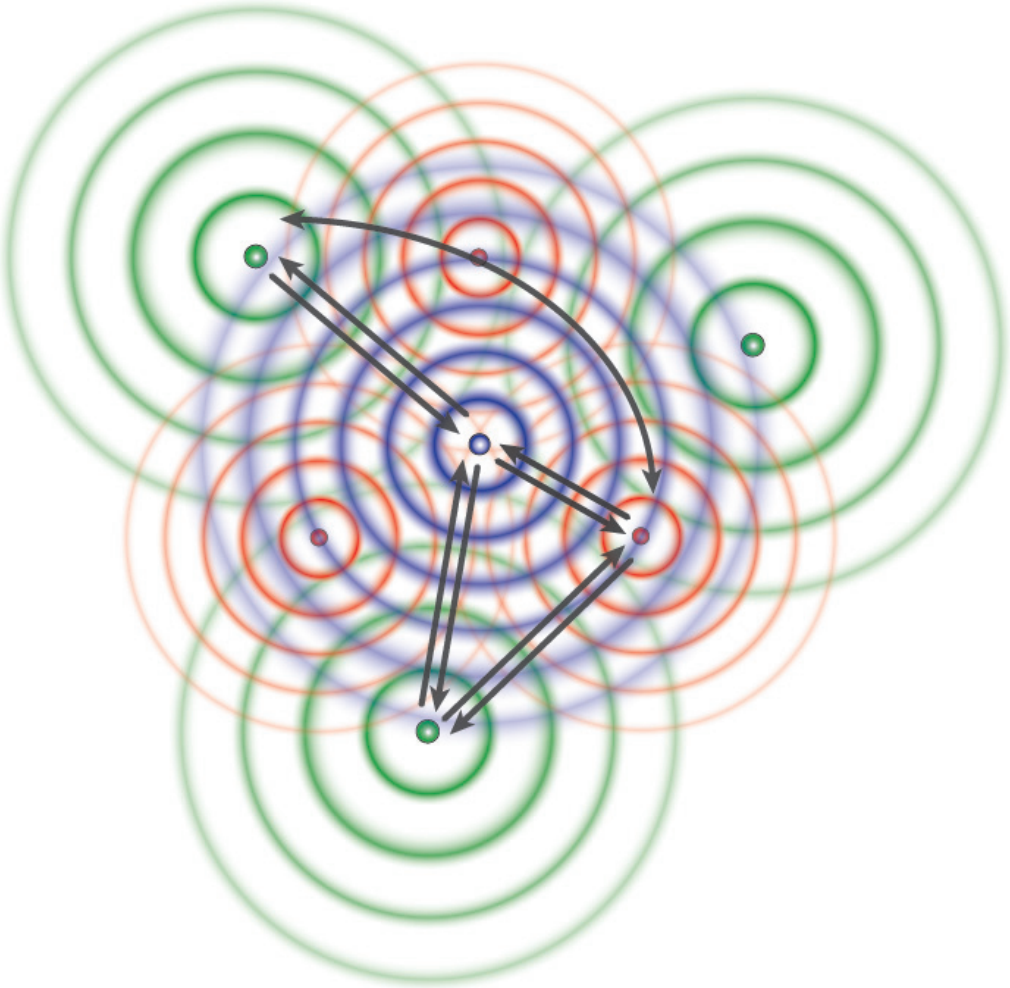

Figure 3.7.: Illustration of single- and multiple-scattering events of an outgoing photoelectron wave (blue) after an x-ray absorption event. The scattering pathways off the first (red) and second (green) neighbours are shown as arrows.

3.3.1. Multiple scattering theory

The calculation of final state wavefunctions ψ_f in the Dyson equation 3.10 is a computationally challenge at high energies. It can only be efficiently calculated for small and highly symmetric systems. Instead of explicitly calculating ψ_f it is preferable to re-express the cross-section in terms of the real space photoelectron Green's function $\mathbb{G}$ in an approach known as the *Real-space Green's function formalism* (RSGF). The spectral representation of the photoelectron RSGF is given by:

$$\mathbb{G}(E) = \frac{1}{E - \mathbb{H}' + i\Gamma} = \sum_f |f\rangle \frac{1}{E - E_f + i\Gamma} \langle f| \tag{3.11}$$

where Γ is the core-hole lifetime. The spectral representation of the Green's function as given by the last term in Equation 3.11 can be used to implicitly sum over the final states, thus allowing the calculation of the XAFS spectrum without the need for explicit calculations of the final state wavefunctions. Using the Green's function in Equation 3.9, and recalling the relationship between the x-ray absorption coefficient and the absorption cross-section (Equation 3.6), the contribution a given core initial state $|i\rangle$ located at the site R gives to the XAS can be calculated by [89, 90]:

$$\sigma(E) = 4\pi^2 \frac{\omega}{c} \sum_{L,L'} M^*_{L,i}(E)\, \rho_{L,L'}(E)\, M_{L',i}(E) \tag{3.12}$$

where $M_{L,i}(E) = \langle i \,|\, \mathbb{H} \,|\, L \rangle$ is the transition matrix element between the initial core-state $|i\rangle$ and the scattering-state $|L\rangle$ given in terms of angular momentum variables $L = (l, m)$, and $\rho_{L,L'}(E) = -(1/\pi)\ \mathrm{Im}\ \mathbb{G}_{L,L'}(E)$ is an element of the density-matrix at the absorbing atom ($\mathbb{G}_{L,L'}(E)$ is the propagator matrix and Im represents the imaginary part). The propagator matrix $\mathbb{G}_{L,L'}(E)$ used on the RSGF formalism is naturally separable into intra-atomic contributions from the central (absorbing) atom $\mathbb{G}^c$ and multiple-scattering (MS) contributions from the environment $\mathbb{G}^{sc}$, such that $\mathbb{G} = \mathbb{G}^c + \mathbb{G}^{sc}$. This way the XAS can be factored as $\mu = \mu_0(1 + \chi)$ as in Equation 3.7. The close relationship between the XAFS and the electronic structure can be seen by the similarity between the contribution μ_{li} to the XAS from a given site i and orbital angular momentum l and the local l-projected electronic density of states (l-DOS) ρ_{li} at a specific site i [101]:

$$\begin{aligned} \mu_{li}(E) &= \mu^{0'}_{li}(E) \left[1 + \chi'_{li}(E)\right] \\ \rho_{li}(E) &= \rho^{0}_{li}(E) \left[1 + \chi_{li}(E)\right] \end{aligned} \tag{3.13}$$

in which $\mu^{0'}_{li}(E)$ and $\rho^{0}_{li}(E)$ are the smoothly varying atomic background contributions, and $\chi'_{li}(E)$ is the fine-structure XAFS spectrum [d] (the equivalent to μ_0 and χ introduced in Section 3.2, Equation 3.7).

The striking similarity between $\mu_{li}(E)$ and $\rho_{li}(E)$ often leads to the misconception that XAS directly measures the l-DOS. One has to be aware that the density of states (DOS) is usually calculated for the ground state without a core hole, whereas the presence of a core hole and the presence of inelastic losses (by the use of the self-energy $\Sigma(E)$) are crucial for the accurate calculation of the XAS spectrum. In the RSGF formalism the relation between the XAS and DOS can be immediately seen by the fact that the spatial and energy dependence of the electron DOS is given in terms of the the imaginary part of the one-electron Greens-function operator as used in Equation 3.11 [101].

The used form of the Green's function used to calculate $\mu(E)$ (or $\sigma(E)$) can be expanded as a sum of terms, each of which corresponds to a scattering path that begins

[d] The prime is used to indicate final-state quantities calculated in the presence of a screened core hole

and ends at the central atom and involves scattering one or more times from atoms in the vicinity. The one-particle Green's function operator $\mathbb{G}$ can be expressed in terms of free propagators $G^0 = [E - H_0]^{-1}$ (H_0 is the free-electron Hamiltonian) and scattering t-matrices $T = t + tG^0t + tG^0tG^0t + \cdots$, thus the scattering contribution to the full Green's function operator is given by [102–104]:

$$\mathbb{G}^{sc} = e^{i\delta} \left[\mathbf{1} - G^0T\right]^{-1} G^0 \, e^{i\delta'} \tag{3.14}$$

δ represents partial-wave phase shifts. Similarly, $\left[\mathbf{1} - G^0T\right]^{-1}$ can also be expanded and the propagator matrix $\mathbb{G}_{L,L'}$ is then expressed in terms of a sum over all the multiple scattering paths that the photoelectron can take starting on the absorbing atom. This yields a *multiple scattering path expansion* (MS):

$$\mathbb{G}^{sc}_{L,L'} = \left[G^0 + G^0TG^0 + G^0TG^0TG^0 + \cdots\right]_{L,L'} \tag{3.15}$$

$$\mathbb{G}^{sc}_{L,L'} = \left[(1 - G^0T)^{-1} G^0\right]_{L,L'} \tag{3.16}$$

Despite greatly simplifying the calculation of the XAFS, the RSGF formalism gives rise to a physical picture of the scattering process in terms of the MS path expansion. The MS approach can be interpreted in physical terms, with $\mathbb{G}$ describing all the possible ways the photoelectron can scatter from the atoms composing the atomic cluster before the core hole is refilled. The successive terms on the right side of Equation 3.15 represent the different orders of the (multiple) scattering process, *e.g.*, G^0 is related to the atomic-like background function $\mu^{0'}_{li}(E)$ and $\rho^0_{li}(E)$ in Equation 3.13, G^0TG^0 describes all single-scattering events and $G^0TG^0TG^0$ contains the contribution of all scattering paths involving two surrounding atoms. The full-multiple scattering technique (FMS) is the explicit inversion of the matrix $(1 - G^0)T$ and the subsequent multiplication by G^0, being appropriate to the XANES region. The reason being that the dimension of the matrix to be inverted [e] increases with energy relative to the edge due to need to increase l_{max} for accurate calculations. However, it has been shown that the MS path expansion series in Equation 3.15 is generally convergent in the EXAFS region [90, 101].

Muffin-tin approximation

The *muffin-tin* approximation (MT) consists of partitioning the space occupied by the atomic cluster under consideration in three distinct regions, each of which contain a different description for the potential to be included in the MS formalism. In region I the atomic potentials are approximated as spherically symmetric out to a finite radius, usually determined on the basis of the Norman criterion [f] [105, 106]. In region II the

[e] The dimension of the matrix is given by $N(l_{max}+1)^2$, where N is the number of atoms taken to compose the cluster and l_{max} is the maximum allowed angular momentum to represent the propagators

[f] A Norman radius R_i^{Nor} is determined for each site i such that $\int_0^{R_i^{Nor}} 4\pi r_i^2 \rho_i^{tot}(r_i)dr = Z_i$. Given two nearest-neighbour sites i and j, the touching sphere MT radii are given by $R_{i(j)} =$

the interstitial potential between the atomic sphere is approximated as constant and region III lies outside an outer sphere circumscribing the whole cluster. A muffin-tin potential is sketched in Figure 3.8, showing the distinct regions of the potential. This approximation tends to work well for close-packed structures, but is less successful with open structures since the voids inside the cluster cannot be properly modelled. In practice the MT radii are often scaled up so that they overlap slightly, which can partially account for deficiencies in the MT approximation [84, 106].

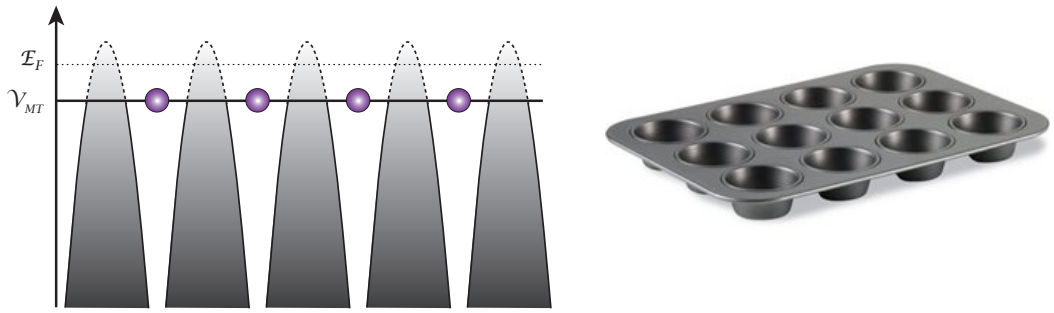

(a) Schematic drawing of a one-dimensional MT potential.

(b) Representation of a two-dimensional muffin-tin potential.

Figure 3.8.: Illustration of a MT potential showing the three different regions. (a) shows a schematic of a one-dimensional MT potential. The solid horizontal line represents the limit between regions I and II. The effect of truncation on the real shape of the potential (dashed lines) is obvious. The Fermi level is indicated by E_F. (b) shows an illustration of a two-dimensional MT potential.

In the EXAFS region, the kinetic energy of the electron is large enough that small variations in the interstitial potential do not make much difference and the MT approximation works well. In the XANES region the muffin-tin approximation is less satisfactory for quantitative analysis. Alternative approaches, sometimes referred to as *full potential methods* have been developed for the XANES region that avoid the MT approximation altogether. One example is the finite difference approach embodied on the FDMNES package [107]. Extending real-space multiple-scattering approaches beyond the MT approximation is currently an area of active development [91].

3.3.2. Many body effects

The inclusion of damping due to inelastic losses is of fundamental importance for an appropriate description of the XAFS process. These losses give the final photoelctron state a finite lifetime and hence lead effectively to a broadened one-electron spectrum. Traditionally, the losses are separated into *extrinsic* and *intrinsic*. Extrinsic losses are those in which the propagating photoelectron loses energy and include excitations due to plasmons, formation of electron-hole pairs and inelastic scattering and are more precisely

$\left[R_{i(j)}^{Nor} R_{ij}\right] / \left(R_i^{Nor} + R_j^{Nor}\right)$

described in terms of the complex, energy-dependent self energy $\Sigma(E)$. Intrinsic losses arise from excitations in response to creation of the core hole.

3.3.3. Single-scattering region

As stated in Section 3.2.3, the XAS spectrum can be divided in two distinct regions according to the energy of the photoelectron: XANES and EXAFS. Those two regions contain different information about the material under study. The XANES signal is strongly influenced by the symmetry and local environment around the absorbing atom, containing many contributions of both structural and electronic nature. Moreover, the low kinetic energy of the photoelectrons in this region results in large scattering amplitudes, which means that the photoelectrons travel through most of the molecular cluster scattering multiple times. Therefore, a proper description of the potential (and the self-energy $\Sigma(E)$) is of significant importance and it is where most of the deviations between experiment and theory comes. The XANES region is usually challenging to be properly calculated and interpreted. The calculation of XANES spectra usually are performed employing the FMS approach, requiring the inversion of the matrix $(1 - G^0)T$ and the subsequent multiplication by G^0. This process is computationally demanding and all the approximations made to the potential contribute to these diminished accuracy compared to the EXAFS region.

In the EXAFS region on the other hand, many of these contributions play a minor role. As the photoelectron energy increases, single-scattering events between pairs of atoms start to dominate the signal and Equation 3.15 can be solved with a limited number of terms (the path-expansion series converges rapidly [84]). The EXAFS region of the spectrum can be properly analysed by making use of the *EXAFS equation*. The derivation of this equation is covered extensively on the literature and will not be repeated on this thesis. Instead, the meaning of its various components and how the equation is used to extract information from the XAS spectrum will be covered briefly. The EXAFS equation expressed as a scattering path expansion generalized to include MS pathways [84] is given by:

$$\chi(k) = \sum_{\gamma} \frac{N_\gamma S_0^2 |f(k)|}{k R_\gamma^2} \, e^{-2\sigma^2 k^2} \, e^{2R_\gamma/\lambda_{tot}(k)} \sin\left[2kR_\gamma + 2\delta_c + \phi(k)\right] \tag{3.17}$$

with γ being the scattering path index, N_γ the number of equivalent scattering paths, R_γ the half-path distance and σ^2 the squared Debye-Waller (DW) factor. When dealing with single-scattering (SS) processes only, R_γ represents the interatomic distance between the absorber and a certain scatterer. Additionally, $f(k) = |f(k)|e^{i\phi(k)}$ represents the complex backscattering amplitude for the path γ, δ_c is the central-atom phase shift of the final state, $\lambda_{tot}(k)$ is the energy-dependent photoelectron mean free path and S_0^2 is the overall amplitude reduction factor, which accounts for the many-body effects.

3.3.4. XAS data analysis methods

This Section describes the necessary steps to reduce the raw data obtained from the experiment to the quantity of interest necessary for a proper EXAFS analysis, the $\chi(E)$ or $\chi(k)$. The sequence at which each step is performed is not mandatory and many different data reduction philosophies are present on the literature [30, 82]. The steps described below are the ones taken during the analysis of the XAFS data of $[Fe^{II}(bpy)_3]^{2+}$ and Myoglobin (shown on Chapters 5 and 6, respectively) using the program ATHENA [108].

Deglitching Occasionally the XAFS data has some spurious points that are obviously not part of the data. They are called *glitches* and can be caused by a variety of reasons, most commonly the monochromator, the electronics or sudden variations on the sample (it is not uncommon on the case of flowing liquid samples). Standard procedures for correcting glitches are simple removal of the affected data points or interpolation of the data in the region including them.

Energy calibration and edge position determination The determination of an absolute energy scale is not of particular importance during the XAS data analysis since the position of absorption edge E_0 is later optimized in a fitting procedure. However, the knowledge of the absolute edge position of an element embedded in a compound compared to the pure element - the *chemical shift* - is a parameter of practical use, giving chemical information about the sample. It is common to calibrate the energy coordinate of a given experiment by measuring the XAS spectrum of a pure material for which the edge position is tabulated. The absorption edge energy E_0 is somewhat arbitrarily determined. A common criterion, the one used in the analysis of the data presented on this thesis, is to take it as the energy where the first derivative of the spectrum is maximum. Other criteria include setting E_0 to the energy where the absorption is maximum or halfway between the minimum and the maximum of the absorption spectrum.

Pre- and post-edge baseline removal The baseline removal is an important step in XAS data treatment since it is directly connected to the edge-jump normalization *vide infra*. It is the first step in extracting the oscillatory part of the XAS spectra from the other contributions coming from scatter, absorption from lower-energy edges and any other processes that are not of interest. Usually a linear function is applied to the pre-edge region, and a linear or quadratic function is applied to the post-edge region. In some special cases, *e.g.* XAS of highly diluted systems measured in fluorescence mode, the baselines do not follow the common trend of the $\sim E^{-3}$ dependency. In these cases, it is common that the baseline in the pre-edge region resembles the end tail of a Gaussian curve, while in the post-edge region it increases with the energy (instead of decreasing). In the pre-edge region, the curved baseline appears due to elastic x-ray scatter, which below the absorption edge can be close to one fluorescence window set on a energy-resolved

fluorescence detector. As the incoming x-ray energy increases during the scan, the elastic scatter also increases its energy and is no longer detected because it falls off the fluorescence window, thus this contribution disappears. This type of post-edge baseline has another origin: as the x-ray photon energy increases, the incoming x-ray intensity (I_0) usually decreases, while the fluorescence intensity (I_F) remains constant. Since μ_F is defined as the ratio I_F/I_0, it will lead to a monotonically increasing μ_F with energy. Since the baselines' exact shape are not known *a priori*, these contributions have to be removed by fitting an appropriate function to the different regions of the spectrum: a Gaussian curve on the pre-edge region and a quadratic or even cubic polynomial on the post-edge region.

Edge-jump normalization The normalization is the procedure applied to XAFS data so as to take into account the variations with respect to sample preparation and thickness, atomic absorber concentration, detection philosophy and settings, and any other aspects of the measurement. The normalized $\mu(E)$ (and $\chi(E)$) are the quantities calculated by theory and should, therefore, be compared with normalized data. The relationship between $\mu(E)$ and $\chi(E)$ are given in Equation 3.7, though this is not how $\chi(E)$ is extracted in practice. $\mu_0(E)$ is not always sufficiently well behaved to be used in the denominator. Additionally, $\mu_0(E)$ is neither independently measurable, nor can it be calculated accurately. This limitation can be overcome by avoiding the functional normalization, doing instead an *edge-jump normalization* dividing the measured $\mu(E)$ by an energy-independent value $\Delta\mu_0(E_0)$, the *edge-jump*. The edge-jump is evaluated by extrapolating the pre- and post-edge polynomials used in the baseline correction to the edge energy E_0. The $\Delta\mu_0(E_0)$ is then the difference between the pre- and post- edge functions at E_0. Using $\Delta\mu_0(E_0)$ as a normalization factor instead of $\mu_0(E)$ introduces an attenuation in $\chi(E)$, which introduces an artificial quadratic contribution to the EXAFS that is incorporated in the Debye-Waller factor (σ^2).

Background subtraction The ATHENA suite uses an iterative background removal procedure, called AUTOBKG [109]. The basic idea is to explore the fact that $\mu_0(E)$ mainly contains low-frequency components, so by using Fourier theory it is possible to minimize the contribution of these components to the extracted XAS signal $\chi(k)$. The background function is constructed from *splines* that are connected with *knots*. The parameters of the spline are chosen iteratively in a way that, after Fourier transforming the resulting fine structure $\chi(k)$, the components below a certain threshold R_{bkg} are minimum. Even though the procedure is highly automated, there are many ways for the user to control and affect the outcome of the AUTOBKG procedure, including changes in the spline parameters (clamps on the low- and high-energy limits), the cut-off distance and the k-weight of the Fourier transform [108].

Averaging Several successive scans are usually averaged together in order to improve the signal-to-noise (S/N) ratio of the measurements, which is important for the

EXAFS region where the signal magnitude is small. The averaging is generally performed on the absorption data $\mu(E)$, but in this thesis the averaging was done on the normalized $\mu(E)$ as the last step of the data processing procedure, as will be shown in Chapter 6. A weighting factor can also be used to discriminate data sets of different quality, *e.g.* data sets measured with longer integration times will produce higher quality spectra, so they should be more heavily weighted in the averaging than lower quality spectra. Weighted averaging was not applied in the data presented in this thesis.

3.3.5. FEFF9

`FEFF9` [89, 90, 110] is a software package for calculation of XAS spectra, including EXAFS and XANES, and other types of spectroscopies. In addition, the code calculates electronic structure including local density of states l-DOS. It uses an *ab initio* self-consistent real space multiple scattering (RSMS) approach for cluster of atoms, including core-hole effects and local field corrections; based on self-consistent, spherical muffin-tin scattering potentials. The calculations are based on an all-electron, real space relativistic Green's function formalism with no symmetry requirements, which makes it applicable to both molecules and periodic systems. `FEFF9` calculations include inelastic losses in terms of a GW self-energy, as well as vibrational effects in terms of correlated Debye-Waller factors. It has a modular structure allowing the user to run certain parts of the calculation separately from others. In the `FEFF9` code the x-ray absorption cross-section is calculated based on an atomic cluster with a set of coordinates defined by the user, including the central absorbing atom that has to be placed at $(0, 0, 0)$. Based on the input geometrical structure and using the MT approximation, the electron density and the scattering potentials are calculated in a self-consistent field (SCF) manner [90], by iterating the Coulomb potentials, electron densities and the Fermi energy. An energy-dependent self-energy $\Sigma(E)$ is then added to the self-consistent potential to account for the inelastic losses. Finally, by using the $\mathbb{T}$-matrix formalism and the Green's function propagators, the effective scattering amplitudes and phase shifts are calculated, which can then be used to calculate the theoretical XAS spectrum via Fermi's golden rule.

The input to the program is contained in one single file, the `feff.inp` file, which contains the necessary instructions to perform a calculation - the different modules that are controlled by the `CONTROL` card - and the input geometrical structure in the form of x,y,z-coordinates. The `feff.inp` file that was used in the `FEFF9` calculations of the XAS spectra of Myoglobin is given in Appendix F. A detailed description on how to set a proper `FEFF` calculation, including the description of the modules and control cards can be found on the literature [110, 111] and will not be described in this thesis.

3.3.6. MXAN

`MXAN` [85–87, 112] is a computer code that uses a set of programs [86, 113] for the calculation of the full multiple-scattering x-ray absorption cross-sections, allowing the fit of the XANES region of the XAS experimental spectrum. Its strength resides in the fact that a quantitative structural analysis can be performed by doing a search on the parameter space. The search is done by changing the relevant geometrical parameters of the site around the absorbing atom and comparing the theoretical spectrum with the experimental data. The method is based on minimization of the square residual $\mathcal{S}^2$, defined by:

$$\mathcal{S}^2 = n \frac{\sum_{i=1}^{m} w_i \left[\left(y_i^{th} - y_i^{exp} \right) \epsilon_i^{-1} \right]^2}{\sum_{i=1}^{m} w_i} \tag{3.18}$$

where n is the number of independent parameters, m is the number of data points, y_i^{th} and y_i^{exp} are the theoretical and experimental values of the x-ray absorption at the point i, ϵ_i is the individual error (standard deviation) of the data set at the point i and w_i is a statistical weight applied on the $i-^{th}$ point. In the case of $w_i = 1$ the square residual $\mathcal{S}^2$ becomes the statistical χ^2 (not to be confused with the x-ray fine structure function $\chi(E)/\chi(k)$). The calculation of the theoretical XAS spectra is performed using the FMS approach as described in Section 3.3.1, *i.e.*, by explicit inversion of the scattering matrix $(1 - G^0)T$. The potentials are calculated using the MT approximation, the radii being determined based on the Norman criterion with a specific percentage of overlap - usually about 10-15%. The exchange and correlation part of the potential are calculated in the framework of the Hendin-Lundqvist (HL) scheme [106, 114]. The potential is recalculated at each step of the minimization procedure, as the atomic coordinates are changed in the search for a better configuration. Only in the first step is the potential calculated using a SCF procedure, its implementation in a fitting procedure is complicated and too time consuming [87]. In reality, the use of a SCF charge density in the case of particular geometries that does not resemble the real geometry can lead to a less accurate potential or even incorrect electronic configurations [84, 87]. The HL potential is known to be excessively lossy at low energies [84, 86, 104, 112, 115], so to avoid overdamping of the spectrum one can use only the real part of the HL potential and account for all the inelastic processes by way of a phenomenological Lorentzian broadening function that has an energy-dependent width. The broadening has the form $\Gamma(E) = \Gamma_c + \Gamma_{mpf}(E)$ and it is convoluted with the calculated spectrum to generate the y_i^{th}. The parameter of the broadening function are calculated at each step of the computation using a Monte Carlo procedure.

The `MXAN` procedure needs three input files containing respectively the experimental data to be fitted, the starting atomic coordinates of the cluster and the commands and options necessary for the chosen minimization strategy. The file containing the experimental data is a simple two-column `ASCII` file relating the energy and the measured

(normalized) XAS intensity. The commands file contains a list of the parameters to be varied during the fit procedure, the interval over which those parameters can span (relative values with respect to the initial value) and most of the instructions for the optimization procedure. It has, necessarily, to be named `COMMAND.MIN`. The coordinates file contains information about the XAS energy range to be used in the fit procedure, details of the potential and symmetry (if present), and the cluster of atoms, including the initial geometrical structure in *x,y,z-* or r,θ,ϕ-coordinates. One example of the `coordinates` and `COMMAND.MIN` files used on the `MXAN` fit procedure of nitrosyl-Myoglobin (MbNO) is given in Appendix D.

`MXAN` can be used to fit directly the transient difference spectra measured during a time-resolved XAS experiment. In addition, some of the non-structural parameters, like chemical shift, can be modelled and quantified during the fitting procedure, which yields additional electronic information about the investigated system. The code uses an energy interpolation on the experimental data, which is specifically relevant when doing fits of transient spectra. This interpolation avoids the possible problem of having spectra with different energy stepping, allowing it to calculate the excited-state cross-section $\sigma_{ex}(E)$ and then subtract it from the ground-state $\sigma_{gs}(E)$. The `slope` option means that the interpolated experimental spectrum used by `MXAN` is rotated with respect to the real spectrum. This option is present to correct for possible errors on the normalization and background subtraction of the experimental data when only a limited energy range is available. It produces a small (visual) deviation between the input experimental data and the experimental data `MXAN` actually uses in the calculations, but with no effect on the calculated structure.

"In every branch of knowledge the progress is proportional to the amount of facts on which to build, and therefore to the facility of obtaining data."

James Clerk Maxwell

4

Implementation of the experimental methodology

This chapter provides a description of the experimental methods used in the measurements performed in this thesis, with special focus on the implementation of the high-repetition rate scheme for measuring ultrafast time-resolved x-ray absorption experiments. The results obtained with this new scheme will be presented in Chapter 5 and Chapter 6. Additionally, a copy of the printed version of the article referring to the implementation of the high-repetition rate time-resolved XAS experiments is presented in Appendix B.

In the following sections will be presented the basic aspects of an XAS experiment, including two common detection schemes: transmission and fluorescence yield. A short review of the history of ultrafast time-resolved x-ray absorption spectroscopy experiments is given, as well as some limitations of the technique as it was implemented so far. One of the main limitations, *i.e.*, the repetition rate, lead the way to the developments presented on this thesis. A brief description of the main elements of the picosecond x-ray absorption experiment apparatus used, namely, the synchrotron x-ray source, the laser system, the beamline endstation(s), the data acquisition and timing controlling schemes, are presented. Furthermore, the signal detection and the noise influence on the measurements will be discussed.

4.1 History of Previous Ultrafast Time-resolved XAS

The very first time-resolved XAS experiments were performed in biological systems. In this work, the authors investigated of the photo-detachment of the CO molecule in Carboxy-Myoglobin in solution [5, 116, 117]. Although done with low temporal resolution (ms to μs), changes in the pre-edge structure and in the position of the iron edge of this protein were detected as a function of time. This pioneering investigation showed the feasibility of the time-resolved XAS experiments and its applicability to dilute molecular systems in solution. As better temporal resolution became available, and both the experimental setup and theoretical tool advanced, more metal-based complexes in solution were studied. Chen and collaborators studied the structural transformation resulting from the photo-dissociation of a Ni-porphyrin with ns temporal resolution [118]. Following this work, the same group investigated the metal-to-ligand charge transfer (MLCT) process in a Cu-centered complex [119]. Using time-resolved XAS spectrum, they were able to extract information about the oxidation-state change and the structural modifications. Our group at EPFL have used time-resolved XAS to studied extensively a series of photo-catalysts and spin cross-over compounds [35, 40, 120–123]. The systems investigated comprising metal (Ru, Fe, Re, Pt) polypyridyl compounds. Chergui *et al.* used time-resolved XAS with $\sim$ 50 ps resolution to determine the excited-state structure and oxidation state change in $[Ru(bpy)_3]^{2+}$ [121]. It was found that the Ru-ligand distance decreases by $\sim$ 0.03 Å in the charge-separated triplet excited state. Afterwards, an apparently similar complex became the focus of the time-resolved XAS studies in the Chergui's group. The $[Fe(bpy)_3]^{2+}$ system showed a light-induced spin transition effect. In the excited-state, the geometry modification corresponds to an expansion of the three bpy ligands by $\sim$ 0.2 Å, which results in very large changes in the XAS spectrum. The combined data quality and sophisticated analysis procedure culminated in a high precision in the derived structural changes (Fe-N elongation of 0.203 ± 0.008 Å) [40, 122]. The success of these measurements with ps temporal resolution motivated further studies using time-resolved XAS with femtosecond resolution. Chergui and co-workers performed fs-XAS experiments on $[Fe(bpy)_3]^{2+}$ using the laser-slicing technique at the SLS [35]. The fs temporal resolution allowed to unravel the early relaxation pathways in the spin transition process. These measurements were the first femtosecond x-ray studies of metal complexes in solution, which led the way through other similar experiments, like the investigation of the changes of the solvent shell structure upon electron abstraction of aqueous iodide [37]. Experiments in the ps regime continued to show its power with the studies of the excited-state structure of Pt-based catalysts. The analysis of the time-resolved data using a set of different models for the structural distortions allowed the determination the structural changes in the lowest triplet excited state resulting from the metal-centered transition [36]. A novel analysis of the low-energy region of the XAS spectrum using a Bayesian fitting procedure was implemented, permitting an investigation of the this region of the spectrum by *ab initio* means [124]. The field of time-resolved XAS is keeps expanding its activity, with new interesting systems being

investigated and providing very interesting results.

Most of the previous time-resolved optical pump/x-ray probe XAS experiments in our group were done typically with kHz data acquisition rate in order to profit from the high pulse energies delivered by commercial amplified ultrafast laser systems (usually more than 1mJ/pulse) [33–35, 38–40, 119, 120, 125–130]. Most of them made use of the x-rays generated by the isolated electron bunch of the hybrid filling mode available at 3^{rd}-generation synchrotron sources and are usually based on recording the transient (difference) absorption on a pulse-to-pulse basis, though experiments using a single-bunch operation mode are also reported in the literature. The data acquisition is such that the x-ray transmission and fluorescence signals are recorded alternately, originating from the excited and unexcited samples, at twice the pump laser repetition rate (typically 2 kHz) using electronic gated detectors. This scheme has proven to be able to provide measurements limited only by the shot noise of the synchrotron source [127, 131].

The x-ray flux is fairly reduced in these types of time-resolved x-ray experiments, originating from the fact that only certain x-ray pulses are selected either electronically via gated integration [34, 125, 127, 131] or mechanically using choppers [16, 132–135], to be used as the probe. This reduced x-ray flux is a major limiting factor for having data with better signal-to-noise ratio (S/N), which in the end not only reduces the accuracy of the structural analysis but also limits the types of systems that can be measured to those that present a high concentration. A more detailed inspection of the experimental setup reveals that, despite of the fact that the isolated x-rays pulses at 3^{rd}-generation synchrotrons occur typically at MHz rates, the experiments are carried out at kHz data acquisition rates, being limited by the repetition rate of the amplified laser systems used as the excitation sources. This mismatch implies that only 1/500-th of the x-ray flux is used in the experiments, a fact that cannot be afforded on an already flux-limited experiment. If one wants to extend the applicability of the time-resolved optical pump/x-ray probe XAS in a way to make possible the investigation of dilute systems, one method of improving the S/N is to make use of all the isolated x-ray pulses delivered by the synchrotron sources operating with hybrid electron filling modes. Going to higher repetition rates represents a 500-fold increase in x-ray flux when compared to the equivalent kHz experiments. If the only source of noise on the experiment is the shot-noise from the source, an increase of $\sqrt{500} \approx 22$ in the signal-to-noise ratio (S/N) should be expected, resulting in significantly lower data acquisition times and expanding the usage of the technique to the study of systems presenting limited solubility.

4.2 Synchrotron radiation and the temporal structure of the radiation

Since the discovery of x-rays in the late 19^{th} century it has been widely used in many branches of science, not only by physicists, but also by medical doctors, chemists, pharmacists, biologists and geologists among others. The technology for producing x-rays was basically unchanged since the times of Röntgen until the introduction of rotating

anode sources in the 1950s. Those new sources did not represent a major step forward in the produced x-ray intensity[a], which limited the applicability and accuracy of x-ray techniques. In the beginning of the 1960's, scientists noticed that the synchrotron radiation emitted from accelerated charged particles was potentially a much more intense and versatile source of x-rays. After an initial parasitic use of synchrotron radiation from facilities designed for experiments in high-energy or nuclear physics, the first dedicated synchrotron sources were brought into operation. The continuous development in the technology of synchrotron radiation culminated with what are now known as 3^{rd}-generation synchrotron sources. In the last four decades the brilliance of the synchrotron sources has increased approximately 10^{14} times compared to regular lab-based sources [77]. Recently, so-called *x-ray free-electron lasers* (XFEL), also known as the 4^{th}-generation x-ray sources, are being brought into operation [136] and many others are in design and/or construction phases [137–139]. These new sources represent one step further in terms of x-ray beam intensity, promising another increase of up to nine orders of magnitude in peak flux. Moreover, new x-ray beam characteristics are to be exploited in new experiments, including extremely short pulses (on the order of a few fs) and high degree of coherence [77], inaugurating a new era in x-ray science.

A synchrotron consists of five main components: a source of electrons, a booster ring, the storage ring, the radio frequency cavity(ies) and the beamlines. Figure 4.1 illustrates the main components of a modern 3^{rd}-generation synchrotron source [140]. The first component in a synchrotron is the source of electrons (electron gun), which also comprises a first accelerating stage - the *linac*. After being accelerated to about 100 MeV the electrons are injected into a *booster* and further accelerated (to about 3 GeV in an intermediate size 3^{rd}-generation synchrotron), either to the right energy at which they will be stored or, less commonly, to a somewhat lower energy. The storage ring is the structure responsible for storing the relativistic electron beam for long periods of time over which the experiments are conducted. It consists of an evacuated metallic pipe of a polygonal shape; in the arced sections are placed the *bending magnets*, whereas on the straight sections the *insertion devices* are located. The bending magnets are used to deflect the electron beam and keep it in a closed orbit inside the storage ring, often being used also as a source of synchrotron radiation. The insertion devices are periodic arrays of alternating magnets which force the electrons to execute an oscillatory path in the plane of the storage ring. They are subdivided in two categories, *wigglers* and *undulators*, depending on the degree to which the electrons are forced to deviate from a straight path. The radio frequency (RF) cavities are a crucial element in a synchrotron, being responsible to supply the electron beam with energy that it is lost due to the emission of synchrotron radiation at the bending magnets and insertion devices. Every orbit the electrons receive a small boost from the RF cavities, in a self-regulated way, *i.e.*, because of the RF is a standing wave inside the cavity only the electrons with the correct phase with respect to the RF electric field receive the correct boost. This results

[a] The quality of an x-ray sources is indicated by its brilliance, which is defined as photons/s/(mrad)^2/(mm^2 source area)/(0.1% energy bandwidth)

in the electrons settling into small packets or bunches. More details on the importance of the RF cavities and their implication of the emitted synchrotron radiation are given in Section 4.2.1. The final components of a synchrotron, the beamlines, serve to collect the emitted radiation, shape and monochromatize it and redirect it to the experimental hutch in which the experiments will be performed.

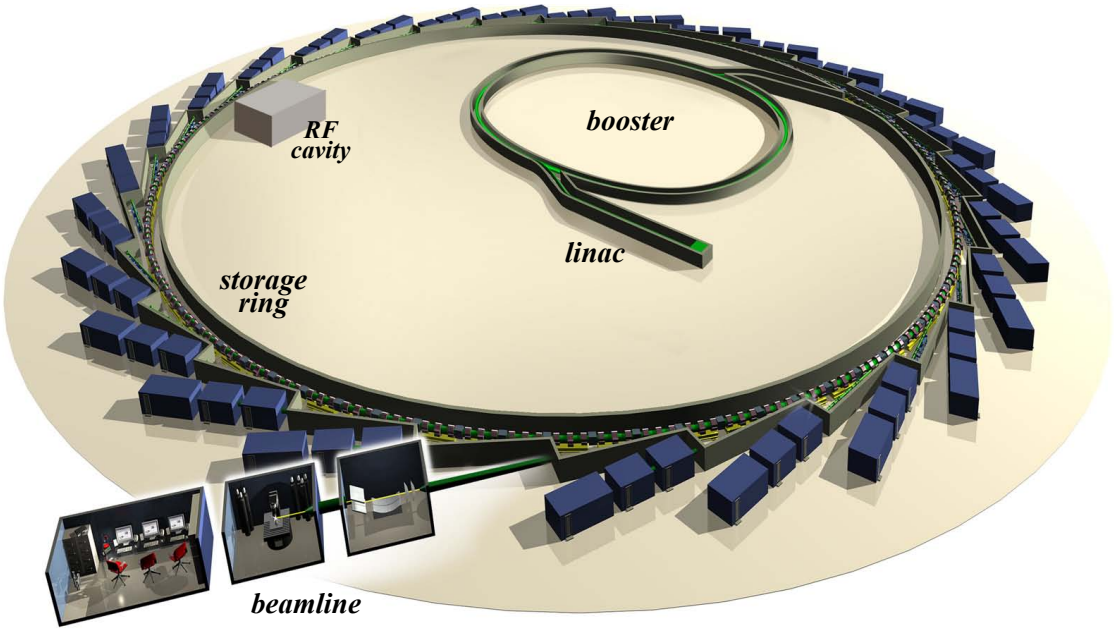

Figure 4.1.: Schematic drawing of the main components of a 3^{rd}-generation synchrotron source. Taken and adapted from Diamond Light Source, UK [140] .

4.2.1. The Swiss Light Source

The facility used to perform the XAS experiments presented in this thesis, the SLS, is a 3^{rd}-generation synchrotron operating at 2.4 GeV, with an average electron current of 400 mA [141]. The storage ring circumference is 288m, resulting on an electron round-trip of 960 ns. The SLS makes use of the *top-up* injection mode to account for the energy lost by the electron beam, being either due to collisions with residual gas molecules inside the storage ring or by Coulomb interactions between the electrons of the beam. The stored electron current is kept at an almost constant value by regular 'top-ups' which reinject electrons in the storage ring. At the SLS a top-up happens every 2-4 minutes, such that the total stored electron beam current is kept constant to within 1 mA. Top-up operation greatly enhances the operational stability of synchrotrons because it provides a constant heat load on the optical elements composing the beamline. Major short-term fluctuations and long-term drifts are thus, greatly suppressed.

The loss of energy due to emission of synchrotron radiation after each magnetic element (bending magnet or insertion device) must be compensated for in order to keep

the electrons on a closed orbit inside the storage ring. This is accomplished by the RF cavity(ies), which provide the electrons with the "missing" energy after each each turn. This process is self-regulated because only the electrons entering the cavity with the correct phase with respect to the RF electric field will gain the correct amount of energy. If the electrons enter the cavity slightly out of phase with the RF electric field, they will either receive more or less energy than the others such that they will have again the average energy of the beam. Electrons entering the cavity totally out of phase will continually receive or lose energy, and will consequently be lost because they will follow a different orbit. An illustration of the working principle of a RF cavity is shown on Figure 4.2. The overall effect is called *bunching*, since the electron beam is forced to group into bunches of well-defined spatial length, which in the end sets limits on the electron filling pattern inside the synchrotron storage ring.

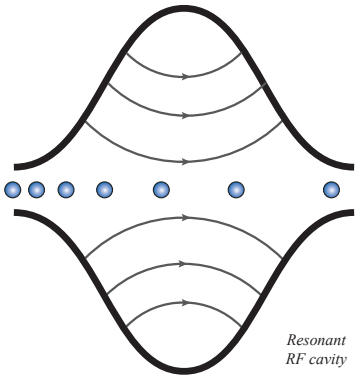

Figure 4.2.: Illustrative drawing of the working principle of an RF cavity, the blue circles represents the electrons. The electric field inside the cavity is represented by the thin lines (the direction is given by the arrows). Electrons entering the resonant cavity with the right phase with respect to the electric field of the RF, like those on in the middle of the figure, receive the proper amount of energy to keep them in the correct orbit.

The bunching inside the storage ring has an important consequence for the produced synchrotron radiation: it is inherently pulsed. At the SLS, the RF cavities operate with a frequency of 500 MHz, corresponding to a bunch spacing of approximately 60 cm which is equivalent to 2 ns. In principle each of those bunches [b] may or may not be filled with electrons, depending on the specific operational mode of each synchrotron. The electron filling pattern not only gives the total stored current inside the synchrotron, it also dictates which and how many x-ray pulses can be used for a certain time-resolved experiment. A total of 480 such buckets can be present on the SLS storage ring, having a revolution period of 960 ns.

[b] If a bunch is not filled with electrons it is called a 'bucket', instead.

Electron filling pattern

At the SLS the electron filling pattern is said to be *hybrid*, being composed by 390 adjacent electron bunches separated by 2 ns, called the *multibunch* (MB), and an isolated electron bunch, called the *camshaft* (CS), which is placed within the remaining 90 empty buckets. This hybrid filling mode has the advantage of providing regular users with a reasonable high photon flux, while providing users who want to perform time-resolved experiments an isolated x-ray pulse. The typical filling pattern used at the SLS is shown on Figure 4.3. The CS has more current than the individual pulses that compose the MB, operating with 4 mA. The frequency at which the pulses of radiation occur are set by the orbit path length and the energy of the stored electrons inside the ring. They occur at a repetition rate of 1.04 MHz, meaning one x-ray pulse every 960 ns. The temporal duration of the radiation produced is directly connected to the longitudinal length of the electron bunches, being approximately 85 ps full-width-half-maximum (FWHM) [142].

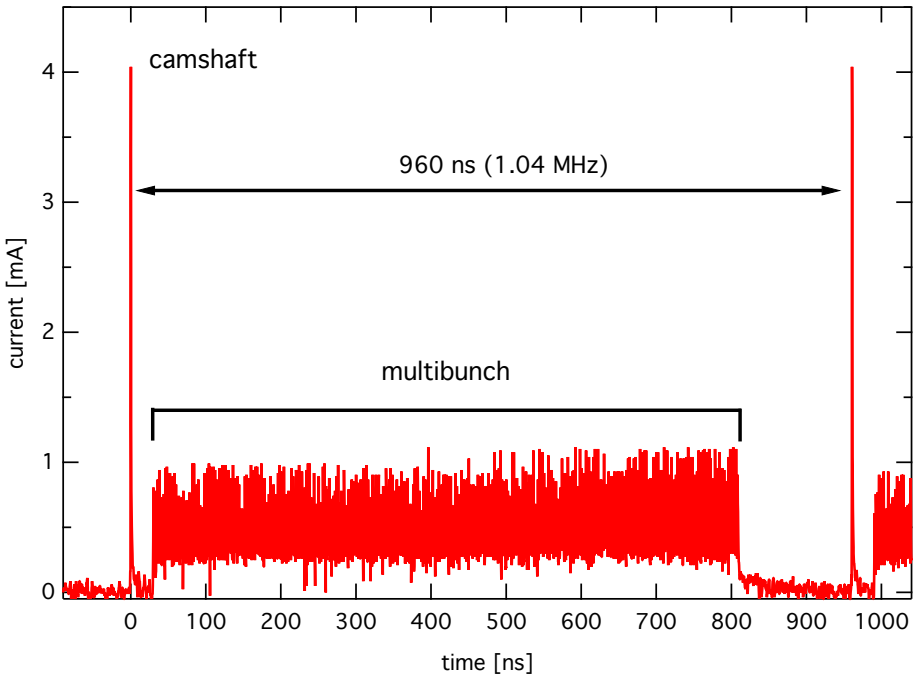

Figure 4.3.: Electron filling pattern used at the SLS. In total, there are 480 possible buckets, of which 390 consecutive ones are filled with electrons (multibunch). Of the 90 remaining empty buckets, one (CS) is filled with 4 times more current than the MB. The repetition rate of the camshaft pulse is 1.04 MHz, setting an upper limit for the data acquisition rate of the experiments using the current hybrid filling mode.

The x-ray pulse duration sets the limits of the time-resolved experiments with respect to the temporal resolution. Shorter x-ray probe pulses can be obtained at the SLS by either employing the *laser-electron slicing technique* [142, 143] or by operating the storage ring in the so-called *low-α mode* [144]. The low-α mode consists of reducing

the electron current and modifying the magnetic lattice of the storage ring in order to obtain low values of the *momentum compaction factor*, α. This way, x-ray pulses as short as ~ 20 ps (with approximately 100 μA average electron current) are obtained at the SLS. X-ray pulses with even shorter temporal duration can be obtained using the low-α mode at the expense of lowering even more the beam current, and consequently the x-ray photon flux [144, 145]. Therefore, the low-α mode is impractical for normal operation because it does not provide enough x-ray flux for regular users. Further details on the low-α operation are given in appendix A. On the other hand, the laser-electron slicing scheme can be employed without any change in the electron beam parameters or the magnetic lattice, thus without affecting any of the other users. It is based on the interaction of an intense, femtosecond laser pulse with the CS electron bunch inside an insertion device (the *modulator*). When in resonance condition, the laser electric field couples with the electron beam, thereby modulating its energy across a narrow 'slice' of the CS electron bunch. The energy modulation is then converted in spatial separation by dispersive elements (the *chicane magnets*), after which the electron beam travels through another insertion device (the *radiator*) to generate the short x-ray pulses. The slicing technique has been successfully employed in the study of ultrafast phenomena in the condensed phase, including the study of coherent phonons and phase transition in crystalline solids [146–149], and structural and electronic dynamics of molecules in solution [35, 37]. One should bear in mind that the extremely low photon flux produced by slicing sources imposes stringent limits on the feasible experiments.

4.3 Setup for steady-state XAS

In order to perform an accurate structural analysis using XAS data it is mandatory that the data possesses good quality, *i.e.*, it is undistorted, presents a high signal-to-noise (S/N) ratio and is absent of any systematic errors. The measurement of such good-quality spectra is a non-trivial task [31, 77, 82] and care must be taken with respect to the stability of the x-ray beam, the reproducibility of successive energy scans and the prevention of measurements with detectors behaving non-linearly. These measures are even more critic in the case of measurements using liquid samples with low concentrations, as it is the case of Myoglobin in physiological conditions. In this Section, the experimental setup used to measure the steady-state XAS presented on Chapter 6 will be described. It starts with the description of the technical aspects and is followed, in Section 4.3.1 by a discussion of two modes of detecting the XAS signal (transmission and fluorescence).

The experimental setup used to perform the steady-state XAS experiments is sketched in Figure 4.4. Two ion chambers (*Oxford-Danfysik*) filled with 1 bar of helium gas were used as incoming (I_0) and transmitted (I_T) x-ray intensity detectors. The current generated from each ion chamber was amplified by a current amplifier (*Femto*, DLPCA-200). Concomitant with the x-ray transmission measurements, the x-ray fluorescence was

also recorded. Two single-element silicon drift detectors (*Ketek*, AXAS-SDD10-138500, 10 mm^2 active area), with an energy resolution of about 150 eV, were placed at an angle normal to the incoming x-ray beam in order to minimize the elastic scattering[c] during the measurements. On the tip of each fluorescence detector a conical-shaped metal piece was placed in order to improve the contrast between the x-ray fluorescence and the elastic scatter. Alternatively, helium gas could be flowed over these conical pieces, reducing even further the contribution from air scatter. The fluorescence detectors were set such that the total number of counts on each of them did not exceed the limit of 200000/s. This was done to prevent the *pile-up effect* typical for this type of detector and eliminate the need for *dead-time correction* which might distort the XAS signal. The energy resolution of the fluorescence detectors were enough to isolate the fluorescence radiation from the contribution of the elastic scatter. The standard procedure is to set a proper region of interest on the energy-resolved spectrum around the iron K-α radiation (6.5 keV) and exclude the elastic scatter.

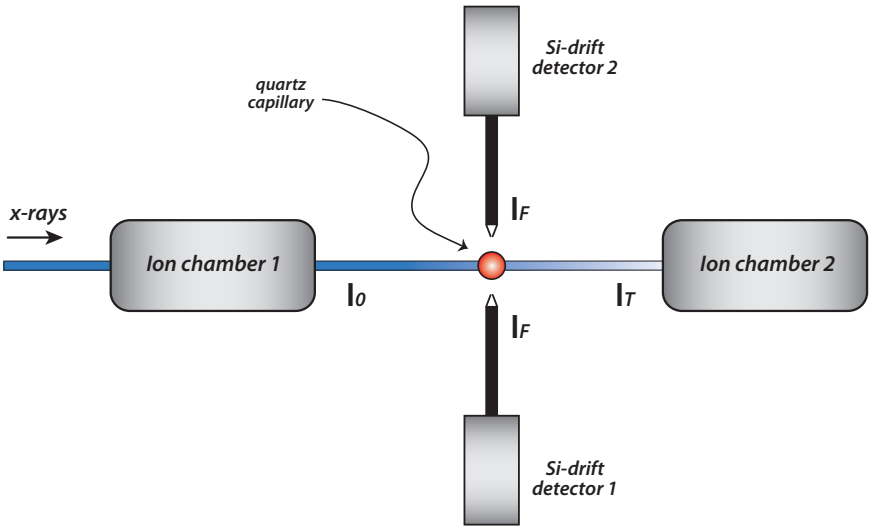

Figure 4.4.: Illustration of the setup used for steady-state XAS measurements at the microXAS beamline.

The samples were continuously flowed through a quartz capillary (*Hilgenberg GmbH*) having approximately 10 μm thick walls and 2 mm path length, mounted on a three-axis manipulator stage. The samples were kept in a closed bottle under nitrogen atmosphere (except the carboxy-myoglobin and oxy-myoglobin which were kept at CO and a mixture of He and O_2 atmosphere, respectively). The capillary was scanned horizontally in order to determine its center and to maximize the sample path length for the transmission signal. The x-ray beam size used was 500 x 500 μm^2, the x-ray energy was calibrated by measuring a reference Fe foil. The XAS data was collected using a rate of 5 cycles per

[c]Synchrotron x-rays are polarized on the horizontal plane, meaning that the elastic scattering produced after the interaction of the x-rays with a sample is minimum in the direction perpendicular to the direction of the beam propagation, on the same horizontal plane

second, in which one cycle represents 190 ms of integration and 10 ms of waiting time. Several successive scans were averaged together in order to improve the S/N.

Despite the relative simplicity of operation of ion chambers, some special attention must be paid to them. Undulator beamlines at 3^{rd} generation synchrotrons provide an extremely bright x-ray beam, which in addition, is usually very small (foci of less than 10 μm are achievable by the use of focusing mirrors, *e.g.*, mirrors pairs in the Kirkpatrick-Baez geometry, also called KB mirrors). For those reasons, saturation effects have to be prevented by choosing appropriate filling gasses (or even mixtures) and monitoring the current generated on the ion chamber. The linear regime is maintained by keeping the current below 100 nA. The number of absorbed photons N_{ph} in the ion chamber can be calculated by [150]:

$$N_{ph}[ph/s] = \frac{C[A] \cdot E_I[eV/e^-]}{E[eV] \cdot e[C]} \tag{4.1}$$

in which C is the measured current in amperes (A), E_I is the ionization energy (in eV/e^-) of the gas in the ion chamber, E is the energy of the x-ray photons (measured in eV) and e is the elementary charge given in coulombs (C). At 7.1 keV, *i.e.* around the Fe K edge, 1 bar of nitrogen absorbs more than 30% for a 30 cm path length, which clearly saturates the ion chamber. Instead, under the same conditions but using 1 bar of helium, the absorption is only 0.06%. Therefore, on the presented experiments the ion chambers were filled with 1 bar of helium and they were regularly re-filled with He to prevent non-linearities on the signal arising from air leakage to inside the ion chambers.

The calculation of the the number of photons from the ion chamber current as a function of the filling gas is implemented in the HEPHAESTUS software which is part of the IFEFFIT suite [108, 151]. It can be easily checked prior to an experiment to help for a proper choice of filling gas mixture.

4.3.1. XAS detection modes: transmission and fluorescence

There are several ways of measuring a XAFS spectrum, the most commonly used being transmission and total fluorescence yield modes. Auger-electron emission and total-electron yield are less common and are technically more demanding. They were not used for the measurements in this thesis, therefore they will not be discussed. The transmission mode is experimentally straightforward, but care should be taken with respect to sample preparation and the linearity of the detectors. It is usually the method of choice when working with high concentration samples. On the other hand, fluorescence yield mode results in a higher sensitivity, especially in the case of dilute samples. It is experimentally more elaborate and the signal might suffer from distortions in case of concentrated samples, the reasons for which will be explained in the next sections.

Transmission mode

Section 3.2 introduced the equation prescribing the transmitted intensity I_T of a beam of incident intensity I_0 after passing through a certain material with uniform thickness d. The equation governing this process is known as the Lambert-Beer law (Equation 3.5). The x-ray absorption spectrum $A(E)$ can be measured as a function of the incoming and transmitted x-ray intensities, and the x-ray energy E:

$$\begin{aligned} A^T(E) &= \ln\left(\frac{I_0(E)}{I_T(E)}\right) \\ &= \mu(E) \cdot d \\ &= \sigma_a(E) \cdot c_{mol} N_A d \end{aligned} \tag{4.2}$$

To write the expression for $A^T(E)$ in terms of the absorption cross-section, Equation 3.6 was used. In principle $\mu(E)$ refers to the total absorption coefficient of the sample, which includes not only the absorber atom but also all the other atomic species present: solvent molecules, counter-ions, etc. Moreover, what it is actually measured by the transmission detector is the absorption of everything present on the path between the two detectors, including air, entrance and exit windows, capillary walls or flow cell windows, etc. All these contributions enter in Equation 4.2 as multiplicative factors on the ratio I_0/I_T. In the process of constructing the XAS transmission signal, the natural logarithm is applied, meaning that the mentioned multiplicative factors become a slowly additive component that is superimposed to the background. Since the background contribution is subtracted prior to the data treatment (see Section 3.3.4), these aforementioned contributions do not represent a big issue for XAS recorded in transmission mode. Conversely, fluorescence signals can be affected by such contributions, as will be clear in the next Section.

Despite of the relative simplicity in measuring an XAS spectrum in transmission mode, care should be taken during the sample preparation and handling. In the case of solid samples, one should ensure that the sample is uniform on a scale determined by the absorption length ($1/\mu$) of the material, *i.e.*, the individual particles should be smaller than one absorption length. Moreover, the sample should have a uniform thickness and be free of "pinholes" (regions on which the transmission is locally higher). Failure to fulfill those conditions can severely distort the XAS spectrum [30, 152], especially when the measurements are done using focused beams on the μm range. Working with liquid samples avoid the complications about uniformity, since the sample will be homogeneous to start with. It has to be guaranteed, however, that the sample flow is stable and that the solvent signal does not mask the sample one, in which case the fluorescence detection is more advantageous.

The analysis of XAS is always performed using normalized spectra. This is done so that it is possible to compare theoretically calculated spectra with the experimental data, as well as to compare different XAS data collected under different conditions. The normalization of the XAS spectrum measured in transmission mode is achieved by dividing the measured spectrum $A^T(E)$ by the edge-jump magnitude ΔA^T_{edge}, according to:

$$\begin{aligned} A^T_{norm}(E) &= \frac{A^T(E)}{\Delta A^T_{edge}} \\ &= \frac{\mu(E)}{\Delta\mu_0(E_0)} \end{aligned} \tag{4.3}$$

The normalized x-ray absorption spectrum $A^T_{norm}(E)$ has an unitary edge-jump, the wiggles on the EXAFS region oscillate around a constant value. After the normalization the XAS can then be directly compared against the theory and analyzed.

Fluorescence yield mode

It has been noted earlier that the XAS spectrum can also be measured, indirectly, by recording the consequent fluorescence resulting from the absorption process. To a first approximation, the absorption coefficient measured in fluorescence mode is proportional to the ratio of the fluorescence intensity I_F and the incoming intensity I_0 ($\mu(E) \propto I_F/I_0$). Furthermore, the measured fluorescence intensity is proportional to the incoming intensity, the fluorescence yield, the absorption cross-section and fractional solid angle of detection. Because the XAFS is given by a simple ratio of the incoming and fluorescence intensities, any factor altering the intensities that is not due to the sample itself will distort the XAFS signal in an unpredictable way. This makes the fluorescence-detected XAFS particularly susceptible to systematic errors. It is important to note that in this treatment we are considering fluorescence-detected XAFS as a total fluorescence spectrum, *i.e.*, the signal is composed by integrating the fluorescence resulting from all the possible radiative channels as a function of the incoming x-ray photon energy. Alternatively, the fluorescence from the sample can be dispersed before being recorded, in a way that specific fluorescence channels can be studied separately [93, 95, 153–156].

The relation $\mu(E) \propto I_F/I_0$ represents an oversimplification of the x-ray fluorescence detection. The fluorescence probability is proportional to the absorption probability, but the fluorescence x-rays have to travel though the sample before it reaches the detector. Since the x-rays are attenuated as it traverses matter, the XAFS signal can be damped. This effect is called *self-absorption* and it has to be taken into account when recording XAFS in fluorescence mode.

A more complete expression for the fluorescence intensity originated form the layer dz at the depth z is given by [30, 152, 157]:

$$dI_F(z,E) = I_0(E)\,\frac{\epsilon_f \Omega}{4\pi}\,\mu_\chi(E)\,e^{-\mu_{tot}(E)z/\sin\phi}\,e^{-\mu_{tot}(E_f)z/(\sin\theta\cos\tau)}\,\frac{dz}{\sin\phi} \tag{4.4}$$

where μ_{tot} is the total linear absorption coefficient at the primary x-ray energy E or the fluorescence energy E_f, μ_χ is the contribution from the element of interest, ϵ_f is the fluorescence quantum yield, Ω is the solid angle of detection, and ϕ and θ are the angles of the incoming (I_0) and outgoing (I_F) beams with respect to the sample surface, respectively. The geometry for detecting XAFS in fluorescence mode is illustrated on figure 4.5. The total absorption coefficient μ_{tot} can be decomposed as $\mu_{tot} = \mu_\chi + \mu_{other}$, with μ_{other} containing the background absorption due to all other atomic species present on the sample. Equation 4.4 can be integrated over z in order to obtain the total fluorescence intensity. Assuming that the sample is at 45° with respect to both the incident beam and the fluorescence detector, which is often the case for fluorescence detection, the dependence on ϕ and θ disappear and the fluorescence intensity is then described by:

$$I_F(E) = C\,\frac{\mu_\chi(E)}{\mu_{tot}(E)+\mu_{tot}(E_f)}\left[1 - e^{-\left[\mu_{tot}(E)+\mu_{tot}(E_f)\right]d}\right] \tag{4.5}$$

in which the constant C includes all the energy independent factors. It is treated as an unknown because the actual solid angle of detection is usually unknown and also because it implicitly includes the detector efficiency. This equation has two interesting limits according to the relative values of the terms on the exponential [30, 152, 157]. They are known as the *thin-sample limit* and the *thick, dilute-sample limit*. For the thick, dilute-sample limit it is assumed that the sample thickness is much larger than the absorption length, which is equivalent to $[\mu_{tot}(E) + \mu_{tot}(E_f)]\,d \gg 1$ and $\mu_\chi(E) < \mu_{other}(E)$. Hence the exponential term goes to zero, so that:

$$I_F(E) = C\,\frac{\mu_\chi(E)}{\mu_{tot}(E)+\mu_{tot}(E_f)} \tag{4.6}$$

For the thin-sample limit, both the sample thickness and the absorption length are small. This way the argument of the exponential term becomes $[\mu_{tot}(E) + \mu_{tot}(E_f)]\,d < 1$ and can therefore be expanded in a Taylor series. By keeping the first two terms, Equation 4.5 reduces to:

$$I_F(E) = C\,\mu_\chi(E)\,d \tag{4.7}$$

For the thick, dilute-sample limit $\mu_\chi(E) < \mu_{other}(E)$ and we can ignore the energy dependence of μ_{tot}, implying that $I_F(E) \propto I_0(E)\,\mu_\chi(E)$. Thus, for both limits, the resulting x-ray fluorescence can be directly related to the changes in the absorption coefficient of the absorbing atom. Detecting the XAFS in fluorescence mode should

yield quantitatively the same spectrum as in transmission. If the sample is relatively thin and concentrated, then $\mu_\chi(E) \sim \mu_{other}(E)$ and the energy dependence on μ_{tot} cannot be neglected. In this case the self-absorption plays a role and the spectrum will be distorted.

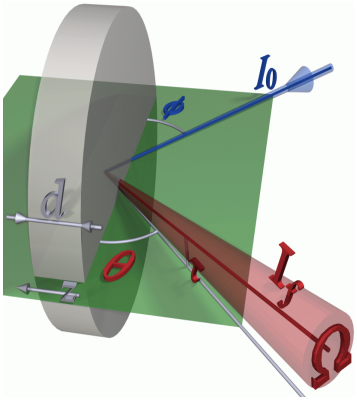

Figure 4.5.: Illustration of the geometry for a XAS experiment in fluorescence mode. The incoming (ϕ) and outgoing (θ) angles with respect to the sample surface are indicated, as well as the total solid angle Ω for the fluorescence x-rays. Taken from reference [157]

As in the case of transmission, the analysis of fluorescence-detected XAFS is done using normalized spectra. The sample thickness and geometrical dependencies due to the solid angle of detection are taking into account by dividing the fluorescence spectrum $A^F(E)$ by its corresponding edge jump. The normalized fluorescence spectrum A^F_{norm} is given by:

$$A^F_{norm}(E) = \frac{I_F(E)}{I_0(E)\Delta A^F_{edge}} \tag{4.8}$$

in which ΔA^F_{edge} is, similarly as the case of transmission, the edge-jump magnitude of the fluorescence signal $I_F(E)/I_0(E)$.

4.4 Setup for time-resolved XAS at high repetition rates

In Section 4.1 a short review of the previous ultrafast time-resolved XAS experiments was given. Apart from a few exceptions [158–161], all the experiments were performed with a rather limited repetition rate, on the order of 1-2 kHz. The reason being the ready availability of commercial amplified laser systems at that repetition rate. Therefore, we have implemented a new scheme to perform time-resolved XAS experiments using MHz acquisition rate.

The x-rays pulse duration and repetition rate set the limits of a certain time-resolved experiment with respect to the temporal resolution and data-acquisition rate. The maximum repetition rate is limited by the frequency the individual x-ray pulses. In principle it is possible to use all of the 390 pulses composing the MB as probe pulses,

however one needs to distinguish them (they are spaced by only 2 ns) and they have lower current than the CS pulse, which does not motivate this approach. With respect to the temporal resolution it is given by the cross-correlation between the laser and x-rays duration. Since the x-ray pulse is about 85 ps long [142], it is clear that this is the limiting parameter preventing a better temporal resolution. Shorter x-ray probe pulses can be obtained by making use of the slicing scheme [142, 143] or by operating the storage ring on the low-α mode [144, 162]. However, the slicing scheme is not implementable at MHz rates using the current hybrid mode at the SLS. This is due to fact that the "sliced" electron bunch should relax back to its stationary state before being sliced again. This process takes several hundreds of microseconds, which is longer than the time interval between adjacent pulses, thus making slicing not easily implementable at MHz repetition rates. In addition, a kW laser source would be needed. Alternatively, one can alter the electron filling mode of the synchrotron in order to have more camshaft pulses available to be sliced consecutively [163]. Such an alternative hybrid filling mode has recently been tested at the SLS, containing five CS pulses uniformly distributed along the orbit path [164]. Another way to improve the time-resolution is to make use of streak cameras. Recently, a streak camera operating on the hard x-ray regime and at kHz repetition rate made its debut [165].

Despite the obvious advantage of matching the laser pump repetition rate with that of the probe, thus substantially increasing the data quality and decreasing the acquisition times, such a high repetition rate scheme for ultrafast time-resolved XAS has so far not been attempted. In this thesis we have developed a new, portable experimental setup for time-resolved XAS with ps temporal resolution. The experimental setup used to record the data presented on Chapters 5 and 6 is described in the following sections. The high-repetition rate data acquisition strategy is presented, together with an investigation of the electronic noise of the system.

4.4.1. Synchrotron experimental endstations

The time-resolved XAS experiments reported in this thesis were collected at the microXAS beamline at the SLS. A brief description of the beamline and the experimental setup for high repetition rate ultrafast time-resolved XAS are shown in the following. In addition, the implemented scheme is very compact and flexible, which has allowed its implementation at other beamlines at the SLS, thus extending the time-resolved XAS towards lower energies (at the PHOENIX beamline) and establishing time-resolved x-ray emission spectroscopy (XES) and resonant inelastic x-ray scattering (RIXS) at the SuperXAS beamline.

Synchrotron beamline: microXAS

The microXAS beamline is located in the long straight section X05L of the SLS ring and is also host to the FEMTO slicing source [142, 166, 167]. The radiation is generated

by a minigap in-vacuum undulator capable of generating x-rays from 4-23 keV with a flux of approximately 10^{12} photons/second/0.015 % bandwidth. The photons are then collected and collimated by a first Rh-coated toroidal mirror which also acts as a focusing mirror, producing a horizontal 1.3 : 1 image of the source. Monochromatic x-rays are obtained over a range of bandwidths by a double-crystal, fixed exit monochromator (DCM) containing Si(111), Ge(111), and Si(311) crystal pairs. An elliptically shaped mirror pair in the Kirkpatrick-Baez (KB) geometry is located immediately before the experimental station, and is capable of focusing the x-rays down to less than 1x1 μm^2 spot [168].

Figure 4.6 shows a schematic drawing of the new setup implemented to measure time-resolved XAS at MHz repetition rates. This setup was used to record the data presented in Chapters 5 and 6, but it remains very similar when used at other beamlines. Monochromatic x-rays are focused in both directions by the KB mirrors to a spot of approximate dimensions of 40 x 40μm^2 at the sample position, approximately 40 cm from the exit of the KB mirror unit. The incoming x-ray beam intensity I_0 was monitored by measuring the fluorescence and scatter generated by a thin (0.5μm) Cr foil placed perpendicular to the x-ray beam. It was measured by a large-area avalanche photodiode (APD). The transmitted x-rays though the sample were measured by a silicon photodiode, whereas the fluorescence signal was recorded by two large-area APDs positioned perpendicular to the incoming x-ray beam to minimize the scatter. The sample environment was either a free-flowing jet or a diamond-wall flow cell. To maximize the solid angle Ω of detection in fluorescence, the APDs were placed as close as possible to the sample, at about 10 mm from the the jet/flow-cell.

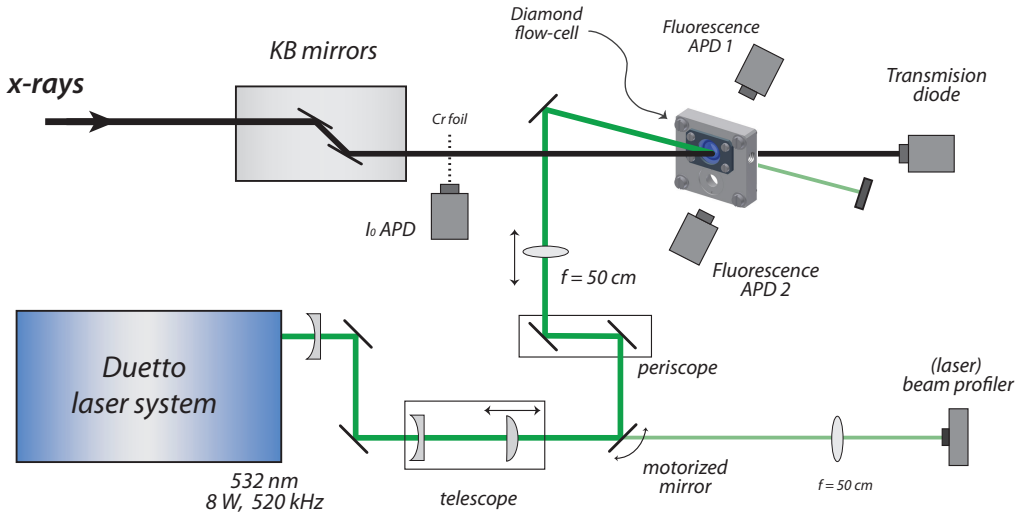

Figure 4.6.: Sketch of the time-resolved XAS setup at the microXAS beamline at the SLS. The description of the components is given in the text.

4.4.2. Laser source

Since the temporal resolution of time-resolved XAS experiments is generally limited by the duration of the x-ray pulse generated at the synchrotron source (typically 85 ps at the SLS), there is no real advantage to use amplified fs laser systems to pump the sample as done so far [33, 34, 38, 126]. These laser sources are amplified, which means they need both a large amount of space and substantial cooling. They are often outside the experimental hutch, implying beam transport over tens of meters to the sample, which results in an increased sensitivity to the laser pointing stability and the far-field laser mode. Therefore, here we used a compact picosecond laser (Duetto, Time Bandwidth Products, Zürich) operating at variable repetition rates (50 kHz to 8 MHz) and producing 10 ps pulses. This laser is primarily aimed at industrial users meaning emphasis has been placed on turn-key operation and long-term stability. It delivers up to two orders of magnitude more energy per pulse than current high-repetition rate femtosecond oscillators, but still two orders of magnitude less energy per pulse than kHz amplified femtosecond systems. The Duetto laser system optimizes the amplifier stage diode pump current to extract the maximum possible pulse energy at any given repetition rate. When operated at half the repetition rate of the isolated camshaft pulse (520 kHz) this results in 28 μJ per pulse at the fundamental wavelength, 1064 nm. By frequency doubling and tripling one obtains 15 μJ per pulse at 532 nm and 6 μJ per pulse at 355 nm. It is also possible to double the 532 nm light to obtain 266 nm light. The laser mode has an M^2 value of 1.2 for both the doubled and tripled beams which permits it to be efficiently focussed to very small diameter spots, thus allowing similar fluences compared to the kHz experiments at modest beam diameters (50-80μm).

The use of this kind of pump laser offers three additional advantages with respect to the 800 nm amplified fs pulses at 1 kHz: a) the longer pulse duration compared to femtosecond pulses results in lower peak powers, which minimizes sample damage and nonlinear effects and generally results in more efficient sample excitation; b) the variable repetition rate allows adjustment depending on the type of system under study *e.g.* systems with long-lived excited states. In extreme cases it might happen that the sample does not have enough time to relax to its ground-state, nor is it be possible to refresh it fast enough before another laser pulse arrives. In those cases, working at a lower repetition rate (while still using more than 1 kHz) is a good alternative to be able to perform the experiment. c) The second harmonic wavelength of the pump laser (532 nm) is a much more convenient one for exciting most chemical and biological samples than the 400 nm of Ti:Sa amplified systems, since molecular systems typically absorb in the visible region of the spectrum (400-700 nm). In special cases, one can also use the tripled (355 nm) or the quadrupled (266 nm) wavelengths, which are easy to generate.

The Duetto laser is a very compact system, weighting less than 150 kg in total (including the control and cooling units). The laser head measures only 425 x 135 x 750 (W x H x L), which means that it can be easily moved around and placed very close to the experiment. This results on less sensitivity to laser pointing stability, which is

critical for time-resolved experiments where overlap of very small laser and x-ray beams (both smaller than 100 μm) has to be guaranteed over the course of several hours (or even days). It has one peculiarity that the exit beam is very small ($\sim$ 0.6 mm) and slightly divergent. Therefore, one has not only to ensure proper collimation of the laser beam but also prevent that the high average power combined with the small beam at the exit of the Duetto damages any optical elements. The average energy density on the first mirror is reduced by placing a diverging lens ($f = -50$ mm) at about 5 cm from the laser exit, thus considerably increasing the beam size. The collimation of the beam is done by setting a telescope combining a divergent and a convergent lenses. The divergent lens used has a focus distance f = -75 mm and the convergent lens focus distance is $f = 500$ mm. The convergent lens is mounted on top of a translation stage which permits to change the relative distance between the two lenses in order to obtain the proper collimation of the laser beam. After the collimating telescope, the beam is guided to the sample position by a motorized mirror and a periscope mirror set that is used to increase the beam height to the level on the x-rays (about 50 cm up from the experimental table surface). The motorized mirror is used to perform the fine spatial overlap of the laser on the x-ray beam by scanning the laser in the horizontal and vertical directions while monitoring the magnitude of the time-resolved signal. The procedure of spatial (and temporal) overlap will be described in the following sections. The residual laser leakage through the motorized mirror was used to monitor the final beam position. This leakage was imaged on a beam profiler that was placed after this motorized mirror. After the motorized mirror, a focusing lens with the same focal distance as the focusing lens was placed. This way, a 1:1 image of the beam at the sample position was obtained.

4.4.3. Synchronization and timing control

Overall stability and synchronization between the pump and probe sources are crucial for the success of any time-resolved experiments. The pump laser pulses have to be accurately synchronized to the x-ray probe pulses in order to have control of the relative temporal delay between them. Here we adopted a similar synchronization and timing control scheme used on previous optical pump/x-ray probe experiments, [127, 131] which has been proven to work reliably over the time required for the experiments. A simplified scheme of the synchronization and the timing control, and the data acquisition system is shown in Figure 4.7.

The synchronization is achieved by exploiting the intrinsic synchronization of the Radio Frequency (RF) master clock of the SLS with the x-ray pulses. This master clock is synchronized to the 500 MHz signal of the RF cavities which is, in turn, responsible for creating the potential wells inside the storage ring, thus providing the time structure of the generated radiation. If a stable phase relationship between the RF and the laser oscillator pulses is established, synchronization is achieved. The relative phase stabilization is done via a commercially purchased system (CLX-1100 timing stabilizer, Time Bandwidth Products), which locks the phase of the Duetto laser to the SLS master

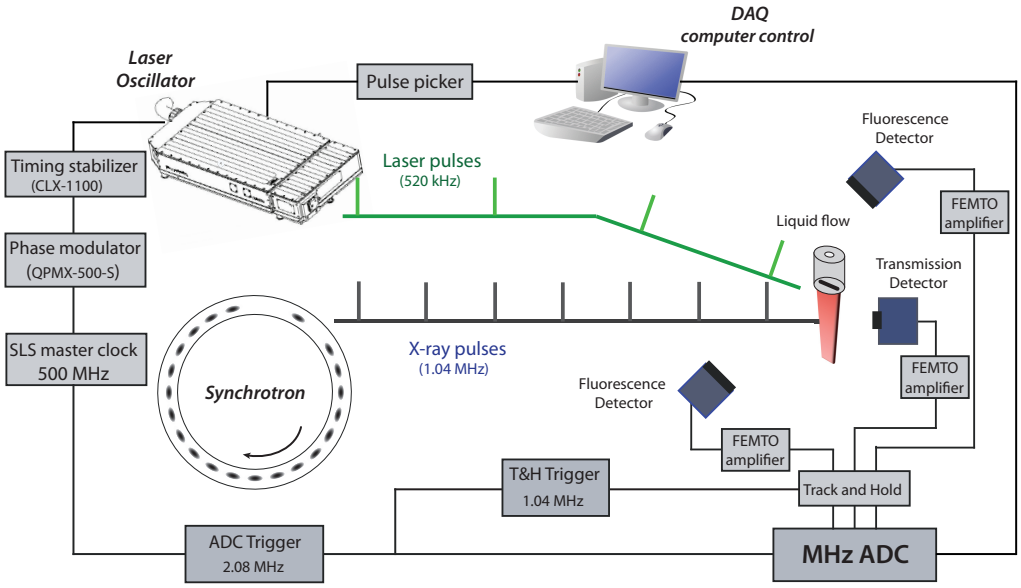

Figure 4.7.: Diagram of the synchronization and timing control scheme. The 500 MHz master signal from the SLS is fed into the phase modulator, which controls the relative phase between the x-ray and laser pulses. The CLX-1100 timing stabilizer locks the phase of the laser pulses with respect to the SLS master RF, thus completing the synchronization loop. The relative delay between laser and x-ray is controlled by computer, which is part of the data acquisition program.

RF with a timing jitter of less than 0.4 ps.

The relative time delay between the x-rays and laser pulses can be adjusted via a computer controlled timing system, which is integrated in the data acquisition system. It is composed by a laser pulse-picker and a phase modulator (QPMX-500-S, I. F. Engineering). The pulse-picker, inside the Duetto laser system, is responsible for adjusting the timing in coarse steps of 12 ns. By giving it a proper trigger it is possible to select different seed pulses from the oscillator pulse train inside the Duetto. For finer tuning the phase modulator is used, which adjusts the relative phase of the oscillator with respect to the phase of the RF, thus changing the relative time of the laser and x-ray pulses.

4.4.4. Data acquisition system

The employed data collection strategy is basically the same as the one previously used for kHz experiments, [33, 34, 127, 169] with the important difference that the data acquisition repetition rate is increased to 2 MHz. Briefly, the XAS signal is recorded at twice the laser repetition rate on a pulse-by-pulse basis, alternating between the signal originated from the excited sample at a specific x-ray energy and laser/x-ray relative delay, followed 1 μs later by the same XAS signal of the unexcited sample. Usually, the repetition rate is set such as to include all the available isolated x-ray pulses (CS) of the

hybrid filling mode on the measurements, *i.e.*, 1.04 MHz. It can also be easily reduced to any even sub-multiple of this frequency (down to a minimum of 50 kHz set by the limitations on the repetition rate of the Duetto) to accommodate the particular needs of a given experiment with respect to sample damage or sample lifetime. In addition, a *zero* measurement is made for every x-ray measurement by reading the detector signal in the fill pattern gap where no x-rays are present. This electronic zero level is then subtracted off the corresponding x-ray signal to compensate for any drift in the data acquisition baseline over time. The signals provided correspond to the *pumped* XAS signal, the *unpumped* XAS signal and the pulse-to-pulse difference. [d]

We used track-and-hold circuits to sample the signal in combination with fast digitization on a pulse-to-pulse basis, always selecting all the CS pulses provided by the SLS. The use of gated detection as in the kHz experiments [33, 34, 38, 127, 128, 169] is not possible at MHz repetition rates because they are limited to typically 10 kHz repetition rate. Thus the new data acquisition hardware (DAQ) uses a *track-and-hold* system (AD9100, Analog Devices) to perform the signal sampling and a multi-MHz ADC (Struck Innovative System GmbH, model SIS3302) for digitizing the data. The operation of a track-and-hold is such that it samples the (continuous) input signal at one specific point and holds its value for a specified period of time, until the digitization is complete. The time of the 'track' mode is set to the peak of the hybrid pulse so as to maximize the x-rays signal. The digitizer is an eight-channel ADC/digitizer board with a sampling rate of up to 100 MHz and a resolution of 16 bits, capable of sampling up to 8 channels in parallel for each given trigger. The ADC is housed in a *virtual machine environment* (VME) crate together with the hardware for generating all the timing signals. When operating at the maximum repetition rate, *i.e.* 1.04 MHz, the trigger signals required to trigger the ADC is at 2.08 MHz, the (laser) pulse picker 520 kHz and the track-and-hold circuits 1.04 MHz. In addition, two marker signals are generated and digitized in parallel with the data channels to indicate if a signal originates from the laser-excited or from the unexcited sample. The VME crate uses these marker signals to sort the data prior to performing the signal averaging. At this repetition rate, the DAQ makes two million measurements over the course of 1 second. They correspond to 500000 pumped x-rays, 500000 pumped zeroes, 500000 unpumped x-rays, and 500000 unpumped zeroes. These signals are then sorted according to the markers, the requisite calculations are performed and then each of the three signals is averaged, returning to the scanning PC the averaged data and the standard error of the pumped/unpumped/difference measurement for each of the ADC channels.

The detected signals are pre-amplified using low-noise, fast current amplifiers (DHPCA-100, FEMTO) being subsequently fed into the track-and-hold sampling electronics and then digitized. The data stream from the ADC is pre-processed on a VME computer before it is sent to the acquisition program running on a regular PC, meaning that

[d] On the pulse-to-pulse difference XAS signal the zero signals are ignored since the electronic baseline does not have time to drift considerably during the 1μs separating the two x-ray measurements.

in the case of the maximum repetition rate, for each recorded data point the average and standard deviation of the 2 million individual measurements (corresponding to approximately 1 second integration time) are calculated. The complete diagram of synchronization, timing control and data acquisition is shown in Figure 4.7.

The time-resolved measurements of this thesis includes XAS signals of transmission and/or fluorescence yield modes, recorded simultaneously. For some special cases, *e.g.* as for the $[Fe(bpy)_3]^{2+}$ sample, it is possible to adjust the sample concentration in order to optimize the signal for either transmission or fluorescence yield or to find a compromise and acquire in both modes simultaneously in order to increase the S/N. Earlier it was noted that the incident x-ray intensity was also recorded, measuring the scatter and fluorescence of a thin Cr foil placed immediately before the sample. Recording the incoming x-ray flux on a pulse-to-pulse basis allows the normalization of incoming x-ray fluctuations due to monochromator imperfections or changes due to the storage ring, and to correct for the sudden variation in x-ray flux after a top-up. Moreover, normalization of the unexcited spectra to the incident flux yields the static XAS of the sample, as it can be seen from Equations 4.9 and 4.10.

In 1 kHz experiments, this data acquisition methodology delivered results at the shot-noise limit of the x-ray source [127, 131]. In this limit, the S/N increases linearly with the fraction of excited species, while it increases with $\sqrt{N}$ of the number of accumulated x-ray photons, and thus the repetition rate of the experiment [170]. In the present experiment, the repetition rate was increased by a factor of 500, meaning that the expected increase on the S/N ratio is $\sqrt{500} \approx 23$.

Pump-probe XAS signal

In Section 4.3.1 the expressions for the steady-state XAS signals were derived for the case of transmission and fluorescence yield detection. In the time-resolved experiments, the signal measured is the difference between the pumped (laser excited) and unpumped (ground-state) XAS signals. This is true for whatever detection mode, either transmission or fluorescence. The transient (difference) XAS signals is then defined, for transmission mode detection, as:

$$\Delta A^T(E,t) = ln\left(\frac{\left[I^T_{unp}(E)\right]^{x-ray} - \left[I^T_{unp}(E)\right]^{zero}}{\left[I^T_{p}(E,t)\right]^{x-ray} - \left[I^T_{p}(E)\right]^{zero}}\right) \tag{4.9}$$

In the case of fluorescence yield mode, the transient XAS signal is defined by:

$$\Delta A^F(E,t) = \frac{\left(\left[I^F_{p}(E,t)\right]^{x-ray} - \left[I^F_{p}(E,t)\right]^{zero}\right) - \left(\left[I^F_{unp}(E)\right]^{x-ray} - \left[I^F_{unp}(E)\right]^{zero}\right)}{I_0(E)} \tag{4.10}$$

The subscripts *unp* and *p* stand for the ground-state (unpumped) or excited (pumped) sample, respectively. I_0 represents the incoming x-ray intensity, I^T stands for the trans-

mitted and I^F for the fluorescence signals. The superscript *x-ray* indicates that the signal was recorded with the presence of x-rays and the superscript *zero* indicates that it was recorded without any x-rays (in the gap of the fill pattern), representing the electronic background signal of the detection system. Figure 4.8 shows the electron filling pattern at SLS, indicating the pumped, unpumped and zero signals.

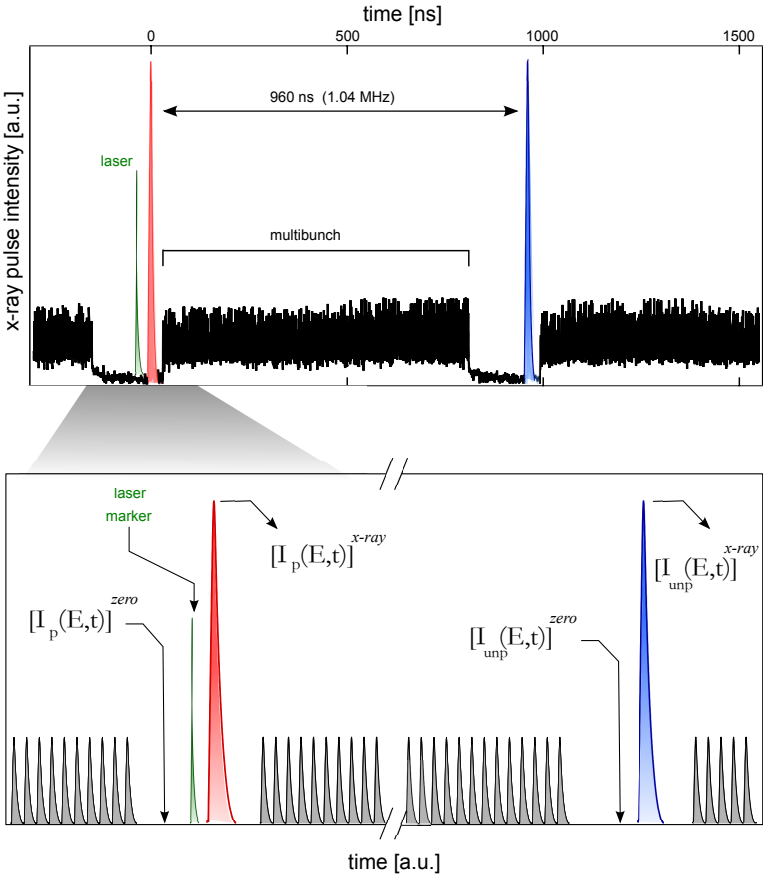

Figure 4.8.: Illustration of the SLS filling pattern showing the pump, unpumped and zero signals measured during the time-resolved experiments. The laser marker is used by the DAQ to identify if the x-ray signal comes from pumped or unpumped event.

It is, in general, not possible to completely promote all the molecules to the excited-state during the laser excitation . Therefore, the pumped signal has a time dependency due to the excited-state population decay. In other words, the pumped signal contains contributions from both the ground- and excited states. For this reason it is necessary to introduce the *excitation yield* $f(t)$, which gives the fraction of excited molecules at a given time t in the sample that is probed by the x-rays.

$$\Delta A(E,t) = f(t)\,[A_p(E,t) - A_{unp}(E)] \tag{4.11}$$

Here $\Delta A(E,t)$ represents the transient XAS, and A_p and A_{unp} stands for the laser pumped and unpumped normalized XAS, respectively. Equation 4.11 is valid for both

fluorescence and transmission collected data. It should be noted that $f(t)$ in Equation 4.11 assumes that only one excited-state species is present in the sample. This expression can be generalized for the case on which multiple excited-state species are present at a certain time t [122], such that $f(t) = \sum_n f^n(t)$ and $A_p(E,t) = A_p^n(E,t)$.

Similarly as in the steady-state case, the time-resolved XAS signals need to be properly normalized in order to perform a proper analysis (and also to correctly compare transmission and fluorescence signals). Normalization of the transient signals is done by dividing the transient XAS $\Delta A(E,t)$ by the edge-jump magnitude of the steady-state absorption ΔA_{edge}, which is obtained from the unpumped signal A_{unp}. This way, the normalized transient XAS is given by:

$$\Delta A_{norm}(E,t) = \frac{\Delta A(E,t)}{\Delta A_{edge}} \tag{4.12}$$

4.4.5. Detectors

In the setup used to measure the time-resolved XAS using high repetition rate, the x-rays are measured using fast detectors *e.g.*, large-area avalanche photodiodes and Silicon photodiodes, which have rise times of the order of 1-5 nanoseconds. They are sufficiently fast to distinguish the individual hybrid x-ray pulses. In transmission mode the high intensity beam impinging on a very small area combined with the built-in internal gain of the APDs can result in non-linearities of the detector. This can be prevented by either using a heat-load chopper to cut part of the unused multibunch pulses or by attenuating the incoming intensity. The former is not feasible since x-ray choppers usually run at kHz repetition rates with typical opening times of several nanoseconds, [132–135] whilst we want to make use of all the available hybrid pulses at 1.04 MHz. Attenuating the x-ray beam is not a reasonable solution since this type of experiment already suffer from low x-ray photon flux, so the choice of a regular Silicon photodiode for transmission detection is justified. The latter is directly against all the purposes of the reported experiment, which is to make use of as much x-ray photons as possible. In fluorescence mode windowless large-area avalanche photodiodes having 10x10 mm^2 active area (C30703F, PerkinElmer) are used close to the sample in order to increase the solid angle for photon collection, while the transmission signal was detected by a small area Silicon photodiode (AXUV20HS1, International Radiation Detectors). Both the Silicon photodiode for transmission and the large area APDs for fluorescence detection were mounted in metallic boxes and had their active area covered by 50 μm thick Beryllium foils to protect them from the intense scatter of the laser pulse.

To test the linearity of the photodiode used as transmission detector a series of measurements of the direct x-ray flux were taken while attenuating it by placing successive thin Aluminium foils in the incoming beam. The x-ray intensity was recorded directly as the track-and-hold output, the data acquisition digitized signal and the diode current.

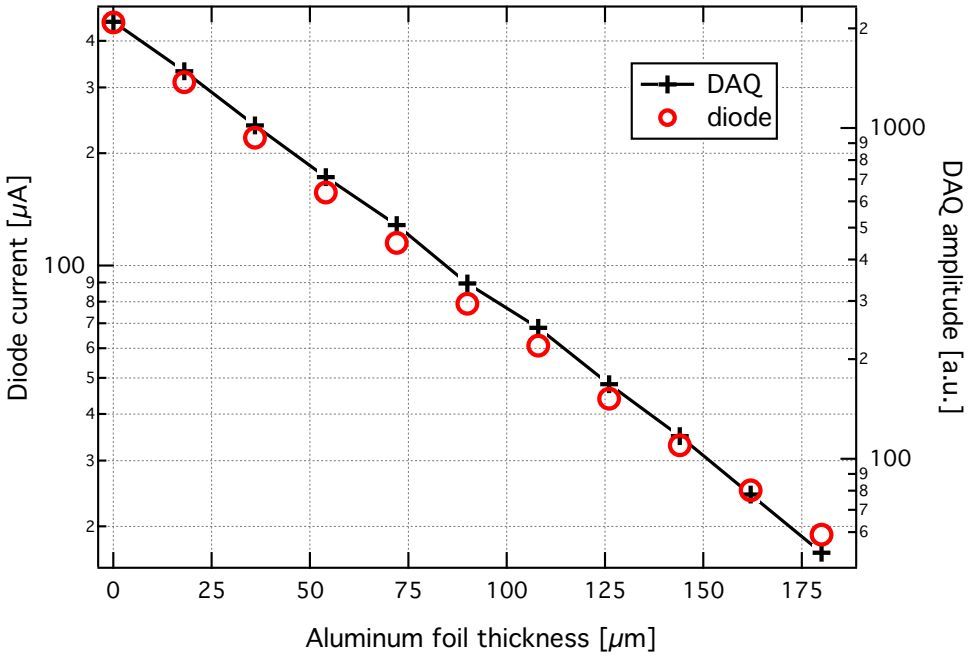

Figure 4.9.: X-rays transmission signal (at 7.05 keV) measured by a fast diode. Left axis shows the diode current (red circles) while the right axis shows the digitized signal amplitude (black crosses). The flux was attenuated by placing aluminium foils of varying thickness in the beam. On a logarithmic scale the signal shows a linear dependence on absorber path length over the full range of x-ray flux indicating that the diode and DAQ are linear, even when no attenuation is used, i.e., the full x-ray flux is used.

Assuming a constant incoming intensity, which is a reasonable approximation for the SLS since it operates in top-up mode (0.5% fluctuation in the electron beam current), we expect the transmitted signal to follow the Lambert-Beer law. In other words, the detector should behave linearly with respect to the incoming intensity. Indeed, the measured signals are proportional to the incoming x-ray flux (see Fig. 4.9), thus attesting to the linearity of the Silicon photodiode; even when the full flux of the beamline - 10^{12} photons/sec. - is used.

4.4.6. Spatial and temporal overlap

The spatial overlap between laser and x-rays was obtained by placing a 50 μm diameter, 25 μm thick tungsten pinhole in the sample position. The x-ray position and size can be determined by scanning the pinhole through the x-rays using a two-dimensional translation stage (0.1 μm resolution), while monitoring the transmission intensity. Once the x-ray position is found, the pinhole is moved to that position and the attenuated laser beam is then guided through the pinhole and its position is optimized via a motorized laser mirror. Figure 4.10 shows the horizontal and vertical beam profiles of the laser and x-rays at the sample position. The x-ray spot size was determined to be less than

50 μm in both dimensions (FWHM). The microXAS x-ray image monitor indicates that the x-ray beam is focused down to ca. 40 μm. The laser beam size was made larger than the x-ray spot (85 μm horizontally and 65 μm vertically), to ensure a uniformly excited sample and to facilitate the overlap of the pump and probe beams.

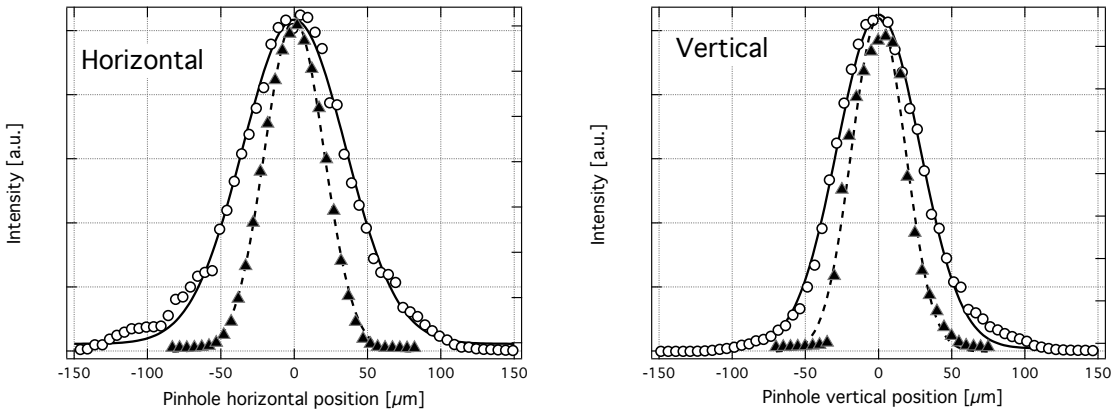

(a) Horizontal profile of the laser and x-ray beams

(b) Vertical profile of the laser and x-ray beams

Figure 4.10.: Laser (circles) and x-ray (triangles) beam profiles scanned through a 50 μm diameter pinhole. Solid and dotted lines are Gaussian fits.

To set the temporal overlap a fast windowless photodiode having a rise time of 0.7 ns (AXUVHS5, International Radiation Detectors) was placed at the sample position. Using a 2.25 GHz oscilloscope (Agilent Infiniium) the relative laser and x-rays temporal delay could be determined. Using the procedure described in Section 4.4.3 to change the relative delay between pump and probe, the laser pulse-picker timing was then adjusted to shift the laser timing in coarse steps of 12 ns, and then the phase-shifter was used for finer time steps. In this way, the laser and x-ray pulses can generally be overlapped to within 200 ps which is sufficient to establish a pump-probe signal for samples where the excited state lifetime is $>$ 200 ps. Once the signal is detected, it can be optimized by fine time scans around the time-zero and also moving the motorized laser mirror on both directions to improve the laser and x-rays overlap.

4.4.7. Electronic noise investigation

In order to assess the sensitivity of the new high repetition rate data acquisition system and to investigate the sources of electronic noise, we recorded the digitized individual output signals in transmission and fluorescence modes, corresponding to 2 million samples, or approximately 1 second integration time. In this way we can analyse the pulse-height distribution for single x-ray pulses and compare the width of the distribution function for the different detection geometries (transmission and fluorescence) to estimate the sources of noise on the setup.

Figure 4.11 shows the histograms of the distribution of 500000 zero measurements and 500000 x-ray measurements for an unpumped signal of a 7 mM aqueous solution of $[Fe(bpy)_3]^{2+}$ recorded at 7.125 keV. In Figure 4.11a is shown the results for transmission and Figure 4.11b corresponds to fluorescence. In both cases we can clearly identify the zero signal, which corresponds to no x-rays hitting the detectors (as part of the data acquisition strategy, according to Section 4.4.4). The distribution of measurements without x-rays is sharply peaked around 0 V with a small offset in the fluorescence signal. This offset is, however, completely irrelevant since the real signal is always calculated using the difference between x-rays and zeroes. In addition, this zero-level line can drift over time due to electronics, but the difference x-ray on minus x-ray off is maintained. The fact that the transmission zero measurement distribution is narrower than the transmission x-ray measurement distribution shows that the electronic noise is smaller than the photon noise [39, 127, 171].

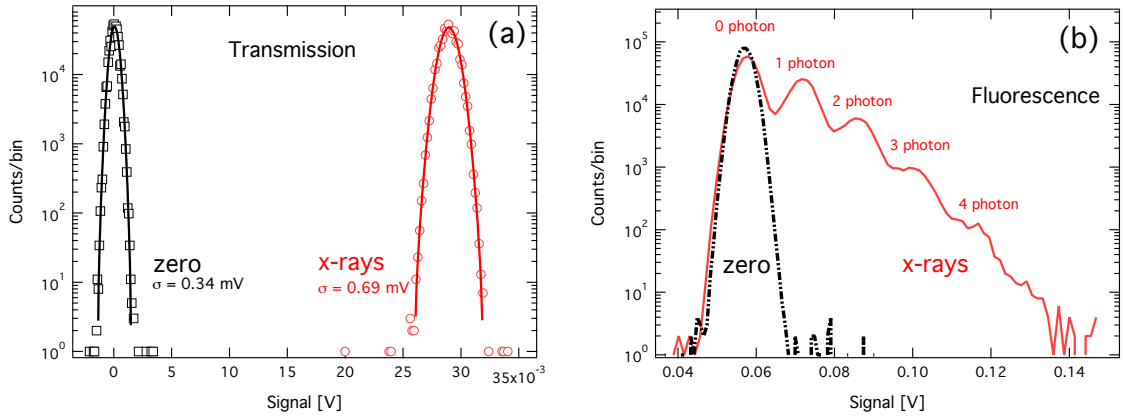

(a) Transmission histogram

(b) Fluorescence histogram

Figure 4.11.: Pulse-height distribution of 10^6 samples recorded in (a) transmission mode and (b) fluorescence mode at 7.125 keV for a 7 mM sample of $[Fe(bpy)_3]^{2+}$. Gaussian fits to the histograms are shown as lines for the transmission signals. Note the clear peaks from multi-photon events in the fluorescence signal.

In fluorescence yield detected XAS, the limited solid angle imposed by the geometry and the overall small efficiency of the fluorescence process results in orders of magnitude lower photon fluxes when compared to transmission mode. Thus one can expect to enter the photon-counting regime. The pulse height distribution shows that it is possible to reliably distinguish between single photon events. Events with up to 4 photons could be identified in the fluorescence signal of the 7 mM $[Fe^{II}(bpy)_3]^{2+}$. Additionally, the Poisson distribution of the photon-counting events can clearly be resolved, delivering 0.56 photons/pulse on average.

4.4.8. Sample environment for air sensitive samples: diamond-walled flow cell

Over the course of time-resolved XAS experiments it is highly desirable to flow the sample, not only to avoid sample degradation, but also to ensure that a certain sample volume is excited with only one laser pulse and it has sufficient time to relax back to the ground state before being excited again. Our conventional setup for time-resolved XAS makes use of an open-flow jet, which is created by forcing the liquid sample to pass through a very thin aperture - typically 100-200 μm - in a sapphire nozzle. Usually a magnetically-driven gear pump is used since it combines a high flow with a stable operation, guaranteeing a laminar flow. When dealing with biological systems, the open-flow jet presents two main disadvantages: the whole system is exposed to air, which causes problems for any air-sensitive sample and the total volume of sample needed is on the order of 50 ml, meaning that a large amount of protein is needed for the experiments. In order to overcome these limitations, a flow-cell with diamond windows was designed.

Chemical vapor deposition (CVD) diamond was chosen as the material to be used for the windows because of its excellent mechanical, thermal and optical properties. CVD diamond presents an unsurpassed hardness, extremely high thermal conductivity, broadband optical transparency and is chemically inert. Moreover it can be made very thin - down to several tens of nanometers. The thickness of the windows was chosen maintaining a compromise between x-ray transmission (in the energy range used for the current experiments, ca., 7 keV) and robustness. A good result was obtained using 50 μm thick CVD diamond, polished to optical quality, assuring (visible) light transmission $> 70\%$ at 532 nm and x-ray transmission [172] $> 89\%$ at 7.1 keV (data obtained from Center of X-ray Optics [173]).

The concept of the flow cell is simple and robust, providing a very flexible sample handling during the time-resolved x-ray experiments. It was designed in a way that the liquid enters through a cone-shaped adaptor placed on the side of the cell, allowing easy exchange of a flexible tubing size (*PharMed BPT, Viton, etc.*) according to the specific needs of each experiment. The liquid flows inside a channel of about 2-3 mm width formed by the two 50 μm thick diamond windows and two half-moon shaped teflon sheets. The windows are kept separated at a fixed distance by the teflon spacers since they also have the role of controlling the path length of the flow cell. The path length can be varied between 100-500 μm by simply exchanging the spacers. Sealing is provided by the use of Viton o-rings. On the same flow cell support a pinhole is mounted allowing for easy laser/x-ray spatial overlap. This pinhole is placed such that it lies in the same plane as the sample, so that overlap is ensured even when rotation of the flow cell is performed in the case of fluorescence yield measurements. The flow cell illustration and assembly scheme are shown on Fig. 4.12.

The stability of the diamond windows was tested with respect to laser irradiation by using the output of the Duetto laser at 200 kHz and 532 nm, which was focused down to about 60 μm. It was found that due to the high average power, the sample light

absorption plays a significant role in the damage threshold of the diamond windows. For this reason the tests were executed with flowing samples; in the extreme case of a 70 mM solution of aqueous $[Fe(bpy)_3]^{2+}$ under the above-mentioned conditions, the damage threshold was found to be about 0.4 J/cm^2.

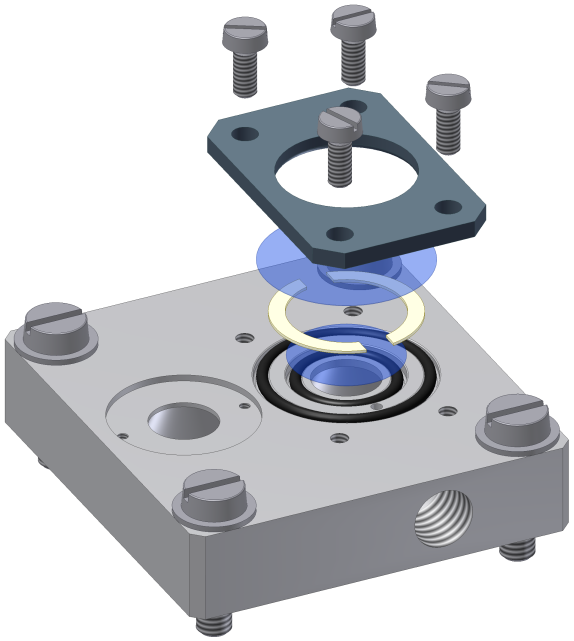

Figure 4.12.: Illustration of the complete flow-cell, showing the 50 μm thick CVD diamond windows (transparent blue) and the half moon shaped spacers (light yellow). Note the location to attach the alignment pinhole, which is in the same plane as the sample.

In using the diamond flow cell as sample environment a complication arises due to sample aggregation at the inner wall of the diamond membrane at the spot where the laser and X-rays hit the sample. Depending on the sample, this aggregation can be caused by either the laser or the X- rays, or both. It is seen as an increase in the total amount of fluoresced x-rays, as well as a corresponding decrease in the pump-probe signal. To reduce the aggregation, one can move the flow cell vertically to a new spot. By going through a few spots on the diamond membrane, while changing the position after each scan, the aggregation in the time-resolved XAS experiment on Myoglobin could be suppressed.

4.5 Myoglobin preparation procedure

Myoglobin (Mb) is a relatively simple and robust protein, which is readily available as lyophilized powder from commercial companies, *e.g.*, Sigma-Aldrich. Many mammalian Mb can be obtained in big quantities, including canine, bovine, equine, from sheep, sperm-whale and even human. The use of sperm-whale Mb is being steadily reduced

due to the moratorium of whale hunt imposed by the *International Whaling Commission* in the middle 1980's [174]. Despite of having been studied for over a century [175], consistent protocols for preparing the different forms of Mb (especially in physiological conditions) are not easily available in the literature. Myoglobin readily oxidises with the oxygen present in air [3], meaning that the initially the samples are predominantly on the oxidized form. The unligated oxidized (ferric, Fe^{3+}) form of Myoglobin is also known as "met Myoglobin" or simply metMb and the unligated reduced (ferrous, Fe^{2+}) form of Myoglobin is called "deoxyMb". This terminology will be used from now on. Apart of the Cyano-Myoglobin (MbCN), which is a ferric form, all the other ligated forms of Mb are ferrous. In order to obtain these ligated ferrous forms it is necessary to first reduce the iron atom so it can bind the ligand. In our experiments we decided to use Mb from equine skeletal muscle, with purity $95 - 100\%$. It has a molecular weight of 17600 Da [e], based on the amino acid sequence.

The solvent used in our experiments was a Sodium phosphate buffer, with pH 7.0. To avoid any contact with oxygen, the solvent was degassed by bubbling with nitrogen gas (purity $> 99.99\%$) for at least 10 hours. To keep the solvent on a controlled atmosphere we kept it on a glass bottle sealed with plastic caps with four apertures under a slight overpressure of nitrogen. These apertures were sealed with silicone disks, from which all the liquid extraction and gas input were done, using gas-tight syringes. The same type of bottle was used as sample reservoir during the XAS experiments, with two of the silicone disks being replaced by tubes connected to the diamond flow-cell or the capillary. Additionally, two thin tubes can be inserted through one of the silicone disks to provide a parallel flow circuit to monitor the visible absorption (UV-Vis) of the sample in order to check for sample integrity.

Unligated ferric Myoglobin - metMb

The preparation of Unligated ferric Myoglobin (metMb) solutions is relatively simple. The Mb lyophilized powder is already in the oxidized form and no special care is required to avoid contact with oxygen. It is only needed to add the corresponding amount of Mb to the solvent (Sodium phosphate buffer with pH 7.0) and stir the sample container until the powder is completely dissolved. It is always a good practice to check if the sample really corresponds to what it is expected. This can be easily done by inspecting the UV-Vis spectrum and comparing the position of the main absorption bands. The metMb visible absorption spectrum is characterized by two main absorption bands, one at around 400 nm, the *Soret* band, and other at around 500 nm, the Q-band.

[e] The **unified atomic mass unit(u)**, or **Dalton (Da)** or,sometimes, **universal mass unit**, is a unit of mass used to express atomic and molecular masses.It is the approximate mass of a hydrogen atom, a proton or a neutron. The precise definition is that it is one-twelfth of the mass of an isolated atom of Carbon-12 (^{12}C) at rest and on its ground state. $1u \equiv 1/N_A$ gram $= 1.660538782(83) \times 10^{-27}$ kg.

Unligated ferrous Myoglobin - deoxyMb

The unligated ferrous Myoglobin (deoxyMb), is obtained by adding Sodium dithionite ($Na_2S_2O_4$), dissolved in the previously degassed buffer, in slight excess to a solution of metMb. In all the samples used in the experiments presented in this thesis we used a 5-fold molar excess of $Na_2S_2O_4$. The complete sample preparation was done under N_2 atmosphere. A noticeable effect from going to oxidised to reduced Myoglobin is the sample color. It changes from dark red-brown, characteristic from the oxidized metMb, to vivid red which is characteristic not only of the deoxyMb, but of all other ligated forms. In the unligated reduced Mb the heme is no longer flat, being now in a domed state. This is accompanied by corresponding changes on the UV-Vis spectrum. The main bands suffer a pronounced red-shift, the Soret going to 434 nm and the Q-band to about 556 nm.

Nitrosyl-Myoglobin - MbNO (ferrous)

The Nitrosyl-Myoglobin was prepared following a procedure similar to the one used by Kim *et al.* [176]. They used a 12 mM solution of MbNO, prepared by dissolving lyophilized skeletal horse Myoglobin in sodium phosphate buffer (pH 7.4, 0.1 M), so to have metMb. Then it was reduced to deoxyMb with a two-fold excess of freshly prepared $Na_2S_2O_4$ solution, and then added an equivalent quantity, *i.e.*, two-fold excess of 0.1 M degassed Sodium nitrite ($NaNO_2$) solution in the presence of an equimolar quantity of 0.1 M $Na_2S_2O_4$. We used solutions of 4 mM Myoglobin, which corresponds to 3 times less concentrated solution of metMb than on Ref [176]. Therefore, we simply used a 3 times less concentrated solution of $NaNO_2$, *i.e.*. 33.3 mM, to prepare the MbNO. The $NaNO_2$ solution in the desired concentration was prepared using commercially-available $NaNO_2$ (100 mM) dissolved in degassed buffer and kept under N_2 atmosphere. The procedure starts by producing a solution of metMb at the desired concentration (4 mM, taking into account that extra solved will be added in conjunction with $Na_2S_2O_4$ to reduce the Mb and to add the NO ligand). Once the metMb is ready, Sodium dithionite dissolved in degassed buffer was added to the solution and right after, added the 33.3 mM of $NaNO_2$. At this point the sample was MbNO, so it was kept under Nitrogen atmosphere at all times to prevent oxidation and the slow exchange of NO by the oxygen on the air.

Carboxy-Myoglobin - MbCO (ferrous)

The preparation of Carboxy-Myoglobin follows the same philosophy for producing any ligated ferrous Mb, *i.e.*, we should first produce the oxidized metMb, then reduce the iron atom by adding Sodium dithionite in a oxygen-free atmosphere and then add the desired ligand. metMb was prepared in the desired concentration by adding the Mb powder to previously degassed buffer. The second step involves saturating the metMb

solution with Carbon monoxide by bubbling CO gas in the solution for a minimum of 15 minutes. The last step is to reduce the iron atom, adding the corresponding molar amount of $Na_2S_2O_4$ dissolved on degassed Sodium buffer, allowing it to bind the CO molecules present in the solvent. At this point the sample should be composed of MbCO. Even though the Mb affinity for CO is very high [177] we kept the MbCO sample under a CO atmosphere to ensure the sample integrity. The Soret band of MbCO shifts to 422.5 nm and, the Q-bands around 550 nm are split in two, peaking at 541.5 nm and 578.5 nm

Oxy-Myoglobin - MbO_2 - (ferrous)

The procedure for making MbO_2 is very similar to the one of making MbCO. Basically all it is needed is to follow the same procedure, substituting the CO gas by the O_2 gas. In fact it is not advisable to use pure oxygen since it is highly flammable. A gas mixture composed of 40% oxygen in helium was therefore used. The Soret band of MbO_2 lies at 416 nm and the Q-bands at 543 nm and 581 nm. The MbO_2 preparation was stable for > 5 hours, which was enough to complete all the measurements.

Cyano-Myoglobin - MbCN - ferric

The preparation of MbCN is very simple. Since it is a ferric form, all is needed is to used a solution of metMb and add the proper amount of cyanide (CN) that should bind to the iron atom. However, during the procedure one has to be extremely careful because CN is toxic. All the manipulations have to be done inside a fume hood and with the presence of a CN detector. Cyanide was derived from a solution of NaCN in basic environment (pH $\sim$ 14) to prevent the formation of CN gas when it encounters water. The UV-Vis of the MbCN is characterized by the Soret band at 423 nm and one single Q-band ataround 540 nm.

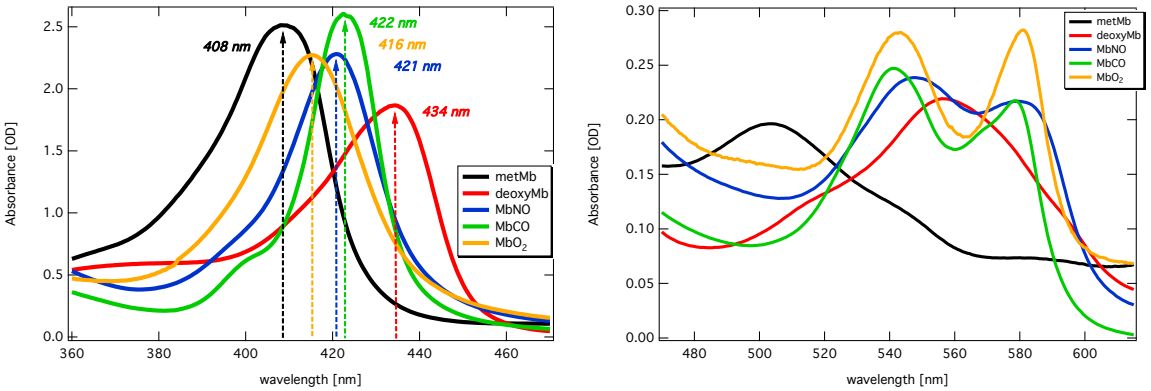

Figure 4.13.: Comparison of the UV-Vis spectra of several different forms of Myoglobin.

"Although we often hear that data speak for themselves, their voices can be soft and sly."

Frederick Mosteller

5

Benchmark experiments: $[Fe(bpy)_3]^{2+}$

In this chapter, the results of the benchmark experiments using the new high repetition rate scheme for ultrafast time-resolved X-ray absorption experiments are presented. The complete characterization of the system was done by reinvestigating the light-induced spin transition in aqueous solutions of the $[Fe(bpy)_3]^{2+}$ molecule, with 50 ps temporal resolution. We start in Section 5.1 by showing the measured transient XAS with emphasis on the high quality of the data and the short acquisition times. This is followed, in Section 5.2, by the demonstration that the overall experimental temporal resolution is not affected by the use of 10 ps laser pulses to excite the sample, and is instead given mainly by the temporal duration of the x-ray probe pulses. In Section 5.3 is presented a quantitative estimate of the increase in signal-to-noise (S/N) ratio by using MHz data acquisition rates compared to previous kHz schemes, reflecting the increase in quality of the transient XAS data. In Section 5.4 it is shown that the increase in data quality and acquisition times (increase in S/N) makes possible the measurement of highly dilute samples. Finally, in Section 5.7 we revise the analysis of the XAS spectra of $[Fe(bpy)_3]^{2+}$, both for the ground-state and the transient XAS data. We confirm the Fe-N bond elongation of 0.20 ± 0.01 Å upon laser-induced spin transition and discuss the electronic structure of the high-spin state in view of the density-of-states (l-DOS) obtained by the analysis of the XAS spectrum.

5.1 Time-resolved XAS results

Figure 5.1 shows the K-edge steady-state XAS of a 25 mM aqueous solution of $[Fe(bpy)_3]^{2+}$ together with the transient spectrum obtained using the high repetition rate scheme for time-resolved XAS described in Chapter 4. Excitation was at 520 kHz using the 10 ps laser pulses of the Duetto laser system at its second harmonic wavelength (532 nm). The transient XAS was collected at 50 ps after laser excitation and using approximately 100 mJ/cm^2 laser fluence, which corresponds to about 2 W average power. The time-resolved signal shown in Figure 5.1 corresponds to the data of only one fluorescence detector and is an average of 11 individual scans, in which each data point corresponds to 1 second integration time. From this it is already possible to infer the first advantage of collecting data at MHz repetition rates. The data presented in Ref. [39] is composed of 53 individual scans and averaging together the signals from a transmission and two fluorescence detectors, in comparison to only 11 scans of the present data. Following the procedures given in Section 4.4.4, the transient XAS was normalized to the incoming intensity $E_0(E)$ and subsequently divided by the fluorescence edge-jump magnitude, according to Equation 4.12. The resulting normalized transient XAS spectrum can then be used to derive the excited-state XAS, once the fraction of excited-state species $f(t)$ is known, as given in Equation 4.11.

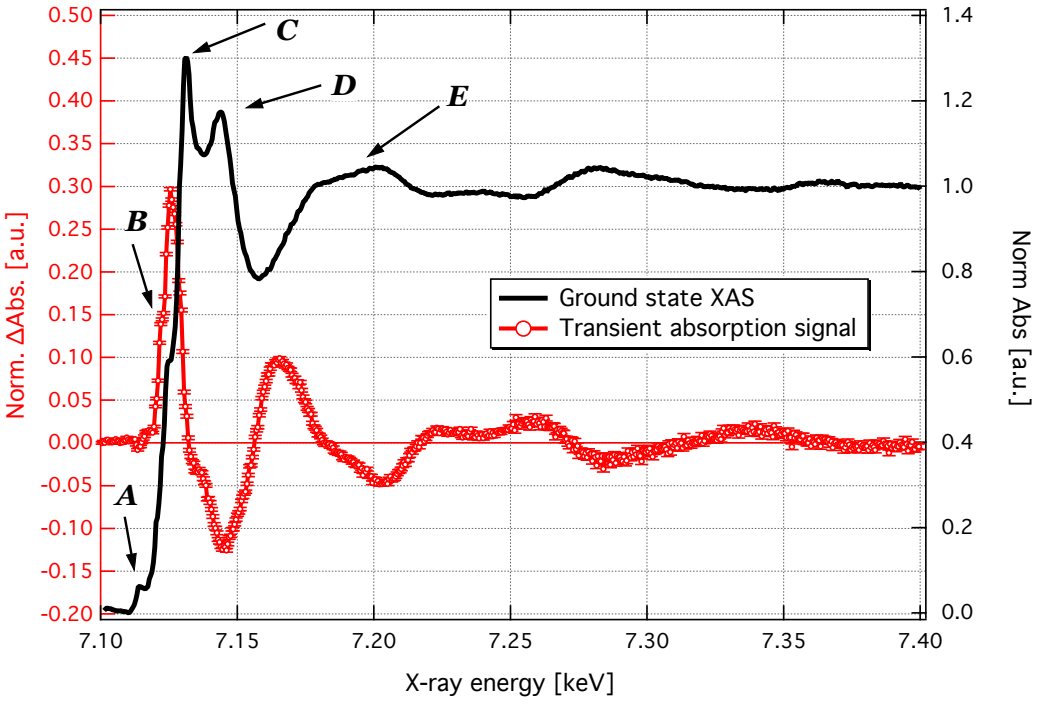

Figure 5.1.: Normalized steady-state XAS spectrum of a 25 mM aqueous solution of $[Fe(bpy)_3]^{2+}$ (black line, right axis) and transient XAS collected in fluorescence mode at 50 ps time delay, using the 10 ps, 532 nm laser pulses of the Duetto system at 520 kHz and approximately 100 mJ/cm^2 laser fluence (red circles, left axis). The most pronounced features (A to E) are labelled as in Ref. [39].

A zoom on the XANES and EXAFS region are shown in Figures 5.2a and 5.2b, respectively. The changes on the XAS spectrum, given by the transient spectrum, directly reflect the electronic and geometrical changes on the $[Fe(bpy)_3]^{2+}$ due to the laser excitation. This is true to any system investigated using time-resolved XAS. The maximum of the transient XAS spectrum, at 7.126 keV amounts to almost 30% of the edge jump, whereas in the EXAFS region they are smaller than 5%. Those are relatively large values compared to previous experiments done at kHz repetition rate [40, 122]. The main reasons are the longer pulse duration, which results in more efficient excitation due to less non-linear excitation processes in the solvent and/or sample, and the fact that the optical absorption coefficient of $[Fe(bpy)_3]^{2+}$ at 532 nm is almost 3 times higher than at 400 nm [39, 178].

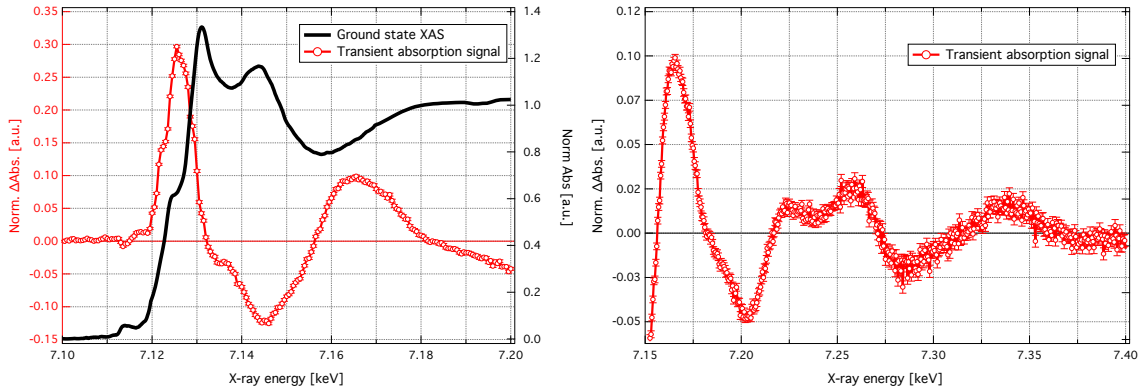

(a) Transient XANES region at 50 ps. The steady-state XAS (black line) is also shown

(b) Transient EXAFS region at 50 ps.

Figure 5.2.: Zoom on the (a) XANES and (b) EXAFS regions of the transient XAS (red circles) of a 25 mM solution of aqueous $[Fe(bpy)_3]^{2+}$ at 50 ps. Note the changes in the pre-edge region around 7.115 keV.

5.2 Temporal resolution

A scan of the relative delay between the laser and x-ray pulses is an important step in any time-resolved experiment. First it allows the determination of the precise timing of the overlap between the pump and probe pulses and second, it allows the study of the dynamics of the excited-state photo-products.

A temporal scan is performed by monitoring the intensity of a certain feature in the XAS spectrum as a function of the relative delay between the laser and x-ray pulses. In the case of $[Fe(bpy)_3]^{2+}$ in aqueous solution the x-ray energy was tuned to 7.126 keV and we probed the differential absorption ($\Delta A(t)$) as the relative pump and probe delay time was varied. The result of such a temporal scan using a 70 mM concentration sample is shown in figure 5.3, together with the optical transient absorption measurements probed at 505 nm after 532 nm excitation. Optical transient absorption has shown that

the ground state bleach (GSB) signal, which is dominant in the $450 - 550$ nm region [39, 179, 180] and is caused by depletion of the ground state due to the photoexcitation by the pump pulse, can be used to identify the decay of the HS state [39, 40]. In order to mimic the longer optical pulses used in the time-resolved XAS measurements, the femtosecond pump pulses used in the optical transient absorption experiments were stretched using a 20 cm long quartz rod. This way we obtained a pump-probe cross-correlation of about 1 ps, which is still 10 times shorter than the Duetto laser pulses. At early times (< 70 ps) the decays probed by the x-ray experiment and the optical transient absorption do not match due to longer x-ray pulse duration that decreases the temporal resolution. Elsewhere, the two curves agree, showing that the time-resolved XAS is indeed probing the photoexcited HS state of $[Fe(bpy)_3]^{2+}$. The x-ray temporal scan was fit with a monoexponential curve, convolved with a Gaussian having a 70 ps FWHM, representing the cross-correlation between the laser and x-rays. It was found that the decay has a lifetime of 650 ± 16 ps, which is known to be the lifetime of the HS state [35, 39, 40, 122, 180]. Despite using 10 ps-long laser pulses to excite the sample in the time-resolved XAS, the temporal resolution of the experiment is not affected. Even when using 100 fs laser pulses for the excitation, the temporal resolution was found to be on the order of $50 - 100$ ps [39, 40, 111, 120, 123, 127, 131, 169, 179].

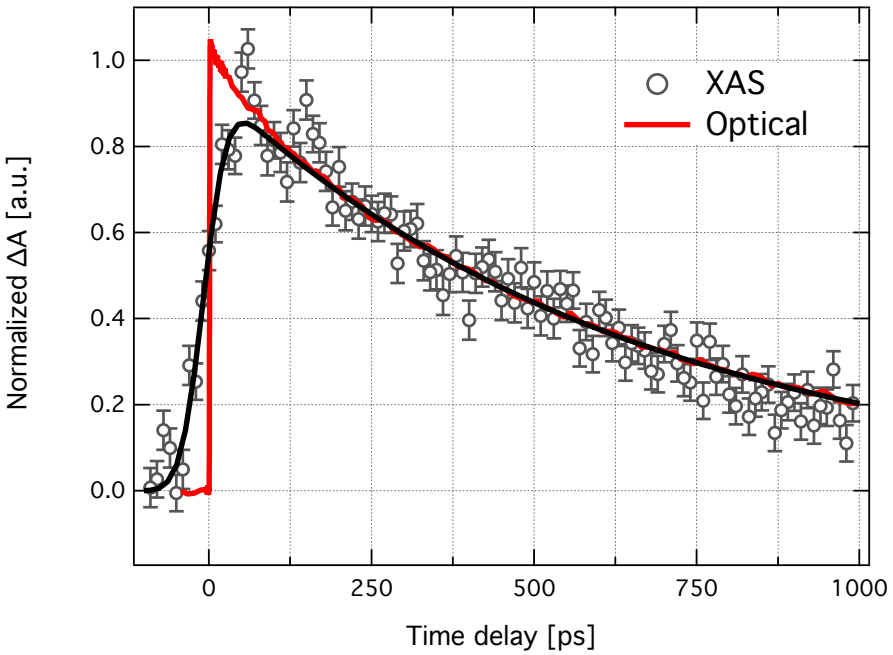

Figure 5.3.: Temporal scan of the transient XAS of aqueous $[Fe(bpy)_3]^{2+}$ recorded at 7.126 keV upon laser excitation - 10 ps, 532 nm. Open circles represent the x-ray data, the red line is the optical signal probed at 505 nm recorded in an optical transient absorption experiment. The black line is a fit of the transient XAS temporal scan to a monoexponential with 650 ps duration convolved with a 70 ps FWHM Gaussian.

5.3 Comparison of Signal-to-noise

As a test of the high repetition rate scheme and to estimate the increase in S/N compared to the 1 kHz experiments we used aqueous $[Fe(bpy)_3]^{2+}$ in several different concentrations. However, it should be kept in mind that it is not possible to precisely compare the two experiments because of the 532 nm/10 ps excitation here versus the 400 nm/100 fs in the kHz experiments. Nevertheless, given the ultrafast departure of population from the MLCT states, which we previously determined to be $\sim$ 150 fs [35, 181] and the fact that there is no known excited-state absorption at 532 nm [178, 180], the difference in excitation pulse width should not affect the results. Moreover, the absorption cross section is approximately three times higher at 532 nm than at 400 nm, a fact that has to be taken into account when comparing the data recorded using the two different schemes.

The transient XAS of $[Fe(bpy)_3]^{2+}$ shown in Figure 5.1 was recorded using a laser fluence of 100 mJ/cm^2 and agrees very well with the transient recorded previously using kHz acquisition rate [39, 40]. At the maximum of the transient signal, 7.126 keV, the S/N is approximately 158. This refers to the fluorescence detection mode data, but we also have recorded data using transmission detection, in which the S/N was about 142. This translates in a S/N $\simeq$ 45 per scan in both detection modes. Increasing the laser fluence to 200 mJ/cm^2, a value closer to that used in the kHz experiments, the S/N per scan increases to $\sim$ 70 in both modes. The big improvement in data quality can be immediately seen by comparing single scans of the time-resolved XAS using both the kHz and the new high-repetition rate scheme, as shown on Figure 5.4.

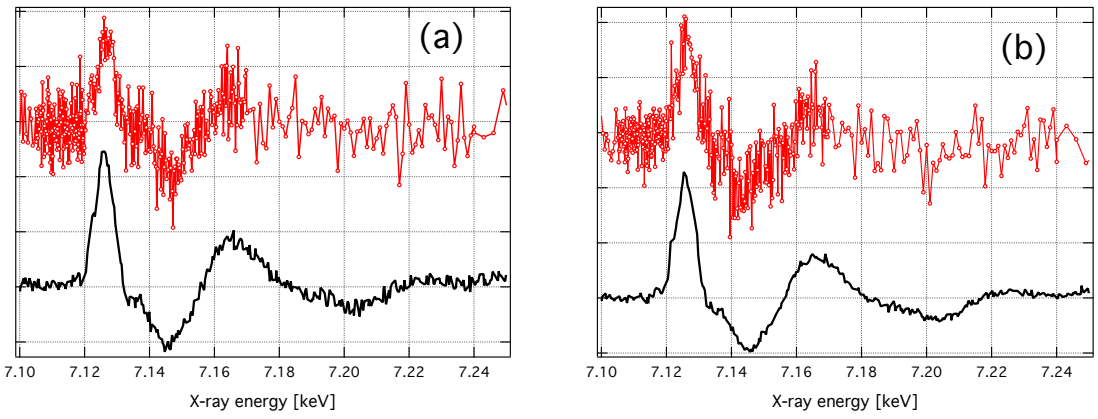

(a) Transient XAS collected in transmission mode. (b) Transient XAS collected in fluorescence mode.

Figure 5.4.: Comparison of the data quality of the two different schemes of time-resolved XAS, using kHz and MHz data acquisition. Single scans of the near-edge region of the transient XAS of a 25 mM solution of aqueous $[Fe(bpy)_3]^{2+}$ in transmission (a) and in fluorescence (b) modes. Red circles represent the data collected using kHz, and the black lines high-repetition rate data acquisition techniques.

Since the Fe K-edge XAS spectrum of the laser-excited $[Fe(bpy)_3]^{2+}$ is known [40] it is possible to extract the excited-state population by subtracting the unexcited spectrum

(low spin) from the laser-excited spectrum (high spin). The excited state spectrum is related to the measured transient XAS, the fraction of excited species and the unexcited spectrum via Equation 4.11. Using this approach we obtained an excitation yield of 60% for the 25 mM sample excited with 100 mJ/cm^2. When using a laser fluence of 200 mJ/cm^2 the derived excitation yield increases to $80-90\%$. This value is over three times larger than the previously reported 22% achieved in the kHz experiments,[40, 122] and can be explained by the approximately three times larger optical absorption coefficient at 532 nm compared to at 400 nm, and by the fact that the longer excitation pulse duration of 10 ps compared to 100 fs results in less nonlinear excitation of the solvent [39] and more efficient excitation of the sample.

For a direct comparison os the S/N, we used a 25 mM concentration solution of $[Fe(bpy)_3]^{2+}$, as in the kHz experiments. We can then, attempt a more quantitative estimate of the gain in S/N at 520 kHz compared to 1 kHz. The S/N is proportional to the excitation yield, the square root of the incoming x-ray flux and the repetition rate of the laser. Therefore the gain in S/N is given by the ratio:

$$\frac{(S/N)_{520\,\mathrm{kHz}}}{(S/N)_{1\,\mathrm{kHz}}} \simeq \frac{70\%}{22\%}\sqrt{\frac{I_{\mathrm{x-ray}}^{520\,\mathrm{kHz}}}{I_{\mathrm{x-ray}}^{1\,\mathrm{kHz}}}}\sqrt{\frac{520}{1}} \tag{5.1}$$

where we have taken as average photolysis yield (70%) from the above estimates. Estimating the difference in x-ray flux between the former 1 kHz experiments and the present ones is not straight-forward however we estimate an approximate factor of 8 decrease between the two experiments, due to differences in the beamline setup.[a] Thus the factor of three higher photolysis yield is compensated for by the decrease in x-ray flux. We conclude that the increase in S/N mainly scales with the square-root of the increase in repetition rate, as expected [32, 170, 182]. A summary of the per scan S/N obtained with the high-repetition rate scheme for time-resolved XAS is given in Table 5.1, together with the S/N obtained on previous experiments using kHz data acquisition.

Table 5.1.: Signal-to-noise comparison between the kHz and MHz experiments. The reported S/N refers to the maximum of the transient at 7.126 keV.

		kHz (from Ref. [39])	**MHz**
concentration	detection mode	S/N (per scan)	S/N (per scan)
25 mM	Fluo	2.6	69
	Trans	3.9	68
1 mM	Fluo	–	4.6
	Trans	–	3

[a] A factor of two comes from the tighter x-ray focussing, a factor of two from monochromator changes and a factor of two from the air path.

5.4 Low concentration and low fluence measurements

Given the gain in S/N, we can now decrease the sample concentration and/or the laser excitation fluence. Figure 5.5 shows the average of 10 individual scans of the transient XAS measured in FY mode of a 1 mM solution of aqueous $[Fe(bpy)_3]^{2+}$. This measurement was taken with a fluence of 150 mJ/cm^2 and both transmission and FY data were recorded simultaneously at 50 ps after excitation. The total acquisition time for the data shown was about 1 hour, yielding S/N $\simeq$ 4.6 per scan in fluorescence and S/N $\simeq$ 3 in transmission. Overlapped with this is shown the transient XAS signal in FY mode of a 25 mM solution of aqueous $[Fe(bpy)_3]^{2+}$, again at 50 ps time delay, but excited with only 13 mJ/cm^2 (scaled up by a factor of 10 for better visualization). In the limit of low laser fluence, we are still able to measure a time-resolved signal with a S/N $\simeq$ 8 in a single scan. The results of Figure 5.5 show that we can now measure very dilute or photochemically unstable samples within reasonable data acquisition times, opening the way for the investigation of biological samples under physiological conditions.

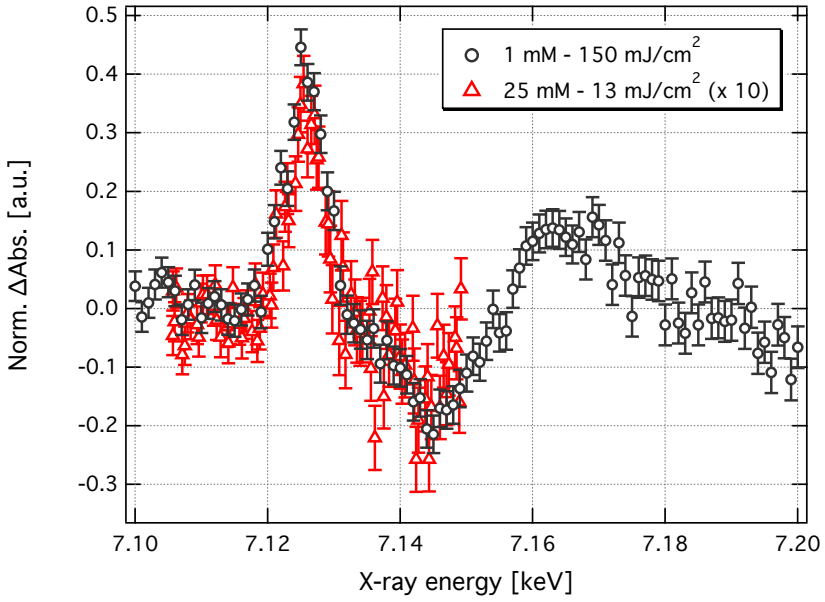

Figure 5.5.: Transient XAS of aqueous $[Fe(bpy)_3]^{2+}$ at 50 ps collected in fluorescence mode. The data corresponding to a 1 mM sample (black circles) consists of an average of 10 scans, and was measured using a laser fluence of 150 mJ/cm^2. Overlaid (red triangles) is the transient XAS data corresponding to a single scan of a 25 mM solution of the same sample, but excited with only 13 mJ/cm^2.

5.5 Laser fluence dependence

In order to investigate the dependence of the transient signal as a function of the incident laser fluence we have performed a series of transient XAS measurements on aqueous

$[Fe(bpy)_3]^{2+}$. For consistency with previous studies [39] we used a solution with 25 mM concentration and laser fluences up to 250 mJ/cm^2. The results of this study are shown in Figure 5.6, where it is clear that a pump-probe XAS signal is still measurable even when using very gentle excitation, *i.e.*, less than 15 mJ/cm^2. Figure 5.6b shows that the maximum intensity of the transient XAS, measured at 7.126 keV increases almost linearly with the incident laser fluence used to pump the sample, up to the limit of about 100 mJ/cm^2.

Optical-only ultrafast transient absorption measurements have shown that multi-photon absorption occur at $>$ 35 mJ/cm^2 when using 100 fs laser pulses to excite $[Fe(bpy)_3]^{2+}$ [39]. The multi-photon processes are seen as the appearance of an additional component in the kinetics, with a rise time of 3-4 ps. These processes have been attributed to absorptions to higher-lying states from the initial metal-to-ligand-charge-transfer (MLC). Once again we can point out the advantages of using ps laser pulses to pump the sample, together with our high repetition rate scheme for time-resolved XAS. Due to the use of longer pulses, it was possible to extend the range of laser fluences in which the transient signal is linear, from *ca.* 35 mJ/cm^2 using 100 fs pulses to about 100 mJ/cm^2 using 10 ps pulses. Therefore, the excitation process is more efficient in the sense that less non-linear effects are present at a certain laser fluence. This, allied with the high repetition rate data acquisition, allows the measurement of high quality time-resolved XAS using very low excitation fluences, which is important for systems that suffer of laser and/or x-ray damage. In addition, it is now possible to measure very subtle details on the transient spectrum.

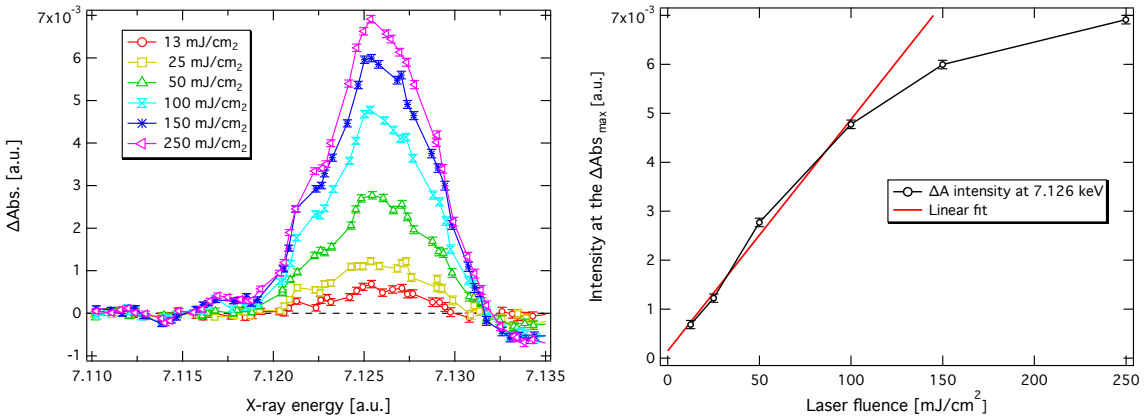

(a) Zoom in the B feature region of the transient XAS. (b) Intensity of the B feature *vs.* laser fluence.

Figure 5.6.: Laser fluence dependence of the transient XAS signal of a 25 mM aqueous solution of $[Fe(bpy)_3]^{2+}$. (a) Zoom in the region of the highest signal, showing the variation of the B feature as the fluence increases. (b) Intensity of the maximum the transient XAS (ΔA_{max}) as a function of the laser fluence. The signal is found to be linear up to about 100 mJ/cm^2.

5.6 Slow pump-probe mode

Recording the time-resolved XAS experiments at high repetition rates using the pulse-to-pulse data acquisition is not convenient for systems whose ground-state recovery is longer than the pulse repetition period. This is the case of MbCO which has a ligand recombination time of milliseconds [65]. Reducing the repetition rate of the laser so that the sample can relax between x-ray probe pulses cancels the advantages of the high repetition rate. An alternative approach would be to measure data at alternating intervals, *e.g.* 1 s, for the laser-excited and the unexcited XAS. The unpumped measurement is achieved by moving the laser position horizontally with a motorized laser mirror to ensure a complete lack of laser/x-ray overlap. The differential absorption, or slow-difference transient, can then be calculated using these data. The transient XAS signals are still calculated as in Equations 4.9 and 4.10, the difference being that now the pumped signal is defined as the signal measured when the laser and x-rays are overlapped spatially and unpumped is the signal with no overlap. This is, however, a quasi-steady state measurement from which no dynamics can be extracted.

Using this alternative scan technique, other sources of noise can contribute to the measured signal since the differential absorption is now being calculated on a 1 s timescale as opposed to a 1μs timescale. In order to investigate the noise characteristics of this slow-difference technique, we recorded a set of transient energy spectra of a sample of 7 mM aqueous $[Fe(bpy)_3]^{2+}$ at 50 ps time delay using simultaneously both the regular (pulse-to-pulse) and slow-difference scan modes, enabling a direct comparison of both modes under identical experimental conditions. The transient XAS data collected in fluorescence mode is shown in Figure 5.7a and the data collected in transmission mode is shown in Figure 5.7b. A comparison of the transient XAS data recorded in FY mode using both data acquisition modes show no new sources of noise that can obscure the signal in the slow-difference mode. The S/N of both data sets is shown in the inset of Figure 5.7a, being almost identical from which we conclude that in the case of samples having long-lived excited states, we can use the slow- difference scan mode in fluorescence to collect transient XAS data while only incurring a factor of two penalty in data acquisition times. The transmission signal recorded using the slow-difference scan reveals an enormous source of noise which obscures the signal, in stark contrast to the pulse-to-pulse mode. This indicates that there is an external source of noise on the 1 s time scale, which is absent on the 1μs timescale, and is most probably due to the flow of the liquid sample. Indeed small fluctuations in the jet flow speed, pressure and thickness easily introduce changes in the x-ray absorption signal on the 1 s timescale resulting in large random changes in the differential absorption. This noise easily overwhelms the transient transmission signal and reinforces the importance of measuring the difference signals on a pulse-to-pulse basis.

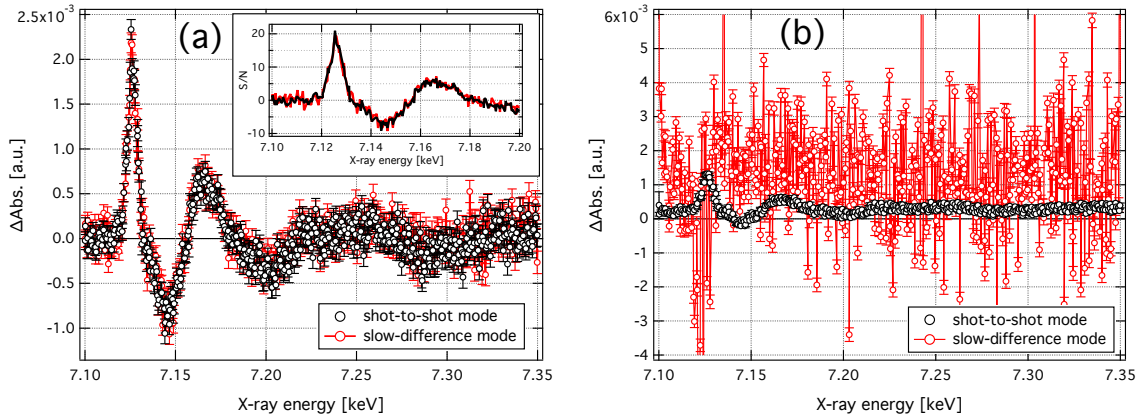

Figure 5.7.: Comparison of the transient XAS signal of a single measurement of a 7 mM aqueous solution of $[Fe(bpy)_3]^{2+}$ excited with 150 mJ/cm^2 laser fluence, using the pulse-to-pulse and the slow-difference modes in fluorescence (a) and transmission (b). Black circles show the data collected using the pulse-to-pulse mode and the red circles show the data collected using the slow-difference mode. Note that both measurement modes have the same S/N for fluorescence, as can be seen in the inset on (a), while being drastically different in transmission.

5.7 Analysis of the XAS spectra

The quantitative structural analysis of the ground- and excited-state $[Fe(bpy)_3]^{2+}$ have already been performed previously [39, 40, 122]. In this thesis we review the past analysis using the `MXAN` [85–87, 112, 183] and `FEFF9` [89, 90, 110] packages in order to investigate the effects of our high quality data on the retrieved structure and the limitations currently present in the theory of x-ray absorption spectroscopy.

First we have used the `MXAN` package to simulate the ground- and excited-state spectra of aqueous $[Fe(bpy)_3]^{2+}$ in the energy range limited to the first 200 eV from the absorption edge. Using the already established methodology of fitting the transient XAS directly in energy space [39, 40, 183] we performed a series of such fits and were able to derive the excitation yield, which agrees with the previous estimates based on the approach of comparing our transient spectrum with the difference between the ground- and excited-state spectra available in the literature [39, 40, 122]. Following this analysis, we used the `FEFF9` suite to calculate the XANES spectra of both the ground- and excited-state spectra, using as input structures the ones obtained as best fits from `MXAN`. This last approach allowed the investigation of the local l-projected electronic density of states (l-DOS) (see Equation 3.13) to investigate the electronic structure of the molecule on its low- and high-spin state. The analysis of the l-DOS agrees with recent Time-dependent density functional theory (TDDFT) calculations [184].

5.7.1. Fits of the XAS spectra

The results of the MXAN analysis applied to both the ground-state and the transient XAS are shown on Figures 5.8 and 5.10, respectively. All the calculations shown in this thesis using the MXAN were done with respect to a relative x-ray energy scale, *i.e.*, the energy axis is set with respect to the E_0 energy. Here, this energy origin was set as the position of the maximum of the first derivative of the XAS spectrum, in the case of $[Fe(bpy)_3]^{2+}$ it is equal to 7122.5 eV.

The only structural parameter used in the fit procedure of the $[Fe(bpy)_3]^{2+}$ XAS spectrum were the distance between the Fe and the N atoms in the bipiridine ligand. In addition, as it is the case for all fits in MXAN the usual non-structural parameters related to the spectral broadening were also fit. The fit spectrum is in excellent agreement with the experimental data, showing the ability of the code to simulate the XAS spectrum once the atomic coordinates are known and also to perform fits by varying these coordinates so as to obtain a better agreement between theory and experiment. The results of an MXAN fit to the ground-state XAS spectrum of $[Fe(bpy)_3]^{2+}$ is very good, delivering a Fe-N bond distance of 1.999 ± 0.001 Å, agreeing with the distance given by x-ray crystallography ($R_{Fe-N} = 1.967 \pm 0.006$ Å) [185] and with the prediction derived from TDDFT calculations ($R_{Fe-N} = 1.99 \pm 0.02$ Å) [186, 187]. The total cross-section calculated by MXAN reproduces all the features present in the experimental data, including the *A* feature (see Figure 5.1 for the labelling of the features), which has bound-bound character. However, the fit in this region is rather poor compared to the rest of the spectrum. The reason lies in the FMS theory itself and in the many approximations made in calculating the potential. The electronic structure of the absorbing atom play no role in the scattering MT potential formalism used by FMS, thus the calculation of these potentials does not correctly account for the difference in electron occupancy of the t_{2g} and e_g states of the Fe 3*d*-orbitals, which is the main reason why the *A* feature is present. As a result, MXAN correctly predicts the existence of such bound-bound features on the XAS spectrum, however at the wrong position with respect to the other features in the spectrum. This can be seen by looking at the un-broadened result of the calculation, *i.e.*, the total cross-section (thin gray line in Figure 5.8, right axis). It shows a strong peak centered at 12 eV below E_0, representing a shift of about 3 eV with respect to the position of the *A* feature in the experimental data. Moreover, since the fit spectrum is calculated by convolving the total cross-section with a broadening function - which is zero below a certain onset energy - the bound-bound features are not properly accounted for in MXAN. For these reasons, all the bound-bound transitions were not taken into consideration during the fits using MXAN, they were instead analysed using the FEFF9 program, which lists the individual atomic contributing density of states. The results of this analysis will be presented in Section 5.7.2. Another interesting feature in the total cross-section is the appearance of a sharp peak at about 13 eV, indicated by a vertical arrow in Figure 5.8. This feature is not present in our experimental spectrum, neither on previous XAS measurements of aqueous $[Fe(bpy)_3]^{2+}$ [39]. We believe this

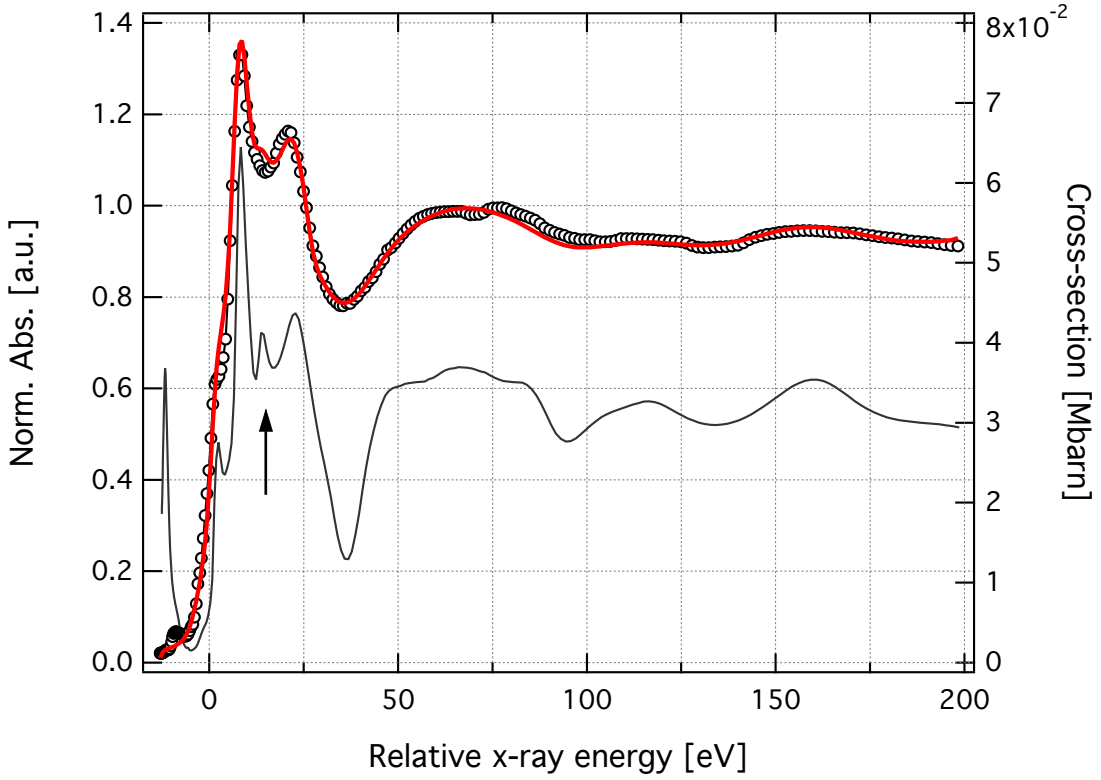

Figure 5.8.: Steady-state XAS spectrum of aqueous $[Fe(bpy)_3]^{2+}$ (open circles, left axis), together with the best fit obtained using the `MXAN` software. The total cross-section is shown as a thin gray line (right axis), showing that despite of applying the broadening function to account for the losses, all the features on the experimental spectrum are correctly calculated. The spectrum is plotted in relative energy with respect to E_0, determined by the maximum of the first derivative, *i.e.*, 7122.5 eV. Note the feature at 13 eV (indicated by a vertical arrow), not present in the experimental data.

feature is not real, and its presence in the calculated cross-section may be due to the MT approximation being a poor representation of the real potential or by miscalculations of multi-channel excitations that are not present in this case.

The next step in the analysis of the $[Fe(bpy)_3]^{2+}$ XAS is to make use of the unique capability of `MXAN` to fit the time-resolved transient data directly in energy space. In this procedure the previously fit ground-state spectrum is used as an input fixed reference spectrum from which several calculated other spectra will be subtracted at each iteration step of the minimization procedure. `MXAN` calculates the total cross-section $\sigma(E)$, and this has to be scaled for a direct comparison with the normalized absorption XAS ($\mu(E)$). This fact can be explored during the fits of transient spectra to get an independent measure of the excitation yield. The cross-section (in Barns) is related to the normalized XAS by a normalization constant, *i.e.*, $\mu_{gs}(E) = \sigma_{gs}(E)/N$. In the case of the excited-state spectrum, the same relationship holds and it is assumed that the normalization

factor is the same for both ground- and excited-state spectra, *i.e.*, $\mu_{es}(E) = \sigma_{es}(E)/N$. Because all the calculations in `MXAN` are done with respect to the cross-sections, the transient XAS also has to be scaled in order to be comparable to the experimental data. The calculated transient XAS is then given by $\sigma_{es} - \sigma_{gs} = N^{\Delta}\Delta A(E,t)$ [b], which can be directly compared to Equation 4.11. Therefore, the ratio of the scale factors used to calculate the steady-state and transient XAS, N/N^{Δ}, gives the excitation yield $f(t)$. In addition, it allows investigation of the energy shift due to the change of the ionization potential energy in the excited-state. The result of the `MXAN` fit of the transient XAS of $[Fe(bpy)_3]^{2+}$ is shown in Figure 5.10. It reproduces well all the spectral features of $\Delta A(E, t = 50ps)$, despite some minor deviations at > 50 eV that we attribute to imprecisions in the FMS theory, specially the MT approximation. The high quality of our transient data points to the need of a more elaborate description of the potential and the losses in the XAS spectrum . Concerning the $[Fe(bpy)_3]^{2+}$ excited-state, not only the bond distances are expected to vary with respect to the ground-state, but the ionization threshold and the bound-bound transitions are also expected to be affected by the laser-induced spin transition. Clearly, the structural changes in the excited-state will produce changes in the features present in the XAS spectrum, either due to change in the MS interaction between the emitted photoelectron on the x-ray absorption process or due to changes in the ionization threshold energy and the different electronic configuration of

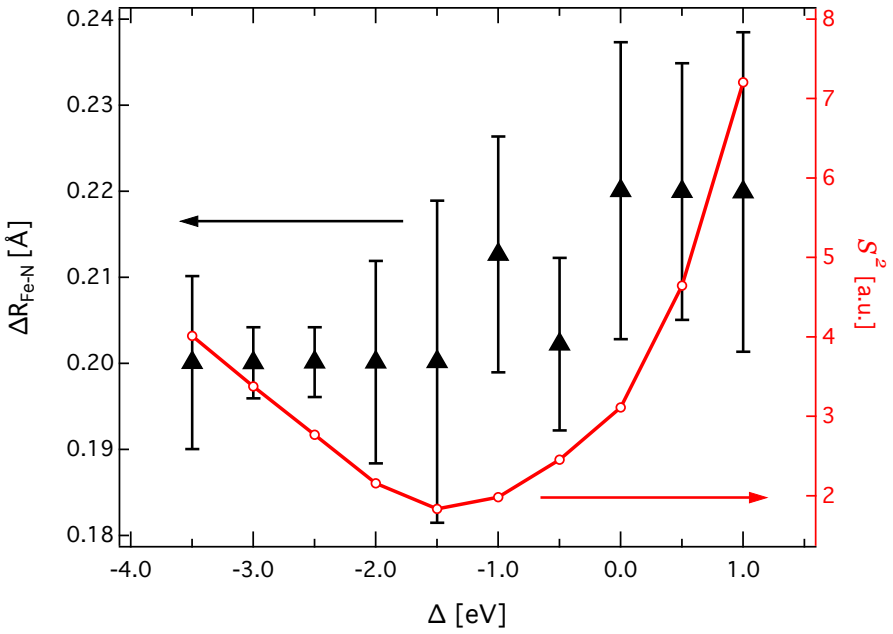

Figure 5.9.: Correlation plot between the structural distortion in the [Fe(bpy)$_3$]2+ excited-state and the square residual of the fits ($\mathcal{S}^2$) as a function of the energy shift (ΔE). The $\mathcal{S}^2$ minimization corresponds to an energy shift of -1.5 ± 0.5 eV and an Fe-N bond elongation of 0.20 ± 0.02 Å.

[b] N^{Δ} is the scale factor used in the fits of transient spectra. It is applied to the differential cross-section ($\sigma_{es} - \sigma_{gs}$) allowing a comparison with the experimental data

the excited-state; this last affecting mainly the bound-bound transitions. The *chemical shift* of the XAS spectrum can be used to describe the changes in the local chemical environment around the absorber atom [188], which in the case of $[Fe(bpy)_3]^{2+}$ is due to changes in the Fe-N bond length [39, 122] and in the mixing between the iron $3d$ and nitrogen $2p$ orbitals from the ligands. These modifications reflect in the change of the ionization potential energy and can be qualitatively linked to the shift in E_0, which is expected to shift to lower energies [39]. The precise value of the chemical shift, as well as the excitation yield are not known *a priori* and might affect substantially the results of the structural determination of the excited-state structure [36, 39, 40, 111, 122, 124]. Therefore, prior to the fits of the transient spectrum we proceeded with a Monte Carlo optimization of the E_0 value, assuming an initial excitation yield of 60%, according to the estimates based on the difference between the ground- and excited-state XAS in the literature. Following this procedure, we found that the energy shift in the excited-state is -1.5 ± 0.5 eV. Although this value is in agreement with the one given in Ref. [122] (-1.6 ± 0.6 eV), it produces a slightly larger uncertainty in the bond length elongation and a visual inspection of the generated transient XAS reveals that the intensity of the B feature is not properly reproduced. The relative small changes in the square residual $\mathcal{S}^2$ used as the quantifying parameter on this analysis make the determination of the E_0 shift rather ambiguous. Therefore, we decided to fix the E_0 shift value to -1.5 eV

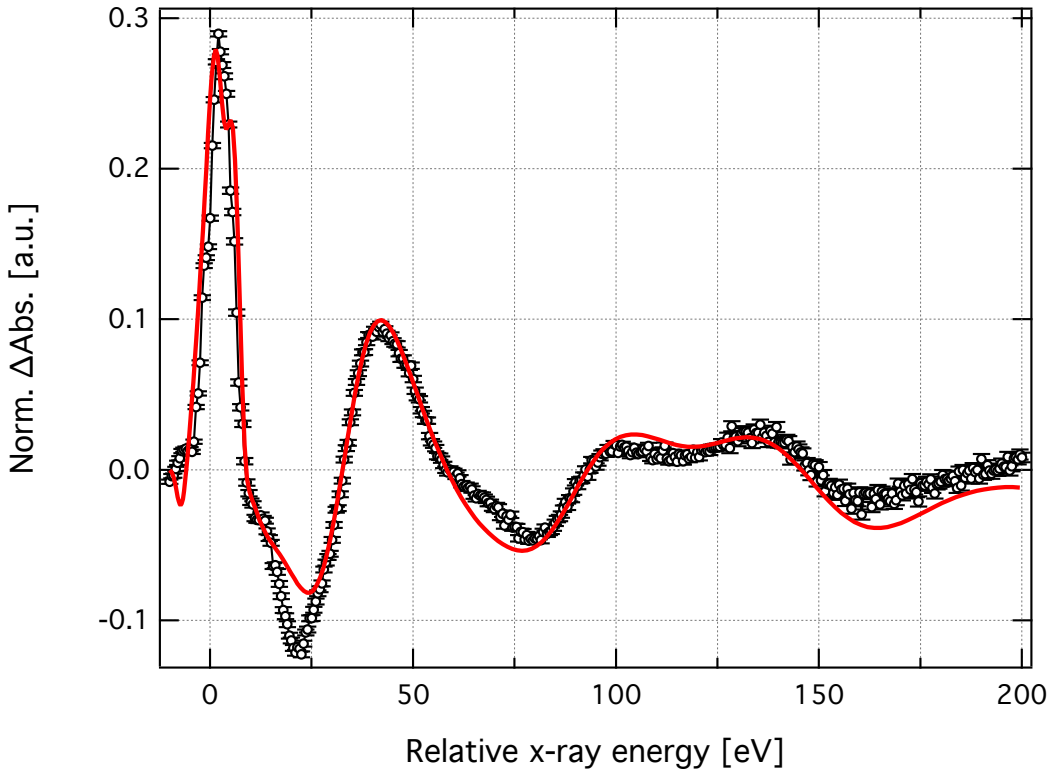

Figure 5.10.: Normalized transient XAS from a 25mM solution of $[Fe(bpy)_3]^{2+}$ at 50 ps (black circles), together with the corresponding best fit (red line) obtained with `MXAN`

and proceed with the complete fit procedure, minimizing both the excitation yield and the structure parameters in `MXAN`. The best fit obtained, yielded a Fe-N bond elongation $\Delta R_{Fe-N} = 0.20 \pm 0.01$ Å, *i.e.*, $R_{Fe-N} = 2.20 \pm 0.01$ Å, in agreement with previous studies [39, 40, 122]. The best fit, corresponding to the minimum in $\mathcal{S}^2$, corresponds to an optimized excitation yield of $f(t = 50ps) = 59 \pm 1\%$, in accordance with our previous estimates based on the calculated difference of the published ground- and excited-state XAS.

5.7.2. Bound-bound transition probed by K-edge XAS

The most pronounced consequences of the spin change, from the electronic point of view, is the electron redistribution among the t_{2g} and the e_g states of the metal d orbitals. The decrease in the ligand-field splitting affects the energies of these states. This effect is seen in the x-ray absorption spectrum as changes in the bound-bound transitions in the pre-edge region, *i.e.*, the A feature. Figure 5.11 shows a zoom of the pre-edge region. The black curve shows the ground-state pre-edge signal while the markers show the transient XAS measured using a fluence of 200 mJ/cm^2. In third-row transition metal complexes these pre-edge features correspond to the dipole-forbidden $1s \rightarrow 3d$ bound-bound transitions and are sensitive to the spin-state of Fe-containing molecules [189]. Since these features are less than 1% of the absorption edge jump, very high signal-to-noise is required to detect them [190]. As expected for an octahedrally-coordinated

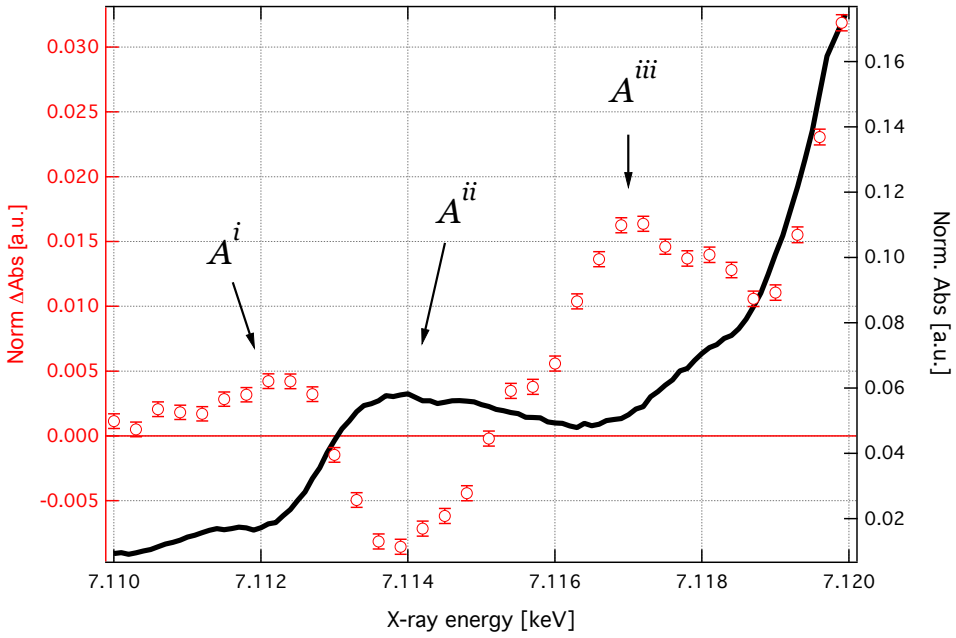

Figure 5.11.: Zoom on the pre-edge region of the XAS spectrum of $[Fe(bpy)_3]^{2+}$ showing the A^i, A^{ii} and A^{iii} features in the transient data. The black line is the ground-state spectrum and the red circles represent the transient XAS at 50 ps, measured with a laser fluence of 200 mJ/cm^2.

low-spin Fe^{2+} metal center the ground-state shows a clear absorption peak corresponding to the $1s \rightarrow 3d$ (e_g) transition (7.1135 keV). Upon excitation to the high-spin state, we see an increase in absorption at lower energies corresponding to the transition $1s \rightarrow 3d$ (t_{2g}) at 7.1125 keV and a decrease at higher energies as the 3d(e_g) levels are populated in the high-spin state (7.114 keV). There is also an increase in absorption at higher energies (7.117 keV) in a region of the spectrum where peaks have been tentatively assigned to edge-transitions [189]. These pre-edge features were also seen by Nozawa *et al.* using kHz laser excitation[190], but the increased S/N in the present experiments allow us to perform a much more detailed analysis of the origins of these features.

Figure 5.12 shows the calculated local density of states obtained by the calculation of the XANES spectrum of $[Fe(bpy)_3]^{2+}$ in the ground-state using `FEFF9`. The *s*-, *p*- and *d*-DOS of the absorbing iron atom and the nitrogen atom of the ligand bipyridine (first neighbours) are indicated. It can be seen that the *A* feature in the pre-edge region (around 7113 eV) contains contributions both from the Fe *d*- and the N *p*-DOS. The N *s*-DOS also contributes to a smaller extent. The B feature sits very close to the ionization threshold (0 eV) and the origin of this transition is subject to debate. In earlier works [191, 192] it has been attributed to a $1s \rightarrow 4p$ transition, containing a certain degree of mixed Fe($4s$) and N($2p$) orbitals. More recently, based on the full multiple scattering (FMS) theory, it has been proposed that this feature has a structural origin [35, 193, 194], being an above-ionization multiple-scattering resonance. Bressler

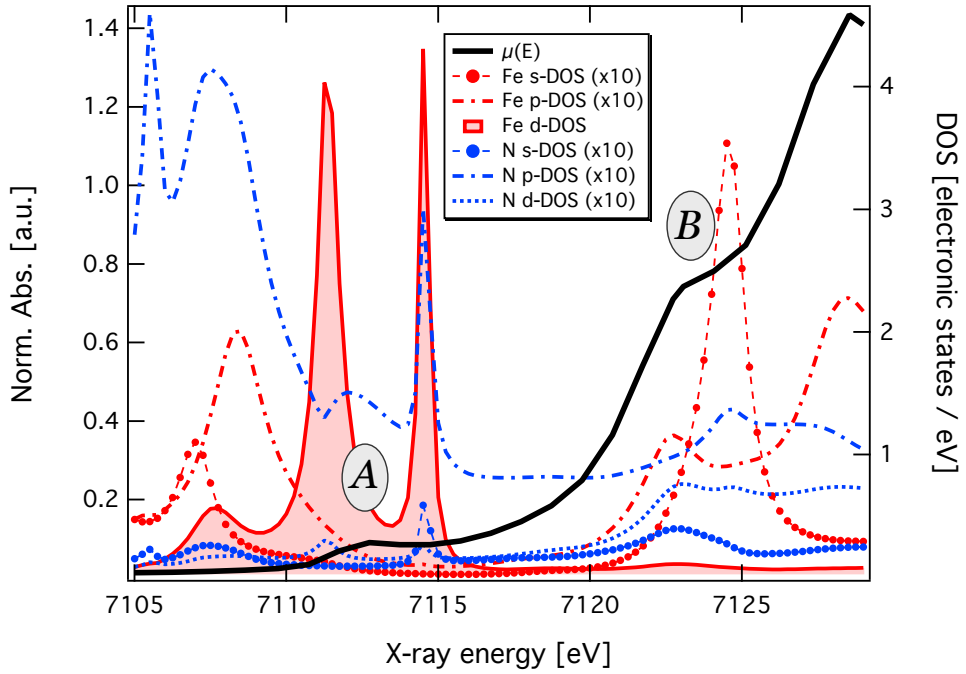

Figure 5.12.: Density of states of the individual atoms of $[Fe(bpy)_3]^{2+}$ and the calculated XANES spectrum $\mu(E)$ (solid black curve, left axis) in the ground-state. The *s*-, *p*- and *d*-DOS of the absorbing iron atom and the nitrogen atom of the bipyridine ligand (first neighbours) correspond to the right axis.

et al. [35] found a nearly linear relationship between the Fe-N bond elongation and the intensity of the B-feature, which they used to quantify the structural changes due to the laser-induced spin-conversion of $[Fe(bpy)_3]^{2+}$. The present FEFF9-calculated DOS disagrees with the interpretation of Briois *et al.* [193, 194] and Bressler *et al.* [35], indicating that the B feature is due to an Fe $1s \rightarrow 4p$ transition, with some small degree of mixing with the N $2p$ orbital. Also in the region of the B feature there is a strong peak from a Fe s-DOS, which would account for this relatively broad transition. However, based on the fact that it lies very close to the ionization threshold, it is more likely that it is indeed a purely structural, multiple-scattering resonance. The approximations made in calculating the MT potentials can easily contribute to a 1-3 eV error on the Fermi energy, putting the B feature above the ionization threshold, which would confer a structural origin to this feature. Moreover, recent TDDFT calculations on $[Fe(bpy)_3]^{2+}$ [184] successfully identified the origin of the A feature, arising from a dipole-mediated transition $1s \rightarrow 3d(e_g)$ in the iron atom. Figure 5.13 shows a zoom in the region of the A feature, highlighting the contribution of the individual atomic species for the DOS. Here, each DOS has been normalized to the totall DOS. Ligand field theory predicts a splitting of the $3d$ orbitals due to the presence of ligands in the neighbourhood of the metal atom. In an octahedral geometry, the splitting is into the t_{2g} and e_g levels, which can be seen qualitatively in Figure 5.13. FEFF9 predicts the Fermi energy very close to the t_{2g} level, which is filled with 6 electrons on the ground-state. A bound-bound

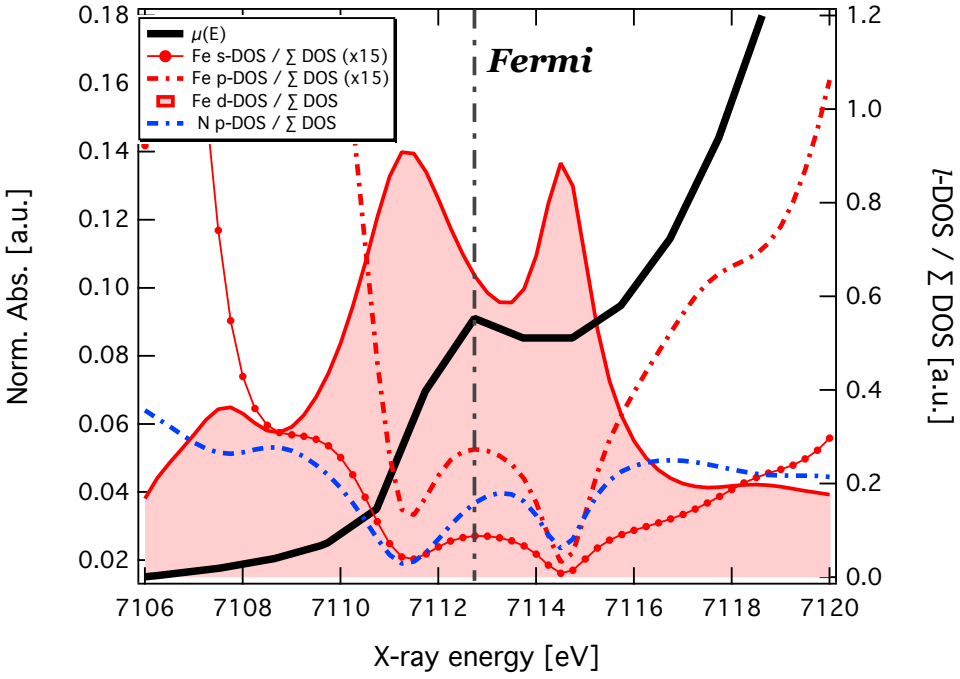

Figure 5.13.: Fe d- and ligand N p-DOS of the $[Fe(bpy)_3]^{2+}$ molecule in its ground-state (right axis) as calculated with FEFF9. The Fermi level as calculated is indicated by the dashed line. The calculated XAS spectrum is shown as a black line (left axis).

transition to the $3d(e_g)$ is therefore dipole allowed due to mixing between the Fe d- and N p-orbitals, and by the symmetry of the complex (O_h). It is important to mention that all the XANES calculations of the $[Fe(bpy)_3]^{2+}$ molecule using `FEFF9` were done using the dipole approximation. Multipole transitions can be included in calculations using the `MULTIPOLE` card [110], however including a quadrupole contribution did not affect the results obtained. We can then conclude that the bound-bound pre-edge features in the ground-state of $[Fe(bpy)_3]^{2+}$ are mainly of dipole character. This is in agreement with our TDDFT calculations, which show that dipole terms dominate the transitions in the A feature indicated in the spectrum.

Despite providing valuable information about the electronic structure of $[Fe(bpy)_3]^{2+}$, the analysis of the DOS was not able to provide a full picture of the transitions causing the A feature. In addition, it did not reproduce the correct splitting of the t_{2g} and e_g levels. A finer treatment of the origin of the transitions causing the features in the pre-edge region of the XAS spectra is needed. To this purpose we performed a series of Time-dependent density functional theory (TDDFT) calculations of the K-edge XAS [184]. The TDDFT calculations were performed using the ORCA quantum chemistry package [195], following the same methodology of DeBeer George *et al.* to calculate the ligand K-edge XAS spectra [196], using the electric quadrupole approximation for the interaction with the x-ray field. The XAS spectrum calculated using TDDFT was convolved with a Lorentzian function having 0.70 eV FWHM to simulate the experimental resolution and thus provide a better comparison with the experimental data. The result of this calculation for the case of the ground-state $[Fe(bpy)_3]^{2+}$ is shown in Figure 5.14. The increased level of details provided by TDDFT is remarkable. It not only reproduced the A feature, but also indicated the presence of another group of transitions contributing to very subtle features in the pre-edge region of the spectrum. We have therefore, re-labelled the A feature as A^{ii}, and the next two as A^{iii} and A^{iv}. All the transitions shown are predominantly dipole-mediated, confirming our finding using the DOS analysis that the inclusion of quadrupole transitions does not affect the calculated spectrum. A^{ii} is a pure Fe $1s \rightarrow 3d(e_g)$ transition, which is becomes partially allowed due to the O_h symmetry and by the orbital-mixing. Features A^{iii} and A^{iv} are due to transitions from the Fe $1s$ to N p orbitals, with the ligand contribution increasing with energy. These two features are not obvious in the DOS analysis, though there are some N p- and Fe s- and p-DOS in this region.

A similar analysis can be performed for the pre-edge region of the excited-state spectrum of $[Fe(bpy)_3]^{2+}$. Contrary to the `MXAN` fits, the `FEFF9` code does not perform fits directly in energy space. In order to analyse the high-spin state we used Equation 4.11 and the excitation yield of $f(t = 50ps) = 59\%$ derived from the `MXAN` analysis to extract the high-spin XAS spectrum, which is shown as the black solid line in Figure 5.16. We then used the final structural parameters obtained from the `MXAN` best fit as input for calculating the XANES spectrum using `FEFF9`. The B feature, as previously discussed, does not have a bound-bound origin and thus will not be discussed here. Figure 5.15 shows the resulting DOS obtained from the calculations of the XANES spectrum of the

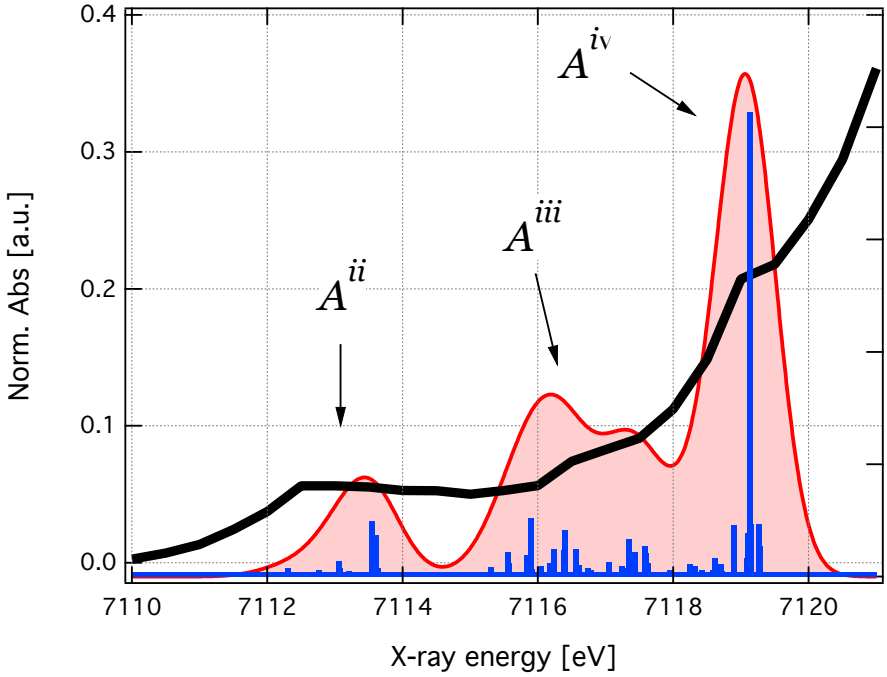

Figure 5.14.: TDDFT calculation of the XAS spectrum of the $[Fe(bpy)_3]^{2+}$ molecule in the ground-state (from Ref. [184]). The electronic transitions are shown as vertical blue bars, and the broadened spectrum as the red line. The experimental spectrum is shown in black. Note the identification of further transitions.

$[Fe(bpy)_3]^{2+}$ molecule in the high-spin state. The laser-induced spin transition results in the transfer of two electrons from the t_{2g} to the e_g levels, leaving the molecule in a high-spin state. Again, the mixing of the Fe $3d$ with the N $2p$ orbitals makes the bound-bound transitions partially allowed, which results in the peak at about 7113 eV. Above this energy there is no localized peak in the DOS until the region corresponding to the B feature (not shown), which we already attributed to MS effects. Between 7116 eV and 7119 eV we find a broad peak in the N p-DOS, overlapped with strong contributions of the Fe s- and p-DOS. However, in the calculated spectrum there are no clear peaks indicating which of these transitions are actually present. The analysis of the electron distribution on the Fe atom using the integrated d-DOS allows us to identify the two split levels, t_{2g} and e_g. The t_{2g} level, filled with 4 electrons lies at 1 eV bellow the Fermi energy. Recall that the Fermi energy as calculated by any FMS code should not be taken as an absolute value. The approximations made on the MT potentials, together with the inclusion of the self-energy term can account for an 1-3 eV error, even when SCF loops are used. Because the t_{2g} level is now not completely full, a new transition $1s \rightarrow 3d(t_{2g})$ can also occur. This transition is seen in the calculated DOS as the peak around 7112.5 eV. The decrease in the splitting between the levels can also be seen qualitatively in the Fe d-DOS as the separation between the peaks in the d-DOS is smaller.

As in the ground-state case, we turn to TDDFT to provide a more detailed picture

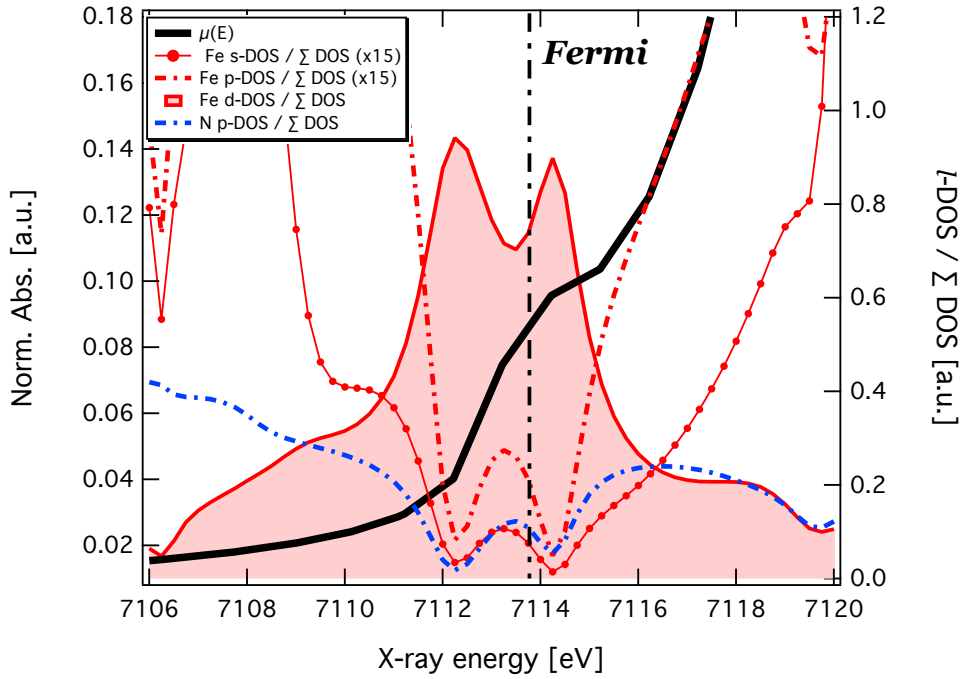

Figure 5.15.: Fe d- and ligand N p-DOS of the $[Fe(bpy)_3]^{2+}$ molecule in its excited-state (right axis) as calculated with `FEFF9`. The energy-integrated Fe d-DOS is shown as the thin black line (left axis).

of the transitions present in the pre-edge region of the XAS spectrum of the excited $[Fe(bpy)_3]^{2+}$. Figure 5.16 shows the results of a TDDFT calculation for the excited-state $[Fe(bpy)_3]^{2+}$, together with the transient XAS data and the reconstructed excited-state spectrum. The region 7110-7115 eV correspond to the A feature. The TDDFT calculation shows that quadrupole transitions play a minor role on the spectrum, which is dominated by dipole transitions, confirming the result obtained with `FEFF`. The A^i and A^{ii} features contain transitions corresponding to Fe $1s \rightarrow 3d$, again corroborating our interpretation using the DOS analysis. Most interesting is the fact that TDDFT predicts the origin of the transitions causing the feature A^{iii} on the transient XAS spectrum. While the DOS calculated using `FEFF9` only indicated a broad peak of N p-DOS overlapped with Fe s- and p-DOS, the TDDFT results point to several Fe $1s$-ligand transitions. There are no d-DOS for the orbitals involved in the A^{iii} transitions, but the p-DOS is higher, making the transitions dipole allowed and consequently stronger. Above 7120 eV all the transitions are structural, due to multiple-scattering events of the photoelectron wave.

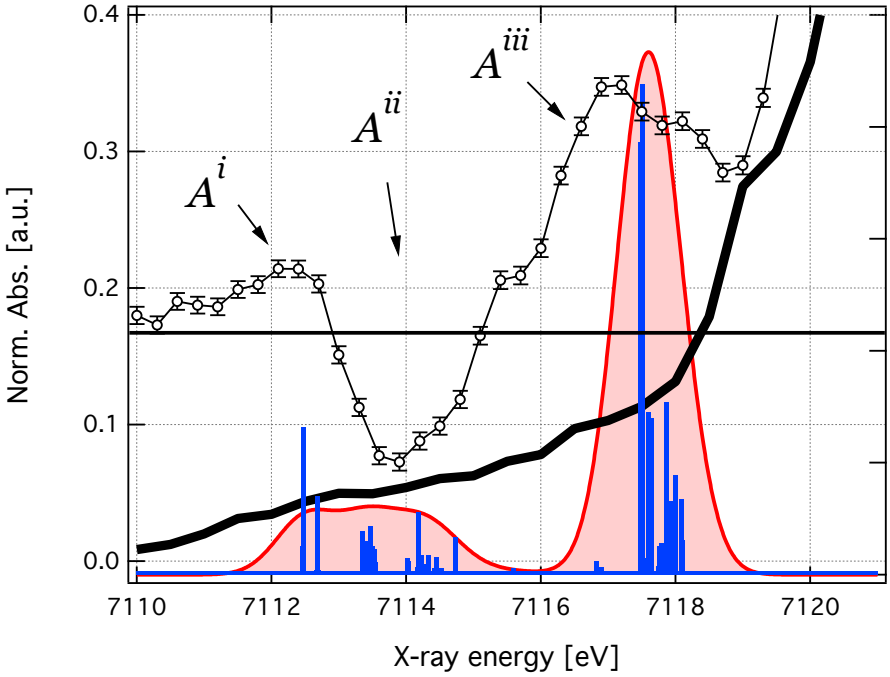

Figure 5.16.: TDDFT calculation of the $[Fe(bpy)_3]^{2+}$ molecule in its excited-state (from Ref. [184]) compared to the reconstructed high-spin state of $[Fe(bpy)_3]^{2+}$ (black line). Also shown is the transient XAS at 50 ps (black circles).

5.8 Conclusions

In this Chapter we have analysed the results of the time-resolved XAS experiments of $[Fe(bpy)_3]^{2+}$ in aqueous solution using our high repetition rate scheme for data acquisition. We have shown an increase of about 20 in the S/N when increasing the repetition rate by a factor of 520. The dominant source of noise in this new scheme is the shot-noise of the source, which allows measurements of very small changes in the XAS signal and highly dilute samples.

We have revised the analysis of the XAS spectra of $[Fe(bpy)_3]^{2+}$, both for the ground-state and the transient XAS data. The structural analysis of the transient spectrum confirmed the Fe-N bond elongation of 0.20 ± 0.01 Å upon light-induced spin transition. Additionally, we have presented a discussion of the origins of the transitions causing the the features in the pre-edge region. The analysis of these transition was done in view of the interpretation of density-of-state provided by `FEFF9` and also by using TDDFT calculations. It has been shown that a simple picture of $1s \rightarrow 3d$ transition in the iron atom is not always correct to describe these pre-edge features. The strong orbital hybridization between the iron and the ligands is the determining factor for the appearance of these transitions.

"Almost all aspects of life are engineered at the molecular level, and without understanding molecules we can only have a very sketchy understanding of life itself."

Francis Crick

6

X-ray absorption spectroscopy of Myoglobin in physiological solution

This chapter presents the analysis of the XAS spectra of several different forms of Myoglobin in physiological conditions. It starts, in Section 6.2 with the results of the steady-state measurements using liquid solutions, showing the remarkable differences in both the geometrical and electronic structure upon ligand substitution. The philosophy of the calculation of the XAS spectra using the `MXAN` code is given in Section 6.4. The analysis of the steady-state spectra is presented in Section 6.5.2. The distance between the iron and the nitrogen in the porphyrin is found to converge to a common value (approximately 2.0 Å), reflecting the relative rigidity of the porphyrin ring. An interpretation of the features present in the pre-edge region, reflecting bound-bound transitions, is presented. These features are interpreted based on Full-multiple scattering (FMS) theory and Time-dependent density functional theory (TDDFT) calculations, in Sections 6.5.4 and 6.5.5, respectively. Section 6.5.3 comprises the results of the time-resolved XAS of Nitrosyl-Myoglobin (MbNO), which is analysed directly in energy space. The geminate recombination of the NO molecule with the protein is found to happen in 216 ± 24 ps. A transient structure of photo-excited MbNO at 50 ps is proposed, based on a model in which the NO molecule moves 2.88 ± 0.09 Å away from the iron atom, with a slight heme doming movement; combined with the iron atom moving 0.16 ± 0.03 Å and the nitrogens and closest carbons moving ~ 0.01 Å below the heme plane in a doming effect.

6.1 Introduction

Myoglobin, as well as the other respiratory proteins, has the property of reversibly binding molecular oxygen [175]. It is composed of a folded polypeptide portion, the *globin*, and a prosthetic group, the *heme*. Figure G.1 shows an illustration of the heme group of Carboxy-Myoglobin (MbCO) and its surroundings. The heme, also called protoheme or proto porphyrin IX, is formed by four pyrrole rings, connected by methine bridges [3]. The pyrrole rings are shown in gray in Figure G.1. The central position in the porphyrin ring is occupied by a metal atom in metallo-proteins. In the case of hemes, this metal is an iron atom. The heme is where binding of oxygen (and other diatomic molecules, often called *ligands*) occurs, and the process of detaching this molecule produces significant structural changes. This process has been studied extensively [2, 3, 49, 175], aiming at complete understanding of which parameters control the ligand release and solving a long-lasting puzzle in biochemistry.

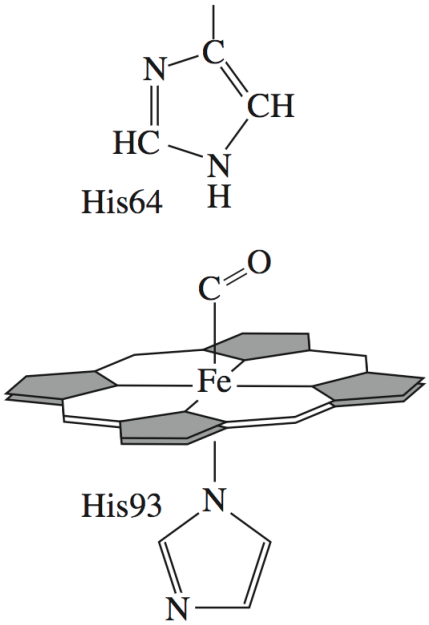

Figure 6.1.: Illustration of the heme structure of Carboxy-Myoglobin. Also shown are the imidazole rings of the proximal (His93) and distal (His64) histidines.

It is of general consensus that the biological function of many proteins is controlled by conformational changes of different magnitudes. These structural changes, though crucial for protein function, are seldom characterized at the atomic level, which results in a poor understanding of the fundamental connection between structure, dynamics and function. In this sense Myoglobin (Mb) has played a central role in the investigation of protein dynamics. Despite its complex behaviour, reflected in many different functions apart from simply storing oxygen [19, 21, 22, 49], it serves as a model system of general

significance. Some reasons why Mb is a good model include the vast characterization of the geometrical structure with respect to different ligands and its intrinsic reactivity [3] and the sensitivity of the iron-ligand bond to light exposure [24, 197]. Thus, the biological function of ligand release can be mimicked by illuminating Mb with light with the appropriate wavelength. In addition, the photo-sensitivity varies depending on which ligand is bound to the Mb [24]. Myoglobin has a higher affinity for CO than for O_2 [2], and considering the almost unitary quantum efficiency for photo-excitation [63], MbCO has often been chosen in studies of protein dynamics. In Mb, the aminoacid side chains in the vicinity of the heme have been reported to have a primary importance in controlling the binding of gaseous and non-gaseous ligands, and also in the discrimination among them [198]. Therefore, in studying the structure and dynamics of Mb, these sub-structures should not be neglected.

6.2 Static XAS of different Myoglobin forms

We studied several different forms of Mb by means of steady-state XAS, in the ferric (Fe^{3+}) and ferrous (Fe^{2+}) oxidation states, with and without ligand. The ferric Myoglobins are the unligated *metMb* [a] and the ligated Cyano-Myoglobin *MbCN*. The ferrous Myoglobins include the unligated *deoxyMb*, and Oxy-Myoglobin (MbO_2), Nytrosil-Myoglobin ($MbNO$) and Carboxy-Myoglobin($MbCO$), the last three are ligated forms. The whole set of steady-state XAS spectra of the six different forms of Mb are shown in Figure 6.2. The XAS spectra were measured with the setup described in Section 4.3 using Mb solutions of 4mM concentration. The measurements were carried out in fluorescence-yield mode, using liquid samples in physiological conditions, *i.e.*, room temperature (25^{o}C), pH 7.0, atmospheric pressure (760 Torr). The samples were under nitrogen atmosphere (except the carboxy-myoglobin and oxy-myoglobin which were kept at CO and a mixture of He and O_2 atmospheres, respectively) and were continuously flowed through a quartz capillary to avoid damage caused by x-ray irradiation. Several successive scans were averaged together in order to improve the signal-to-noise (S/N) ratio. The striking observation in these spectra is the significant changes caused by ligand substitution (*e.g.*, NO vs. CO), which points to extensive structural changes, which affect both the XANES and the EXAFS regions. The most prominent features in the XAS spectra are labelled *A*-*E*. Figure 6.3 shows a zoom into the pre-edge region (below 7120 eV), which contains bound-bound transitions mainly dominated by iron $1s \rightarrow 3d$. It can be seen that it is also dramatically affected by ligand substitution (or even its absence). The analysis of the steady-state XAS and its direct relation with the electronic and geometrical structure is given in the following sections. To our knowledge this is the first systematic study of the different forms of Myoglobin by x-ray absorption spectroscopy using liquid solutions in physiological conditions.

[a] There is a controversy about the presence or not of a water molecule close to the heme site. *metMb* is also referred to as aqua-metMb.

Previous XAS studies of proteins in solution can be found in the literature [76], but an inspection of the experimental details reveals that the measurements were carried at 20 K, a regime in which the protein can no longer be considered a liquid solution. Carboxy-Myoglobin is probably the best characterized heme protein [2, 19, 49, 64]. Many time-resolved x-ray diffraction experiments were carried out on MbCO [11–15, 55], which allowed a direct observation of the global structural changes in MbCO upon photo-excitation. At the same time, XAS has been used to tackle the same problem [25–29]. The common point in this group of studies was the use of cryogenically cooled crystals. The cooling is a common practice in crystallography to avoid x-ray damage and reduce the thermal vibration of the atoms, thus providing better resolution for the structural parameters. However, it has been shown that at cryogenic temperatures, exposure to x-rays can lead to a reduction of the heme iron in ferric Myoglobin (metMb) [199]. Recently, Della Longa and Arcovito also studied the x-ray-induced lysis of the Fe-CO bound in MbCO at cryogenic temperatures [27]. They have shown that prolonged x-ray irradiation induces the Fe-CO bond breakage, and showed that the process is reversible when increasing the temperature. In addition, they reported the absence of damage to the protein. The structure of metMb has been studied by Kachalova *et al.* [200] and Vojtěchovský [201] using single-crystal x-ray diffraction, and by D'Angelo *et al.* using XAS [76]. The last reports using solid protein solutions at 20 K, a temperature which may influence the structure. The structure of Cyano-myoglobin (MbCN) was also studied by D'Angelo *et al.* using XAS [76]. Arcovito and co-workers employed a combined approach based on XAS and polarized X-ray diffraction (XRD) to study crystals of MbCN [29]. Both measurements were done at cryogenic temperatures. Arcovito *et al.* [29], investigated the structure of MbNO crystals using polarized XANES. They derived a structure consistent with one of the crystallographic results. Interestingly, the resulting crystallographic structural details depends on the preparation method [202] used to obtain the crystals. The NO geometry relative to the iron atom is found to vary considerably depending if the crystals are prepared from the reaction of metMb with nitrite/dithionite or when prepared directly from the reaction of NO gas with deoxyMb [202, 203]. It has been speculated that the distal pocket in MbNO plays a role in stabilizing local FeNO conformational minima [202]. Oxy-Myoglobin (MbO_2) is the most abundant type of Mb, being present in mammal muscles in a very high concentration. Surprisingly, the crystallographic structure of MbO_2 presents a very low resolution, 1.6 Å and indicates that the Fe atom does not lie on the heme plane, being 0.19 Å below it, in the direction of the proximal histidine. This deviation is very uncommon in ligated ferrous Mb, and it is believed to be due to the low resolution of the crystal structure and to the fact that oxygen can change the oxidation state of the iron atom. From all the studies about the geometrical structure of the different Mb forms, deoxyMb is probably the most controversial case. The iron is in the ferrous state and it is deligated, *i.e.*, the Fe atom has only 5 first neighbours. This makes a unique geometry, and the iron environment no longer has octahedral symmetry. In addition, this state is very unstable, requiring extra care during the experiments in order to avoid

contact with the oxygen present in air. This immediately transforms deoxyMb to MbO_2, and the results cannot be trusted. The heme doming effect in the deoxyMb case (and also in the deligated Mb's) is very difficult to quantify. Many studies only report an iron displacement from the heme plane [29, 76, 204], which induces considerable strain in the carbon-carbon bonds in the porphyrin. Kachalova *et al.* reported one of the first studies of the crystal structure of deoxyMb at atomic resolution [200]. In their proposed structure, the Fe displacement from the heme plane is 0.29 Å, and the average distance between the iron and the nitrogen atoms in the porphyrin is Fe-N_p = 2.057 Å. In addition, they report the N_p rms deviation from the average plane, being 0.018 Å. D'Angelo and co-workers performed a FMS analysis on the XANES spectra of a series of frozen Mb [76]. In the case of deoxyMb, their results show that the distance Fe-$N_p = 2.06 \pm 0.03$ Å and the iron-histidine distance Fe-His $= 2.15 \pm 0.05$ Å. Using a water as the ligand, the reported distance between the iron and the ligand was 3.7 ± 0.02 Å. They also included the Fe displacement from the heme plane as a variable, the final value of which was 0.2 ± 0.02 Å. Arcovito *et al.* analysed the XANES region of deoxyMb at 15 K and derived a Fe-N_p distance of 2.07 ± 0.03 Å and a Fe-His distance of 2.19 ± 0.05 Å, while proposing that the iron displacement from the heme plane was 0.5 ± 0.2 Å[204]. They also report a ligand 3.8 ± 0.2 Å away from the iron atom. Three years later, the same authors used polarized XANES to study the local structure of a series of Mb crystals [29]. Their analysis pointed to an average Fe-N_p distance of 2.04 ± 0.03 Å, an iron-histidine distance of 2.08 ± 0.02 Å and an iron-ligand distance of 3.3 ± 0.02 Å. In these studies, the porphyrin ring size, given by the average distance Fe-N_p, is found to have a consistent value, reflecting the rigidity of the structure. On the other hand, all the other structural parameters vary considerably outside the reported errors, suggesting that their values are affected by the fact of using crystals in the experiments or by a sample not constituted by 100% deoxyMb. Moreover, the preparation method and environmental parameters (pH, temperature) are known to affect the chemical and structural state of at least one of the Mb forms [202]. Our XAS data do not suffer from radiation-induced effects, neither are affected by the use of cryo-cooled samples. Using liquid samples has the advantage of allowing a fast exchange of the molecules probed by the x-rays and consequently the x-ray dose deposited in each molecule is much smaller. Furthermore, the XAS measurements in liquids were done under physiological conditions, which is a better representation of the protein natural environment.

In the following we will assign the *A*-*E* features either to bound-bound transitions or multiple-scattering resonances, connected with structural features. In the pre-edge region (7108-7122 eV), feature *A* originates mainly from $1s \rightarrow 3d$ transitions in the iron atom, which in the dipole approximation are symmetry-forbidden. However, distortions of the octahedral symmetry make them partially allowed. Additionally, the intensity of these features on other iron-based complexes reflect the degree of mixing of the molecular orbitals, *e.g.* the Fe $3d$ overlaps with the $4p$ and the nitrogen $2p$ from the porphyrin ring, due to vibronic interractions and quadrupole transitions [192]. Depending on the type of ligand bound to the Mb, feature *A* can split and show a more detailed structure

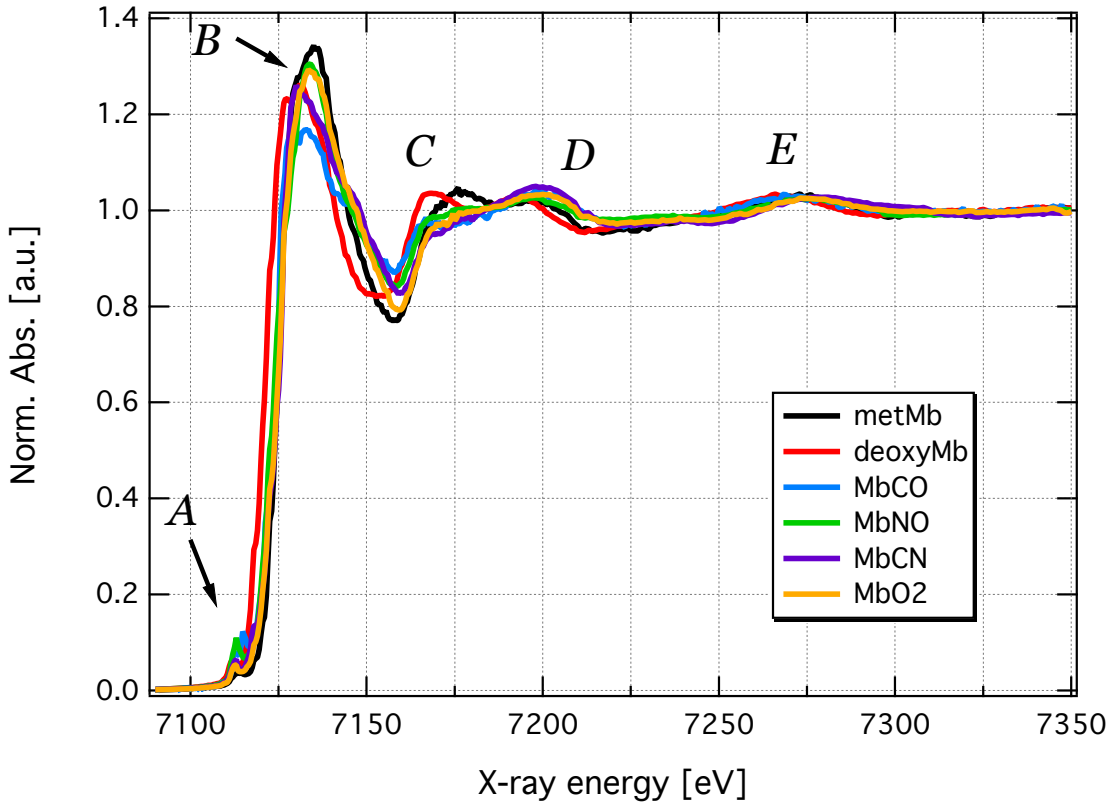

Figure 6.2.: Steady-state XAS spectra of different forms of Myoglobin in solution. The main spectral features are indicated.

than a single peak (see Figure 6.3). The importance of higher-order multipole moments in the correct description of the electrostatic potential of MbCO and its influence on the ligand rebinding dynamics [205, 206] indicate that subtle details in the ligand structure and its interaction with the heme play a significant role and cannot be neglected. The next clearly distinguished feature, labeled B, is about 6 eV from the inflection point of the absorption edge (the defined position of E_0). It is the maximum of the absorption, lying already in the continuum. It has previously been assigned to multiple-scattering resonances (see Section 3.3.1) [26, 207]. The relative position of the B feature with respect to E_0 is an indication of chemical shift and the details present in it give a first hint at the geometry of the ligand with respect to the heme [26, 207]. However, the interplay between the MS process and the local geometrical structure is very complex, making a complete analysis of a particular feature with selected structural parameters difficult. Features C, D and E are all due to the specific geometry of the Myoglobin under study. While C and D are very close to each other and can be assigned to MS effects, feature E is already in the EXAFS regime and therefore contains mainly single-scattering contribution from the nearest N atom in the first coordination shell. The literature does not contain any reference relating feature C with a specific geometric parameter in Mb, but a close inspection in the spectra motivate the correlation of this

feature with the presence (or equivalently, the absence) of a ligand. In the metMb and deoxyMb forms, which are *unligated forms*, the C feature is much more pronounced than on the *ligated* ones (MbCO, MbNO, MbCN and MbO_2). In the analysis of the XAS spectra given in Section 6.5.2 we will shown that the C feature is also sensitive to the well-known *doming effects* in the unligated/photodissociated Myoglobins.

Figure 6.3 shows the details in the pre-edge region of the XAS spectra of the different Mb forms. There are rich information present in this region of the spectra, which is reflected by the relative position of the A feature and the subdivision into other features (A^i and A^{ii}). The different pre-edge features of the different forms of Mb point to a complex interaction between the Fe atom and the neighbours, altering the electronic structure of the molecule as a whole. It is clear that a simple picture of $1s \rightarrow 3d$ transitions in the iron atom is an oversimplified interpretation of the process underlying these features.

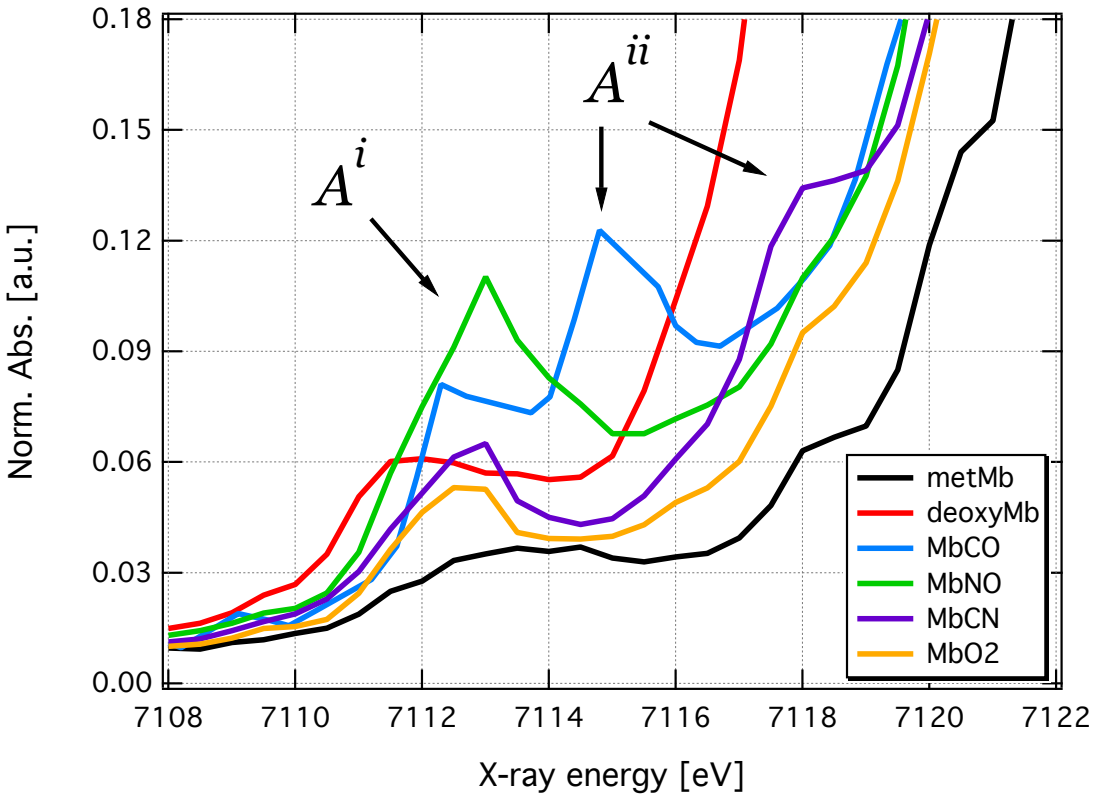

Figure 6.3.: Zoom on the pre-edge region of the XAS spectra of the different forms of Myoglobin in solution. Note the presence of multiple features and the evident differences depending on the Myoglobin form. Feature A^i is present in all spectra, while A^{ii} is absent in deoxyMb.

6.3 Time-resolved XAS

MbCO

As described in Chapter 4, the outcome of a time-resolved XAS experiment are the transient difference spectra $\Delta A(E,t)$ and the time-delay scans. After proper normalization with respect to the steady-state spectrum, or more precisely, to the unpumped signal, the transient spectrum is ready to be analysed. In this thesis, the transient XAS were measured at 50 ps time delay between the pump and probe pulses, with the exception of the MbCO transient which was measured using the slow pump-probe mode as explained in Section 5.6. This mode was used because the ligand recombination time of MbCO is on the order of milliseconds [65] and reducing the repetition rate of the laser so that the sample could relax between x-ray probe pulses would cancel the advantages of the high repetition rate scheme. In the slow pump-probe mode, the time delay is not well defined. Since the time interval between consecutive laser pump pulses at 520 kHz is 2 μs, the excited-state population is an ensemble composed of the population at 50 ps, which is the time delay set between the pump and probe pulses, and the 2 μs interval between two consecutive laser pulses.

Figure 6.4 shows the K-edge time-resolved XAS of a 2 mM solution of Carboxy-Myoglobin (MbCO). This transient represents the difference in XAS spectra of the *ligated* (CO bound) minus the *unligated* (CO unbound) protein. It was measured using the slow pump-probe mode described in Section 5.6, using a free-flowing jet in open atmosphere and keeping the sample reservoir under a CO atmosphere. This was possible because the Mb affinity for CO binding is about 30 times higher than that of O_2 [3, 177]. The signal shown in Figure 6.4 is an average of 32 individual scans, using two different fluorescence detector signals. Prior to averaging, the fluorescence signals of each scan was corrected by the incoming x-ray flux (I_0) and then normalized to the edge-jump. This resulted in a normalized transient XAS of about 7% with respect to the steady-state absorption. The total acquisition time was about 4.5 hours. Photo-excitation was done with the 10 ps pulses of the Duetto laser at 532 nm, using a repetition rate of 520 kHz and a laser fluence of 125 mJ/cm^2. It exhibits several pronounced changes in the XANES region of the spectrum, with the largest at 7.123 keV being due to a shift to lower-energy of the iron absorption edge. Overlaid with the MbCO transient XAS is the expected signal, corresponding to a simple subtraction of the steady-state XAS spectrum of the MbCO and the unligated ferrous Mb (deoxyMb). After ligand photo-detachment and in the absence of any intermediate structure on the time scale of the measurement, we expect the spectrum of the photo-product to resemble that of deoxyMb. The transient spectrum should then be similar to the difference spectrum of the deoxy form minus the ligated form. This difference spectrum represents a limiting case in which all the ligands are photo-detached and no intermediate structure is present. This is a good approximation for MbCO where there is almost no geminate recombination [65, 208] and no evidence of any partially bound structural intermediates [14]. A scale factor can therefore be

used when comparing it to the measured transient XAS, allowing us to estimate the fraction of excited species. The difference static spectrum has been scaled by a factor of 0.21 for comparison with the transient XAS, implying an excitation yield of $\sim 21\%$. Because the MbCO transient XAS was measured in the slow pump-probe mode every laser pump pulse excites a sample which is only partially relaxed, leading to a larger average population of unligated Mb (deoxyMb) than in the case of a single excitation pulse.

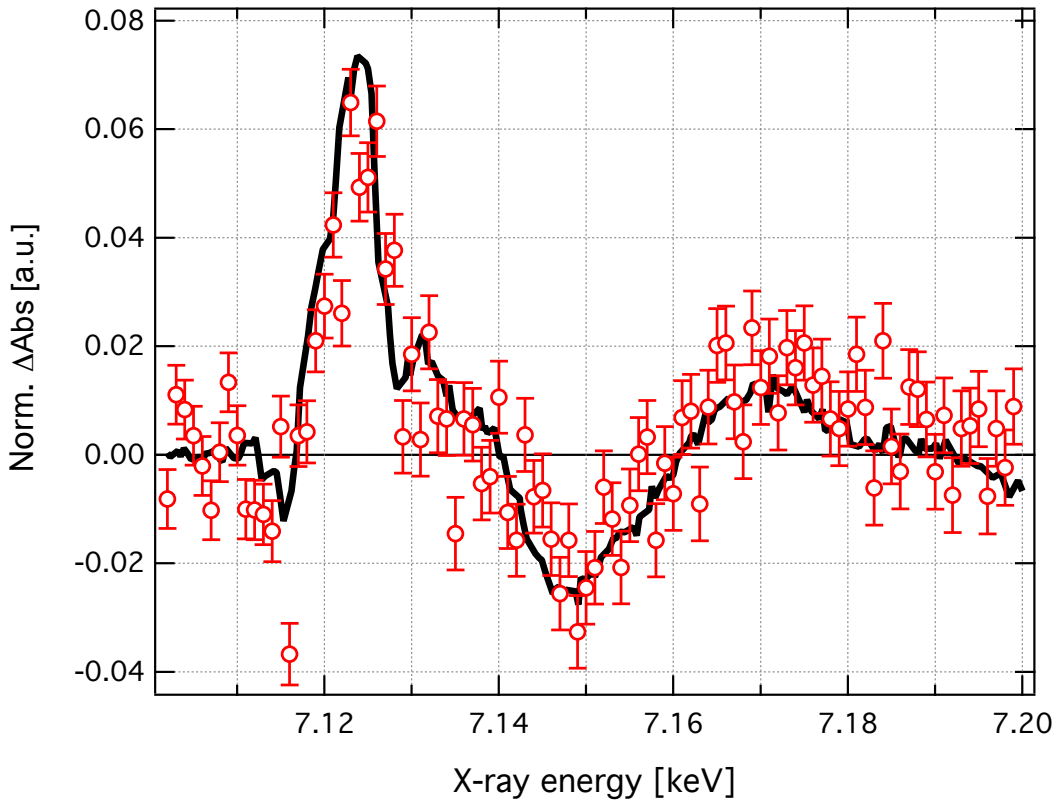

Figure 6.4.: Transient XAS of a 2mM solution of MbCO in physiological conditions. The photo-excitation was done using 10 ps laser pulses at 532 nm and a repetition rate of 520 kHz. The transient data was recorded using the slow pump-probe mode (see Section 5.6). Overlaid with the transient XAS is the simulated difference, constructed using the steady-state spectra of the unligated and the CO-bound Myoglobins.

MbNO

Figure 6.5 shows the K-edge time-resolved XAS of a 4 mM solution of Nitrosyl-Myoglobin (MbNO) at 50 ps time delay. The ligand recombination time of MbNO is only about 200 ps [63, 209, 210], compared to several miliseconds of MbCO [65]. This is much faster than the pulse repetition rate, which allowed us to use the usual scheme to record transient XAS data, *i.e.*, on the basis of the pulse-to-pulse differential absorption. A diamond flow cell was used as sample environment, in which the MbNO solution was recirculated

in a closed loop system. The sample was flowed at about 60 ml/min and a secondary flow-loop was used to monitor the UV-Vis spectrum of the sample, ensuring its integrity during the experiment. During the measurements the MbNO sample was kept under nitrogen atmosphere, in order to avoid degradation caused by slow substitution of the NO ligand by the O_2 present in air. The MbNO sample was excited using 532nm/10 ps laser pulses at 520 kHz repetition rate. The laser fluence used was 100 mJ/cm^2, but this value has to be corrected by the visible transmission of the diamond used in the flow cell walls. In the visible range around 500 nm the diamond light transmission is $> 65\%$ [172], which results in effectively only about 65 mJ/cm^2 laser fluence in the sample. On the other hand, the x-ray transmission through 50 μm diamond is $\sim 90\%$ at the vicinity of the Fe K-edge (7.1 keV), which does not significantly affect the x-ray flux probing the sample. A common problem when using closed environments for ultrafast time-resolved XAS experiments is sample deposition in the walls of the container (*e.g.*, quartz capillary). To avoid this type of problem the flow cell was translated vertically in between scans. This procedure completely prevented the sample accumulation at the diamond walls. The transient XAS in Figure 6.5 is the average of the fluorescence signal of 51 individual scans over 4 hours of data collection. Following the usual procedure of data analysis, each individual scan was corrected for the incoming x-ray flux (I_0), following the normalization to the edge-jump. In this way, the normalized transient XAS corresponds to less than 2% of the change in transmission. It is interesting to note that the normalized signal magnitude of the MbNO transient is four times smaller than that of the MbCO. Several factors contribute to this: the the lower laser fluence (65 mJ/cm^2 in the MbNO experiment, compared to 125 mJ/cm^2 in the MbCO), the smaller photodissociation quantum yield, which is only $50 \pm 5\%$ for MbNO in contrast to 100% for MbCO [63] and the fact that the MbCO was measured in the slow pump-probe mode. Moreover, the transient XAS data is recorded at 50 ps and taking into account that the NO recombination time is around 200 ps [63, 176, 209, 211–213], the transient signal magnitude is expected to have decreased to approximately 78% of its maximum intensity. Adding all these factors together we would expect a reduction factor of 5 in the MbNO transient signal of when compared to the MbCO transient, which is in good agreement with the normalized magnitude of the MbNO transient XAS signal. We show in Figure 6.5, overlaid with the transient XAS, the expected signal obtained by the subtraction of the steady-state XAS spectrum of the MbNO and the unligated ferrous Mb (deoxyMb). The latter static difference spectrum was scaled by a factor of 0.05 for comparison with the transient XAS, implying an excitation yield of $\sim 5\%$. This value is approximately four times smaller than the one used in the MbCO case, in correspondence with the smaller signal magnitude. Contrary to the MbCO case, in which the transient XAS matches the static difference spectrum, for MbNO the static difference deviates from the transient XAS at 50 ps. The A feature of the transient data seems to follow the trend of the static difference, however it is not possible to analyse the pre-edge region due to the small S/N and the relatively large energy step using in the time-resolved measurements (the A^i feature of MbNO is about 2 eV FWHM, while

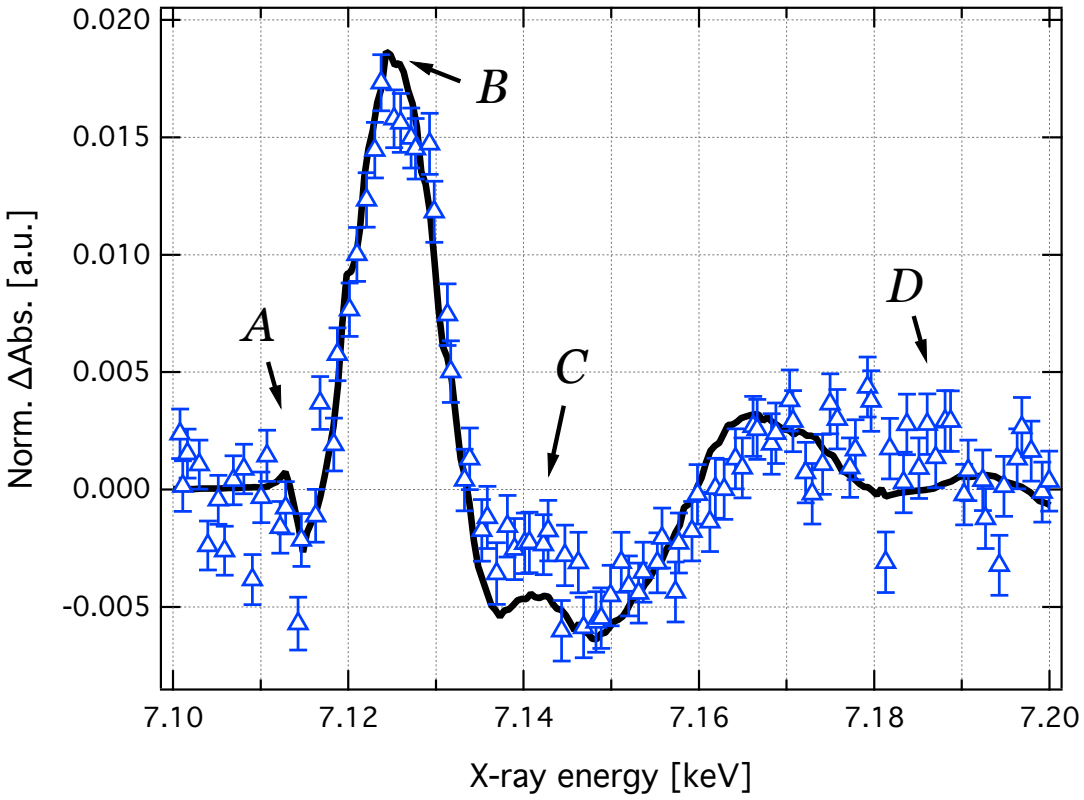

Figure 6.5.: Transient XAS of a 4 mM solution of MbNO in physiological conditions, recorded at 50 ps time delay. The photo-excitation was done using 10 ps laser pulses at 532 nm and using a repetition rate of 520 kHz. The total laser fluence was 100 mJ/cm^2, but taking into account the light transmission through the diamond window used in the flow cell, the fluence in the sample was effectively 65 mJ/cm^2. Overlaid with the transient XAS is the simulated difference, constructed using the steady-state spectra of the unligated and the NO-bound Myoglobins.

the energy step in the transient XAS was 1 eV/data point). Features *B*, *C* and *D* seem to deviate from the predicted signal based on the difference between the steady-state spectra, which is an indication that an intermediate species may be contributing to the transient XAS signal. In fact, Kruglik *et al.* [210] have recently proposed the existence of a domed ligated (6-coordinate) configuration for the MbNO after deligation. Although this configuration has been reported to live for $\sim$ 30 ps, its contribution at 50 ps may still account for the small deviations seen in features *B* and *C* in Figure 6.5. The population ratio of the nonplanar 6-coordinated to 5-coordinated species of MbNO is $\sim$ 0.3 at 50 ps [210], which means that a domed ligated configuration contributes only 30% to the total signal. Such a small contribution lies on the limit of the S/N of the present data, therefore the deviations from the predicted signal cannot be unambiguously associated with an intermediate domed ligated MbNO species.

6.3.1. Time-delay scans

In order to make sure that the transient spectrum indeed belongs to the unligated MbNO, we performed time scans by monitoring the time dependence of the maximum transient XAS feature around 7.125 keV. The result of such a time-delay scan of the MbNO sample is shown in Figure 6.6. A first inspection of this time-delay scan seems to indicate the presence of at least two components, one dominating contribution of about 250 ps and a long one that accounts for the signal not decaying to zero even after 1 ns.

The rebinding kinetics of NO to the heme iron has been previously investigated by optical spectroscopy and found to vary with temperature and excitation wavelength [63, 209]. Two distinct phases have been reported, corresponding to fast rebinding of NO from a localized state near the heme and a slower transition associated with the rebinding of the ligand from a somewhat more distant site. Different time-constants have been associated with these phases, indicating the importance of correctly identifying the species probed at 50 ps. In this thesis the lifetime associated with the fast rebinding will be referred to as τ_1 and the one associated with the slow phase will be referred to as τ_2. Whenever other characteristic times are introduced, the proper label will be given.

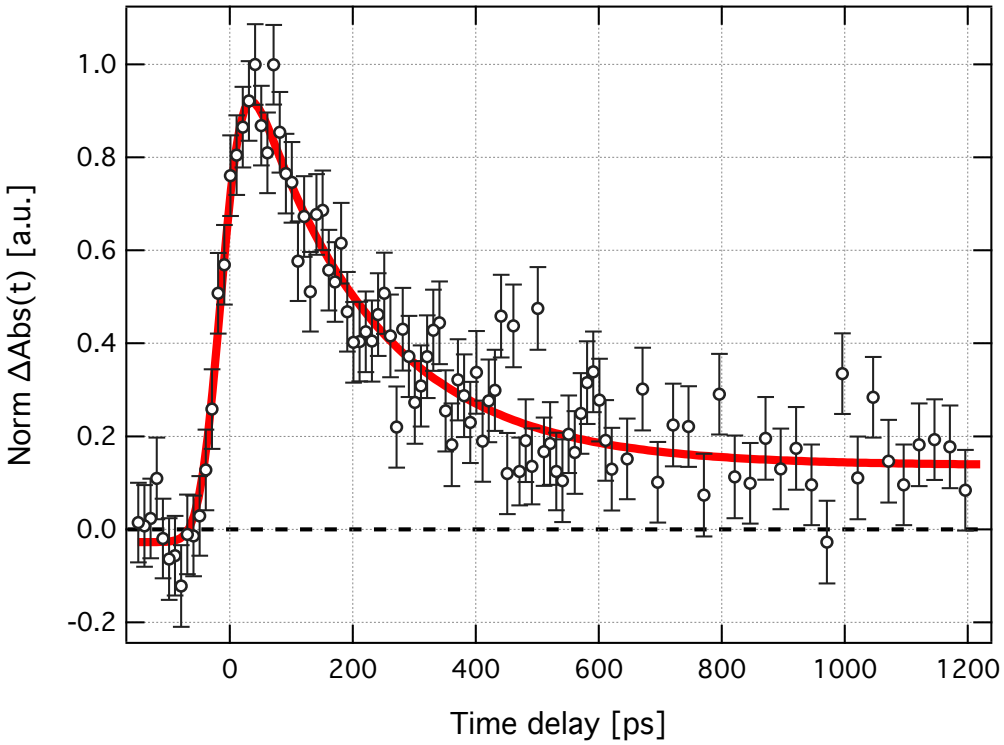

Figure 6.6.: Time delay scan of a 4 mM solution of MbNO at 7.125 keV (black circles) and the fit for a multi-exponential curve (red line), with decay times $\tau_1 = 30$ ps, $\tau_2 = 216 \pm 24$ ps and $\tau_3 = 1.5$ μs. The exponential decay curve is convoluted with a Gaussian function with FWHM equals 65 ps accounting for the experimental temporal resolution. The decay times τ_1 and τ_3 are kept fixed to values given in the literature.

Petrich *et al.* studied the NO recombination of sperm-whale Myoglobin using ultrafast absorption spectroscopy in the visible range [212]. They report a biexponential recombination, with times $\tau_1 \simeq 28$ ps and $\tau_2 \simeq 279$ ps. They interpret the data using molecular dynamics simulations of the heme-imidazole system after photodissociation, concluding that non-exponential behaviour of the recombination can be either due to a range of energetic barriers present in an inhomogeneous protein population or to relaxation of a protein coordinate following the initial perturbation, *e.g.* the ligand dissociation. Later, the same authors used flash photolysis to study the NO recombination to several wild-type and mutant human Myoglobins [213]. They show that the recombination rates are very different for the mutants, but are generally bimodal. They found that for the wild-type human Mb, $\tau_1 \simeq 21$ ps and $\tau_2 \simeq 135$ ps. Kholodenko and co-authors studied the same process in iron and cobalt Mb by visible ultrafast transient absorption [214]. They show that upon excitation in the Soret band, at 405 nm, recombination dynamics is wavelength-independent and non-exponential with components $\tau_1 \simeq 19$ ps and $\tau_2 \simeq 126$ ps. Ye *et al.* report the measurement of the photodissociation quantum yields of MbNO and MbO_2, as well as the vibrational relaxation of these Mb species [63]. The time constant for vibrational relaxation of the six-coordinated ligated Mb studied is found to be close to 1 ps for both of them. By making extrapolations to $t = 0$ they derived the photodissociation quantum yield of MbNO to be $50 \pm 5\%$, compared to 100% of MbCO. They also confirm the biexponential NO recombination to the heme, with time constants τ_1 and τ_2 approximately equal to 10 ps and 200 ps, respectively. Moreover, the MbNO species is said to present significant geminate recombination over the first 120 ps. The amplitude and rate of the fast rebinding phase appear to distinctly depend on the pump photon energy. Kim *et al.* [176] used femtosecond mid-IR absorption spectroscopy to study the geminate recombination of the NO molecule to the Mb, reporting $\tau_1 = 5.3$ ps and $\tau_2 = 133$ ps, while arguing that signals from vibrational relaxation of the six-coordinate heme and conformational and vibrational relaxation of photodissociated Mb and recombined MbNO contaminate the transient signals in the optical spectra and hinder accurate recovery of the parameters. Zemojtel and co-authors applied femtosecond infrared polarization spectroscopy to elucidate the Fe-NO geometry in MbNO [211]. The analysis of the bleach recovery dynamics of the NO stretching band was modelled by a multiexponential decay. The components in the NO recombination dynamics are found to be $\tau_1 = 42$ and $\tau_2 = 238$ ps. In addition, they report two other components, with time constants of 1 and 4 ps. The latter is attributed as evidence of a significant fraction (35%) of NO recombining with the heme. Ionascu *et al.* investigated the temperature-dependence of NO recombination in several heme proteins [209]. They report bi-exponential kinetics of approximately 12 and 200 ps, with a small dependence on temperature and wavelength. Both rates slow down slightly in Mb above 200 K. In addition, they found another small slow-geminate phase near 1 ns. Kruglik *et al.*, used subpicosecond time-resolved resonance Raman and femtosecond transient absorption spectroscopy, investigated the ultrafast structural transitions in several heme proteins induced by NO binding [210]. They found that the heme response and iron motion do

not follow the kinetics of NO rebinding, and concluded the existence of an intermediate species in which the NO is bound to a domed heme. This non-planar 6-coordinate heme complex has a lifetime of 30 ± 10 ps.

Our time scans recorded at 7.125 keV, following the rebinding dynamics of the NO molecule after photodissociation indicates a multi-exponential recombination. The fast processes on the order of 1-5 ps cannot be seen due to the temporal resolution of our time-resolved XAS experiments of *ca.* 70 ps. Therefore, the data was fit with a multi-exponential curve, including three time constants: a fixed $\tau_1 = 30$ ps accounting for the non-planar bound (6-coordinate) species reported by Kruglik *et al.* [210], a second $\tau_2 \approx 200$ ps representing the NO geminate recombination, and a third constant $\tau_3 = 1.5$ μs which accounts for a long component in the signal. A Gaussian curve with FWHM equals to 65 ps was convoluted with the multi-exponential function to account for the experimental time resolution, and the relative fraction of non-planar bound species was kept constant and equal to 30%, according to Ref. [210]. The exponential fit, shown as a red line in Figure 6.6, yielded a decay time $\tau_2 = 216 \pm 24$ ps, an average value with respect to the ones derived from optical results [63, 176, 209–214]. At this point one may argue that the temporal resolution is not sufficient to distinguish the fast component of 30 ps in the rebinding dynamics curve. In order to test the effect of this component we used another multiexponential function to describe the time-delay data, containing just two components, τ_1' and τ_2'. This new fit yielded a time decay $\tau_1' = 198 \pm 21$ ps, and τ_2' was kept fix and equal to 1.5 μs. The current S/N in the time-delay data does not allow the choice of either models, both provided equally acceptable fits to the data. Moreover, the values of the decay time associated with the NO geminate recombination using the two models agrees within the error bars. We have also tried fits using a mono exponential decay curve, which failed to reproduce the data. The large variation in the reported decay times found in the literature ($\tau_1 \sim$ 5-42 ps and $\tau_2 \sim$ 126-279 ps) indicate that optical measurements do not provide a unique answer to the time scales associated with the structural changes caused by NO photodissociation in MbNO, and a structure-sensitive technique is the best option. The fact that the time-resolved XAS experiment recovers the long component of *ca.* 200 ps confirms that the probed state is indeed the NO recombination with the heme, and an *a posteriori* proof that the high repetition rate excitation does not damage the sample.

6.4 Calculation of the XAS spectra of Myoglobin

In this section we will present the strategy used in the calculation of the XAS spectra of the different forms of Myoglobin. We start with the description of the parametrization of the environment around the Fe atom, followed by some details of the fit procedure used in the `MXAN` code.

In order to calculate the XAS spectra of Myoglobin a first guess of the geometrical structure is necessary, and we have used the crystallographic structures for this purpose.

The Protein Data Bank [215] is a general source of protein structures and it is the first place to look for possible structures. Alternatively, structures from DFT calculations or any other generated by theoretical methods, *e.g.* molecular dynamics (MD) simulations, can be used. Additionally, the preparation method used in the crystallization process can also severely influence the resulting structure, *e.g.* MbNO, if prepared from metMb with with nitrite/dithionite or from the reaction of NO gas with deoxyMb, results in two different structures with respect to the Fe-NO bond length and FeNO angle [202]. The relevant entries in the PDB database containing the structures of the Myoglobin forms studied in this thesis are listed in Table 6.1. The appropriate files to be used as input in the calculations were chosen according two different criteria: a) the preparation method used to obtain the crystals should match the one used in our experiments and, b) for a certain Mb form, the best resolution structure was chosen.

Table 6.1.: Table with the types of Mb and the selected PDB entries inspected to be used as the starting points in the calculations.

Mb type	PDB ID	resolution [Å]	year
metMb	1BZ6	1.20	1998
	1YMB	1.90	1993
	1MBN	2.00	1973
deoxyMb	1BZP	1.15	1998
	2V1K	1.25	2007
MbO_2	1MBO	1.6	1981
MbCN	2JHO	1.40	2007
	1EBC	1.80	1999
	1YMC	2.00	1993
MbNO	2FRJ[†]	1.30	2006
	2FRK[§]	1.30	2006
	1NPF	1.90	2003
MbCO[♯]	1A6G	1.15	1998
	1DWR	1.45	1999

[†] nitrite/dithionite method
[§] nitric oxide gas method
[♯] wild-type Myoglobin

The different forms of the ligated Myoglobin differ basically as to which diatomic ligand is bound (if at all) and its relative position with respect to the Fe atom in the center of the heme. A more detailed investigation of the crystallographic structure shows that the distance and orientation of the proximal/distal histidines are also different. Another subtle difference is the size of the heme, which is manifested as the average distance between the central iron atom and its first neighbours (the N atom of the porphyrin

ring). The relative position of the F atom with respect to the heme plane was also found to vary slightly depending on the Mb form investigated. Therefore, these will be the relevant parameters to be varied in the fit procedure used to obtain the best structure that describes a certain Mb form.

The analysis of the Myoglobin XAS spectra was done using the MXAN procedure [85–87, 112]. In the fits of the steady-state spectra, the same calculation philosophy employed by Della Longa *et al.* [25]. For this purpose, there is an alternative calculation mode in MXAN, in which the heme and surrounding atoms are parametrized in a special way, to minimize the number of structural parameters necessary to describe the heme environment. The set of parameters used to describe the Mb structure are listed below. An illustration of these parameters is given in Figures 6.7 and 6.8.

- `Core` - This parameter controls the movement of the Nitrogen atoms on the porphyrin ring connected to the Fe atom, moving the whole porphyrin as a rigid structure. It is analogous to a breathing mode of the porphyrin ring. The variation of this parameter is given as fractional values with respect to the initial value.
- `Fe-Np` - Controls the distance between the Fe atom and the nitrogen atoms of the porphyrin ring. Is a duplicate parameter, since this distance is already controlled by `Core`. It is given as an absolute value, the average distance between the iron and each of the four nitrogen atoms in the porphyrin.
- `Displ` - Controls the Fe atom displacement out of the heme plane. It moves the Fe atom in absolute values with respect to the average heme plane.
- `Dom1` - Controls the *doming* of the porphyrin ring. It moves the four N atoms of the porphyrin ring in a direction perpendicular to the heme plane (see Figure 6.8). It is used only on the case of deoxyMb or other deligated forms, *e.g.*, photo-dissociated Mb.
- `Dom2` - Controls the *doming* of the porphyrin ring in a similar way as `Dom1`. It moves the 8 C atoms closest to the Fe in the porphyrin ring in a direction perpendicular to the heme plane (see Figure 6.8.). It is used only on the case of deoxyMb or other deligated forms, *e.g.*, photo-dissociated Mb.
- `Fe-L1` - This parameter controls the distance between the Iron atom and the ligand closest atom (*eg.*, C of the CO molecule or N of NO molecule).
- `Tilt` - Controls the angle between the direction perpendicular to the heme plane and the vector defined by the bond between the Fe and the closest atom of the ligand. It is the angle α in Figure 6.7.
- `Bend` - This parameter controls the angle between the vectors defined by the bond between the Fe and the closest atom of the ligand and the one defined by the bond between the two atoms of the ligand. It is the angle β in Figure 6.7.
- `Azim` - Controls the azimuthal angle of the closest atom of the ligand with respect to the direction perpendicular to the heme plane. It is the angle γ in Figure 6.7.

- `Fe-Hi` - Controls the distance between the Fe atom and the proximal histidine (His93).
- `HiT1` - Controls the proximal histidine (His93) tilt angle with respect to the vector defined by the heme normal.
- `HiT2` - Controls the proximal histidine (His93) bend angle with respect to the vector defined by the heme normal.
- `L1-L2` - This parameter controls the distance between the two atoms of the ligand molecule.

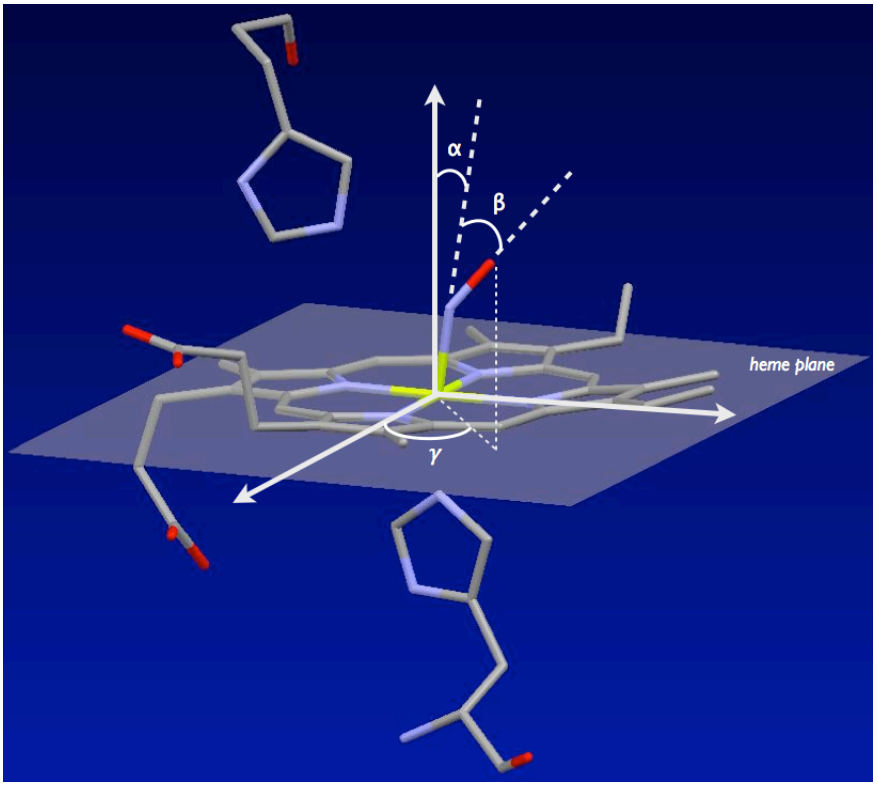

Figure 6.7.: Schematics of the relevant parameters used on the fits of the Myoglobin XAS using the MXAN code. The heme plane and relative ligand geometry (angles α and β) are shown.

In the `MXAN` procedure, the potential is calculated using a self-consistent field (SCF) approach including the whole atomic cluster in the first step of the structural optimization, but it is not recalculated with SCF in the following calculation steps. The calculation of SCF potentials is still too complex and time-consuming, making its use impractical in a fitting procedure. Additionally, the calculation of a SCF charge density for a geometry that does not resemble the real geometry can lead to a less accurate potential or even incorrect electronic configurations [84, 86]. In many publications involving the XAS analysis of heme proteins, this approach of using SCF potentials only in the first step of the calculation was employed [25, 28, 216]. This can be a source of systematic errors

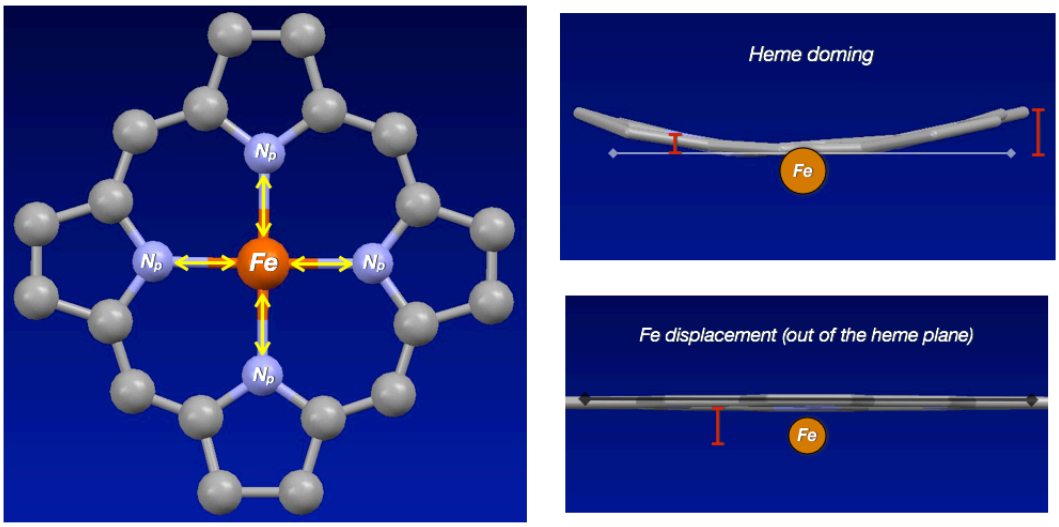

Figure 6.8.: Schematics of the parametrization used on the fits of the Myoglobin XAS using the MXAN code.

in the fitting procedure, especially if the starting structure differs considerably from the real geometry. Recently, it has been shown that refining some non-structural parameters related to the MT potential can partially account for the limitation of not considering a SCF potential at each step of the calculation [29, 76]. In fact, other systematic errors can appear if a relevant statistical correlation exists between the refined potential parameters and some structural parameters. However, the overall accuracy of the structural parameters calculated by `MXAN`, including these systematic errors, are comparable to the crystal structure from high-resolution diffraction. The maximum value of the angular momenta basis (l_{max}) of the spherical harmonic expansion of the scattering path operators was chosen based on a convergence criterion. Its value was successively increased until the x-ray cross-section converged, with a value $l_{max} = 3$. We used a cluster of about 7 Å around the Fe atom to calculate the MT potential, including a total of 79 atoms. It includes the whole porphyrin ring, the ligand when present (CN, O_2, NO or CO), the proximal (His93) and part of the distal (Hist64) histidines. Scatterers up to about 5 Å, which is equivalent to 32 to 36 atoms, depending on the Mb form, were used in the FMS procedure. These values were also chosen according to the convergence of the scattering cross-section. The MT spheres radii were chosen according to the Norman criterion [105, 106], with a percentage of overlap varying between 0 and 20%, which is refined at each calculation step together with the potentials. The exchange and correlation part of the potential are calculated in the framework of the Hendin-Lundqvist (HL) scheme [106, 114], using only the real part of the complex potential to avoid overdamping of the spectral features at low energies, characteristic of this type of potential [84, 86, 104, 112, 115]. All the inelastic losses were taken into account by a phenomenological approach in which the calculated cross-section is convoluted with a Lorentzian broadening function having an energy-dependent width given by $\Gamma(E) = \Gamma_c + \Gamma_{mpf}(E)$.

The constant part Γ_c accounts for contributions coming from the core hole lifetime and the experimental resolution, while the energy dependent term $\Gamma_{mpf}(E)$ represents all the intrinsic and extrinsic inelastic processes. Γ_c is zero below a certain onset energy E_s [b] and begins to increase from a value A_s following the universal functional form of the mean free-path in solids [86, 112, 217]. Both the onset energy E_s and the amplitude A_s are introduced into the $\Gamma_{mpf}(E)$ function using an arctangent functional form to avoid discontinuities. The numerical values of E_s and A_s are derived via a simulated annealing-like method before the structural calculation starts and are fit by Monte Carlo search at every minimization step. Recently, the `MXAN` code modified the way it calculates the losses by introducing a further convolution in the constant term Γ_c [218]. It now includes a convolution with a Gaussian function (Γ_{exp}) to mimic the experimental resolution. Therefore, the contribution coming from the energy-independent Lorentzian (Γ_c) now accounts only for the core-hole. In this way a more accurate description of the inelastic losses suffered by the photoelectron is produced.

6.5 Analysis of the XAS spectra of Myoglobin

The quantitative structural analysis of the steady-state XAS spectra of the different forms of Myoglobin in physiological solution will now be presented. Different theoretical tools were used, the `MXAN` package was used to fit the low-energy region (up to 200 eV from E_0) of the steady-state XAS of the different Mb. For each type of Mb, the starting structure was taken from the PDB database (see Table 6.1); the structure with the best resolution available was chosen. By varying the relevant structural parameters and comparing the calculated spectrum with the experimental data, a structure corresponding to the best fit was found. To analyze the pre-edge region of the spectrum we used two different methods. We employed the `FEFF9` code to calculate the l-projected electronic density of states (l-DOS) for each atomic species, which allowed a detailed description of the electronic structure of the different Mb forms in physiological solution. This analysis was further complemented by recent TDDFT calculations [184], which not only support the DOS analysis but also provided a more detailed picture of the origin of the electronic transitions causing the features in the pre-edge region of the XAS spectrum.

A complete quantitative analysis of the XANES region of the spectrum is often a challenging task [111, 124]. The many approximations made in the theory, *e.g.* use of MT potentials, inaccuracies in the calculation of the energy-dependent self-energy and the description of particle-hole interactions, are the fundamental reasons for semi-quantitative interpretation of the XANES spectrum. These approximations are even more critical in the case of transient XAS, in which usually only a limited energy range of the spectrum is available and the S/N is relatively small. However, the proper choice of an initial geometrical structure and the relevant structural parameters affecting the XAS, combined with a phenomenological approach to treat the inelastic losses in the

[b] In extended systems, the onset energy E_s corresponds to the plasmon excitation energy.

XAS spectrum allowed us to successfully reproduce the transient XAS data for the photo-excited MbNO in solution at 50 ps. For the analysis of this time-resolved XAS we employed the `MXAN` package to perform fits of the transient spectrum in energy space.

6.5.1. Cluster-size analysis of static XAS spectra

In the analysis of XANES spectra we started with the study of the dependence of the calculated spectrum on the size of the atomic cluster used in the FMS calculations. The cluster-size analysis is important not only to guarantee the convergence of the calculated spectrum with respect to the number of scattering paths but also to optimize the calculation time. The dimension of the matrix to be inverted in the FMS calculations is $N(l_{max}+1)^2$, where N is the number of atoms in the cluster and l_{max} is the maximum value of the angular momenta basis of the spherical harmonic expansion of the scattering path operators [89, 90]. The computing time for matrix inversion scales approximately with the third power of the matrix dimension. In a fit procedure, in which several spectra are calculated for different geometries, a too big cluster, or l_{max} can make the calculation impractical. For small molecules, the ideal cluster size is usually the entire molecule, but a cluster-size analysis is still useful to identify the dependence of certain spectral features with given parts of the molecule, which allows the assignment of the XANES spectrum to specific structural parameters.

The cluster-size analysis for the six different forms of Mb studied in this thesis was done using both the `MXAN` and `FEFF9` codes. The analysis using `FEFF9` is preferred because it does not include a phenomenological treatment of the losses in the XAS spectrum, which may mask the appearance of certain spectral features. The size of the atomic cluster was varied on a shell-by-shell basis. The first shell is given by the four N atoms in the porphyrin ring, the N atom of the proximal histidine (His93) and the closest atom of the ligand (except in the case of metMb and deoxyMb), which corresponds to a FMS radius of $R_{FMS} \simeq 2.1$ Å. The second shell includes the first 8 C atoms in the porphyrin ring, the closest C atom in the Hist93 and the complete ligand, with $R_{FMS} \simeq 3.1$ Å. The third shell contains the next ring of C atoms in the porphyrin ring, giving $R_{FMS} \simeq 3.5$ Å. The fourth shell is formed by including the remaining carbon atoms in the porphyrin ring, the first N of the distal histidine (Hist64) and one more C and N of the Hist93 up to $R_{FMS} \simeq 4.35$ Å. The fifth shell, with radius $R_{FMS} \approx 5.1$ Å includes the two more C atoms from the histidines. The sixth shell is made with all the atoms inside a radius $R_{FMS} = 6$ Å . Above the sixth shell, it is not possible to define a cluster because many atoms compose the cluster, the distances between adjacent atoms increasing by > 0.2 Å. Therefore, the seventh shell is represented by all the atoms within a radius $R_{FMS} = 7$ Åfrom the Fe atom. This analysis was done using identical SCF potentials for each shell, *i.e.*, the potential was calculated using the whole atomic cluster (7 Å) and only the radius of the FMS was varied. This way, any differences between the calculated spectra are only due to MS effects.

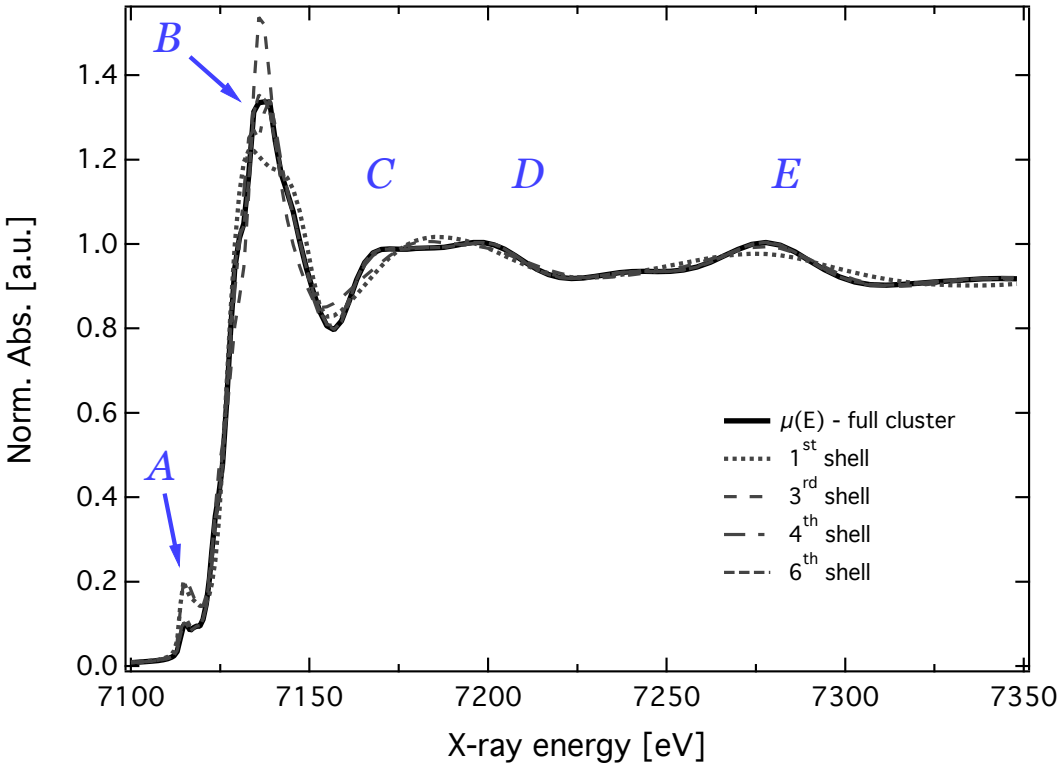

Figure 6.9.: Cluster-size analysis of the FMS calculation for MbNO. The calculation with all the other Mb forms followed the same trends. The MbNO cluster-size analysis serves as guideline for the other Mb species.

The cluster size analysis for the MbNO form is shown in Figures 6.9 and 6.10. For all six Mb forms analysed it was found that the influence of the cluster size on the spectral features followed the same trends. Therefore only the MbNO case will be discussed here, as it serves as guideline for the other Mb forms. An inspection of Figures 6.9 and 6.10 indicates that the FMS almost converges after the inclusion of the 4^{th} shell. There are minor details in the spectrum that are only completely reproduced afer the inclusion of the 6^{th} shell, *e.g.* features *A* and *B*. The differences in the spectrum calculated using the 2^{nd} and 3^{rd} shells are minimum, so only the result with the 3^{rd} are shown. The lack of a big change in including the 3^{rd} shell comes from the fact that only 4 more C atoms are present in this shell in comparison with the 2^{nd}. The same is true in the case of the 5^{th} and 6^{th} shells. The reason is that with 5 shells present, the FMS has already reached a level in which only minor changes are introduced by increasing the cluster size. A relatively big cluster (> 5 Å) had to be used so that the FMS converged. The Mb structure is very asymmetric, which makes the atomic contributions of sites far from the absorber important for the MS. On the other hand, many almost collinear (Fe-N_p-Fe-N_p-Fe) and triangular (Fe-N_p-N_p-Fe) paths are present, which are known to significantly contribute to the MS process. Figure 6.10a shows a zoom in the pre-edge region. Feature *A* only converges to its final calculated intensity after the inclusion of the

6^{th} shell, indicating that the bound-bound transitions are also affected by the size of the cluster used in the calculations. Additionally, the region between 7122 and 7125 eV seems to vary in an unusual way as more and more shells are included in the calculations. If only the 1^{st} shell is included, the general intensity is lower than that of the whole cluster calculation. Adding one more shell makes this intensity be overestimated, and as more shells are included the spectrum slowly converges to the final calculation. This unusual behaviour (intensity decrease, increase and decrease again) indicates that the ionization threshold lies in this region. Therefore, scattering paths up to 5 Å were used in the FMS routine of the calculation of the XAS spectra shown in the next sections.

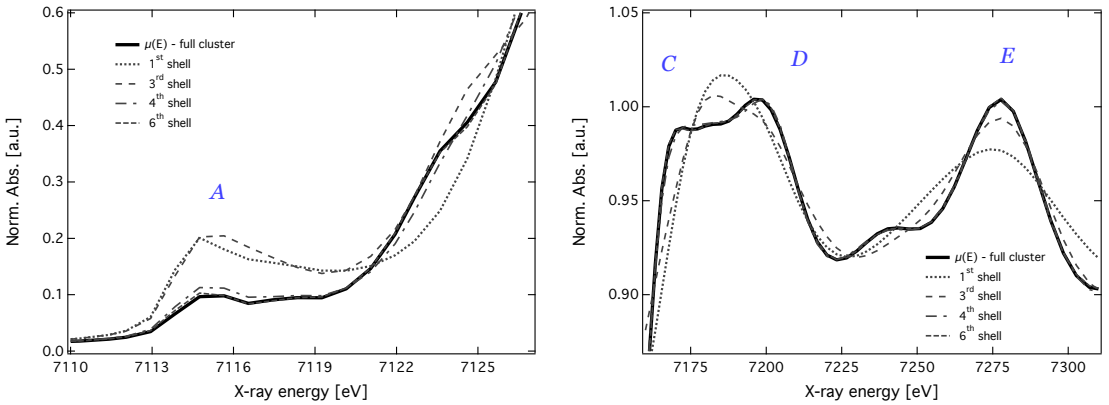

(a) Zoom in the pre-edge region

(b) Zoom in the post-edge

Figure 6.10.: Cluster size analysis of the FMS calculation for MbNO. a) Zoom in the pre-edge region, showing that the calculation only converges after the inclusion of the 6^{th} shell. b) Zoom in the post-edge region, showing the most prominent features. Note that features *C*-*E* converge more rapidly than *A*, *B*.

6.5.2. Simulation and fits of the steady-state XANES

In this section we will be show the results of the simulation and fits of the steady-state XANES of the six different Mb forms investigated in this thesis. We used as starting points, the atomic coordinates of the best resolution structures derived from crystallography available in the PDB database. The structural parametrization was performed using the set of parameters defined in Section 6.4. The calculated spectra were fit to the experimental data using the `MXAN` code. In the following we show the results of the fits for each of the Mb species studied. It starts with the two ferric Mb cases, *i.e.*, the unligated metMb and the ligated MbCN. It is then followed by the results of the ferrous Mb cases: the deligated deoxyMb and the ligated ones, MbCO, MbNO and MbO_2.

Met-Myoglobin

The result of our fits using the MXAN program are shown in Figure 6.11. We used as input structure, the atomic coordinates determined by x-ray crystallography given in the PDB entry $1BZ6$. The structural parameters used in the fit were the average bond distance between the iron atom and the nitrogens in the porphyrin ring, the displacement of the Fe from the heme plane and the distance between the proximal histidine (Hist93) and the iron atom. The metMb form is often referred to as aquo-Myoglobin or aquo-metMb due to the presence of a water molecule in the vicinity of the heme. We placed an oxygen atom in the initial position given by the crystallographic coordinates, bound to a helium atom to simulate the presence of the two hydrogen atoms in the water molecule [c]. This way, the relative coordinates of the ligand atom were also part of the structural parameters. Four non-structural parameters are used in the fits by MXAN: two associated with the width of the broadening function (as explained in Section 6.4) and two associated with the potential, the percentage of overlap of the MT radii and the zero-level of the MT potentials (V_{0imp}). A good agreement between the fit spectrum and the experimental data is found, as can be seen in Figure 6.11, which shows not only the calculated normalized XAS spectrum, but also the total cross-section $\sigma(E)$ without convolution with the broadening function. All the spectral features are present in the calculated cross-section, indicating that none of them is masked by the use of a phenomenological treatment of the losses. The cross-section also shows a pronounced peak at about -5 eV, which corresponds to the bound-bound transitions that are responsible for the A feature in the Mb XAS spectra (see Figure 6.2). Even though MXAN correctly predicts the existence of such transitions (it is seen in the cross-section by the sharp peak at ~ -5 eV) these transitions are not taken into account in the fits. The reason is two-fold, a) FMS theory using the MT approximation does not predict these transitions to occur at the correct energy with respect to the rest of the spectrum and often their intensity is incorrectly calculated, b) the broadening function, which is zero below a certain onset energy E_s automatically sets the intensity of the normalized XAS spectrum to zero in this region. A proper interpretation of these bound-bound transitions in terms of the DOS will be given in Section 6.5.4. The Gaussian part of the broadening function converged to a value $\Gamma_{exp} = 0.70$ eV, in accordance with the bandwidth of the monochromator used in the measurements. The final value of the Lorentzian part of the broadening function was $\Gamma_c = 1.52$ eV, a value slightly higher than the tabulated one for the iron core-hole lifetime (1.25 eV [94]). The fit resulted in a metMb structure with an average Fe-N_p distance of 2.027 ± 0.003 Å and the distance between the iron and the proximal histidine Fe-His$= 2.14 \pm 0.01$ Å. For the oxygen ligand position, the best fit delivers a distance Fe-O$= 2.31 \pm 0.05$ Å. Our results agree within the error with both the crystallographic and the XANES structure of D'Angelo *et al.* The structural parameters obtained in our fits of the metMb XAS spectrum are shown in Table 6.2. We also tried a model which did not include the oxygen in the position of the water molecule. The

[c] The Norman criterion to calculate the MT radii cannot be used if the cluster contains hydrogen atoms

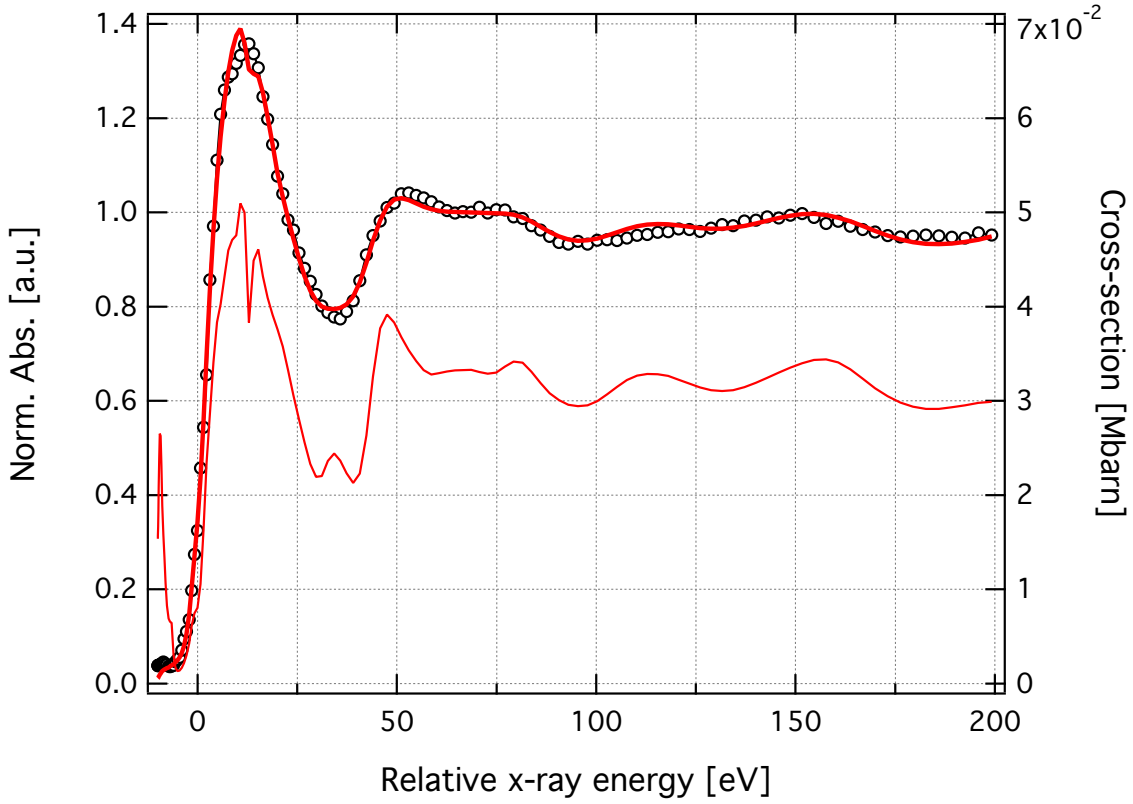

Figure 6.11.: `MXAN` best fit of the XAS spectrum (thick red line, left axis) of unligated ferric Myoglobin (metMb). Open circles are the experimental data interpolated on an energy grid as $e_i = -10 + 0.01(i-1)^2$). Also show is the calculated total cross-section (thin red line, right axis). The input atomic coordinates were taken from the PDB dtabase, entry $1BZ6$. The structural parameters resulting from the best fin are listed in Table 6.2.

resulting calculated spectrum and the convergence of the structural parameters were found to be insensitive to the presence of this oxygen atom.

Cyano-Myoglobin

Following the same philosophy as the one used to fit spectrum of metMb, we used the `MXAN` code varying the heme size (controlled by the average distance between the iron and the nitrogen of the porphyrin), the relative geometry of the CN ligand and the distance from the iron to the proximal histidine. The outer atoms of the porphyrin ring and the histidine rigidly followed the motion of the nitrogens to which they are connected, *i.e.*, no distortions of the porphyrin and histidine were taken into account. The structure obtained by Arcovito *et al.* [29], corresponding to the entry $2JHO$ in the PDB database, is used as starting point in our fits.

The final result of the MbCN structural fit using `MXAN` is shown in Figure 6.12, which includes both the fit spectrum and the total cross-section as calculated. The fit is found

to be in good agreement with the experimental data, despite the relatively low-resolution structure as input. The total cross-section contains all the features present in the data, indicating the accuracy of the calculation, while the broadening does not exclude any details in the spectrum. The broadening values resulting from the best fit are $\Gamma_{exp} = 0.60$ eV and $\Gamma_c = 1.36$ eV, which as in the case of metMb does not deviate significantly from the expected ones based on the experimental resolution (*ca.* 0.70 eV) and the Fe core-hole lifetime. The structure corresponding to the best fit had the distances Fe-$N_p = 1.99 \pm 0.04$ Å, Fe-His $= 2.058 \pm 0.003$ and the Fe-ligand (CN) bond length equals 1.92 ± 0.04 Å. The CN molecule lies almost perpendicular to the heme plane, with the angles α and β equals to $11 \pm 5°$ and $9 \pm 3°$, respectively. The CN interatomic distance was found to be 1.11 ± 0.03 Å. The resulting structural parameters of the MbCN fit are shown in Table 6.2, together with the values obtained in the literature.

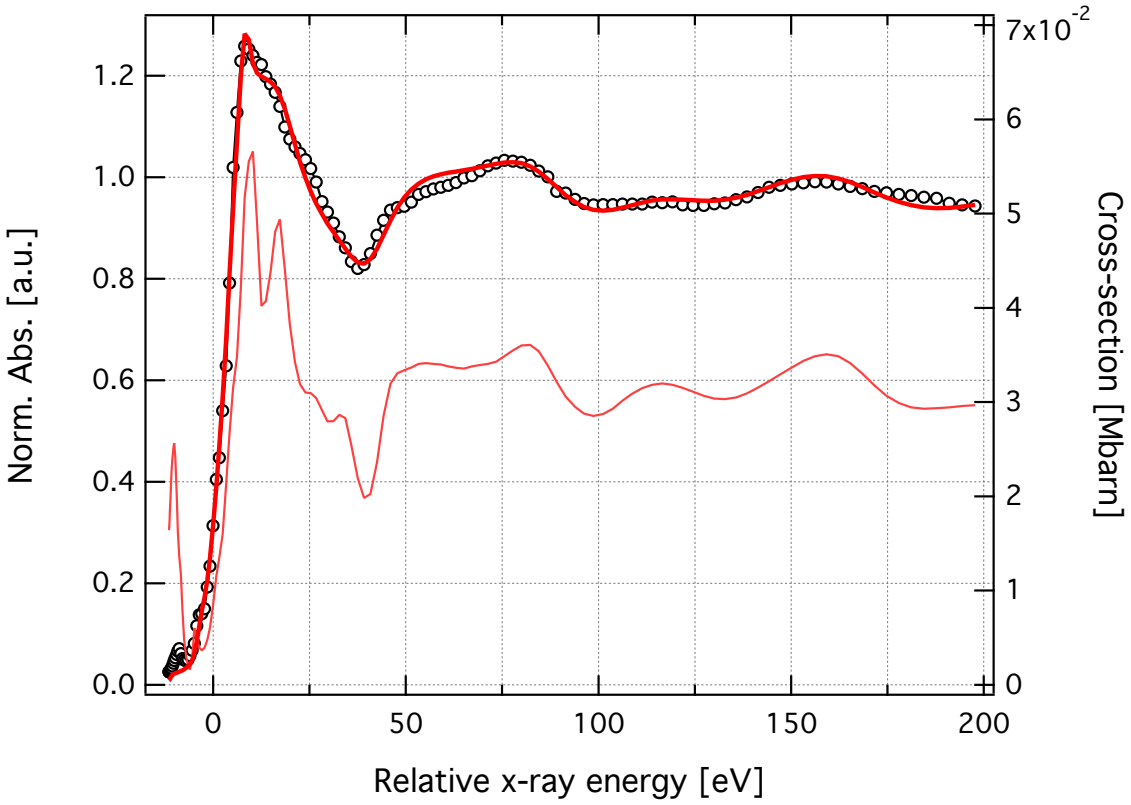

Figure 6.12.: Result of the best fit of the MbCN structure using `MXAN` (thick red line, left axis). The fit used as starting point the atomic coordinates of the PDB entry $2JHO$. Open circles are the experimental data and the thin red line (righ axis) is the total cross-section. The structural parameters resulting from the best fin are listed in Table 6.2.

Table 6.2.: Comparison of the structural parameters obtained by the MXAN fits using physiological solutions of ferric Mb (metMb and MbCN) and previous works. PDB refers to the values used as input, taken from the entries $1BZ6$ (metMb) and $2JHO$ (MbCN) in the Protein Data Bank [215]. The definition of the parameters are given in Section 6.4.

		metMb	**MbCN**
S^2		0.57	2.83
Fe-N$_p$ [Å]	PDB	2.03	2.04
	XANES†	2.01 ± 0.02	1.98 ± 0.02
	MXAN	2.027 ± 0.003	1.99 ± 0.04
Disp [Å]	PDB	0.12	0.08
	XANES†	–	–
	MXAN	0.07 ± 0.02	0.04
Fe-Li [Å]	PDB	2.16	1.92
	XANES†	2.22 ± 0.06	1.96 ± 0.05
	MXAN	2.31 ± 0.05	1.92 ± 0.04
α[°]	PDB	6	6
	XANES†	–	–
	MXAN	16 ± 4	11 ± 5
β[°]	PDB	25	13
	XANES†	–	14 ± 20
	MXAN	35 ± 1	9 ± 3
Fe-His [Å]	PDB	2.16	2.08
	XANES†	2.14 ± 0.06	2.01 ± 0.07
	MXAN	2.14 ± 0.01	2.058 ± 0.003
L$_1$-L$_2$ [Å]	PDB	1.00	1.11
	XANES†	–	1.14 ± 0.02
	MXAN	1.07 ± 0.20	1.11 ± 0.03

† XANES refers to values taken from Ref. [76].

Carboxy-Myoglobin

The results of the fit procedure for MbCO is shown in figure 6.13. The used input atomic coordinates were taken from the crystallographic studies at 1.15 Å , given in the entry $1A6G$ in the Protein Data Bank [215]. As in the case of the studied ferric forms, the fit spectrum is found to be in excellent agreement with the experimental data. The

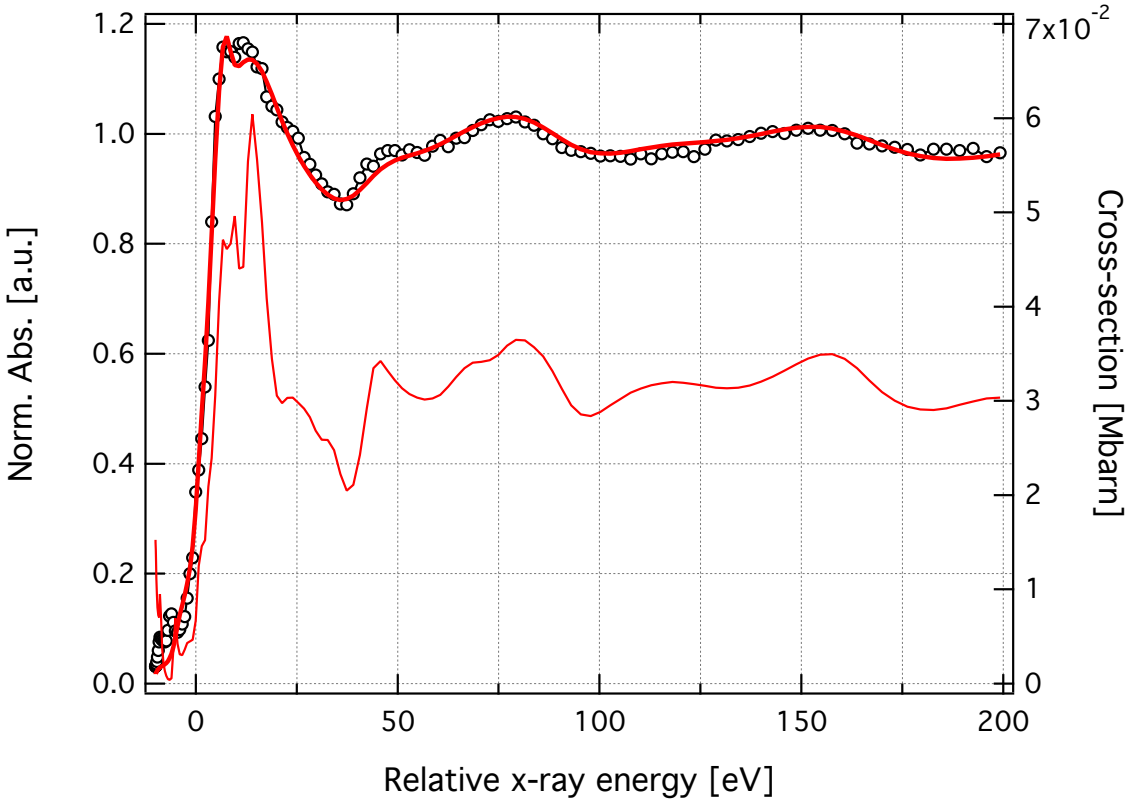

Figure 6.13.: Comparison of the MXAN best fit of the steady-state XAS spectrum of Carboxy-Myoglobin (MbCO) with the experimental data. Open circles are the experimental data and the thick red line is the fit spectrum (left axis). Also shown is the total cross-section (thin red line, righ axis), showing that all the calculated spectral features are present in the experimental data and on the fit spectrum. The structural parameters resulting from the best fin are listed in Table 6.3.

total cross-section correctly predicts all spectral features in the data, giving confidence in the analysis. The use of a phenomenological broadening to account for losses did not affect the structural parameters, which are in good agreement with the literature. The broadening parameter associated with the experimental resolution converged to $\Gamma_{exp} = 0.70$ eV, a value very close to the energy bandwidth of the monochromator used in the measurements. In the best fit, the parameter associated with the core-hole lifetime was $\Gamma_c = 1.42$eV, slightly larger than the Fe core-hole lifetime. The final structural parameters of the MbCO fit are shown in Table 6.3, together with the values used as input for comparison. The sharp features at at about -5 eV in the total cross-section calculation are not not taken into account in the MXAN fits and will be treated in Section 6.5.4 and 6.5.5. In the structure from the best fit, the Fe-N_p distance was 2.01 ± 0.01 Å, while the distance between the iron and the proximal histidine was 2.04 ± 0.02 Å. The final position of the CO molecule is 1.834 ± 0.007 Å away from the Fe atom, and the angles α and β are $22 \pm 10°$ and $5 \pm 5°$, respectively. We confirm that even in solution the CO molecule sits almost perpendicular to the heme plane.

Nitrosyl-Myoglobin

There are two different ways of preparing the solution (and crystals) of MbNO and the resulting structural details depends on the preparation method [202]. If prepared from the reaction of metMb with nitrite/dithionite, the β angle in MbNO is 36°, and the FeNO bond length of 1.87 Å. On the other hand, if the MbNO is prepared directly from the reaction of NO gas with deoxyMb, the β angle is 60° and the FeNO bond length increases to 2.13 Å. In order to prevent these structural differences, all the MbNO samples used in this thesis were prepared by the reaction of metMb with nitrite/dithionite in the absence of oxygen, according to the procedure given in Section 4.5.

The XAS spectrum corresponding to the best fit in our analysis is shown in Figure 6.14, which also shows the calculated total cross-section. The best fit spectrum is in excellent agreement with the experimental data, and apart from the feature A in the pre-edge region (see Figure 6.2), all the other features are captured by the calculation. The structure retrieved by the XAS analysis resulted in an average Fe-N_p distance of 2.010 ± 0.008 Å, and the Fe-NO bond length equals 1.82 ± 0.02 Å. The α and β angles converged to $14 \pm 5°$ and $34 \pm 1°$, respectively. Our results point to a structure similar to the ones derived by crystallography [202, 203] and analysis of polarized XANES [29]. Our results confirm the XANES analysis of Arcovito and co-workers with respect to an increased distance between the iron and the proximal histidine when compared to the crystallographic structure. In addition, we derived the iron-ligand distance Fe-NO to be 0.05-0.10 Å shorter than in previous XAS studies. The ligand bond length N-O was also found to deviate from the values reported in the literature using XAS analysis, being ~ 0.06 Å larger in our analysis.

The minimization procedure used in `MXAN` reports the correlations between the parameters used in the fit, and in the MbNO case, no significant correlation between the F-NO distance and the NO bond length was found. Therefore, these deviations can perhaps be attributed to the fact that our analysis comes from data measured in solution, while previous studies are based on data from crystals. Following the pattern of the other Mb cases, the total cross-section contains all the features present in the experimental data and the parameters of the broadening function converged to reasonable values. Γ_c, representing the iron core-hole lifetime was 1.47 eV and Γ_{exp} (representing the experimental resolution) was 0.65 eV. Moreover, we tried to account for other models of the steady-state MbNO, specifically one based on the structure reported by Copeland *et al.* [202] containing the NO ligand at about 2.13 Å away from the iron atom and with $\beta \sim 60°$, and another model in which the oxygen atom of the NO is bound to the Fe, instead of the reverse. This last model is based on the work of Nutt and Meuwly [219, 220], who used molecular dynamics simulations to propose the existence of an energy minimum in the potential corresponding to a Fe-ON binding geometry. In the first model, the NO molecule converged back to the position found in the best fit. The calculated XAS spectrum corresponding to the second model showed very little sensitivity to the flipped ligand orientation. Even though we cannot use our XAS results to exclude the

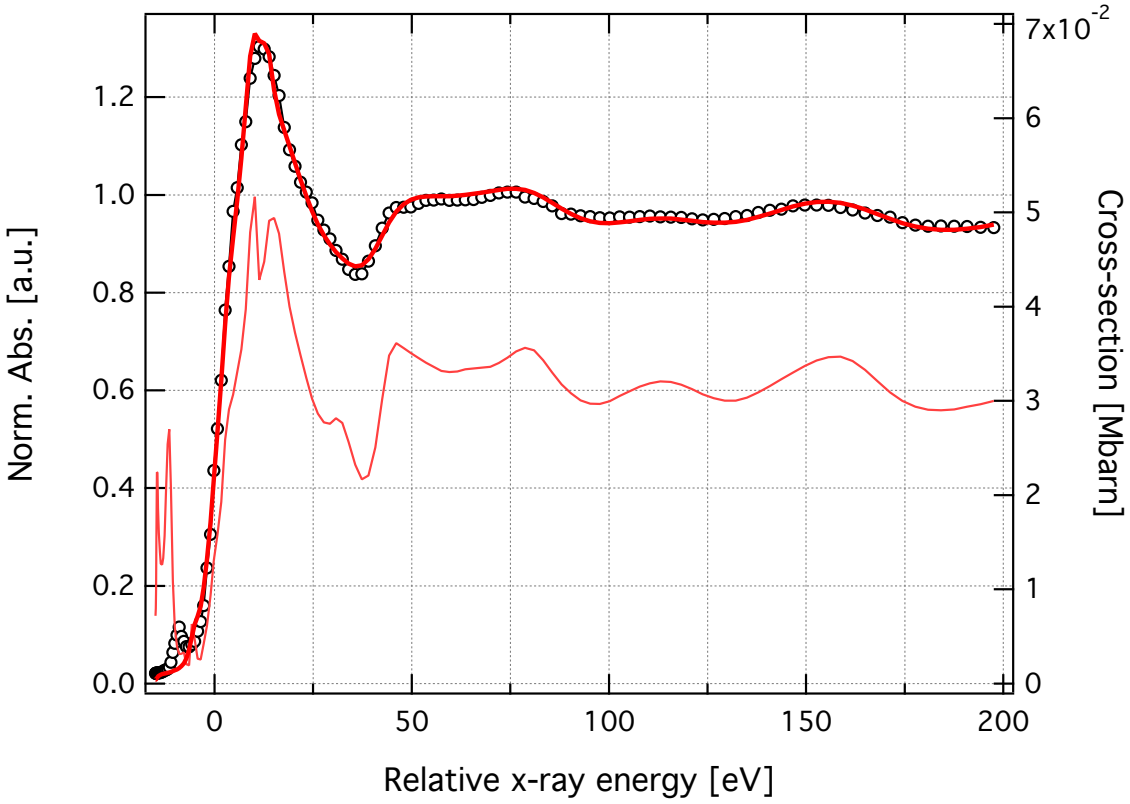

Figure 6.14.: Results of the structural analysis of the Nitrosyl-Myoglobin (MbNO) XAS spectrum using `MXAN`. The best fit spectrum is shown as thick red lines (left axis) and the experimental data as open circles. The fit used as starting point the atomic coordinates of the $2FRJ$ entry from the database. The thin red line (right axis) is the total cross-section prior to normalization and convolution with the broadening function. The structural parameters resulting from the best fin are listed in Table 6.3.

existence of an Fe-ON ligand geometry in MbNO, this represents a very shallow minimum in the potential energy surface, indicating that it corresponds to a very improbable configuration.

Oxy-Myoglobin

The crystallographic structure of MbO_2 used as input in the `MXAN` fits showed that the Fe atom lies 0.19 Å below the heme plane (in the direction of the proximal histidine). This unusual position of the Fe atom in ligated ferrous Mb is thought to be due to the low resolution of the crystal structure and partial oxidation of the sample. Therefore, in the MbO_2 fits the iron displacement from the heme plane was not allowed to vary, since the starting point is far from typical values, *i.e.*, Fe atom lying in the heme plane. Instead, we performed a series of calculations of the MbO_2 XANES spectrum, varying the Fe displacement of the heme plane in steps of 0.03 Å. Once the square residual

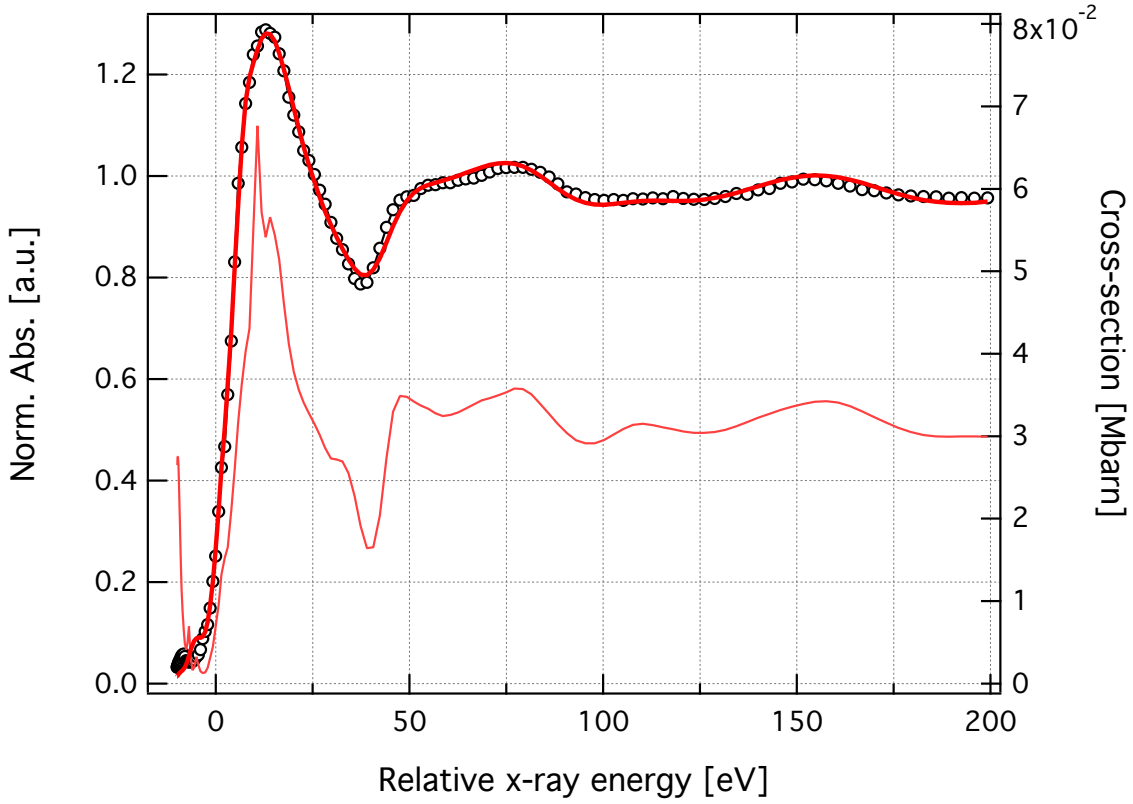

Figure 6.15.: `MXAN` best fit of the XAS spectrum of Oxy-Myoglobin (MbO_2). The fit used as starting point the atomic coordinates of the PDB entry $1MBO$. Open circles are the experimental data and the thick red line the fit to the spectrum. Also shown is the total cross-section (thin red line). The structural parameters resulting from the best fin are listed in Table 6.3.

$\mathcal{S}^2$ was found not to vary considerably when changing the Fe displacement, this value was kept constant and the complete structural fit was performed following the same procedure adopted for the other Mb cases. The XAS fit corresponds to a structure with an average Fe-N_p distance equals to 2.00 ± 0.01 Å. The Fe-O_2 and Fe-His distances being 1.909 ± 0.003 Å and 2.098 ± 0.003 Å, respectively. The O_2 molecule is found to be located almost on the same axis as the heme-normal direction ($\alpha = 3 \pm 2°$) and have a very high bending angle, $\beta = 50 \pm 4°$. The O_2 bond length converged to 1.2 ± 0.03 Å, which is the expected value of the inter-atomic distance of the oxygen molecule. The complete set of values of the structural parameters corresponding to the best fit are given in Table 6.3. The broadening parameters converged to $\Gamma_c = 1.13$ eV and $\Gamma_{exp} = 0.70$ eV. As in the previous Mb fits, the parameter accounting for the experimental resolution is in excellent agreement with the expected value based on the monochromator bandwidth. The same cannot be said of Γ_c, which is slightly smaller than the Fe core-hole lifetime (1.25 eV).

Deoxy-Myoglobin

In the fit procedure for deoxyMb, we used an oxygen atom at 3.66 Å away from the iron atom to account for a water molecule present in the crystal structure close to the heme. To account for the hydrogens on the water molecule, we placed a helium atom at 1.0 Å from the oxygen, since the use of hydrogen imposes problems in the definition of the MT radii used in the FMS formalism. All the other parameters were taken as defined in Section 6.4. The result of the fit of the XAS spectrum of deoxyMb is shown in Figure 6.16. It shows the experimental data overlaid with the fit spectrum, and also the total cross-section *i.e.*, the calculated spectrum prior to normalization and convolution with the broadening function. Following the trend of the other Mb forms, all the spectral features present in the experimental data are reproduced in the cross-section. This gives confidence in the calculations and on the retrieved structural parameters. The parameters of the broadening function were $\Gamma_c = 1.59$ eV and $\Gamma_{exp} = 0.60$ eV. As in the other fits, Γ_{exp} is in agreement with the experimental resolution and Γ_c is slightly bigger than the iron core-hole lifetime. The structural parameters resulting from our

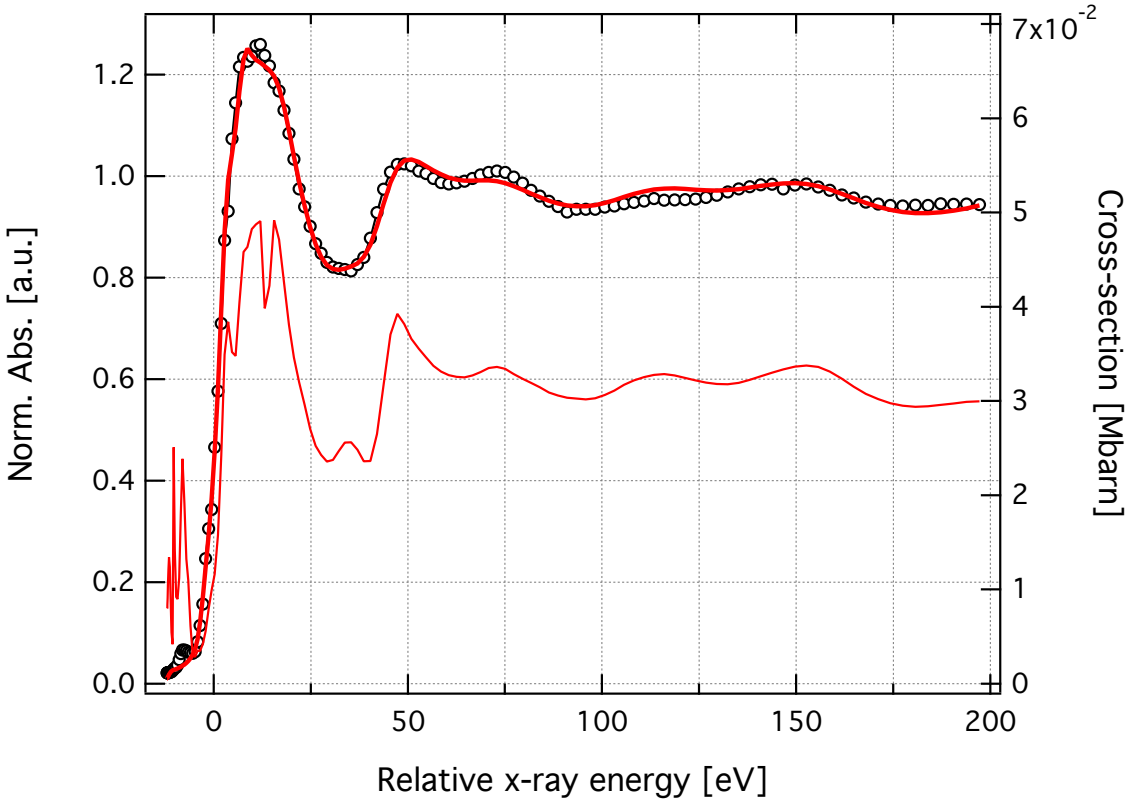

Figure 6.16.: `MXAN` best fit of the XAS spectrum of deoxyMb. The fit used as starting point the atomic coordinates of the PDB entry $2V1K$. Open circles are the experimental data and the thick red line the fit to the spectrum. Also shown is the total cross-section (thin red line). The structural parameters resulting from the best fin are listed in Table 6.3.

analysis are listed in Table 6.3. The average distance between the iron and the nitrogen atoms in the porphyrin converged to 2.075 ± 0.09 Å, and the distance from the iron to the proximal histidine converged to 2.31 ± 0.02 Å. The oxygen-helium system simulating the water molecule was at 3.75 ± 0.09 Å away from the iron atom, with the angles $\alpha = 38 \pm 5°$ and $\beta = 66 \pm 6°$. Note that the bending angle (β) for the oxygen is not defined in the case of a real water molecule. In addition, we were able to quantify the heme doming movement, which to our knowledge, has not been done in previous XAS studies of deoxyMb. The heme doming had a large influence on features *C* and *D*, which only properly matched the experimental data after introducing this distortion in the fit. The best fit to the deoxyMb XAS spectrum was achieved with Dom1 $= 0.03 \pm 0.01$ Å and Dom2 $= 0.04 \pm 0.01$ Å, which point to a highly distorted heme. For the definition of the doming parameters, refer to Section 6.4 and Figure 6.8. We have also investigated the impact of the oxygen taken as ligand in the fit of the deoxyMb XAS. The calculated spectrum obtained without this oxygen and the corresponding fit resulted in practically the same structural parameters. Hence, we concluded that the presence of a water molecule at ~ 3.5 Å away from the iron does not significantly change the XAS spectrum.

Despite the apparent similarities between the different Mb types, the relative position of the ligand (when present) varies considerably. In ferrous Mb, the α angle is $3 \pm 2°$ in MbO_2, increasing to $13 \pm 6°$ in MbNO, and $22 \pm 10°$ in MbCO. Conversely, the β angle decreases in these Mb types, going from $50 \pm 4°$ in MbO_2, to $35 \pm 1°$ in MbNO, to $5 \pm 5°$ in MbCO. In addition, the average distance between the Fe atom in the center of the porphyrin and the nitrogen atoms in the pyrrole rings has a common value of about 2 Å for all the ligated Mb species.

Table 6.3.: Structural parameters resulting from the analysis of the XAS spectra of physiological solutions ferrous Myoglobin using `MXAN`. PDB refers to the values used as input, taken from the entries $1A6G$ (MbCO), $2FRJ$ (MbNO), $1MBO$ (MbO_2) and $2V1K$ (deoxyMb) in the Protein Data Bank [215]. See text and Figures 6.7 and 6.8 for the definition of the parameters.

		deoxyMb[§]	**MbCO**	**MbNO**	**MbO_2**
S^2		1.97	1.99	2.22	0.98
Fe-N_p [Å]	PDB	2.08	1.98	2.05	1.95
	`MXAN`	2.075 ± 0.009	2.01 ± 0.01	2.009 ± 0.008	2.00 ± 0.01
Disp [Å]	PDB	0.30	0.05	0.06	0.19
	`MXAN`	0.20 ± 0.02	0.05	0.04	0.04 ± 0.03
Dom1 [Å]	PDB	—	—	—	—
	`MXAN`	0.03 ± 0.01	—	—	—
Dom2 [Å]	PDB	—	—	—	—
	`MXAN`	0.04 ± 0.01	—	—	—
Fe-Li [Å]	PDB	3.66	1.82	1.87	1.83
	`MXAN`	3.75 ± 0.09	1.834 ± 0.007	1.82 ± 0.02	1.916 ± 0.003
α[°]	PDB	31	9	11	4
	`MXAN`	38 ± 5	22 ± 10	13 ± 6	3 ± 2
β[°]	PDB	28	9	36	64
	`MXAN`	66 ± 6	5 ± 5	35 ± 1	50 ± 4
Fe-His [Å]	PDB	2.14	2.06	2.08	2.06
	`MXAN`	2.31 ± 0.02	2.04 ± 0.02	2.15 ± 0.03	2.098 ± 0.003
L_1-L_2 [Å]	PDB	1.00	1.09	1.20	1.22
	`MXAN`	1.00	1.11 ± 0.02	1.23 ± 0.03	1.20 ± 0.03

[§] The ligand of deoxyMb is taken as a water molecule

6.5.3. Structural fit of the MbNO transient XANES

In Section 6.3 we have shown the MbNO transient XAS at 50 ps (Figure 6.5). In this Section we will present the analysis of this transient spectrum based on a structural fit using the `MXAN` code. We used its unique capability to perform fits of time-resolved transient XAS data directly in energy space. `MXAN` is suitable to treat this type of data, since it is able to calculate the first 200 eV in the spectrum. This region provides the strongest signal magnitude in the XAS spectrum, and in many cases, it is the only transient signal measurable with good S/N. In the case of MbNO in solution, the magnitude of the signal was less than 2% of that of the normalized steady-state MbNO XAS. Because the signal was so small, only a limited energy range of 100 eV around the maximum of the transient XAS was measured. Even with such a limited transient XAS data, we are able to propose a model for the photo-excited MbNO at 50 ps.

The fit of the transient XAS in `MXAN` starts with the calculation of the spectrum of the sample in its ground-state, as described in Section 6.5.2. Using the atomic coordinates of the best fit shown in Figure 6.14, several transient XAS were calculated varying selected structural parameters. One of the first parameters to be checked in time-resolved XAS data is the energy shift in the spectrum due to the change in the ionization potential energy in the excited-state. Because there are many correlated parameters that can affect the determination of the ionization potential (*e.g.*, Fe displacement from the heme plane, distance between the ligand and the iron, doming of the heme), special attention has to be paid during the determination of the energy shift. In our analysis, we applied a small distortion to the MbNO structure based on the similar structure of the photo-excited MbCO [25, 29], and performed a Monte Carlo search on the non-structural parameters. More specifically, the NO molecule was moved 1.0 Å away from its position in the ground-state, and the iron atom moved ~ 0.2 Å below the heme plane in the direction of the proximal histidine. The result of this procedure is shown in Figure 6.17, which also contains the static difference spectrum (deoxyMb minus MbNO) for comparison. The square residual $\mathcal{S}^2$ was minimum for a value of the energy shift $\Delta E = 0.75 \pm 0.25$ eV, corresponding to an excitation yield of $f = 8.7 \pm 0.3\%$. This value of the excitation yield is almost 2 times larger than the estimated value based on the expected signal from the static differences shown in Section 6.3. One possible explanation for this deviation is the fact that during the energy shift determination we used only an approximate structure for the photo-excited MbNO.

Once the energy shift ΔE has been determined, we could proceed with the fits of the MbNO transient structure. Using the same set of structural parameters as in the fit of the steady-state structure given in Section 6.5.2, we performed a minimization of the square residual $\mathcal{S}^2$. The fit converged with $\mathcal{S}^2 = 0.011$, the final result of the fit MbNO transient XAS is shown in Figure 6.18. It can be seen that the fit spectrum reproduces all the features in the experimental transient data, which indicates that the proposed structure represents the photo-excited MbNO. Obviously, any features below about -5 eV are not reproduced in the fit of the transient spectrum, as this region is

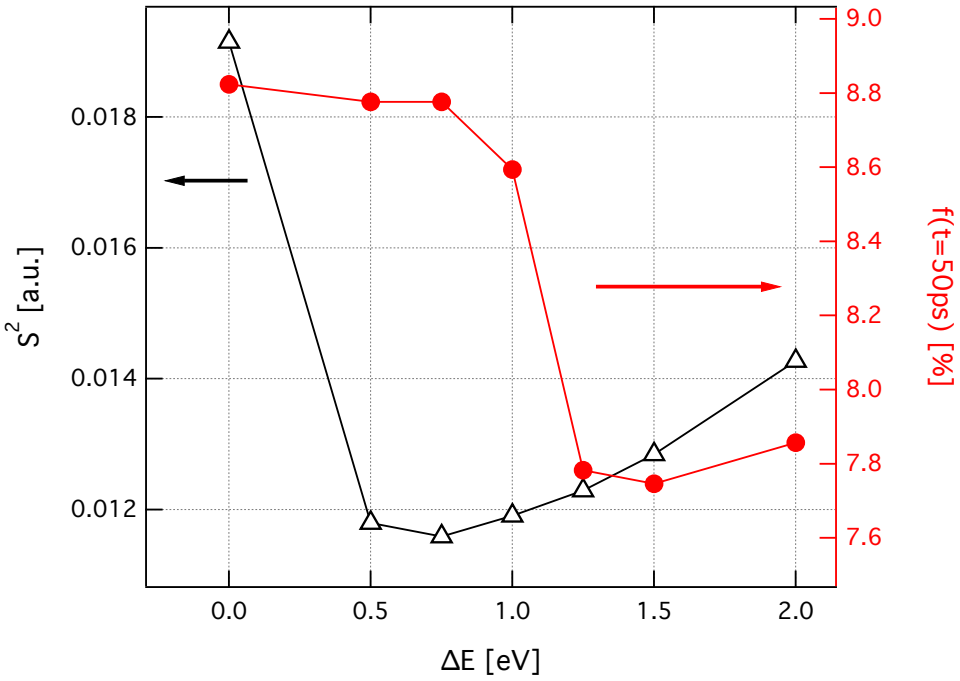

Figure 6.17.: Correlation plot between the excitation yield (f) and the square residual of the fits ($\mathcal{S}^2$) as a function of the energy shift (ΔE). The $\mathcal{S}^2$ minimization corresponds to an energy shift of 0.75 ± 0.25 eV and an excitation yield of $8.7 \pm 0.3\%$.

not accurately described by `MXAN` and was not considered in the fits of the steady-state spectra. At this point one can ask about the influence of the broadening function in the calculation of the transient spectrum. The magnitude of the signal is very small and the use of meaningless broadening parameters may lead to a wrong structure. In our fits, we first set the broadening parameters of the transient spectrum to the same values as the ones used in the ground-state case, *i.e.* $\Gamma_c = 1.47$ eV and $\Gamma_{exp} = 0.65$ eV. Once a minimum is found, the broadening parameters are allowed to vary together with the structural parameters. Their values did not vary considerably, Γ_{exp} kept its original value and Γ_c converged to 1.63 eV. The experimental resolution, associated with Γ_{exp} should be constant, independent of calculating ground- or excited-state XAS. Γ_c on the other hand, varied by about 10%. However, it does not affect the structural parameters once its value was already larger than the Fe core-hole lifetime to start with.

The final structural parameters of the photo-excited MbNO are listen in Table 6.4, together with the parameters of the deligated MbCO (referred to as Mb*CO) from Ref. [25]. The main structural changes are the NO ligand displacement away from the iron atom and the heme doming, reflected by the iron moving out from the heme plane. The NO ligand moved more than 1 Å from its initial position, being now 2.88 ± 0.09 Å away from the iron atom. This indicates that the NO molecule is no longer bound to the iron atom, *i.e.*, the NO has been photo-detached. The α and β angles did not vary considerably, since the NO ligand is already bent with respect to the heme normal in

the ground-state structure. The Fe-N_p distance increased by 0.01 Å, while the Fe moved in the direction of the proximal histidine. The distance from the heme plane to the iron atom is 0.16 ± 0.03 Å in the photo-excited MbNO, and the proximal histidine is 2.23 ± 0.07 Å away from the iron atom. The distance between the nitrogen and the oxygen in the NO molecule had little impact in the final fit results, therefore it was kept fixed in our treatment.

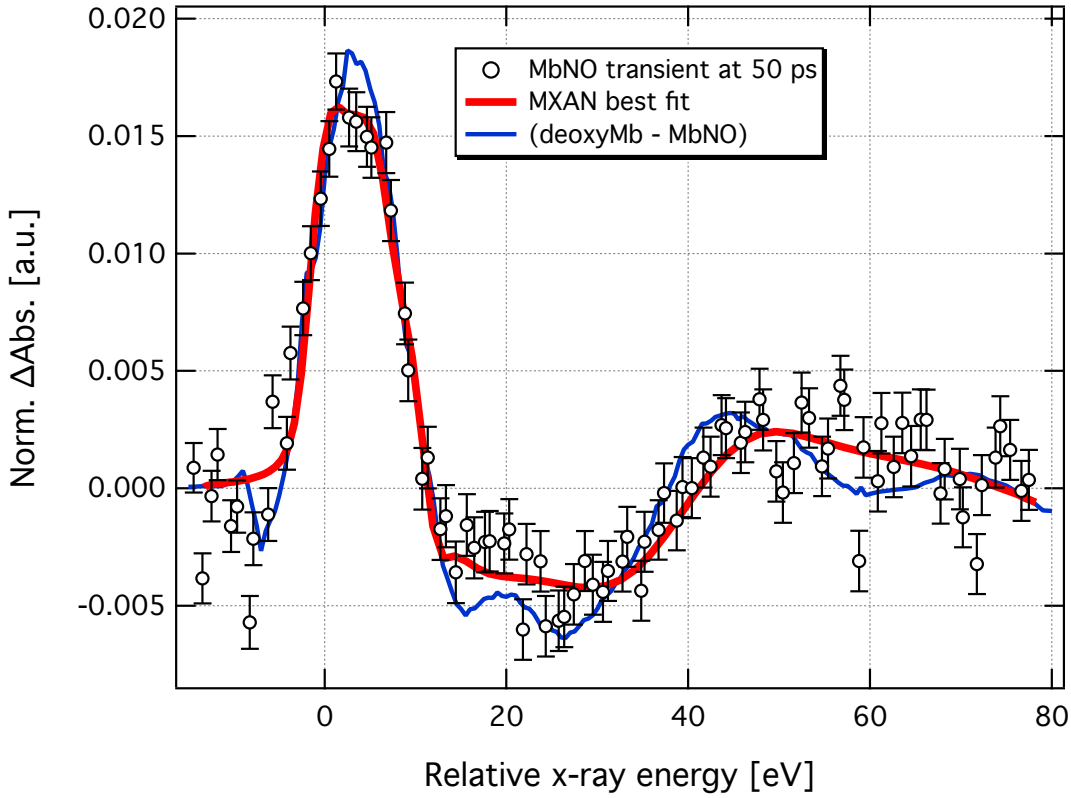

Figure 6.18.: Normalized transient XAS from a 4 mM solution of MbNO at 50 ps (black circles), together with the best fit obtained with `MXAN` (red line). Excitation was done at 532 nm, using an effective fluence of 65 mJ/cm^2. Also shown is the static difference XAS of deoxyMb and MbNO. The structural parameters obtained from the best fit are listed in Table 6.4.

Despite the fit of the transient XAS of MbNO being reasonable with only one excited species considered, we also tried to account for a second population in the fits. Kruglik and co-workers [210] proposed the existence of an intermediate species in which the NO is bound to a domed heme, with a lifetime of 30 ± 10 ps. In order to include a contribution of a domed-ligated structure of photo-excited MbNO in the analysis, we performed the same type of `MXAN` fit, but without introducing a movement of the NO molecule. The structure used corresponded to the best fit of the ground-state MbNO, with an initial doming of 0.02 Å, with the iron displaced 0.016 Å from the heme plane and the NO ligand placed at its initial position as in the ground-state (1.82 ± 0.02 Å away from the iron atom). In this fit procedure the contribution of the domed-ligated

configuration has not being weighted with respect to the pure photo-detached MbNO, *i.e*, only a pure domed-ligated configuration was taken into account. The resulting fit failed to reproduce all the spectral features and the structural parameters from this fit presented a large uncertainty compared to the best fit. This seems to point to a small sensitivity to the doming and the NO relative position, which is not the case.

Our measurements were done at 50 ps, and the relative fraction of non-planar bound species at this time should be less than 20%. A contribution of this magnitude in the transient XAS is at the limit of the S/N of our data. We believe that there may still be some contributions from a domed-ligated MbNO species in our signal, which is reflected in the fact that the NO ligand does not move as far from the iron as in the case of photo-detached MbCO, in which the CO ligand is at 3.08 ± 0.07 Å from the iron atom [25, 216].

Table 6.4.: Structural parameters resulting from the analysis of the transient XAS spectrum MbNO 50 ps after photo-excitation. Mb*NO and Mb*CO stand for the photo-detached MbNO and MbCO, respectively.

	MbNO	**Mb*NO**	**Mb*CO**[§]	**deoxyMb**[†]
Fe-N_p [Å]	2.010 ± 0.008	2.02 ± 0.02	2.03 ± 0.02	2.075 ± 0.009
Disp [Å]	0.04	0.16 ± 0.03	—	0.20 ± 0.02
Dom1 [Å]	—	0.03 ± 0.02	—	0.03 ± 0.01
Dom2 [Å]	—	0.01 ± 0.02	—	0.04 ± 0.01
Fe-Li [Å]	1.82 ± 0.02	2.88 ± 0.09	3.08 ± 0.07	3.75 ± 0.09
α[°]	13 ± 6	25 ± 4	37 ± 7	38 ± 5
β[°]	35 ± 1	39 ± 9	31 ± 5	66 ± 6
Fe-His [Å]	2.15 ± 0.03	2.23 ± 0.07	2.05 ± 0.02	2.31 ± 0.02
L_1-L_2 [Å]	1.23 ± 0.03	1.23	1.24	1.00

[§] Values from Ref. [25]. Heme doming and iron displacement out of the plane are not reported.

[†] The structural parameters of deoxyMb correspond to the best fit structure obtained with `MXAN`.

6.5.4. Bound-bound transition probed by K-edge XAS

The electronic configuration of the Fe atom in Myoglobin can be studied by analysing the pre-edge region of the XAS spectrum. The bound-bound transitions in the Fe K-edge XAS of Mb are affected not only by the oxidation state of the iron (ferric or ferrous), but also how the different diatomic ligands interact with the heme. This effect is reflected in the different peaks in the pre-edge region (A feature) which change with the form of Mb, as shown in Figure 6.3.

The relationship between the XAS spectrum and the electronic structure (Equation 3.13) allows the interpretation of the bound-bound transitions in the spectrum in terms of the local l-projected electronic density of states (l-DOS). For this purpose, we used the `FEFF9` software to calculate the XAS spectra of the different forms of Mb. The calculations were done using the FMS framework, with self-consistent potentials. Two sets of input structural coordinates were used in the calculations, one obtained from the crystal structures available on the PDB database [215] and another using the final structure obtained from the best fit from `MXAN` - results of Section 6.5.2. However, the use of the optimized structures obtained from the fits of the XAS spectra did not affect significantly the results of the density-of-states. For this reason, we will show only the results obtained using the crystallographic structure as input. The SCF (and FMS) calculations were performed using a cluster of radius 7 Å, containing a total of 79 atoms around the Fe in the center of the heme. Six different atomic species were used to calculate the potential, the iron atom (absorber), the nitrogen, carbon and nitrogen in the heme and histidines, and two more to account for the ligand (N, O, or C depending on the Mb form). This way it was possible to distinguish between the N, C or O in the ligand from those in the heme and the remaining parts of the protein cluster. The maximum value of the angular momenta basis (l_{max}) of the spherical harmonic expansion of the scattering path operators was chosen independently for each atomic species. For the iron atom $l_{max} = 3$ (including s-, p-, d-, and f- scattering states) and for the remaining atomic species $l_{max} = 2$ (including s-, p- and d- scattering states). Self-consistency was achieved after 10-13 iterations depending on the Mb form, with the exception of deoxyMb in which case the SCF loop took 18 iterations. These calculations were done considering a neutral molecule since the total charge can not be specified in `FEFF`. The spectra calculated by `FEFF9` successfully reproduces the experimental data, specifically features A^i and A^{ii} in the spectra. In the following the results of the analysis of the bound-bound transitions using the `FEFF`-calculated DOS will be presented.

Met-Myoglobin

The results of the `FEFF` calculations for metMb are shown in 6.19. It shows the Fe and porphyrin N density-of-states, and also the DOS for the oxygen atom put in the position of the water. The atomic DOS is normalized to the total DOS in order to get information about the contribution each atomic species gives to the transitions. The

calculated XAS spectrum is also shown. As in the case of $[Fe(bpy)_3]^{2+}$, the Fe d-DOS shows the splitting between t_{2g} and e_g levels. The Fe d-DOS shows a high degree of mixing with the porphyrin N d-DOS and also to a lesser extent, the Fe s- and p-DOS. Interestingly, the oxygen p-DOS also overlaps significantly with the Fe d-DOS even though it is located more than 2 Å away from the Fe. In metMb, the iron atom is in the ferric state, and the t_{2g} level is not completely full. Therefore, the transition causing the A feature should be mainly to a d level, *i.e.* $1s \rightarrow 3d(t_{2g})$. The FEFF-calculated DOS supports this conclusion, as the peak in the pre-edge region (A feature) sits right at the position of the peak associated with the $3d(t_{2g})$. The calculated spectrum successfully reproduces the A^i feature, but fails in predicting A^{ii} (see Figure 6.3). The DOS indeed shows a strong contribution of p-DOS from the water O and the porphyrin N, but no obvious transition can be attributed to the A^{ii} feature. We believe this is due to the fact that its position is very close to the ionization potential around 7120 eV. Despite the use of SCF potentials, the approximations made in the FMS theory to calculate the XAS spectrum can introduce an error of typically 2-3 eV in both the Fermi energy and the ionization potential. It should be noted that the DOS calculations in FEFF were

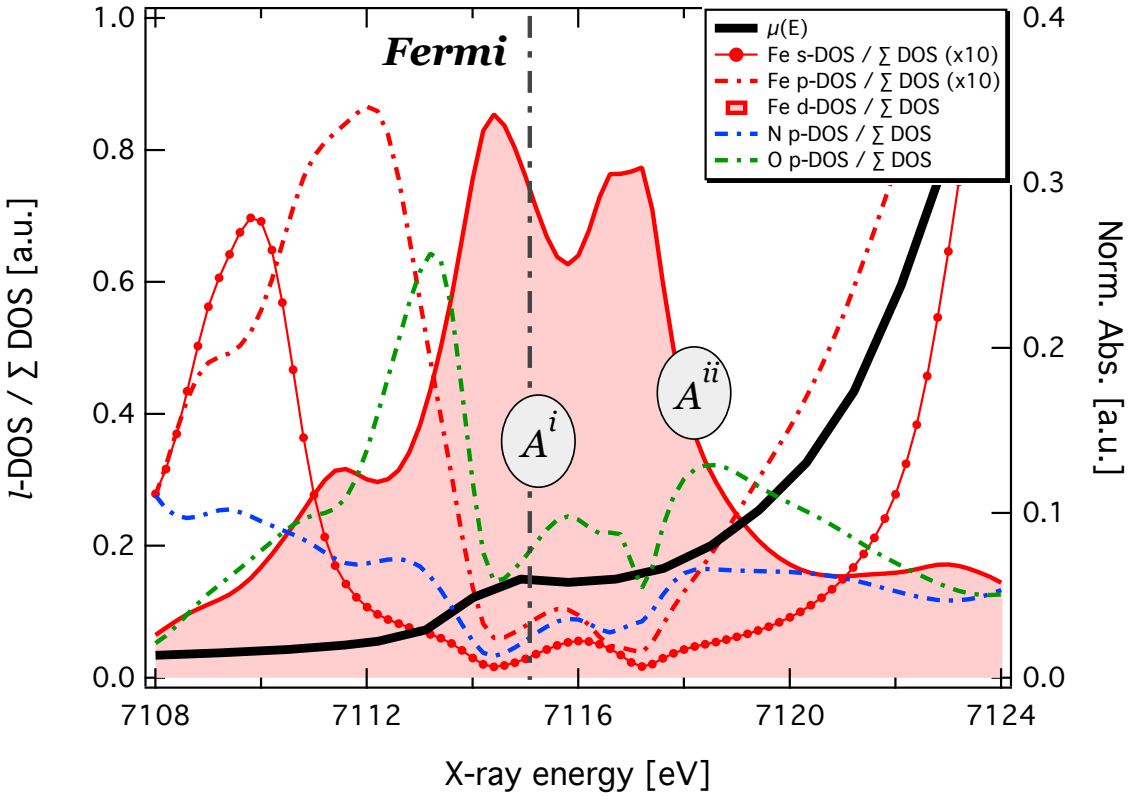

Figure 6.19.: Results of the XAS calculation of metMb using FEFF9. The DOS of the different atoms in the structure are shown (left axis). Fe is represented as red, N as blue and O as green. The calculated XAS spectrum is shown as a black line (right axis). The calculated Fermi energy is represented by a vertical dashed-dotted line.

made using the dipole approximation. The inclusion of a quadrupole term did not affect the results obtained, pointing to a dominating dipole character of these bound-bound transitions.

Cyano-Myoglobin

The results of the FEFF calculation, including the DOS, for MbCN is shown in Figure 6.20. Each atomic DOS has been normalized to the total DOS (sum of all the calculated density-of-states) to provide more information about the states contributing to each transition. It shows the DOS for the iron and the porphyrin N, and also for the carbon in the CN ligand. The calculated XAS spectrum is also shown. The splitting of the d orbitals in t_{2g} and e_g is reproduced, being more pronounced for MbCN than in metMb. In addition, the total contribution of the d-DOS to the transition causing the A^i feature is smaller in MbCN when compared to metMb. This transition also has some Fe p- and N p-DOS associated, with a very small contribution from the Fe s- and porphyrin carbon p-DOS. Furthermore, the region between the 7116 eV and 7120 eV (A^{ii} feature)

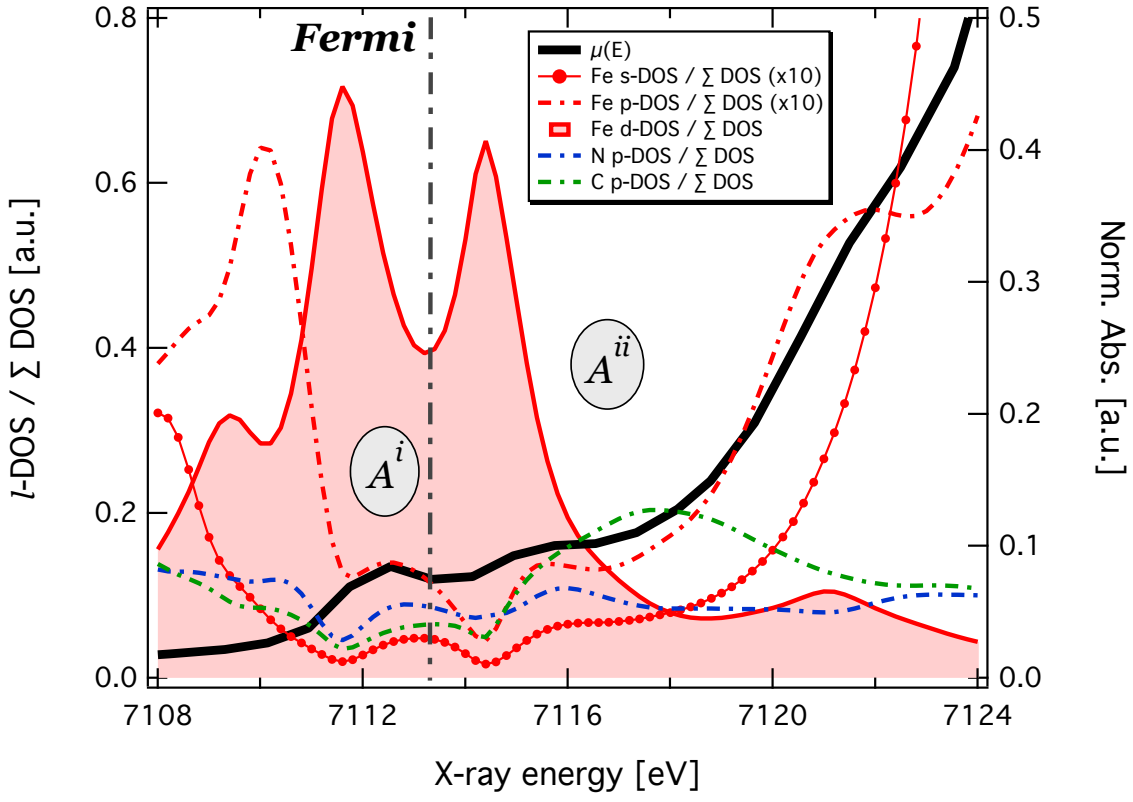

Figure 6.20.: Calculated XAS spectrum and density-of-states of MbCN using FEFF9. The atomic DOS is normalized to the total DOS. The Fe DOS is represented in red, the N in blue and the C from the CN ligand in green - left axis. The spectrum is shown as a black line (right axis). The calculated Fermi energy is shown as a vertical dashed-dotted line.

contains a large contribution from the ligand C p-DOS overlapped with the porphyrin N p-DOS, with also a small content of Fe p-DOS. However, the calculated spectrum does not reproduce the A^{ii} feature, or at least did not place it at the correct energy. We can try to interpret this transition as being due to an overlap between the Fe p and the ligand carbon and porphyrin nitrogen p orbitals. $s \rightarrow p$ transitions are dipole-allowed, and this mixing increases the p character of the orbitals, giving some intensity to the transition. In these calculations, only dipole terms were taken into account. Therefore, the hypothesis of the A^{ii} feature being caused by a transition to p states is justified. There is a weak transition to an Fe p-DOS at 7120-7122 eV, which is dipole-allowed and should correspond to a feature in the XAS spectrum. However, the interpretation of this transition (and any others above it) in terms of a density-of-states analysis is risky. The ionization potential is calculated to be around 7122 eV in MbCN and if we recall that the MT potential contains several approximations, we will not attempt such interpretation.

Carboxy-Myoglobin

The calculated DOS for MbCO is shown in Figure 6.21. This figure contains the s-, p-, and d-DOS for the iron atom, and the p-DOS for the porphyrin nitrogen and for the carbon of the CO ligand. All the atomic DOS have been normalized to the total density-of-states. Also shown is the calculated XAS spectrum, which successfully reproduced the double peak in the pre-edge region. In the calculations of the MbCO spectrum, only dipole contributions were included. Quadrupole transitions played little role in the `FEFF` calculations, thus they were excluded from the current analysis. It can be seen that features A^{i} and A^{ii} are dominated by the Fe d-DOS, but also contain the expected overlap with the porphyrin N and the ligand C p-DOS. The first peak in the spectrum, feature A^{i}, comes from the Fe d-DOS, with a big contribution from the porphyrin p- and a smaller one from the Fe p-DOS. Feature A^{ii} also has a dominant Fe d origin with some overlapped Fe p- and N p-DOS, but contrary to the A^{i}, it also has a big contribution from p-DOS of the ligand C.

At higher energy, between 7120 eV and 7122 eV lies another feature which we labelled as A^{iii}. It arises mainly due to the nitrogen and carbon p-DOS, with a small contribution from the p-DOS of the iron atom (in Figure 6.21 the Fe s- and p-DOS are multiplied by 10 for clarity). We then attribute the A^{iii} feature to a transition Fe $1s \rightarrow p$ from the porphyrin N and the ligand C. At this point, an interpretation of the energy splitting of the t_{2g} and e_g levels is ambiguous and will not be attempted. Moreover, above 7122-7123 eV is the continuum level and the spectral features may have a MS origin.

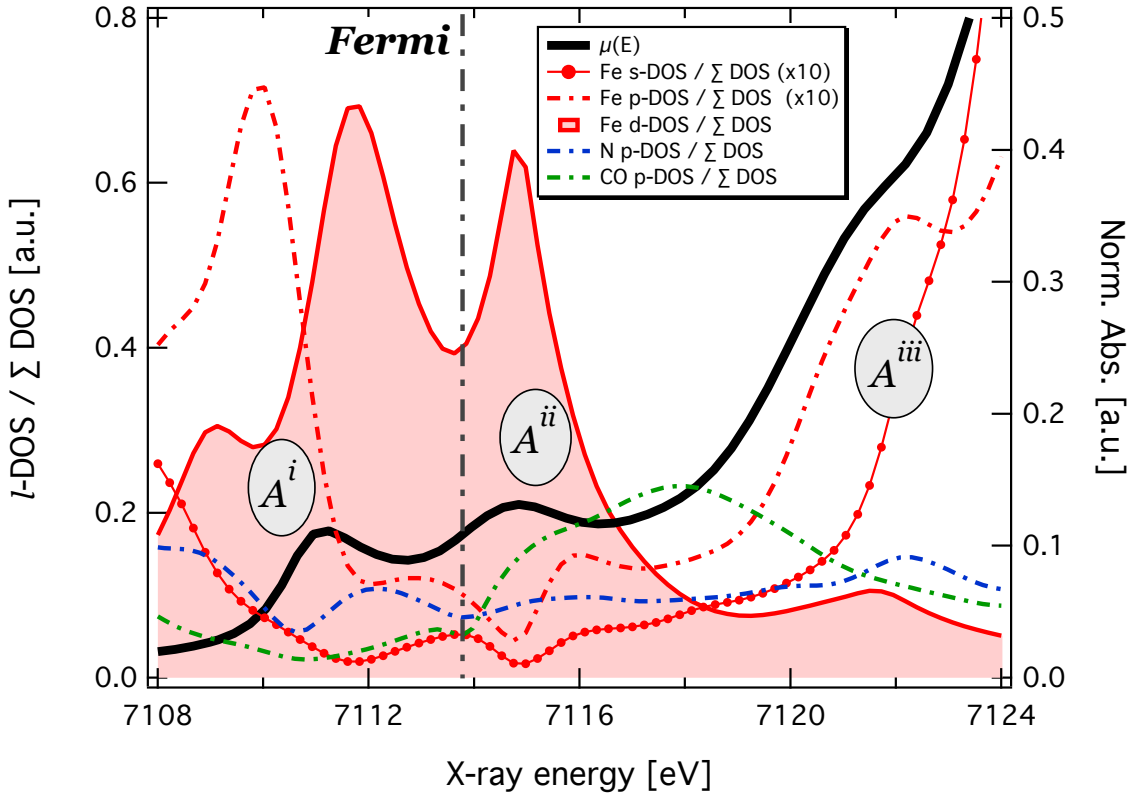

Figure 6.21.: Results of the calculation of the XAS spectrum of MbCO using FEFF9. The DOS of the different atomic species are shown (left axis). Iron is represented as red, porphyrin N as blue and the C from the CO ligand by green. The XAS spectrum is shown as a black line (right axis).

Nitrosyl-Myoglobin

Figure 6.9 contains the results of the FEFF calculations of the XAS spectrum of MbNO. It also shows the DOS of the several atomic species; containing the Fe *s*-, *p*-, and *d*-DOS and the porphyrin N *p*-DOS. The atomic DOS were normalized to the total (summed) DOS so as to account for the relative contribution each atomic species makes to the transitions investigated. FEFF allows to distinguish between the same atomic species in different environments in the potential calculation. This distinction is specially relevant for MbNO, in which the four N of the pyrrole rings in the porphyrin are different from the N in the NO ligand. In this calculation, only dipole terms were included since the quadrupole contribution proved to have little effect on the specrtum. The A^i feature in the MbNO spectrum is, as expected, predominantly due to transitions to the Fe *d* orbital. This feature also contains some contribution from the Fe *p*-DOS and the ligand N *p*-DOS. The porphyrin N does not contribute significantly to the A^i feature because it is further away from the iron compared to the N in the NO ligand (the distances are Fe-NO $= 1.82 \pm 0.02$ Å and Fe-N_p $= 2.009 \pm 0.008$ Å). At 7116 eV there is a strong, localized peak in the ligand N *p*-DOS, overlapped with the porphyrin N *p*- and the Fe *p*-

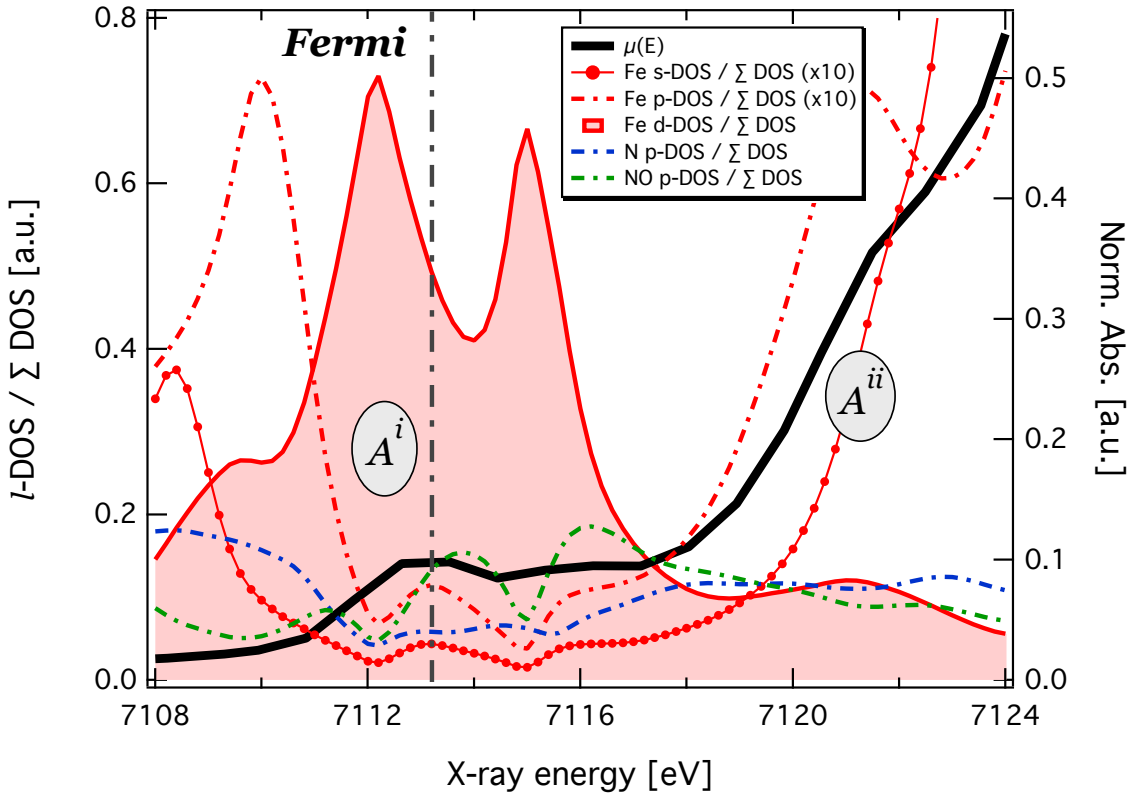

Figure 6.22.: Density-of-states of the atomic species in MbNO calculated using FEFF9 (left axis). The iron DOS are represented in red, from the porphyrin N in blue, and the DOS from the nitrogen in the NO ligand in green. The calculated XAS spectrum is shown as the black line (right axis).

DOS. This indicates that a peak in the XAS spectrum should exist, but it is not obvious in our data. It can be a Fe $1s \rightarrow$ N p transition (including the N of the ligand and the porphyrin), which gained intensity due to the hybridization with the Fe p orbital. It is, however, a very weak feature and it is not clear in the experimental spectrum. At about 7121 eV we see a relatively strong peak in the Fe p-DOS, which at first glance indicates it is a Fe $1s \rightarrow 4p$ transition. A closer look indicates the presence of some porphyrin and ligand nitrogen p-DOS. There is substantial mixing between all these orbitals, which makes this transition dipole allowed and it indeed appears in the spectrum (it is labeled as A^{ii}). In addition, we have previously shown that the ionization potential of MbNO is located at about 7122 eV (see Section 6.5.1), thus confirming that the A^{ii} is still a bound-bound transition. It is tempting to assign the double peak in the Fe d-DOS to the t_{2g} and e_g levels. However, the calculated spectrum shows that the a big part of the A^i feature lies below the Fermi energy and its intensity seems to mainly be due to the first peak in the Fe d-DOS (a t_{2g} level). We believe this does not represent reality in face of the typical errors of 2-3 eV in the Fermi energy calculations using SCF approach. Furthermore, a simple picture of a Fe $1s \rightarrow 3d$ bound-bound transition is oversimplified

in face of the huge hybridization between the orbitals of the iron and its first neighbours.

Oxy-Myoglobin

The results of the the FEFF calculation, including the DOS, for MbO_2 are shown in figure 6.23. The calculations were performed considering only dipole transitions. Including quadrupole terms in FEFF did not change the calculated spectrum and thus were ignored in our analysis. In common with the calculations of the other Mb forms is the qualitative splitting of the d DOS, which dominate the transitions causing feature A^i. This feature contains a rather complicated mixture of many DOS, specifically the p-DOS of the ligand O. The p-DOS of the iron, porphyrin N and ligand O are relatively broad peaks around the region of the A^i feature. In addition, the N and O p-DOS are slightly shifted from the position where A^i occurs. A^i is centered at 7113 eV, while the O p-DOS center is at about 7115 eV. This seems to indicate that another feature is present in the XAS spectrum at 7115 eV, but it is not observed in the experimental data. Following the trend of the other ligated ferrous Mb, at higher energies there are a multitude of peaks in the DOS. At 7116-7118 a big overlap between the iron, porphyrin nitrogen and ligand

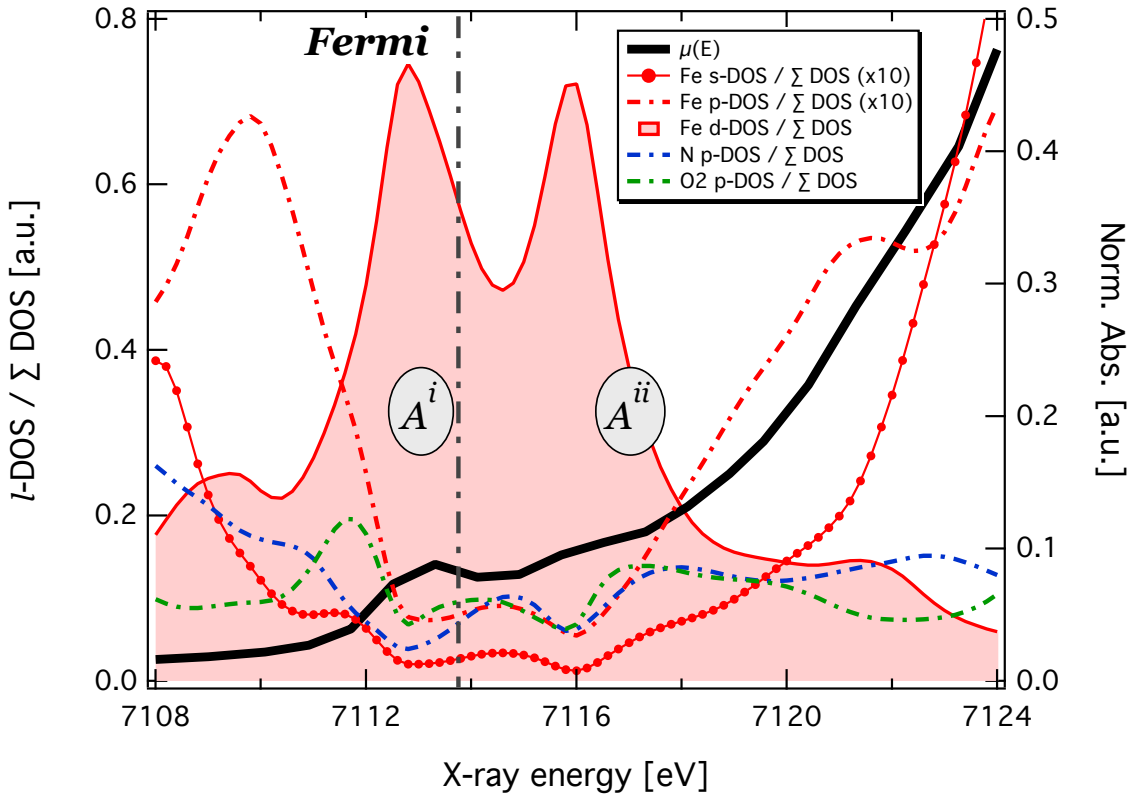

Figure 6.23.: Results of the calculation of the XAS spectrum of MbO_2 using FEFF9. The DOS of the different atomic species are shown (left axis). Fe is represented as red, the N in the porphyrin as blue and the oxygen in the ligand as green. The calculated spectrum is shown as a black line.

oxygen is found, which we attribute to be the origin of feature A^{ii} in the spectrum. At 7120 eV there is a relatively strong peak in the Fe p-DOS and some non-localized N and O p-DOS. However, no feature is observed in the experimental data, indicating that the p character induced by the hybridization with the Fe p orbital is not sufficient to make this transition dipole-allowed. In addition, the ionization potential is at about 7122 eV, so any features above this energy are attributed to MS effects.

Deoxy-Myoglobin

The deoxyMb represents the most challenging of the all Mb forms studied in this thesis, not only experimentally but also in the analysis process. The proper modelling of the heme doming and the unusual 5-coordinated environment of the iron makes the interpretation of the spectrum a non-trivial task. Figure 6.24 shows the results of the calculation of the XAS spectrum of deoxyMb using `FEFF9`. It shows the density-of-states of the different atomic species present in deoxyMb, as well as the calculated XAS spectrum. In this calculation, we have used the atomic coordinates of the crystallographic

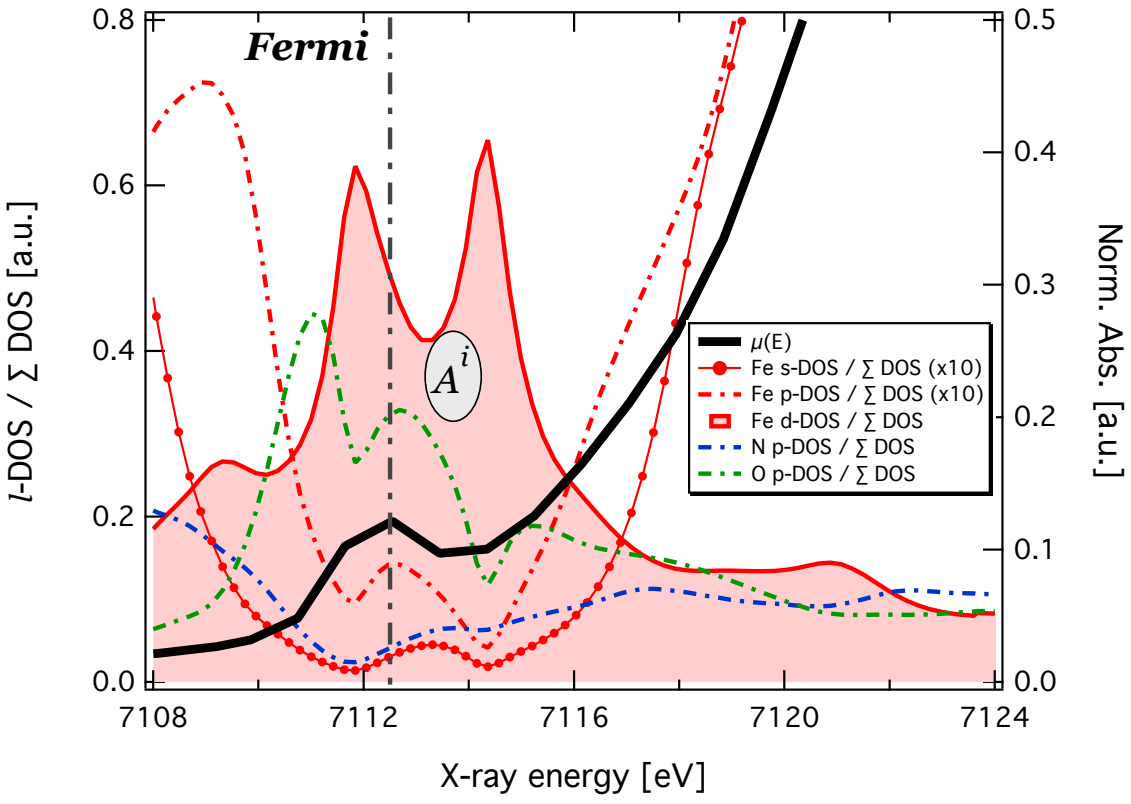

Figure 6.24.: Density-of-states of the atomic species in deoxyMb calculated using `FEFF9` (left axis). The DOS of each species has been normalized to the total DOS. The iron contribution is shown in red, from the porphyrin N in blue and the ligand oxygen (representing the water molecule) in green. The calculated XAS spectrum is shown as the black line (right axis).

structure from the entry $2V1K$ in the PDB data base. Despite our structure from the best fit from `MXAN` deviating significantly from the crystal structure, mainly in the Fe displacement from the heme plane and the distance from the iron to the proximal histidine, the spectrum calculated by `FEFF` showed little difference when using either of the two structures. The A^i feature was successfully reproduced in the calculation. As expected, it has a dominant Fe d character, with a very strong contribution from the ligand oxygen p-DOS. This oxygen contribution to the transition is surprising, since it is more than 3.5 Å from the iron atom. To a lesser extent, the porphyrin N and the Fe p-DOS also contribute to the transitions causing A^i. In the calculated spectrum, the A^i is narrower than in the experimental. However, at 7115 eV a second peak in the ligand oxygen p-DOS is found, with an increased contribution of the porphyrin d-DOS. In our view, this second O p-DOS can account for a broad A^i feature. At higher energies, the calculated spectrum fails to reproduce the shoulder in the data (located at 7118 eV), despite the significant nitrogen and oxygen p-DOS, and the Fe s- and p-DOS. Above 7118 eV, no clear peak in the DOS is found. The oxygen of the water molecule said to be the ligand is so far from the iron atom that no significant overlap between the p orbitals is achieved so to promote a dipole-mediated transition.

The DOS as calculated by `FEFF9` reproduced the subtle features present in the pre-edge region iron K-edge XAS of the different forms of Myoglobin. We showed that, despite the $1s \rightarrow 3d$ transitions in the iron atom being the main reason for the presence of these features, the hybridization between the Fe d- and the ligands p- (N of the porphyrins) orbitals influence the bound-bound transitions causing the pre-edge features. The Fermi energy is not accurately calculated by the FMS formalism using the MT approximation, even when SCF is applied to calculate the potentials. Deviations of 2-3 eV are typical, therefore the position of the Fermi energy should not be interpreted quantitatively.

6.5.5. Pre-edge region: TDDFT results

Despite the valuable information provided by the analysis of the calculated DOS, *i.e.*, the pre-edge features in the XAS spectra of the different forms of Mb are caused not only by Fe $1s \rightarrow 3d$ transitions, but also by transitions to the ligands, it is clear that a finer treatment of the origin of the transitions causing the features in the pre-edge region of the XAS spectra is needed. With this goal we performed a series of Time-dependent density functional theory (TDDFT) calculations of the K-edge XAS spectrum of the different forms of Mb using the ORCA quantum chemistry package [195, 196]. The interaction with the x-ray field was described using the electric quadrupole approximation. The input atomic coordinates were taken from two different sources: the same crystallographic structure from the PDB entries used to calculate the steady-state XAS in Section 6.5.2 and the final coordinates resulting from the `MXAN` fit procedure. In all cases the use of the `MXAN` best fit structure resulted in a better description of the spectral features. The TDDFT-calculated spectra were convoluted with a Lorentzian function having 0.70 eV FWHM to simulate the experimental resolution and thus provide a bet-

ter comparison with the experimental data. A shift of 50-53 eV was applied to the calculated spectra so as to match the experiment. All the calculations were performed considering a neutral molecule and including the hydrogens. The ionization potential energy was calculated as the absolute energy difference between the calculated spectrum using the neutral molecule and the one using the molecule without one electron. Only the results of the ferrous Mb will be shown in this thesis.

Carboxy-Myoglobin

The result of the TDDFT calculation of the XAS spectrum of MbCO are shown in Figure 6.25. We observe the formation of the double peak around 7115 eV, corresponding to features A^i and A^{ii}. These features contain transitions that are predominantly Fe $1s \rightarrow$ porphyrin N, with some Fe 3d orbital mixing and a small contribution from the N of the proximal histidine. Feature A^{iii} at about 7120 eV is mainly Fe $1s \rightarrow$ porphyrin N, which contains a considerable amount of hybridization with the Fe p. Therefore, these orbitals have a strong p character and the transitions causing A^{iii} are dipole-allowed. In addition, quadrupole effects play a significant role in the appearance of some of these transitions. The ionization potential was calculated to be at about 7122 eV, hence no

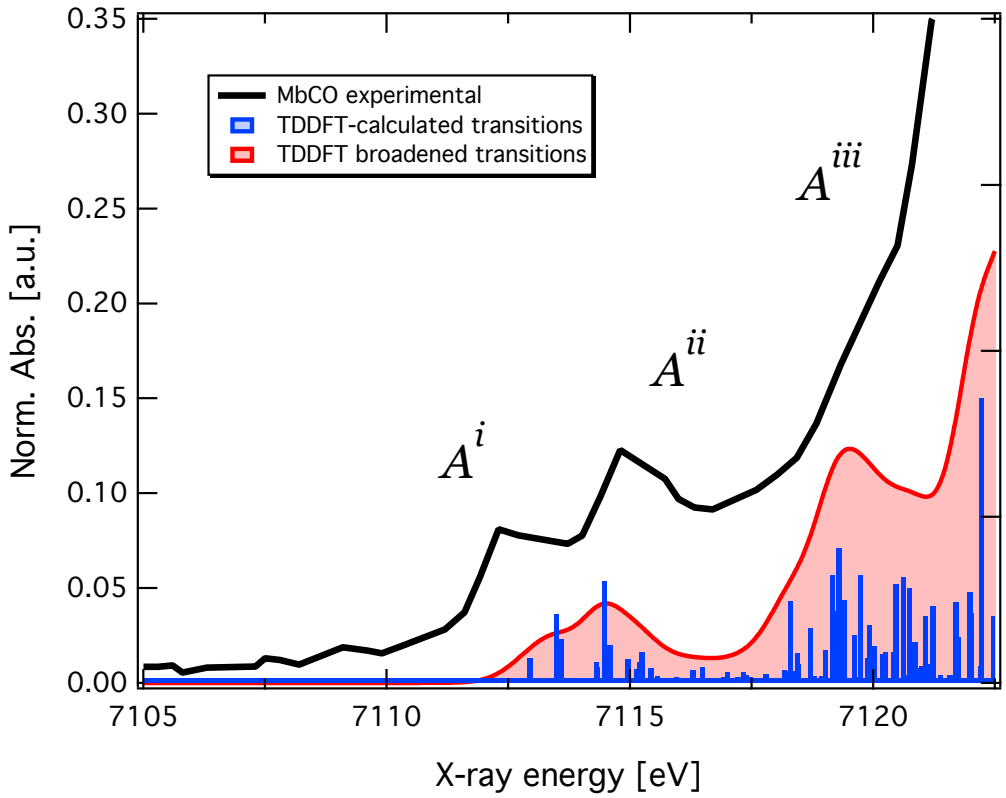

Figure 6.25.: XAS spectrum of MbCO calculated by TDDFT. Blue bars are the calculated transitions, the red curve represent the broadened transitions (convolution with a Lorentzian function with 0.7 eV FWHM). The black line is the experiment.

attempts of identification of the transitions above this energy are made.

The results of the TDDFT calculations of the MbCO spectrum supports our previous interpretation of the origin of the transitions causing A^i-A^{iii} based on the density-of-states. It confirms that a simple picture consisting of a $1s \rightarrow 3d$ transition is not sufficient to describe the features in the pre-edge region of the XAS spectrum. The position and intensity of these features strongly depend on the amount of orbital hybridization between the orbitals of the iron and its closest neighbours.

Nitrosyl-Myoglobin

Figure 6.26 contains the XAS spectrum of MbNO as calculated by the TDDFT procedure described previously. It successfully predicts the single peak at 7113 eV (feature A^i), which is an iron $1s \rightarrow 3d$ transition that appears predominantly due to quadrupole contributions to the spectrum. There is a significant degree of mixing between the iron d and the ligand N p orbitals, but no hybridization with the proximal histidine orbitals. This can be explained by the fact that, in MbNO, the proximal histidine is further away from the Fe compared to MbCO. Hence, not as many states are available

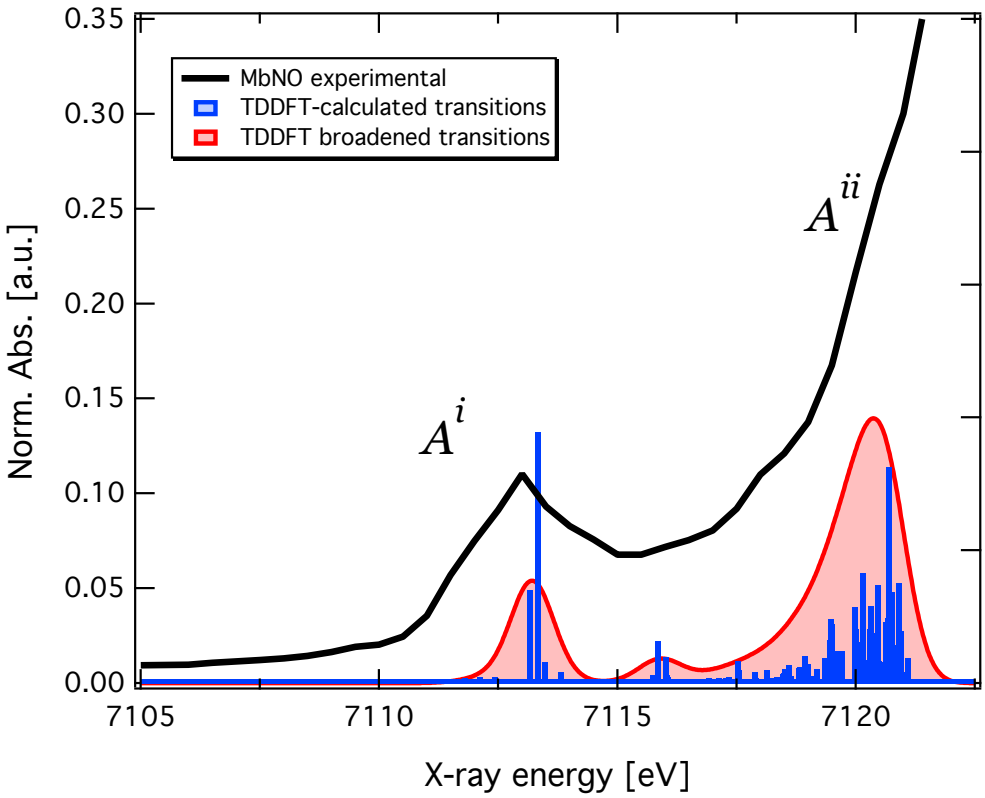

Figure 6.26.: TDDFT calculation of the XAS spectrum of MbNO. The blue bars are the calculated transitions, the red curve represent the broadened transitions (convolution with a Lorentzian function with 0.7 eV FWHM). The black line represent the experimental data.

for the quadrupole-mediated transitions, resulting in a single sharp peak in the pre-edge region. The TDDFT calculations also reproduce the feature at 7116 eV seen in the DOS analysis. We previously did not try an assignment of this feature due to its complicated interaction between several different atomic DOS. The TDDFT shows that it also arises from a $1s \rightarrow 3d$ transition in the iron atom, mixed with the orbitals of the N in the porphyrin ring. At higher energies, sits the A^{ii} feature, centered at 7120 eV. It has the same origin as the A^{iii} feature in MbCO, *i.e.*, it is a dipole-mediated transition between the Fe $1s$ and several porphyrin nitrogen orbitals. It has a strong p character due to the mixing with the Fe p orbital. The ionization potential energy was calculated to be at about 7122 eV. Above the A^{ii} feature, all the transitions are to the continuum level.

The TDDFT calculation of the XAS spectrum of MbNO confirms our previous analysis of the transitions based on the DOS, showing that the pre-edge features in the spectrum are not only due to Fe $1s \rightarrow 3d$. In addition, it provides a more detailed picture of the transitions contributing to the features in the pre-edge region of the spectrum. It also allowed the identification of a subtle spectral feature, that was not obvious in the spectrum. The big mixing between the d-orbitals of the iron and the hybridized orbitals of the porphyrin N contribute to the rich spectrum of transitions, even when a first look indicates it is a simple one-peak feature.

Oxy-Myoglobin

The calculation of the MbO_2 XAS spectrum using TDDFT is shown in figure 6.27. It reproduces the A^i feature at 7113 eV and, surprisingly, indicates the presence of two other features just above it, that are not clearly distinguished in the experimental data. We have labelled these features as $A^{i'}$ (at 7114 eV) and $A^{i''}$ (at 7116 eV). The A^i feature is due an Fe $1s \rightarrow 3d$ transition, with a small mixing with the porphyrin N orbitals. It has the same origin as the other A^i features in MbCO and MbNO. The $A^{i'}$ and $A^{i''}$ features also contain transitions from the Fe s- to the $3d$- orbitals, with an increasing contribution of transitions to the N ligands as the energy increases. This can be seen by the increased number of transitions in these features when compared to A^i. At 7120 eV we find the A^{ii} feature which is dominated by Fe $1s \rightarrow$ porphyrin N transitions. The calculated energy of the ionization potential was around 7122 eV, thus any transitions above A^{ii} are not bound-bound.

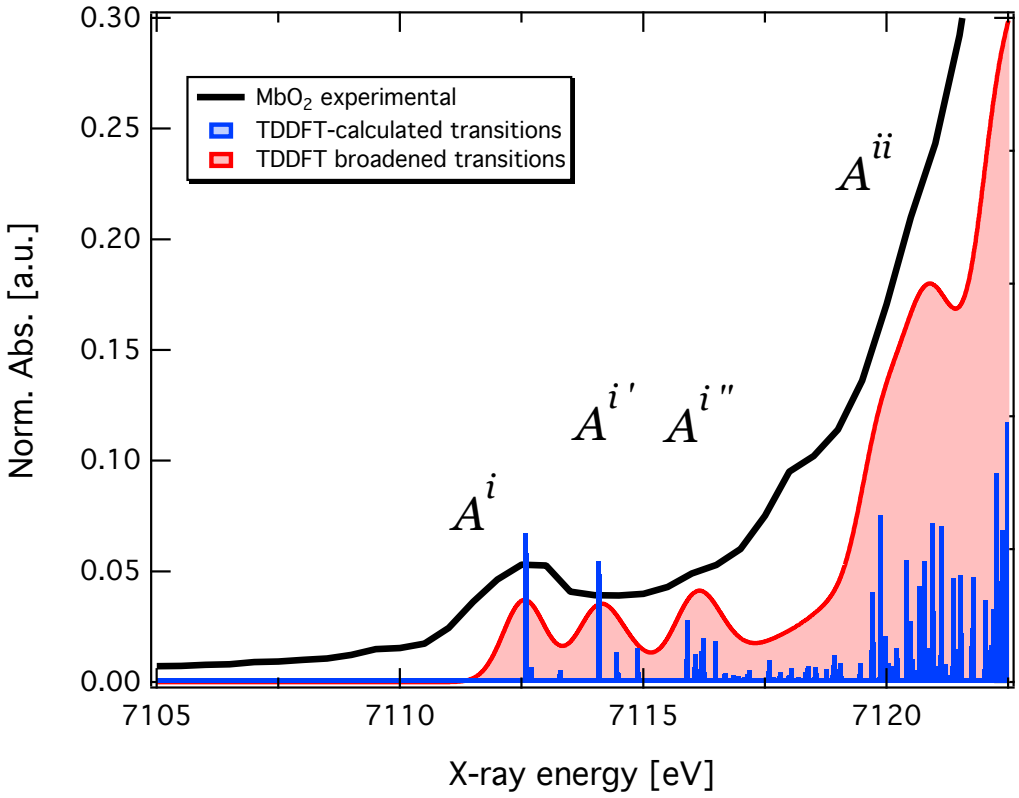

Figure 6.27.: TDDFT calculation of the XAS specrtum of MbO_2. The blue bars are the calculated transitions, the red curve represent the broadened transitions. The black line represent the experimental data.

Deoxy-Myoglobin

The results of the TDDFT calculation of the XAS spectrum of deoxyMb are shown in Figure 6.28. They show the expected broad feature A^i and also indicate the presence of two additional ones, A^{ii} at around 7115 eV and A^{iii} at 7120 eV. These last two features were not seen in the DOS analysis, which only points to a broad contribution of the oxygen and porphyrin N p-DOS. The TDDFT indicates that A^i is mainly due to iron $1s$-$3d$ transitions, which are dominated by quadrupole terms. A rather complicated mixing of the Fe d- and the porphyrin and proximal histidine N p-orbitals is present. Transitions between the Fe $1s$ and several mixed orbitals in the nitrogens from the porphyrin are the main contributors to the A^{ii} feature. This mixing gives a certain p character to the transitions, which then become dipole-allowed. Feature A^{iii} also originates predominantly from dipole-mediated transitions between the Fe $1s$ and mixed orbitals on the nitrogens in the porphyrin. It also contains contributions from mixed orbitals of the porphyrin and the histidine, which results in a large number of allowed transitions and thus a high intensity.

Our TDDFT results provided a detailed picture of the transitions responsible for the pre-edge features in the XAS spectrum of deoxyMb. The DOS analysis could only unambiguously identify the A^i, while TDDFT gives a more complete view of the interaction between the iron d and nitrogen and oxygen orbitals.

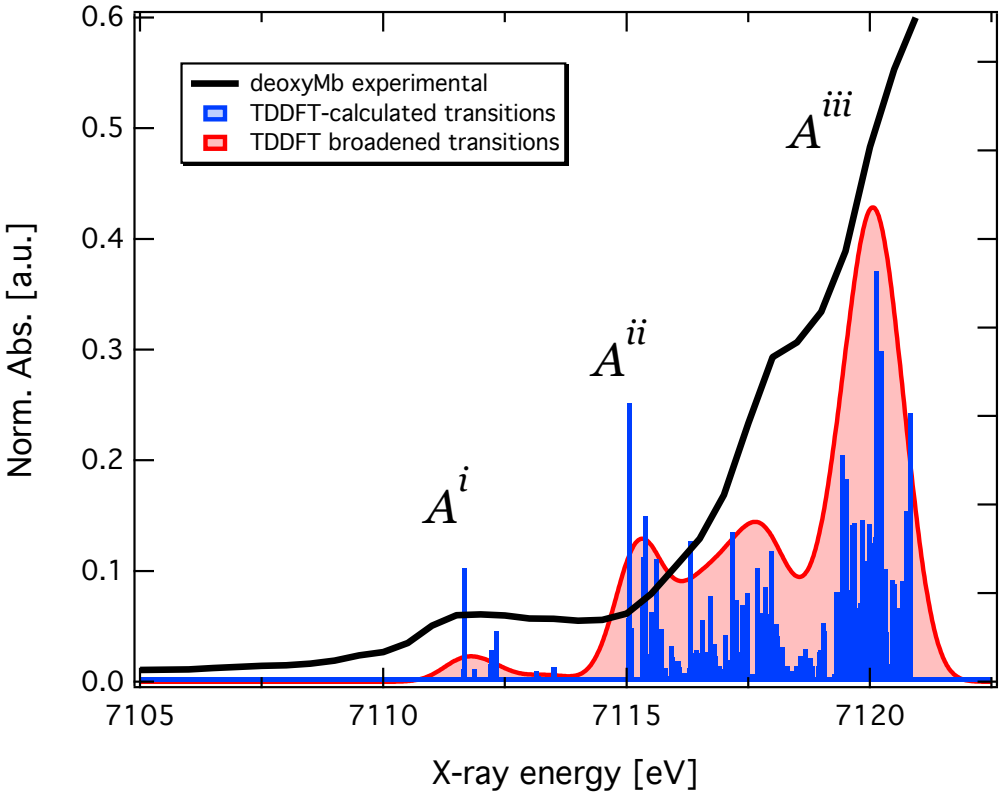

Figure 6.28.: XAS spectrum of deoxyMb as calculated by TDDFT. Note the presence of the A^{ii} feature, which was not seen in the DOS analysis. The blue bars are the calcuated transitions, the red curve represent the broadened transitions. The black line represent the experimental data.

6.6 Conclusions

In summary we have analysed the ground-state XAS spectra of six different types of Myoglobin (Mb) measured under physiological conditions. Ligated and unligated forms were studied, including both ferric and ferrous oxidation state of the iron atom in the protein. A full multiple scattering analysis of the XANES region of the spectrum was conducted, pointing to a common distance Fe-N_p of about 2 Å for all the ligated species. The relative position of the ligand (when present) varies considerably. In ferrous Mb, the α angle is $3 \pm 2°$ in MbO_2, increasing to $13 \pm 6°$ in MbNO, and $22 \pm 10°$ in MbCO.

Conversely, the β angle decreases in these Mb types, going from $50 \pm 4°$ in MbO_2, to $35 \pm 1°$ in MbNO, to $5 \pm 5°$ in MbCO. Our analysis contain a detailed investigation of the geometrical and electronic structures of these Mb forms, representing a more appropriate model of the protein in real conditions. Moreover, our data does not contain any contamination of x-ray damaged, lysed or reduced species because we have used continuously-flowing liquid samples, which dramatically decreases the accumulated x-ray dose in each individual protein. These effects are known to be very common in x-ray studies of metalloproteins.

The pre-edge region of the spectra of Mb, often neglected in the interpretation of the XAS, were investigated in detail. These features reflect transitions to bound states, and provide very detailed information about the electronic state of the absorbing atom and its interaction with the neighbours. We applied FMS formalism to calculate the XAS spectra and interpreted the features present in the basis of the local density-of-states (DOS). Time-dependent density functional theory (TDDFT) supported our analysis and in addition, provided an extra level of details in the assignment of the transitions causing the pre-edge features in the XAS spectra. Our analysis indicates that a simple picture of an Fe $1s \rightarrow 3d$ transition is not sufficient to explain the presence and shape of these pre-edge features. A strong hybridization between the Fe d and the neighbour's outermost orbitals has been found to strongly affect the bound-bound transitions in the pre-edge XAS. In addition, the Fe p orbitals have been found to also contribute to the transitions giving rise to the pre-edge features in the XAS spectra of Myoglobin. In our analysis, we have been able to distinguish the contribution of the same atomic species, but located in different environments, to the transitions in the pre-edge region. Our analysis of the electronic and geometrical structure of the different forms of Myoglobin is believed to be the first conducted in this series of proteins in physiological conditions.

We have studied the ligand rebinding dynamics of MbCO and MbNO, using our high repetition rate scheme for time-resolved XAS. Using a slow pump-probe scheme of measurement we could excite as much as 21% of the MbCO molecules. The transient data indicates that the structure of this species resembles that of the unligated ferrous Mb (deoxyMb). This system has been extensively studied by virtually all experimental techniques known. Therefore, we used the photo-detachment of the CO ligand in MbCO to benchmark the experimental setup [228]. On the other hand, the investigation of the NO rebinding dynamics of MbNO by XAS is completely new. The recombination was found to occur in 216 ± 24 ps, with a long component of about 1.5 μs treated as a constant term in our analysis. The presence of the fast component of *ca.* 30 ps could not be detected due to our temporal resolution (70 ps). The structural changes of the photo-excited MbNO at 50 ps was found to mainly involve a movement of the ligand away from the heme and a displacement of the iron atom outside the heme plane. In addition, the heme undergoes a slight doming movement. Future extensions of these time-resolved x-ray experiments to include other types of spectroscopy, *e.g.* XES, RIXS, promise to deliver a more detailed picture of the electronic structure of biological systems in physiological conditions. With new x-ray sources delivering very intense femtosecond

x-ray pulses becoming a reality [136], we may soon be able to provide more insight into the first moments of the photo-deligation process in Mb and other biologically relevant systems.

"A science is not mere knowledge, it is knowledge which has undergone a process of intellectual digestion. It is the grasp of many things brought together in one, and hence is its power; for, properly speaking, it is Science that is power, not Knowledge."

John Henry Newman

7

Conclusions and outlook

Ultrafast time-resolved X-ray Absorption Spectroscopy has evolved to be mature and well-established experimental technique [33, 34, 38, 126], which gives extremely detailed information about the local geometrical and electronic structure in the early stages of a chemical reaction or biological process. This has been since long a dream of many scientists, follow the atomic movements and electronic changes in the course of such transformations, and study how these changes correlate with specific chemical properties or biological function. In this respect, x-ray absorption spectroscopy (XAS) is an ideal experimental tool because it combines the ability to directly deliver structural information with the capability of being applicable to samples in any medium. This last property represents a big advantage in comparison with other x-ray structural techniques (*e.g.*, diffraction) since many relevant chemical and biological processes occur in liquids. The extension of XAS to the temporal domain, in a laser-pump/x-ray probe manner, allows the investigation of electronic structure modifications driving the molecular structure changes in real time. The implementation of time-resolved ultrafast XAS at high repetition rate represents a big step in the direction of improving the data quality, decreasing the acquisition time and broadening the horizons in application to highly-dilute or unstable systems. The increase in data quality allows the measurement of very detailed spectra, which now requires a much more sophisticated theory in order to produce a quantitative interpretation of the spectral features. In principle, the temporal resolution of time-resolved ultrafast XAS experiments is limited to 50-100 ps, *i.e.*, the time duration of the x-ray pulse delivered by synchrotron sources. However, this limit can be overcome, *e.g.* with the femto-slicing technique or by using the low-α operation mode, always at the expense of photon flux. The slicing technique can produce femtosecond x-ray pulses, but cannot be easily implemented at high repetition rates due to the intrinsic relaxation time needed by the electron bunch before another slicing even take place. Another interesting way to overcome the *ca.* 100 ps temporal limit is to use the so-called *crab cavities*, which compress the electron bunches inside the synchrotron storage ring, therefore generating shorter x-ray pulses. X-ray free-electron lasers are

now a reality: one machine is fully operational [136] and at least two more will come to life in the next years [137, 139]. The x-rays generated by these 4^{th}-generation sources have an incredible short temporal resolution (on the order of a few tens of fs). They also have a much higher x-ray flux when compared to synchrotrons and the radiation present coherent properties. These facts are starting to be exploited in new experiments, providing very exciting results and leading the way to completely new science fields. A few examples include lensless and [221, 222] single particle imaging [223], femtosecond protein cystallography [224, 225] and nonlinear x-ray physics [226].

In this thesis we developed a new scheme for ultrafast time-resolved XAS experiments, increasing the data acquisition repetition rate by a factor of 500. In this way, all the available isolated x-ray pulses (camshafts) in the hybrid mode of the Swiss Light Source (SLS) are used in the experiments. When compared to previous similar experiments, we obtained a gain in data quality and decrease in acquisition time, translating in about 20 times higher signal-to-noise (S/N) ratio. In addition, the present scheme is very flexible and totally portable. In spite of using 10 ps pulses to excite the samples (instead of 100 fs), the temporal resolution of the experiment is not affected. It is dominated by the time duration of the synchrotron x-ray probe pulses (*ca.* 70 ps). In addition, the longer pulses produce a more efficient excitation, which contributes not only to increase the data quality but also to preserve the sample integrity - in cases this might represent an issue. We have recently extended its application to other beamlines at the SLS, including time-resolved XAS using more tender x-rays (*ca.* 3keV) and also implemented ultrafast time-resolved x-ray emission spectroscopy (XES) and resonant inelastic x-ray scattering (RIXS). These two techniques greatly profit from the high repetition rate and low noise capabilities of our system because of the resulting low x-ray photon flux in the emission process.

As a test-case for the characteristics of the high repetition rate ultrafast time-resolved XAS experiments we have studied the light-induced spin crossover transition in the $[Fe^{II}(bpy)_3]^{2+}$ molecule in an aqueous solution. The high level of details of the transient XAS data measured with the high repetition rate allowed the investigation of the electronic structure of $[Fe^{II}(bpy)_3]^{2+}$, both in the low- and in the high-spin states. For this purpose we have applied an analysis based on the local electronic density-of-states (DOS) as calculated by the `FEFF9` software package, which was supported by recent TDDFT calculations on iron-centered molecular complexes [184]. In the ground-state (low spin) the peak in the pre-edge region of the XAS spectrum originates from a mixing of the Fe 3*d*- and N *p*- orbitals, with a small contribution of N *s*- as well. This mixing gives some *p* character to the molecular orbital, which makes the transition $1s \rightarrow 3d$ allowed by dipole selection rules. Including a quadrupole contribution on the calculations did not affect significantly the spectrum, indicating that the transitions are mainly due to dipole terms. The *B* feature in the XAS spectrum is due to multiple-scattering (MS) contributions, even though this region also contains contributions from the iron and nitrogen DOS. This feature lies very close to the ionization threshold, which is not precisely determined due to the limitations in the muffin-tin (MT) potentials. Uncertainties

of about 1-3 eV in the value of the ionization threshold are common in current state-of-the-art XAS theory, even when self-consistent field (SCF) calculations are performed. The analysis of the energy-integrated d-DOS of the iron atom reveals that the $3d(t_{2g})$ orbital lies just bellow the Fermi energy, and as expected is filled with six electrons. The transition causing the A feature is $1s \rightarrow 3d(e_g)$.

In the excited-state (high spin) the $[Fe^{II}(bpy)_3]^{2+}$ molecule experiences a bond elongation $\Delta_{Fe-N} = 0.2 \pm 0.01$ Å, in accordance with previous studies [39, 40, 122]. The analysis of the local DOS reveals that, similar to the ground-state case, the A feature in the excited-state is caused by a mix of the Fe $3d$- and N p- orbitals, with a small contribution of N $2s$. The transitions are of a predominantly dipole character, since the inclusion of quadupole transitions did not affect the results. In spite of providing important information about the electronic structure, the local DOS was not able to capture all the subtle details present on the spectrum of the high-spin state, or equivalently, of the transient XAS spectrum. For this purpose we made use of TDDFT calculations, which indicated that the transitions in the A feature are all $1s \rightarrow 3d$. It was also able to reproduce features A^{ii} and A^{iii} in the transient spectrum, which are $1s$-ligand and do not contain contributions from the iron d orbital. These transitions have an increasing p character and thus are relatively strong being dipole-allowed. These calculations also confirmed that quadrupole contributions play little role on the transitions present in pre-edge region of the spectrum.

The studies of the ground- and excited-state structures of different forms of Myoglobin (Mb) in physiological conditions presented in Chapter 6 represent a major advance in the understanding of the structure of metalloproteins in solution. We have presented a detailed investigation of the geometrical and electronic structures of a series of ligated and unligated Mb, both in the ferrous and ferric oxidation states. Because the reported structural results were derived from measurements taken in solutions, the influence of x-ray-induced reduction, lysis or damage have been minimized. In addition, these structures better represent the "real ones" since our data are not biased by crystal packing forces and/or stress as in crystallography. The analysis of the XANES region of the spectrum using full-multiple scattering (FMS) formalism revealed that the iron-nitrogen bond length in the porphyrin rings of different forms of ligated Mb converged to a common value of about 2 Å, in contrast to the wide variation found in the crystallographic structures. This reflects the relative rigidity of the porphyrin, due to the many carbon-carbon double bounds. The distance between the iron atom and the proximal histidine (His93) was found to vary significantly with the type of Mb. We believe this structural diversity provides a more realistic picture of Mb in solution, indicating that the influence of the different ligands in Mb is more pronounced in the relative position of the proximal and distal (His64) histidines, while the porphyrin assumes a common structure when in solution. This interpretation probably can be extended to other metalloproteins, pointing to a higher mobility of the residues in the active center than currently stated.

The electronic structure of the different forms of Mb in physiological conditions was studied by analysing the features present in pre-edge region of the XAS spectra. These features reflect transitions to bound states, thus providing very detailed information about the electronic states of the absorbing atom and its interaction with the neighbours. The interpretation was based on the use of FMS formalism to calculate the XAS spectra, and also on TDDFT calculations. We have shown that a simple picture of an Fe $1s \rightarrow 3d$ transition is not sufficient to explain the presence and shape of these pre-edge features. The interaction with the neighbours strongly affects the degree of hybridization between the Fe d and the neighbour's outermost orbitals, with direct influence in the pre-edge region of the spectrum. We have been able to distinguish the contribution of the same atomic species, but located in different environments, to the transitions in the pre-edge region. Besides, we have found that atoms as far as ~ 3.5 Å away from the absorber can contribute to an orbital hybridization causing a bound-bound transition, as it is the case of deoxyMb. To our knowledge, this is the first XAS study of the geometric and electronic structures of different forms of Myoglobin in physiological conditions.

The dynamics of ligand rebinding in Mb was studied using time-resolved XAS in two different forms of Mb: MbCO and MbNO. In the MbCO case, we have found a transient structure which resembled the unligated ferrous Mb (deoxyMb). Using a slow pump-probe scheme of measurement we obtained an excitation yield of about 21% when using 10ps/532 nm laser pulses. On the other hand, we have been able to directly probe the NO recombination to the heme in MbNO. The recombination was found to happen in 216 ± 24 ps, with a long component of about 1.5 μs treated as a constant term in our analysis. The presence of the fast component of *ca.* 30 ps could not be detected due to our temporal resolution (70 ps). As expected, the inclusion of a component with 30 ps lifetime did not affect the determination of the NO geminate recombination time, which was still around 200 ps. The structure of the photo-excited MbNO was modelled based in calculating the XAS spectrum of the excited-state using FMS and fitting the transient spectrum directly in energy space. 50 ps after photo-excitation, the NO ligand is found to have moved to 2.88 ± 0.09 Å away from the heme plane. The iron atom is located 0.16 ± 0.03 Å below the heme plane, in the direction of the proximal histidine. The Fe-N_p distance is 2.02 ± 0.02 Å, corresponding to a dilation of 0.01 Å with respect to the ground-state structure. The inclusion of another structural conformation to account for an excited MbNO domed-ligated species hypothesised by Kruglik and co-workers [210] resulted in an unacceptable fit of the transient XAS. At 50 ps, the contribution of such a species is less than 20%, which is on the limit of the signal-to-noise (S/N) ratio of our data.

Ultrafast time-resolved structural techniques using of x-rays, in special XAS, are expanding its applications and producing very exciting results [33, 34, 125, 126, 227]. Time-resolved XAS has long promised to unravel structural and electronic details on the course of chemical and biological reactions, with applications also on materials science [32, 118, 128, 170]. The technical advances in the last decade with respect to the stability and brilliance of the synchrotron sources, improvements in detection and

data acquisition systems, and sample environment control contributed to make ultrafast time-resolved XAS in the picosecond regime almost routine in many synchrotron facilities worldwide. However, the intrinsically low photon flux in these experiments, coming from the fact that only certain specific x-ray pulses are used, represent a limit in the samples possible to be investigated. Most of these limitations are overcome with the advent of the high repetition rate scheme implemented by our group [228] and presented in this thesis. It is now possible to measure transient XAS of highly dilute systems, which represents a big step in the direction of studying the dynamics of biological process, energy conversion in technological materials used in solar-cell panels and electron transfer in coordination chemistry. New ideas and technological necessities are always a driving force motivating the advances, which recently culminated with the extension of ultrafast time-resolved techniques to "tender" [228] and the soft x-ray regimes [229–231], measurements using energy-dispersed x-ray emission [156, 232, 233] and resonant inelastic x-ray scattering [232, 233]. Using the femto-slicing technique, femtosecond x-ray regime for time-resolved XAS is now a reality [35, 37]. The first 4^{th}-generation x-ray sources, the x-ray free-electron lasers, recently were brought into operation [136]. They produce a very intense (high brilliance) x-ray beam, with short pulses and a high degree of coherence. Scientist are designing and performing new types of experiments profiting from these unique characteristics, promising to give insight into completely new discoveries. In the filed of ultrafast science, time-resolved x-ray spectroscopies, diffraction and scattering will provide access to the fundamental time scale of molecular motion. Femtosecond x-ray science will, finally, be able to produce "*molecular movies* "! In this regard, Myoglobin represents a very interesting system to be studied by femtosecond x-rays. As a protein, it is simple enough to present very fundamental biochemical processes to be used as a test-case, yet complicated to the level that many of them are still to be understood. The "*hydrogen atom of biochemistry*" is ready to show all its potential.

A

Low-α operation mode at synchrotrons

This Appendix describes the so-called low-α mode of operation on third-generation synchrotrons. This operation mode is based on modifying the lattice of the storage ring in order to obtain low values of the momentum compation factor, α. As a result, very short electron bunches (less than 1 ps) can be obtained, which in turn promise to be able to generate coherent radiation, as well as improve the temporal resolution on time-resolved experiments. At the Swiss Light Source (SLS), the use of the low-α mode results in a temporal resolution of about 20 ps, using 100 μA stored current.

Bending magnet are used to deflect the electron beam.

Quadrupole magnets they act pretty much like glass lenses in light optics by providing a restoring force or *focusing* force to particles that deviate from the ideal orbit. The quadrupoles are made of four hyperbolic poles with alternating magnetization. They focus on one plane, but defocus on the other.

Sextupole magnets are used to correct for *chromatic aberrations* caused by focusing errors on particles with different energies

Equations of motion

Bending and focusing of high energy, relativistic particles are effected by the Lorentz force

$$\vec{F} = e\vec{E} + \frac{e[c]}{c}\left[\vec{v} \times \vec{B}\right] \tag{A.1}$$

The equation of motion in the presence of a dipole (B_0), quadrupole (g) and sextupole (g') fields can be derived from the general expression for the curvature $1/\rho$ of paraxial beams. The curvature is defined in a very general way, to include all fields (dipole, quadrupole, sextupole, ...). For paraxial beams the curvature $1/\rho$ is

$$\frac{1}{\rho} \approx x'' = [c]\frac{eB}{cp} \tag{A.2}$$

where

$$B = B_0 + gu + \frac{1}{2}g'u^2 + ...$$
$$[c]\,\frac{eB}{cp} = \frac{1}{\rho_0} + ku + \frac{1}{2}mu^2 + ... \tag{A.3}$$

The field term $\frac{1}{\rho_0}$ describes the ideal beam guidance through the bending magnets. The complete solution of the equations of motion is rather complicate and in general, this solution is not interesting because the beam orbit is already constrained by the placement of the bending magnets and the geometry of the synchrotron storage ring. Of major concern, though, is the deviations of particle trajectories from this ideal orbit. It is therefore, useful to redefine the curvature equation eliminating the geometric expression of the ideal orbit by:

$$\frac{1}{\rho} - \frac{1}{\rho_0} \approx x'' = [c]\,e\left(\frac{b}{cp}\frac{B_0}{cp_0}\right) \tag{A.4}$$

Inserting the magnetic filed expansion (dipole, quadrupole, sextupole, ...) into Equation A.4 the equation of motion becomes:

$$\begin{aligned} x'' \;=\; & -kx \;\ldots\ldots\ldots\ldots\ldots \text{ focusing term} \\ & +\frac{1}{\rho_0} \;\ldots\ldots\ldots\ldots\ldots \text{ dispersion} \\ & +kx\delta \;\ldots\ldots\ldots\ldots\ldots \text{ chromatic aberration} \\ & -\frac{1}{2}mx^2 \;\ldots\ldots\ldots\ldots\ldots \text{ chromatic and geometric aberration} \\ & +\mathcal{O}(3) \;\ldots\ldots\ldots\ldots\ldots \text{ higher order terms,} \end{aligned} \tag{A.5}$$

where $\delta = \Delta E/E_0$ is the relative energy deviation of a particle from the ideal energy E_0 amd m is the sextupole strength.

In the low-α mode, all these parameters have to be re-tuned in order to modify the dispersion of the electron beam at each magnetic element. The momentum compaction factor α is related to the energy dispersion caused by a certain magnetic element by:

$$\alpha_i = \int_0^{L_0} \frac{\eta_i}{\rho_i} ds \tag{A.6}$$

where η_i is the energy dispersion and ρ_i is the radius of curvature of the i^{th} element. Thus, minimizing the energy dispersion will minimize α, which results in shorter electron bunches inside the storage ring.

Low-alpha operation on the SLS

On the Swiss Light Source (SLS) storage ring, the (natural) bunch length in normal operation mode is about 16 ps RMS. When in standard top-up operation mode, it stores up to 100 mA current and the bunch length is increased to about 40 ps RMS by means of the third harmonic Landau cavities. Shorter x-ray pulses of only 0.06 ps RMS can be obtained on the FEMTO/Micro-XAS endstation exploiting the slicing scheme (*REF*), at a cost of a 10^3 reduction on the x-ray flux.

Bunch length dependence on the stored current

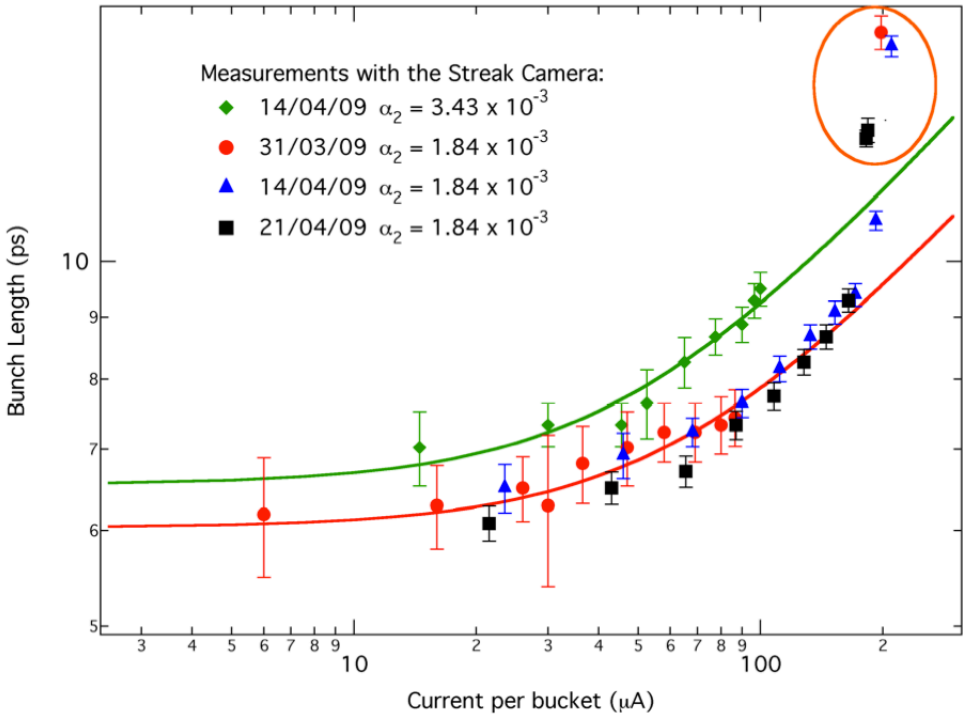

Figure A.1.: Bunch length (RMS) as a function of the current per bucket. Taken from Ref. [144].

B

Publication with the experimental setup

This appendix includes a copy of an article published in the *Review of Scientific Instruments*, which describes the experimental details of the new methodology developed to perform time-resolved XAS experiments at synchrotrons at MHz repetition rates. A reprint of this publication can be obtained from the electronic edition of the journal using the reference: F. A. Lima, C. J. Milne, D. C. V. Amarasinghe, M. H. Rittmann-Frank, R. M. van der Veen, M. Reinhard, V-T. Pham, S. Karlsson, S. L. Johnson, D. Grolimund, C. Borca, T. Huthwelker, M. Janousch, F. van Mourik, R. Abela, and M. Chergui *Rev. Sci. Instrum.* **82**, 063111 (2011).

A high-repetition rate scheme for synchrotron-based picosecond laser pump/x-ray probe experiments on chemical and biological systems in solution

Frederico A. Lima,[1] Christopher J. Milne,[1] Dimali C. V. Amarasinghe,[1,a)] Mercedes Hannelore Rittmann-Frank,[1] Renske M. van der Veen,[1,b)] Marco Reinhard,[1] Van-Thai Pham,[1,c)] Susanne Karlsson,[1] Steven L. Johnson,[2] Daniel Grolimund,[2] Camelia Borca,[2] Thomas Huthwelker,[2] Markus Janousch,[2] Frank van Mourik,[1] Rafael Abela,[3] and Majed Chergui[1,d)]

[1]*Laboratoire de Spectroscopie Ultrarapide, Ecole Polytechnique Fédérale de Lausanne, ISIC, FSB, 1015 Lausanne, Switzerland*

[2]*Swiss Light Source, Paul Scherrer Institut, 5232 Villigen, Switzerland*

[3]*SwissFEL, Paul Scherrer Institut, 5232 Villigen, Switzerland*

(Received 28 April 2011; accepted 23 May 2011; published online 27 June 2011)

We present the extension of time-resolved optical pump/x-ray absorption spectroscopy (XAS) probe experiments towards data collection at MHz repetition rates. The use of a high-power picosecond laser operating at an integer fraction of the repetition rate of the storage ring allows exploitation of up to two orders of magnitude more x-ray photons than in previous schemes based on the use of kHz lasers. Consequently, we demonstrate an order of magnitude increase in the signal-to-noise of time-resolved XAS of molecular systems in solution. This makes it possible to investigate highly dilute samples at concentrations approaching physiological conditions for biological systems. The simplicity and compactness of the scheme allows for straightforward implementation at any synchrotron beamline and for a wide range of x-ray probe techniques, such as time-resolved diffraction or x-ray emission studies. © *2011 American Institute of Physics*. [doi:10.1063/1.3600616]

I. INTRODUCTION

Over the past 10 years, there have been huge efforts aimed at investigating ultrafast photoinduced structural changes in molecules, crystals, materials, and proteins using structural probes such as electron and x-ray diffraction, electron microscopy, and x-ray absorption spectroscopy in a pump-probe scheme.[1] The goal is to retrieve the structural dynamics of the systems on the atomic scales of space (sub-Å) and time (femtoseconds to picoseconds). Ultrafast electron diffraction and microscopy are making rapid progress in following the structural dynamics of gas phase molecules, materials, thin films, and surfaces.[1] Ultrafast x-ray diffraction has found many applications including the study of coherent phonons[2,3] and phase transitions in solid materials,[4] while the first x-ray diffraction study on protein crystals has been achieved with 100 ps time resolution.[5] For the case of chemical reactions in disordered media such as liquids, which is the medium wherein most chemical and biological reactions take place, x-ray scattering has been used in the >100-ps time scale[6,7] but due to the sensitivity of the technique to all atoms in the sample and the complexity of processes occurring on this time scale in both solvent and solute, the analysis of the data is nontrivial. The chemical selectivity of x-ray absorption spectroscopy (XAS) makes it ideal as a local probe, and allows retrieval of both the local geometric structure and the electronic environment around a given atom via analysis of the extended x-ray absorption fine structure (EXAFS) and the x-ray absorption near-edge spectroscopy (XANES) regions of the spectrum. This unique combination provides information about the electronic changes that drive the subsequent structural dynamics as well as information on the structural changes themselves.[1,8–13]

To date, picosecond optical pump/x-ray probe XAS experiments[8,14–28] have been performed with the pump laser operating at kHz repetition rates in order to take advantage of the high pulse energies available from commercially available amplified laser systems (>1 mJ/pulse). In contrast to this, synchrotron x-ray pulses are generally delivered at MHz repetition rates by the storage ring. The experiments typically make use of a fast detector to only measure the x-ray pulses generated by an isolated "camshaft" electron bunch of the hybrid filling mode available at third-generation synchrotron sources (see Fig. 1) and are usually based on recording the transient absorption on a pulse-to-pulse basis. The data acquisition is performed in such a way that the x-ray absorption signal of the sample is recorded at twice the repetition rate of the pump laser using gated detectors, with one x-ray absorption signal corresponding to the laser-excited sample and the next to the unexcited sample. This scheme has proven capable of measurements limited only by the shot noise of the synchrotron source.[17,18] Its main drawback is that while the excitation laser pulses occur at kHz repetition rates, the synchrotron pulses occur at MHz repetition rates, which means that typically 10^3 x-ray pulses are unused. This reduced x-ray flux is a major limiting factor on

a)Present address: Department of Chemical Physics, Lund University, SE-22100 Lund, Sweden.
b)Present address: California Institute of Technology, Pasadena, California 91125, USA.
c)Present address: Pacific Northwest National Laboratory, Richland, Washington 99352, USA.
d)Electronic mail: majed.chergui@epfl.ch.

the achievable signal-to-noise ratio (S/N) of the experiments, which not only reduces the accuracy of the structural analysis but also places a restriction on samples that can be measured with a solubility in the range of tens to hundreds of mM.

In order to exploit all the available camshaft x-ray pulses, it would be necessary to use a pump laser that runs at half the repetition rate of the synchrotron source. At the Swiss Light Source (SLS, Paul Scherrer Institut, Villigen, Switzerland), this corresponds to a repetition rate of 1.04 MHz, which would require a laser at 520 kHz. Provided the conditions (laser fluence, incident x-ray flux per pulse, sample concentration, thickness, etc.) are similar to those of the 1 kHz experiments and assuming that the predominant source of noise is the shot noise of the x-ray source, an increase of $\sqrt{520} \approx 23$ in S/N should be expected, resulting in significantly shorter data acquisition times and expanding the applicability of the technique to the study of dilute liquid-phase systems.

Previous attempts to implement a high-repetition rate pump-probe scheme at synchrotrons were made by Widdra *et al.*[29,30] who used a Nd:YVO_4 oscillator (1064 nm, 200 nJ, 14 ps) with a pulse-picker operating at 1.25 MHz to match the single-bunch repetition rate at the BESSY synchrotron (Berlin, Germany) for time-resolved core-level photoemission studies of surfaces. Stern *et al.*[31,32] used an amplified Titanium:Sapphire laser source (800 nm, 3 μJ, 100 fs) operating at 272 kHz at the APS (Advanced Photon Source, Argonne, USA) to study laser-induced melting of Germanium films. The disadvantage of using high-repetition rate excitation with solid samples is the sample damage resulting from the high average power. For liquid solutions, high repetition rate excitation is ideal since the flowing sample is continuously refreshed, but this has so far not been attempted. Given that the main limitation in the picosecond optical pump/XAS probe studies at 1 kHz is the low x-ray flux, it seems worthwhile to extend the pump/probe scheme to data collection at higher repetition rates.

Here we report on a portable experimental setup for ps XAS studies at both the hard x-ray microXAS beamline and the tender x-ray PHOENIX I beamline of the Swiss Light Source. It uses a compact ps pump laser with variable repetition rate, widening the potential application of picosecond x-ray experiments to the many diverse x-ray techniques (absorption, emission, diffraction, scattering) available at synchrotrons. We demonstrate its performance by investigating the well characterized light-induced spin crossover process in $[Fe(bpy)_3]^{2+}$ (Ref. 33) and the oxidation state change in $[Ru(bpy)_3]^{2+}$,[34] showing improved S/N for high-concentration samples and pump-probe signals at high dilutions. Additionally, as a demonstration of the new scheme on low concentration biological systems in physiological media, we report the results of a pump-probe XAS experiment on photoexcited carboxymyoglobin (MbCO).

II. INSTRUMENTS AND METHODS

The main elements required for a picosecond time-resolved XAS experiment will be briefly reviewed, highlighting the specifics of the MHz data acquisition scheme for comparison to kHz data acquisition.[14,17,18]

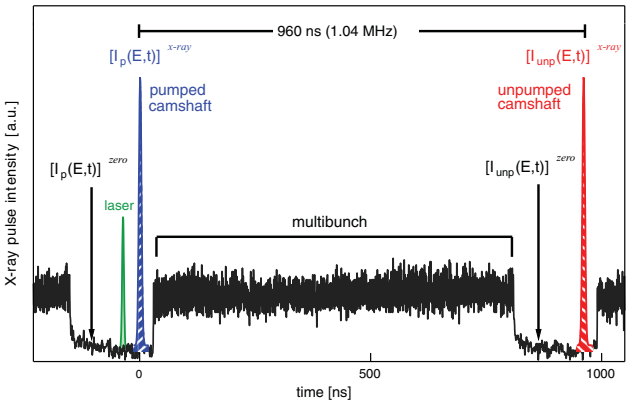

FIG. 1. (Color online) Electron filling pattern used at the SLS. In total, there are 480 possible buckets spaced 2 ns apart, of which 390 are filled with electrons (multibunch). Of the 90 remaining empty buckets, the camshaft pulse in bucket 465 is filled with four times more current than the average multibunch current. The ring repetition rate is 1.04 MHz, which sets an upper limit for the data acquisition rate of the experiments using the current hybrid filling mode.

A. X-ray source

The probe pulses are derived from the camshaft electron bunch provided by the SLS during normal user operation. The isolated pulse is a result of the hybrid electron filling pattern used at the SLS (Fig. 1) which consists of 390 consecutive electron bunches separated by 2 ns, called the multibunch, and an isolated electron bunch, called the camshaft pulse, which is placed within the empty gap of 180 ns. The isolated single bunch has four times more current than the individual bunches in the multibunch structure and a duration of approximately 85 ps (FWHM).[35] During normal user operation the ring current is 400 mA and the camshaft current is 4 mA. The ring current is maintained to within 0.5% by use of top-up filling mode which injects electrons into the storage ring at regular intervals.

The reported experiments were conducted at two different beamlines at the SLS. The microXAS beamline, located in the long straight section X05L of the SLS ring, is equipped with a minigap in-vacuum undulator capable of generating x-rays from 4 to 23 keV with a flux of approximately 10^{12} photons/s/0.015% bandwidth. The photons are collimated vertically and focussed horizontally by a Rh-coated toroidal mirror and then energy selected over a range of bandwidths by a double-crystal, fixed exit monochromator (DCM) containing Si(111), Ge(111), and Si(311) crystal pairs. An elliptical mirror pair in the Kirkpatrick-Baez (KB) geometry is located immediately before the experimental station, and is capable of focusing the x-rays down to $< 1 \times 1 \mu m^2$ spot.[36]

The PHOENIX I beamline covers the tender x-ray spectrum from 800 eV to 8 keV. The photon source is an elliptical APPLE II undulator with a flux of 10^{11} photons/s/0.01% bandwidth. The beamline is equipped with a DCM containing Si(111) crystal pairs, for energies above 2.1 keV, and KB mirrors allowing for μm focal spots.

B. Laser source

Since the time-resolution of the XAS experiments is generally limited by the synchrotron pulse duration (typically 85 ps at the SLS), there is no advantage to using fs laser systems to excite the sample as done so far. In fact there are several disadvantages. These sources are amplified, which means they need both a large amount of space and substantial cooling. They are often outside the experimental hutch, implying beam transport over tens of meters to the sample, which results in an increased sensitivity to the laser pointing stability and the far-field laser mode. Here we use a compact, high-average power Nd:YVO_4 picosecond laser (Duetto, Time Bandwidth Products, Zürich) operating at variable repetition rate (50 kHz to 8 MHz), and producing 10 ps pulses. This product is primarily aimed at industrial users meaning emphasis has been placed on turn-key operation and long-term stability. It delivers up to two orders of magnitude more energy per pulse than current high-repetition rate femtosecond oscillators, but still two orders of magnitude less energy per pulse than kHz amplified femtosecond systems. The Duetto laser system optimizes the amplifier stage diode pump current to extract the maximum possible pulse energy at any given repetition rate. When operated at half the repetition rate of the isolated camshaft pulse (520 kHz) this results in 28 μJ per pulse at the fundamental wavelength, 1064 nm. By frequency doubling and tripling one obtains 15 μJ per pulse at 532 nm and 6 μJ per pulse at 355 nm. It is also possible to double the 532 nm light to obtain 266 nm light. The laser mode has an M^2 value of 1.2 for both the doubled and tripled beams which permits it to be efficiently focussed to very small diameter spots, thus allowing similar fluences compared to the kHz experiments at modest beam diameters (<50 μm).

The use of this pump laser offers three primary advantages with respect to amplified fs systems at 1 kHz: (1) the longer pulse duration results in lower peak power, which minimizes sample damage and nonlinear effects, and generally results in more efficient sample excitation; (2) the fact that the pulse energy varies with the repetition rate allows both the excitation and the repetition rate to be tuned to the experimental requirements; and (3) Titanium:Sapphire-based amplified systems operate at 800 nm, which can easily be converted into 400 and 266 nm light, while molecular systems typically absorb in the visible region of the spectrum (400–700 nm), making these amplified pulses a poor choice for sample excitation whereas the 532 nm wavelength available from the high-repetition rate laser is ideal. For experiments on species with very long-lived excited-state lifetimes a "slow-difference" scan mode can be used in which the transient data are no longer collected by the pulse-to-pulse difference method, but as a difference of the average of 1 million x-ray measurements with laser on, and second average of 1 million x-ray measurements with the laser off. This alternative data collection mode will be detailed in Sec. IV C.

C. Synchronization and timing control

Overall stability and synchronization between the pump and probe sources are crucial for the success of any time-resolved experiments. The pump laser pulses have to be accurately synchronized to the x-ray probe pulses in order to have control of the relative temporal delay between them. Here we adopted a similar synchronization and timing control scheme used for previous optical pump/x-ray probe experiments,[17,18] which has previously proven to work reliably over the time required for the experiments. A simplified scheme of the synchronization and the timing control is shown in Fig. 2.

This is achieved by exploiting the intrinsic synchronization of the radio frequency (RF) master clock of the SLS with

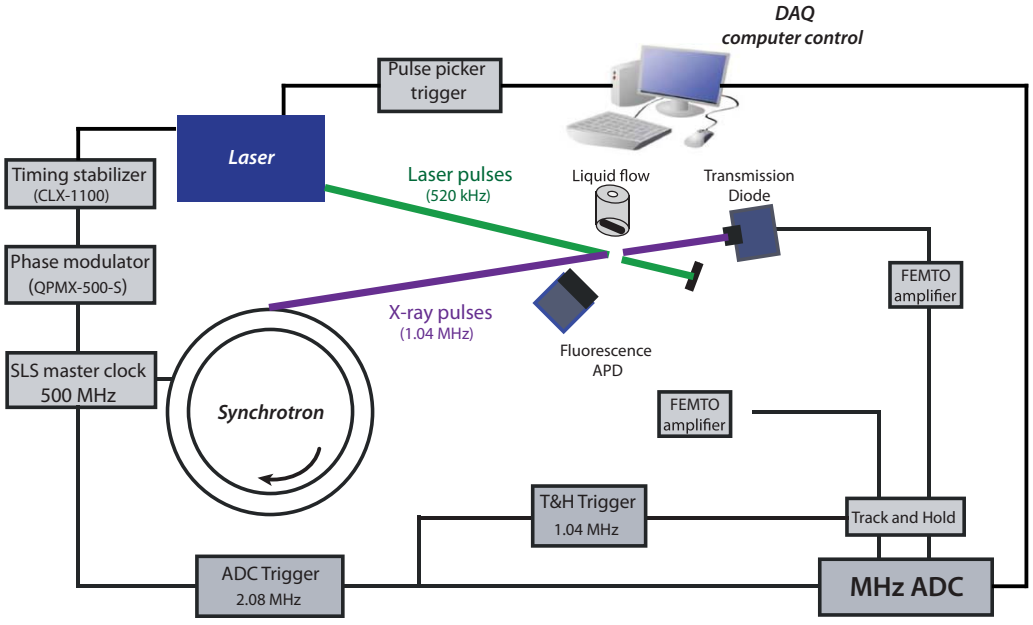

FIG. 2. (Color online) Diagram of the high-repetition rate pump-probe setup, see text for details.

the x-ray pulses. This master clock is synchronized to the 500 MHz signal of the RF cavities which is, in turn, responsible for creating the potential wells inside the storage ring, thus providing the time structure of the generated radiation. If a stable phase relationship between the RF and the laser oscillator pulses is established, synchronization is achieved. The relative phase stabilization is done via a commercially purchased system (CLX-1100 timing stabilizer, Time Bandwidth Products), which locks the phase of the Duetto laser oscillator to the SLS master RF with a timing jitter of less than 400 fs.

The relative time delay between the x-rays and laser pulses can be adjusted via a computer controlled timing system, which is integrated into the data acquisition. The timing of the laser pulse is controlled by synchronous scanning of the trigger for the Duetto pulse picker and an RF phase modulator (QPMX-500-S, I. F. Engineering). The phase modulator allows precise control over the relative phase of the oscillator with respect to that of the RF, thus changing the relative time delay between the laser and x-ray pulses with a few ps precision.

D. Detection and data acquisition

The employed data collection strategy is similar to that used for previous experiments,[11,17,18] with the important difference that the data acquisition rate is increased to 2 MHz. Briefly, the XAS signal at a specific x-ray energy and pump-probe time delay is recorded at twice the laser repetition rate, alternating between the signal from the excited sample and from the unexcited sample 1 μs later (see Fig. 1). In addition, a zero measurement is made for every x-ray measurement by reading the detector signal in the fill pattern gap where no x-rays are present. This electronic zero level is then subtracted off the corresponding x-ray signal to compensate for any drift in the data acquisition baseline over time. The signals provided to the user correspond to the pumped XAS signal ($[I_p]^{\text{x-ray}}-[I_p]^{\text{zero}}$), the unpumped XAS signal ($[I_{unp}]^{\text{x-ray}}-[I_{unp}]^{\text{zero}}$) and the pulse-to-pulse difference signal of pumped-unpumped with the zeroes being ignored as the electronic baseline will have no time to drift during the 1 μs separating the two x-ray measurements ($[I_p]^{\text{x-ray}}-[I_{unp}]^{\text{x-ray}}$). The data acquisition scheme is shown in Fig. 2.

Detectors for a time-resolved XAS experiment must fulfill three main requirements: (a) they should be fast enough to isolate the x-ray pulses that come solely from the camshaft bunch, (b) they must generate sufficient signal when exposed to a range of x-ray energies, and (c) they must have linear response over the range of x-ray flux used. In the present setup, the x-ray pulses are measured using two different types of fast detectors: for fluorescence signals large-area avalanche photodiodes (C30703F, PerkinElmer) with a 1 cm $\times$ 1 cm active area are used when the intrinsic gain of the device is necessary to measure signals down to the single x-ray photon level. In transmission, silicon photodiodes are used (AXUV20HS1, International Radiation Detectors) where device linearity over several orders of magnitude of current becomes critically important. Both types of detectors have rise times $<$5 ns. The detectors are shielded with 25 μm thick Be foils to protect them from scattered laser light. The detector signal is then amplified using broad-bandwidth (80–200 MHz) current-to-voltage amplifiers (FEMTO DHPCA-100) which allow the signal to be transferred to the data acquisition system with a minimum of additional noise. We use track-and-hold circuits (AD9100, Analog Devices) to sample the amplified signal on the maximum of the camshaft pulse. This level is then held for sufficient time for the fast analog-to-digital card to sample the signal level. The digitizer is an eight-channel ADC/digitizer board (Struck Innovative System GmbH, model SIS3302) with a sampling rate of up to 100 MHz and 16 bit resolution, capable of sampling up to 8 channels in parallel for each given trigger. The ADC is housed in a *virtual machine environment* (VME) crate together with the hardware for generating all the timing signals. Triggers are required for the ADC at 2.08 MHz to read the zero signal and the x-ray signal, the laser pulse picker at 520 kHz (or some even sub-multiple of the 1.04 MHz x-ray frequency), and the track-and-hold circuits at 1.04 MHz. In addition two marker signals are generated and digitized in parallel with the data channels to indicate if a signal originates from the laser-excited or from the unexcited sample and if the signal is an x-ray measurement or a zero measurement. The VME crate uses these marker signals to sort the data prior to performing the signal averaging.

The reported measurements are performed in transmission and fluorescence yield (FY) modes simultaneously. Depending on the sample solubility and optical density one can adjust the concentration in order to optimize the signal for either mode.[8] For the hard-x-ray experiments the incident x-ray intensity (I_0) was also recorded by measuring the fluorescence from a thin Cr foil using an APD. Recording the incoming x-ray flux on a pulse-to-pulse basis allows the normalization of incoming x-ray fluctuations due to monochromator imperfections or changes due to the storage ring. Moreover, normalization of the unexcited spectra to the incident flux yields the static XAS of the sample. Note that the transient difference measurement does not in general require I_0 normalization since the incident x-ray flux does not change on a 1 μs timescale.

With the laser operating at 520 kHz, two million measurements are performed over the course of 1 s: 500 000 pumped x-rays, 500 000 pumped zeroes, 500 000 unpumped x-rays, and 500 000 unpumped zeroes. These signals are then sorted according to the markers, the requisite calculations are performed and then each of the three signals is averaged, returning to the scanning PC the averaged data and the standard error of the pumped/unpumped/difference measurement for each of the ADC channels.

The time-dependent transmission transient XAS signal is defined as

$$\Delta A^T(E,t) = \ln\left(\frac{\left[I^T_{unp}(E)\right]^{\text{x-ray}} - \left[I^T_{unp}(E)\right]^{\text{zero}}}{\left[I^T_p(E,t)\right]^{\text{x-ray}} - \left[I^T_p(E)\right]^{\text{zero}}}\right). \quad (1)$$

The time-dependent fluorescence transient XAS signal is defined as

$$\Delta A^F(E,t) = \frac{\left(\left[I_p^F(E,t)\right]^{\text{x-ray}} - \left[I_p^F(E,t)\right]^{\text{zero}}\right) - \left(\left[I_{unp}^F(E)\right]^{\text{x-ray}} - \left[I_{unp}^F(E)\right]^{\text{zero}}\right)}{I_0(E)}. \quad (2)$$

The subscripts *unp* and *p* stand for the ground-state (unpumped) or excited (pumped) sample, respectively. I_0 represents the incoming x-ray intensity, I^T stands for the transmitted, and I^F for the fluorescence signals. The superscript *x-ray* indicates that the signal was recorded with the presence of x-rays and the superscript *zero* indicates that it was recorded without any x-rays, representing the electronic background signal of the detection system.

In 1 kHz experiments, this data acquisition methodology delivers results at the shot noise limit of the x-ray source.[17,18] In this limit, the S/N increases linearly with the fraction of excited species, while it increases with $\sqrt{n}$ of the number of accumulated x-ray photons, and thus the repetition rate of the experiment.[8,37] In the present experiment, the repetition rate was increased by a factor of 520, meaning that the expected increase on the S/N ratio is $\sqrt{520} \approx 23$, if all other parameters (x-ray flux, excitation yield, etc.) are considered unchanged.

To test the linearity of the photodiode used as transmission detector a series of measurements of the direct x-ray flux were taken, attenuating it by placing successive thin aluminium foils in the incoming beam. The x-ray intensity was recorded directly as the diode current, the track-and-hold output, and the data acquisition digitized signal. Assuming a constant incoming intensity, which is a reasonable approximation for the SLS since it operates in top-up mode, we expect the transmitted signal to follow the Lambert-Beer law. In other words, the detector should behave linearly with respect to the incoming intensity. Indeed, the Si diode signal is linearly proportional to the incoming x-ray flux (see Fig. 3), even when the full flux of the beamline, 10^{12} photons/s, is used.

E. Spatial and temporal overlap of laser and x-rays

The spatial overlap between laser and x-rays was obtained by placing a 50 μm diameter, 25 μm thick tungsten pinhole in the sample position. The x-ray position and size can be determined by scanning the pinhole through the x-rays using a two-dimensional translation stage (0.1 μm resolution), while monitoring the transmission intensity (see Fig. 4). Once the x-ray position is found, the pinhole is moved to that position and the attenuated laser beam is then guided through the pinhole and its position is optimized via a motorized laser mirror. Figure 4 shows example scans of the horizontal and vertical beam profiles of the laser and x-rays at the sample position. The x-ray spot size was determined to be less than 50 μm in both dimensions (FWHM). The beamline x-ray image monitor indicates that the x-ray beam is focused down to ~40 μm. The laser beam size was made larger than the x-ray spot (85 μm horizontally and 65 μm vertically), to ensure a uniformly excited sample and to facilitate the overlap of the pump and probe beams.

To set the temporal overlap a fast windowless photodiode having a rise time of 700 ps (AXUVHS5, International Radiation Detectors) was placed at the sample position. Using a 2.25 GHz oscilloscope (Agilent Infiniium) the relative laser and x-ray temporal delay could be determined. The laser pulse-picker timing was then adjusted to shift the laser timing in coarse steps of 12 ns, and then the phase-shifter was used for finer time steps. In general the two pulses can be overlapped to within 200 ps which is sufficient for samples where the excited state lifetime is >200 ps. For $[Fe(bpy)_3]^{2+}$ the excited state lifetime is about 650 ps[20] while

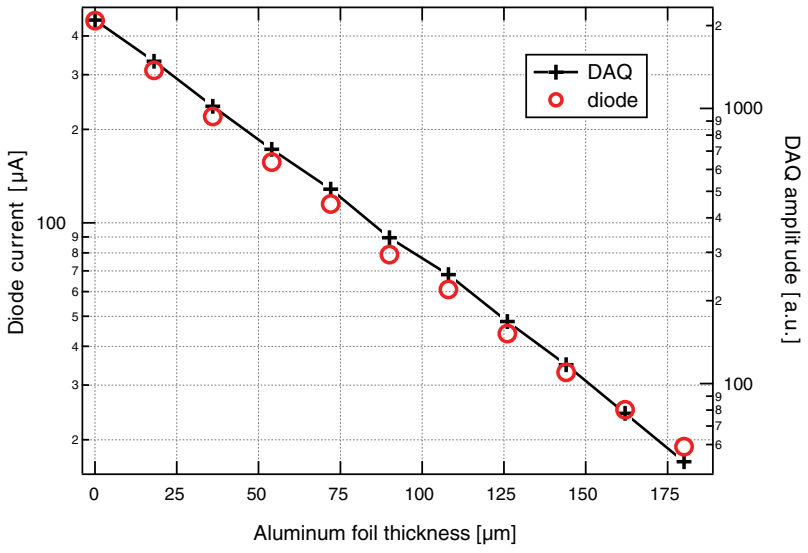

FIG. 3. (Color online) X-ray transmission signal (at 7.05 keV) measured by a fast diode. Left axis shows the diode current (red circles) while the right axis shows the digitized signal amplitude (black crosses). The flux was attenuated by placing aluminium foils of varying thickness in the beam. On a logarithmic scale the signal shows a linear dependence on absorber pathlength over the full range of x-ray flux indicating that the diode and DAQ are linear.

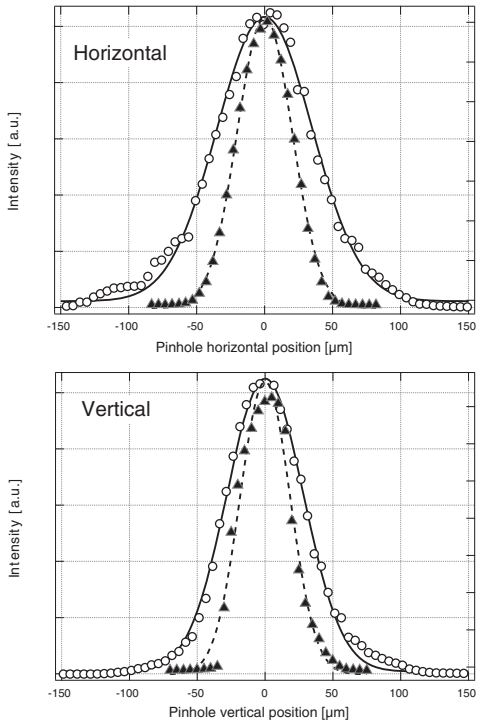

FIG. 4. Laser (circles) and x-ray (triangles) beam profiles scanned through a 50 μm diameter pinhole. Solid and dashed lines are Gaussian fits.

for $[Ru(bpy)_3]^{2+}$ the excited state lifetime is about 500 ns, with a strong dependence on sample concentration and solvent oxygen concentration.[38]

F. Electronic noise investigation

In order to assess the sensitivity of the MHz data acquisition system and to investigate any sources of electronic noise, we recorded the digitized individual output signals in transmission and fluorescence modes, corresponding to the 2 million samples, or approximately 1 s integration time. Figure 5 shows a histogram of the distribution of 500 000 zero measurements and 500 000 x-ray measurements (see Fig. 1) for an unpumped signal of a 7 mM aqueous solution of $[Fe(bpy)_3]^{2+}$ recorded at 7.125 keV. The fact that the transmission zero measurement distribution is narrower than the transmission x-ray measurement distribution shows that the electronic noise is smaller than the photon noise. The fluorescence signal shows similar characteristics with the additional feature that the Poisson distribution of the photon-counting events can clearly be resolved.[39]

III. SAMPLES AND SAMPLE ENVIRONMENT

Iron(II)-tris(2, 2′)-bipyridine chloride hexahydrate ($[Fe(bpy)_3]Cl_2 \cdot (H_2O)_6$) was dissolved in deionized water at concentrations ranging from 1 to 70 mM. The sample solutions were circulated using a magnetically driven gear pump through a sapphire nozzle creating a 100 μm thick jet, approximately 5 mm wide at the nozzle exit. The sample was excited with 532 nm pulses from the Duetto laser, at 520 kHz repetition rate and focussed to a 75 μm spot size (FWHM). Laser fluences ranging from 13 to 400 mJ/cm^2 were used. All measurements were performed in air.

Ruthenium(II)-tris(2, 2′)-bipyridine chloride hexahydrate ($[Ru(bpy)_3]Cl_2 \cdot (H_2O)_6$) was dissolved in deionized water at 80 mM concentration. The sample solution was handled identically to $[Fe(bpy)_3]^{2+}$. It was excited at both 355 and 532 nm at a repetition rate of 520 kHz. The laser spot size used was 75 μm (FWHM) which results in a fluence of 115 mJ/cm^2 for the 532 nm experiments and 86 mJ/cm^2 for the 355 nm experiments. The experiments were performed in a chamber under an 800 mbar atmosphere of 80% He and 20% N_2.

Lyophilized myoglobin (Mb) from equine skeletal muscle (Sigma, 95%–100%, salt free) was used without further purification to prepare liquid samples of ferric myoglobin (metMb) by dissolving the powder in de-gassed sodium phosphate buffer solution with pH 7 and then reducing it to the ferrous state (deoxyMb) under anaerobic conditions. To produce carboxymyoglobin (MbCO), the deoxyMb was bubbled with CO gas for approximately 20 minutes. During the experiments, the sample reservoir was kept under carbon monoxide atmosphere by flowing CO gas over the sample. Complete conversion to the ligated form and sample integrity were monitored by UV-Vis spectra collected simultaneously with the transient XAS experiments. The final carboxymyoglobin sample concentration was around 2 mM. It was excited with 532 nm focussed into a laser spot size of 75 μm (FWHM), at a fluence of 125 mJ/cm^2.

Static XAS spectra of myoglobin were measured on a 2 mM solution circulating through a quartz capillary having 2 mm path length and 50 μm walls using a peristaltic pump. The sample reservoir was kept in an ice bath to prevent degradation. The static XAS of the myoglobin samples were collected in both transmission and fluorescence mode; however, the transmission spectra did not show any clear signal due to the low concentration of the sample. The incoming and transmitted x-ray flux were measured using ion chambers filled with helium at approximately 1 bar, while the fluorescence was measured using a single-element Silicon drift detector (AXAS-SDD10-138500, Ketek). For the time-resolved measurements of MbCO the liquid sample was flowed through the same 100 μm thick jet previously described. It was possible to use an exposed jet in open atmosphere because the affinity of myoglobin to CO is very high[40,41] which makes the sample stable even in oxygen rich environments.

IV. RESULTS

A. Iron-tris bipyridine

As a test of the high repetition rate scheme and to estimate the increase in S/N compared to the 1 kHz experiments we used $[Fe(bpy)_3]^{2+}$ dissolved in water, the photocycle of which was previously fully characterized using a combination of ultrafast optical spectroscopic techniques and ps and fs XAS.[20,33,42–45] Laser excitation of the singlet ground state at 532 nm leads to population of a singlet

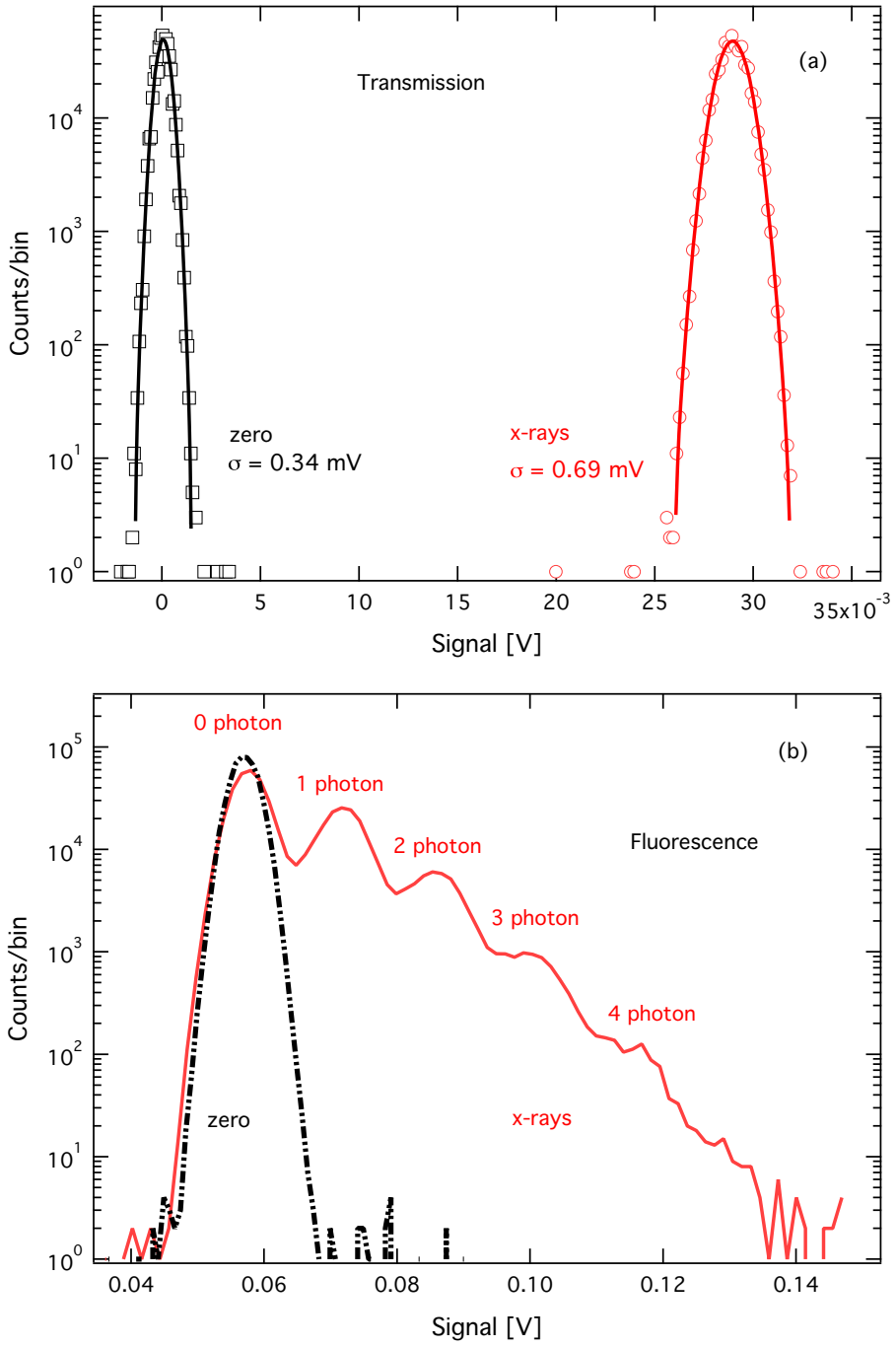

FIG. 5. (Color online) Pulse-height distribution of 1×10^6 samples recorded in transmission mode (a) and fluorescence mode (b) at 7.125 keV for a 7 mM sample of $[Fe(bpy)_3]^{2+}$. Gaussian fits to the histograms are shown as lines for the transmission signals. Note the clear peaks from multi-photon events in the fluorescence signal (0.56 photons/pulse).

metal-to-ligand-charge-transfer (^{1}MLCT) state, which then decays by ultrafast intersystem crossing to the lowest excited high-spin (HS) quintet state $^5T_2$, resulting in the Fe-N bond increasing by ~0.2 Å from the low-spin ground state to the HS excited state. This bond elongation was determined by Gawelda *et al.*[20,43] by analyzing the picosecond XANES and EXAFS transient spectra recorded at the Fe K absorption edge (7 keV) using the previous scheme of kHz data collection. These results serve to benchmark the present scheme.

For accurate comparison, we used a 25 mM concentration of aqueous $[Fe(bpy)_3]^{2+}$ as in the kHz experiments.[20] It should be kept in mind that it is not possible to strictly compare the two experiments because of the 532 nm/10 ps excitation here versus the 400 nm/100 fs in the kHz experiments. However, given the ultrafast departure of population from the MLCT states, which we previously determined to be ~150 fs,[44,45] and the fact that there is no known excited-state absorption at 532 nm,[33,42] the difference in excitation pulse

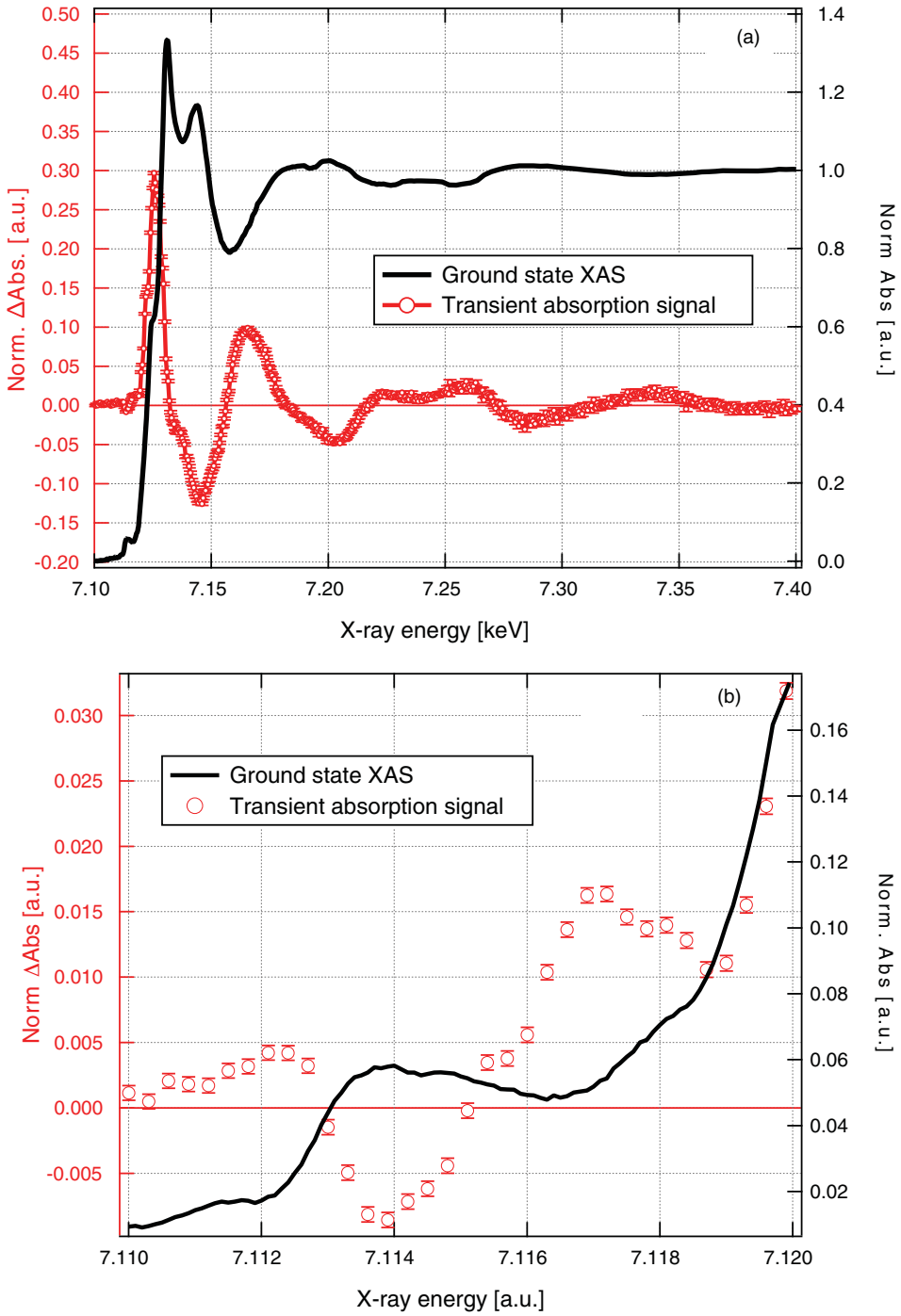

FIG. 6. (Color online) (a) The near-edge XAS of a 25 mM aqueous solution of $[Fe(bpy)_3]^{2+}$ collected in fluorescence yield mode showing the ground-state spectrum (black line) and the average of 11 transient XAS scans measured using the high-repetition rate setup (red markers) and a fluence of 100 mJ/cm^2. (b) Zoom of the ground state pre-edge features (black line) and the transient XAS (red circles) in the same energy range using a pump fluence of 200 mJ/cm^2.

width should not affect the results. However, the absorption cross section is approximately three times higher at 532 nm than at 400 nm.[42]

Due to the lower pulse energy of the Duetto laser compared to amplified kHz laser systems, it was necessary to tightly focus the laser beam in order to maintain a comparable laser fluence on the sample. In the previous kHz experiments[20] the laser focus was around 200–250 μm, while the present scheme makes use of 60–85 μm laser spot sizes. Consequently, the x-rays also needed to be more tightly focussed (see Fig. 4).

Figure 6(a) shows both the ground state XAS of a 25 mM solution of $[Fe(bpy)_3]^{2+}$ and the average of 11 scans of the transient XAS measured 50 ps after excitation at 532 nm using the high-repetition rate system and a fluence of 100 mJ/cm^2. The latter agrees very well with the transient previously recorded at 1 kHz.[20,39] At the maximum of the transient signal, 7.126 keV (all subsequent S/N ratios

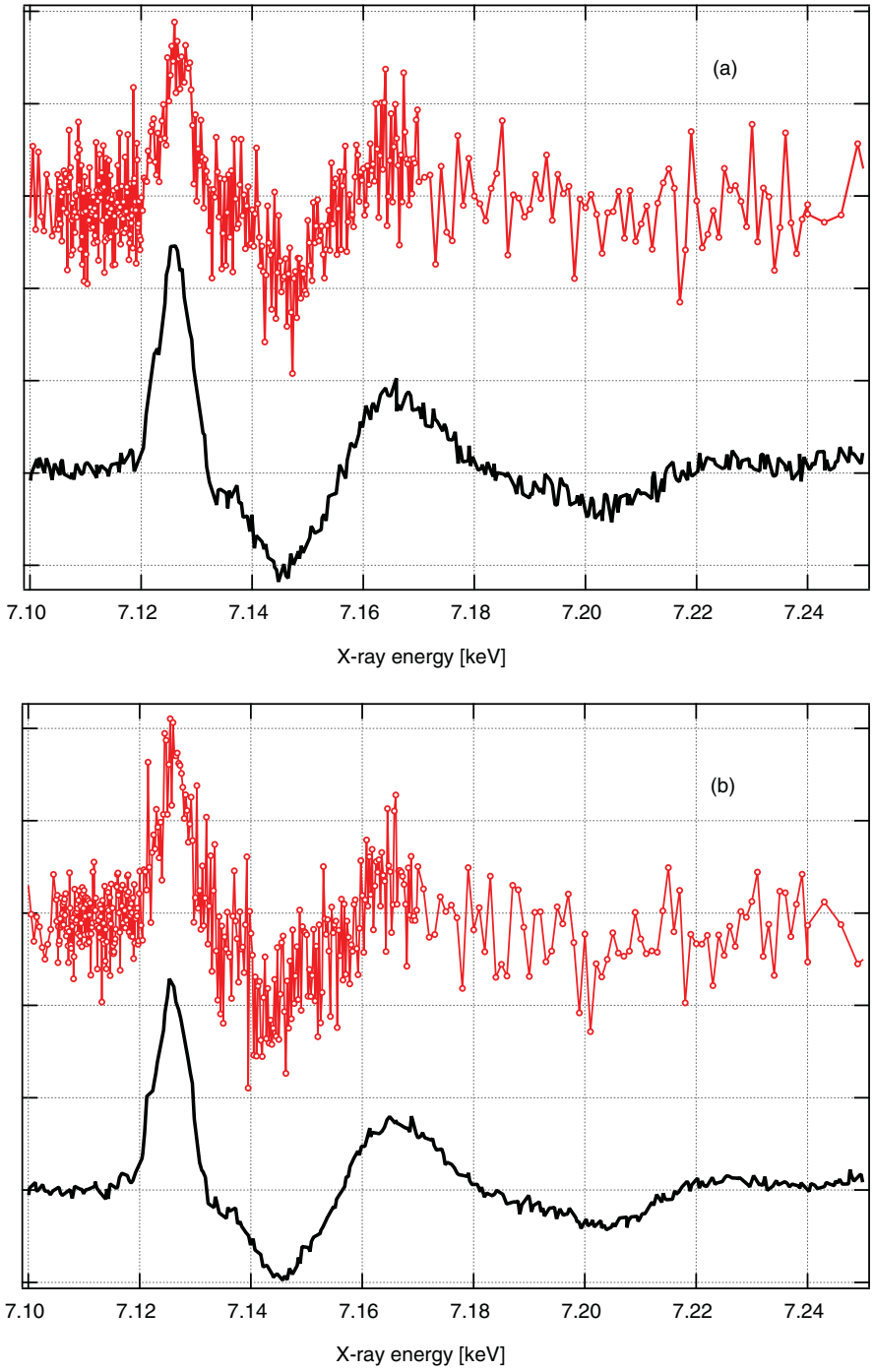

FIG. 7. (Color online) Representative single scans of the near-edge transient XAS of a 25 mM aqueous solution of $[Fe(bpy)_3]^{2+}$, in transmission (a) and fluorescence (b) modes, collected using both the kHz (red circles) and high-repetition rate (black line) data acquisition techniques.

refer to the signal at this energy), we obtain a S/N $\simeq$ 158 in fluorescence mode, and 142 transmission mode. This translates to a S/N $\simeq$ 45 per scan in both modes. Increasing the laser fluence to 200 mJ/cm^2, a value closer to that used in the kHz experiments, the S/N per scan increases to $\sim$70 in both modes. Comparisons of single scans taken using the two different techniques are shown in Fig. 7.

Since the Fe K-edge XAS spectrum of the laser-excited $[Fe(bpy)_3]^{2+}$ is known,[20] it is possible to extract the excited-state population by subtracting the unexcited spectrum (low spin) from the laser-excited spectrum (high spin). The excited state spectrum is related to the measured transient XAS, the fraction of excited species and the unexcited spectrum via the following equation:[20,43]

$$\Delta\mathrm{Abs}(E,t) = f(t)\left[\mathrm{A}_p(E,t) - A_{unp}(E)\right], \qquad (3)$$

with $f(t)$ being the fractional population of the excited state at a given time delay, A_p and A_{unp} the laser pumped and unpumped normalized XAS spectra of the sample being studied, respectively. We then extract an excitation yield of 60%

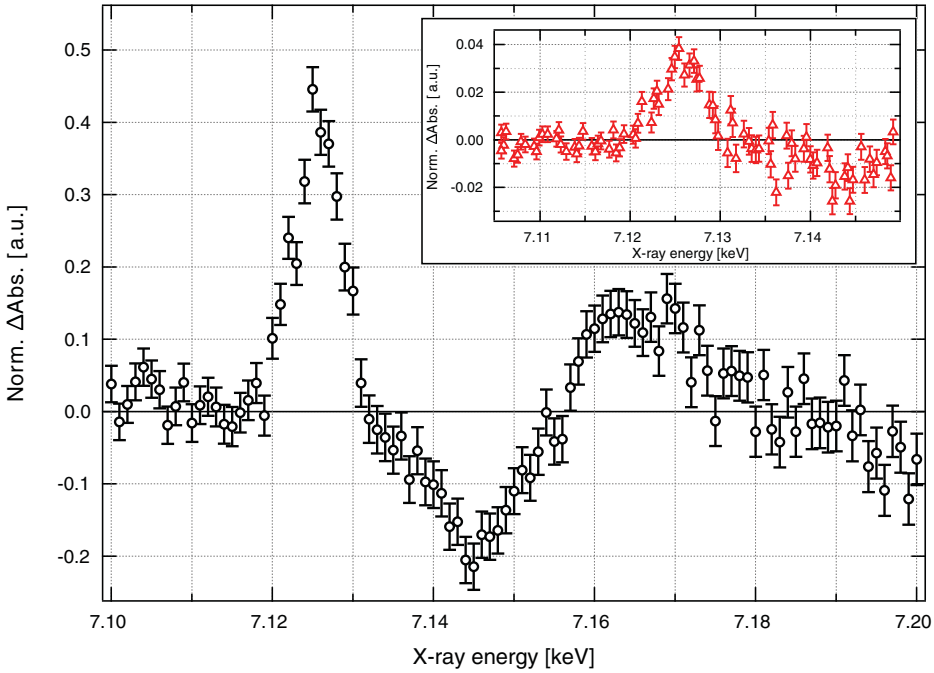

FIG. 8. (Color online) Average of 10 transient XAS scans 50 ps after excitation, of a 1 mM $[Fe(bpy)_3]^{2+}$ solution excited with a pump fluence of 150 mJ/cm^2. The inset shows a single transient XAS scan of a 25 mM aqueous solution of $[Fe(bpy)_3]^{2+}$ at 50 ps delay and collected in fluorescence yield mode with a pump fluence of 13 mJ/cm^2.

for the 25 mM sample excited with 100 mJ/cm^2. When using a laser fluence of 200 mJ/cm^2 the derived excitation yield increases to 80%–90%. This value is over three times larger than the previously reported 22% achieved in the kHz experiments,[20,43] and can be explained by the approximately three times larger optical absorption coefficient at 532 nm compared to at 400 nm, and by the fact that the longer excitation pulse duration of 10 ps compared to 100 fs results in less nonlinear excitation of the solvent[39] and more efficient excitation of the sample.

We can now attempt a more quantitative estimate of the gain in S/N at 520 kHz compared to 1 kHz. The S/N is proportional to the excitation yield, the square root of the incoming x-ray flux and the repetition rate of the laser. Therefore the gain in S/N is given by the ratio:

$$\frac{(\mathrm{S/N})_{520\,\mathrm{kHz}}}{(\mathrm{S/N})_{1\,\mathrm{kHz}}} \simeq \frac{70\%}{22\%}\sqrt{\frac{I_{\mathrm{x\text{-}ray}}^{520\,\mathrm{kHz}}}{I_{\mathrm{x\text{-}ray}}^{1\,\mathrm{kHz}}}}\sqrt{\frac{520}{1}}\,, \tag{4}$$

where we have taken as average photolysis yield (70%) from the above estimates. Estimating the difference in x-ray flux between the former 1 kHz experiments and the present ones is not straightforward; however, we estimate an approximate factor of 8 decrease between the two experiments, due to differences in the beamline setup.[46] Thus the factor of three higher photolysis yield is compensated for by the decrease in x-ray flux. We conclude that the increase in S/N mainly scales with the square root of the increase in repetition rate.

Figure 6(b) shows a zoom of the pre-edge region. The black curve shows the ground-state pre-edge signal while the markers show the transient XAS measured using a fluence of 200 mJ/cm^2. The pre-edge features correspond to the dipole-forbidden 1s → 3d bound-bound transitions and are sensitive to the spin-state of the molecule.[47] Since these features are less than 1% of the absorption edge jump, very high signal-to-noise is required to resolve them.[48] As expected for an octahedrally coordinated low-spin Fe^{2+} metal center the ground-state shows a clear absorption peak corresponding to the 1s → 3d(e_g) transition (7.1135 keV). Upon excitation to the high-spin state, we see an increase in absorption at lower energies corresponding to the 1s → 3d(t_{2g}) transition (7.1125 keV) and a decrease at higher energies as the 3d(e_g) levels are populated in the high-spin state (7.114 keV). There is also an increase in absorption at higher energies (7.117 keV) in a region of the spectrum where peaks have been tentatively assigned to edge transitions.[47] These pre-edge features were also seen by Nozawa *et al*. using kHz laser excitation[48] but the increased S/N in the present experiments allow us to perform a line shape analysis which will be presented in a forthcoming publication.

Given the gain in S/N, we can now decrease the sample concentration and/or the laser excitation fluence. Figure 8 shows the average of 10 individual scans of the transient XAS measured in FY mode of a 1 mM solution of aqueous $[Fe(bpy)_3]^{2+}$. This measurement was taken with a fluence of 150 mJ/cm^2 and both transmission and FY data were recorded simultaneously at 50 ps after excitation. The total acquisition time for the data shown was about 1 h, yielding S/N $\simeq$ 4.6 per scan in fluorescence and S/N $\simeq$ 3 in transmission. The inset to Fig. 8 shows the transient XAS signal in FY mode of a 25 mM solution of aqueous $[Fe(bpy)_3]^{2+}$, again at 50 ps time delay, but excited with only 13 mJ/cm^2.

In the limit of low laser fluence, we are still able to measure a time-resolved signal with a S/N $\simeq$ 8 in a single scan. The results of Fig. 8 show that we can now measure very dilute or photochemically unstable samples within reasonable data acquisition times, opening the way for the investigation of biological samples under physiological conditions.

B. Ruthenium tris-bipyridine

One of the advantages of the high-repetition rate setup is its portability. The tender x-ray beamline PHOENIX I has recently come online at the SLS enabling us to measure core transitions of species not covered by the hard x-ray microXAS beamline. In order to ascertain the feasibility of such low x-ray energy measurements we chose to investigate $[Ru(bpy)_3]^{2+}$ which we previously characterized by ps XAS at the Advanced Light Source (ALS, Berkeley, USA).[16,49] Ruthenium tris-bipyridine is a model system for intramolecular electron transfer reactions and is representative of a large class of compounds for applications in solar energy conversion. Upon visible-UV excitation at either 355 or 532 nm, one reaches the ^{1}MLCT (metal-to-ligand-charge-transfer) state, which decays to the long-lived (several hundred ns in room temperature aqueous solutions[50]) ^{3}MLCT state on ultrafast timescales.[34] The lifetime of the ^{3}MLCT state can be reduced by the presence of oxygen in the solvent.[38] In the MLCT state the electron is localized on one of the bipyridine ligands: $[Ru^{III}(bpy^-)(bpy)_2]^{2+}$.[51] Exciting at 532 nm reaches the red wing of the absorption, but it has the advantage of not being reabsorbed by the ^{3}MLCT state.[50] Exciting at 355 nm has the advantage of a larger absorption cross section, resulting in a higher excitation probability, but there is a strong ligand-centered excited state absorption at 355 nm in the ^{3}MLCT which may result in sequential two-photon absorption. The lifetime of this state is <10 ps, meaning we are not probing it at 50 ps, but the potential exists for other excited photoproducts to occur, including both $[Ru(bpy)_3]^+$ and $[Ru(bpy)_3]^{3+}$.[50] By probing the system at the Ru $L_{2,3}$ edges (2.8–3 keV) in picosecond experiments at 1 kHz, an oxidation state-induced change in the ionization potential of 1.8 eV was detected and a Ru–N bond contraction of ~0.03 Å was derived.[49,52]

Excitation of an 80 mM sample of $[Ru(bpy)_3]^{2+}$ at 532 nm with a fluence of 115 mJ/cm^2 yield the two-dimensional time-energy plot of Fig. 9. The data were collected as monochromator energy scans around the Ru-L_3 edge and taken with time steps of 12 ns out to 200 ns after excitation. Each energy scan represents the average of 4 individual scans and the total data acquisition time required was 2 h. From Fig. 9 it is clear that, within the signal-to-noise, the transient difference signal appears to simply decay in amplitude with no energy shifts over the course of its relaxation, confirming that we are probing the lifetime of the ^{3}MLCT state. Neither the ground-state XAS nor the transient indicate the presence of any photoproducts, permanent or photoexcited, other than the expected $[Ru^{III}(bpy^-)(bpy)_2]^{2+}$. The timescale of the excited-state relaxation is 107 $\pm$ 16 ns, typical of a high-concentration solution with oxygen

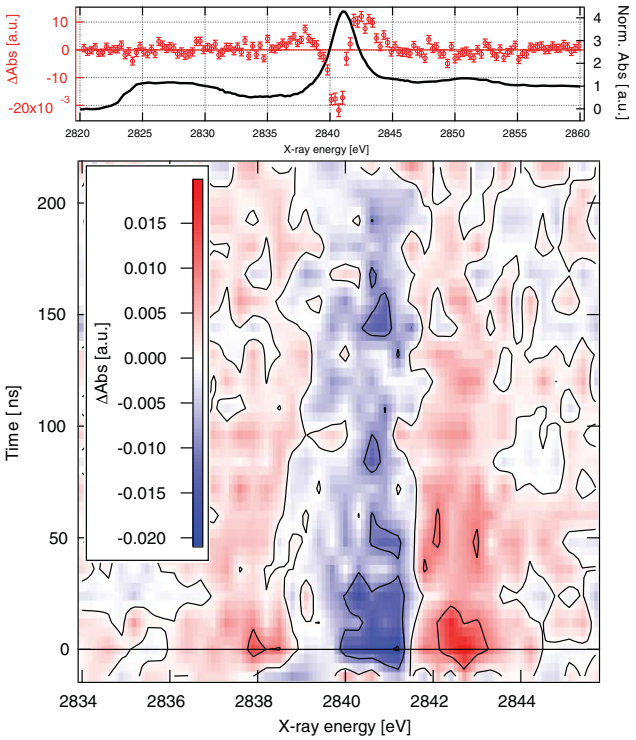

FIG. 9. (Color online) Top: Comparison between the ground-state XAS (black line) and transient XAS (red circles) measured 175 ps after time zero at the Ru L_3 edge of an 80 mM solution of $[Ru(bpy)_3]^{2+}$ excited at 532 nm with a fluence of 115 mJ/cm^2. Note that the pre-edge signal on the ground-state XAS, from 2825 to 2830 eV, is the Cl K-edge absorption of the counter-ion. Bottom: Two-dimensional time-energy XAS measured under the same conditions.

content.[38] Figure 10 shows a transient energy scan comparing excitation at 532 ($\Delta t = 175$ ps, average of 8 scans) and 355 nm ($\Delta t = 5.6$ ns, average of 6 scans). Both signals show the expected decrease/increase in absorption at 2841/2843 eV due to oxidation of the Ru atom from 2+ to 3+. The absorption increase at 2838 eV is due to the creation of a hole in the Ru d(t_{2g}) orbital, which can be accessed from the $2p_{3/2}$ core orbital when an electron is transferred to the ligand.[16,18,49] The fluence at 532 nm was 115 mJ/cm^2 while for 355 nm it was 86 mJ/cm^2. The differential absorption change is similar for the two signals. The absorption cross section at 532 nm is approximately 3–4 times lower than that at 355 nm, however due to the high concentration of the sample (80 mM) the optical density of the 100 μm jet is around 1 for 532 nm.

These proof-of-principle results illustrate the portability of the high-repetition rate system over the amplified kHz system. The primary challenge to moving to lower x-ray energies is the loss of photons to solvent scattering and absorption. The x-ray transmission through a 100 μm jet of pure water is less than 15% at photon energies below 3 keV, making absorption experiments increasingly difficult. Clearly the ability to take data at MHz repetition rates is a distinct advantage for this energy range as the faster data acquisition in part compensates for the loss in x-ray flux.

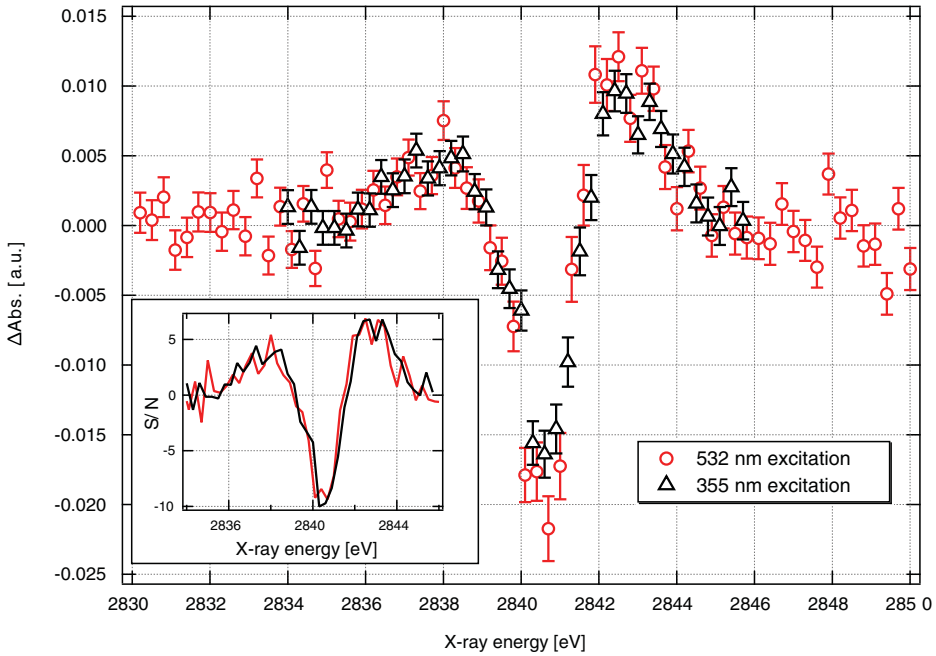

FIG. 10. (Color online) Comparison of the transient transmission XAS of an 80 mM aqueous solution of $[Ru(bpy)_3]^{2+}$ for excitation at 355 nm/Δt=5.6 ns (black triangles) and 532 nm/Δt=175 ps (red circles). The inset shows the S/N of the data with the 355 nm data being an average of 6 scans and the 532 nm data an average of 8 scans.

C. Carboxymyoglobin

The ability to acquire time-resolved XAS data of highly dilute samples with reasonable signal-to-noise is crucial for the study of biological samples. Myoglobin (Mb), whose main function is to facilitate oxygen diffusion in mammal muscle cells, is one of the most studied metalloproteins. Its active center consists of a porphyrin ring with an iron atom in the center (the metalloporphyrin), to which small diatomic molecular ligands such as O_2, CO, NO and CN can bind. The ligand dissociation can be triggered by irradiation with visible light and the recombination dynamics has led to innumerable studies using a broad range of time-resolved optical techniques.[53,54] In the case of carboxymyoglobin (MbCO), the recombination occurs in microseconds to milliseconds.[55–57] It was first investigated by time-resolved XAS with μs resolution by Mills *et al.*,[58] who developed a scheme using a synchronized Nd:YAG laser to photolyze the MbCO in a flowing sample solution and probed around the Fe K-shell XANES region (7 keV). Several early XAS measurements also used cryogenic temperatures to lengthen the CO rebinding time in solid samples with photolysis triggered using flashlamp illumination.[59–61] Later, Clozza *et al.*[62] developed an apparatus that used the synchrotron as a quasi-continuous source where the data acquisition was triggered by the laser making it possible to make FY measurements at well-defined time delays using time-windows down to the millisecond time scale. Several years later Chance *et al.* took advantage of advances in energy-resolving x-ray fluorescence detectors to perform measurements on MbCO using both laser[63] and flashlamp excitation[64] allowing them to collect time-resolved XAS spectra in the several microseconds to milliseconds time domain for dilute cryogenic samples (1–4 mM). More recently Arcovito, Della Longa and coworkers have used myoglobin single crystals to perform polarized XAS measurements to collect data both parallel and perpendicular to the heme normal which has allowed them to see pronounced changes after photolysis in the Fe–CO bond direction.[65–67] They have also investigated the temperature-dependence of the CO-rebinding rate[68] and showed that it is possible to photo-reduce the Fe center with x-rays,[69] emphasizing the potential for sample damage through x-ray exposure. Concurrent with these experimental advances, analysis tools have also matured, making it possible to extract more detailed structural information from both the XANES (Refs. 67 and 70) and EXAFS (Ref. 64) regions of the spectrum. It should be stressed that the majority of these measurements concerned cryogenically cooled solid samples, therefore far from physiological conditions.

Recording the time-resolved XAS experiments at high repetition rates using the pulse-to-pulse data acquisition is not convenient for systems whose ground-state recovery is longer than the pulse repetition period. This is the case with MbCO which has a ligand recombination time of milliseconds.[56] Reducing the repetition rate of the laser so that the sample can relax between x-ray probe pulses cancels the advantages of the high repetition rate. An alternative approach would be to measure data at fixed (e.g. 1 s) alternating intervals for the laser-excited and the unexcited XAS. The unpumped measurement is achieved by moving the laser position horizontally with a motorized laser mirror to ensure a complete lack of laser/x-ray overlap. The differential absorption, or slow-difference transient, can then be calculated using these data. The transient XAS signals are still calculated as in Eqs (1) and (2), the difference being that now the pumped signal is

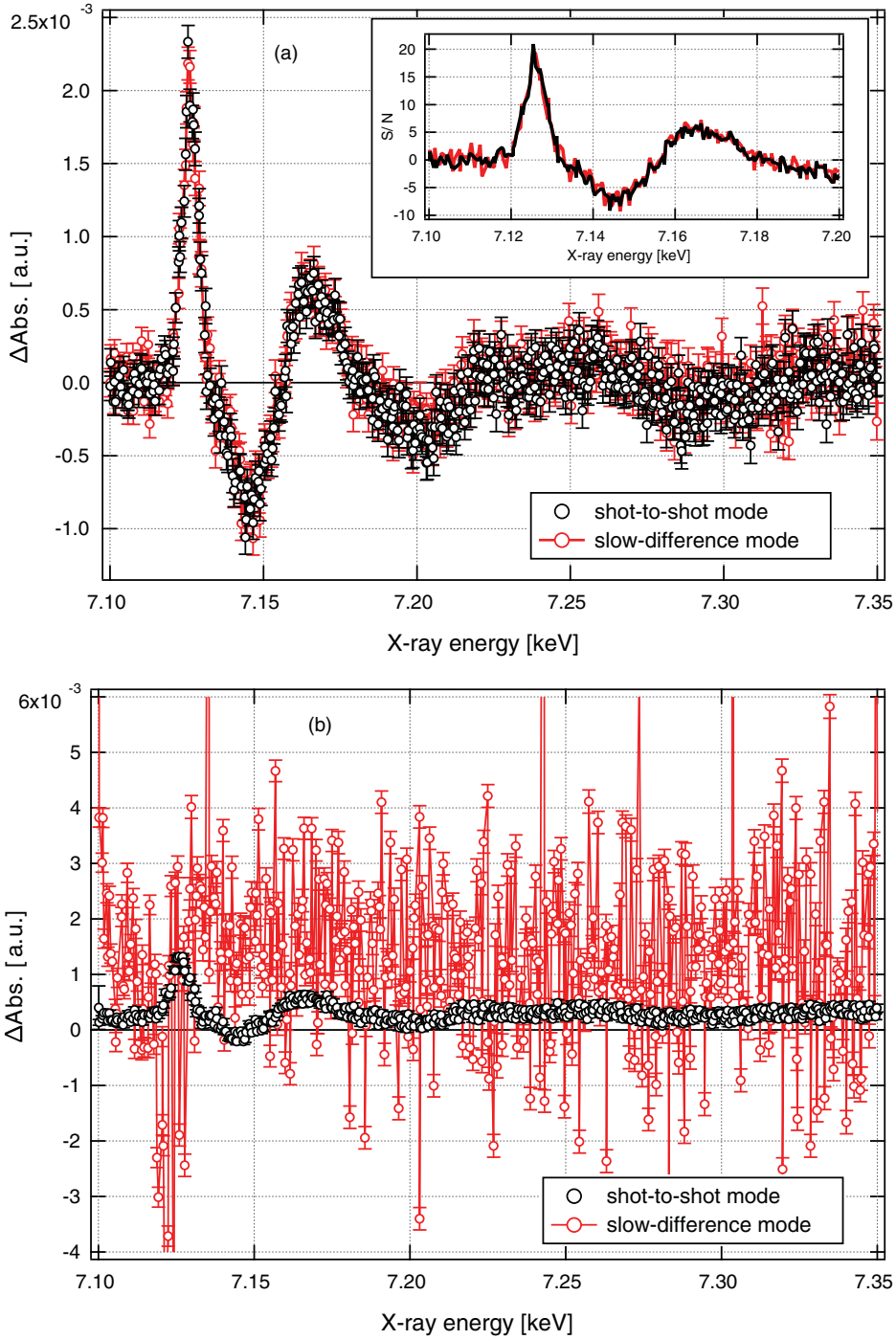

FIG. 11. (Color online) Comparison of the transient XAS signal of a single measurement of a 7 mM aqueous solution of $[Fe(bpy)_3]^{2+}$ excited with 150 mJ/cm^2 laser fluence, using the pulse-to-pulse and the slow-difference modes in fluorescence (a) and transmission (b). Black circles show the data collected using the pulse-to-pulse mode and the red circles show the data collected using the slow-difference mode. Note that both measurement modes have the same S/N for fluorescence (see inset on (a)) while being drastically different in transmission.

defined as the signal measured when the laser and x-rays are overlapped spatially and unpumped is the signal with no overlap.

Using this alternative scan technique, other sources of noise can contribute to the measured signal since the differential absorption is now being calculated on a 1 s timescale as opposed to a 1 μs timescale. In order to investigate the noise characteristics of this slow-difference technique, we recorded a set of transient energy spectra of a sample of 7 mM aqueous $[Fe(bpy)_3]^{2+}$ at 50 ps time delay using simultaneously both the regular (pulse-to-pulse) and slow-difference scan modes, enabling a direct comparison of both scan modes under identical experimental conditions.

The transient XAS data collected in fluorescence and transmission using both modes is shown in Fig. 11. A comparison of the transient XAS data recorded in FY mode

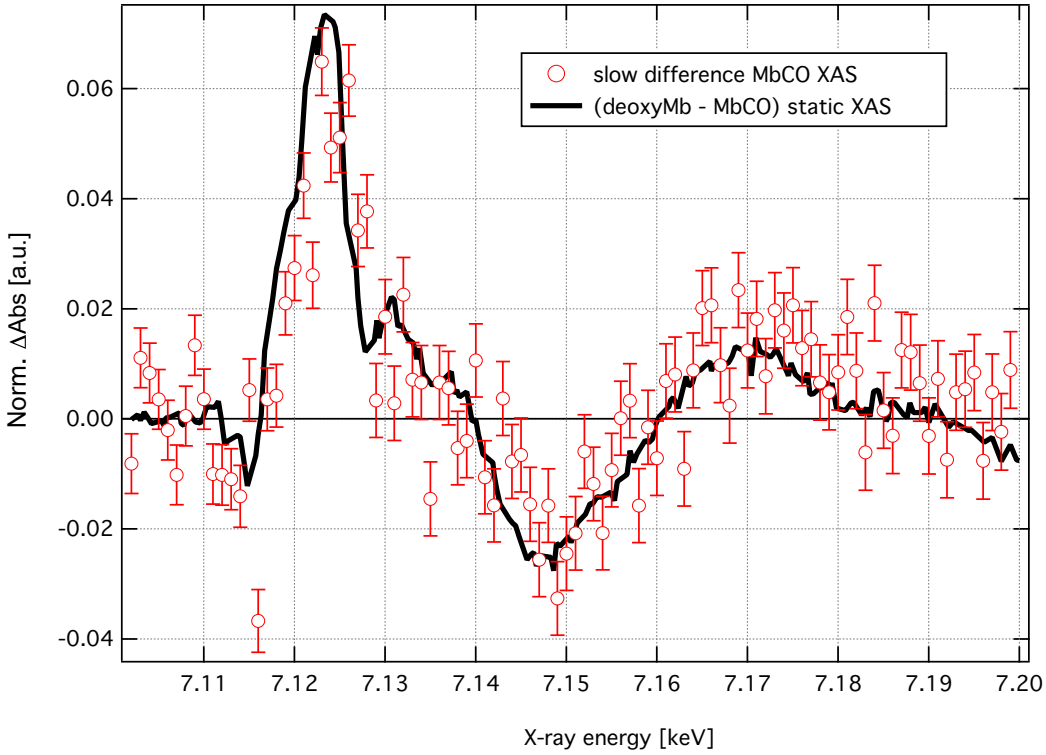

FIG. 12. (Color online) Transient XAS of 2 mM MbCO collected in fluorescence yield mode. The sample was excited at 125 mJ/cm^2 laser fluence. The black curve represents the difference XAS based on the static spectra of deoxyMb and MbCO assuming an excitation yield of 21%.

using both data acquisition modes show no new sources of noise that can obscure the signal in the slow-difference mode. The S/N of both data sets (see inset in Fig. 11 (a)) is almost identical from which we conclude that in the case of samples having long-lived excited states, we can use the slow-difference scan mode in fluorescence to collect transient XAS data while only incurring a factor of two penalty in data acquisition times. The comparison of the two scan modes in transmission is shown in Fig. 11 (b). The transmission signal recorded using the slow-difference scan reveals an enormous source of noise which obscures the signal, in stark contrast to the pulse-to-pulse mode. This indicates that there is an external source of noise on the 1 s time scale, which is absent on the 1 μs timescale, and is most probably due to the flow of the liquid sample. Indeed small fluctuations in the jet flow speed, pressure and thickness easily introduce changes in the x-ray absorption signal on the 1 s timescale resulting in large random changes in the differential absorption. This noise easily overwhelms the transient transmission signal and reinforces the importance of measuring the difference signals on a pulse-to-pulse basis. For the study of dilute samples it is preferable to use FY detection.

The averaged transient FY XAS signal of photo-excited MbCO is shown in Fig. 12. It consists of 32 individual scans and a data collection time of 4.5 h, and was measured using the slow-difference scan mode, with a laser fluence of 125 mJ/cm^2. It exhibits several pronounced changes in the XANES region of the spectrum, with the largest change in absorption at 7.123 keV being due to a shift to lower-energy of the Fe absorption edge. This transient represents the difference in XAS spectra of the ligated minus the unligated protein. We measured the static XAS spectra of the CO-ligated form of myoglobin (MbCO), the unligated form of myoglobin (deoxyMb), and the unreduced form of myoglobin (metMb), as reference. After ligand photo-detachment and in the absence of any intermediate structure on the time scale of the measurement, we expect the spectrum of the photo-product to resemble that of deoxyMb. The transient spectrum should then be similar to the difference spectrum of the deoxy form minus the ligated form. This difference spectrum represents a limiting case in which all the ligands are photo-detached and no intermediate structure is present. This is a good approximation for MbCO where there is almost no geminate recombination[55,56] and no evidence of any partially bound structural intermediates.[5] A scale factor can therefore be used when comparing it to the measured transient XAS, allowing us to estimate the fraction of excited species. Overlaid on the experimental transient XAS is the difference of the deoxy static spectrum minus the MbCO static spectrum which has been scaled by a factor of 0.21 for comparison, implying an excitation yield of ~21%. Because the measurements were done using the slow-difference scan mode, the time delay is not well defined. Since the time interval between consecutive laser pump pulses at 520 kHz is 2 μs, the excited-state population is an ensemble composed of the population at 50 ps, which is the time delay set between the pump and probe pulses, and 2 μs, which is the time interval between two consecutive laser pulses. In essence every laser pump pulse

excites a sample which is only partially relaxed, leading to a larger average population of deoxyMb than would exist after a single excitation pulse.

Comparing the measured transient signal with the predicted difference based on the static XAS, one can see that within the error bars, both signals coincide. A more detailed discussion of these results will be presented in a forthcoming publication.

V. CONCLUSION AND OUTLOOK

We have developed a flexible setup for x-ray absorption spectroscopy with <100 ps temporal resolution at MHz data acquisition rates. Our configuration makes use of all the available isolated x-ray pulses from the hybrid filling mode currently employed at most third-generation synchrotrons. This allows the measurement of laser-induced changes on the x-ray absorption spectra of dilute samples with concentrations of the order of a mM. We demonstrate the ability of the setup to perform shot noise limited measurements with an increase in S/N of the order of $\simeq \sqrt{f_L}$ where f_L is the repetition rate of the laser pump (520 kHz), compared to the 1 kHz data acquisition techniques. The portability of the setup has also been demonstrated on a tender x-ray beamline. As a final test of the high-repetition rate data acquisition technique we also measured the differential XAS of a dilute solution of carboxymyoglobin.

The temporal resolution is limited at present by the duration of the synchrotron x-ray pulses. This can be improved to a few picoseconds using the so-called "low-alpha" mode[71–73] available at several third-generation synchrotron sources. The moderate decrease in x-ray flux is compensated for by the higher repetition rate, providing intermediate temporal resolution between the hundreds of ps obtained directly from synchrotrons and hundreds of fs from the electron-laser slicing scheme.[74] Finally, the simplicity of the present scheme means that it can be implemented at any synchrotron beamline, and extended to any time-resolved x-ray technique (absorption, emission, or diffraction).

ACKNOWLEDGMENTS

We thank Dr. Gaudenz Jud, Mr. A. Oggenfuss, Mr. Beat Meyer, and Mr. R. Wetter for their assistance during this project and Drs. W. Gawelda and M. Johnson for fruitful discussions. This work was financed by the FNS via Contract Nos. 200020-12723, 200021-116394, and 206021-117401 and the NCCR MUST.

[1] M. Chergui and A. H. Zewail, ChemPhysChem **10**, 28 (2009).
[2] S. L. Johnson, P. Beaud, E. Vorobeva, C. J. Milne, E. D. Murray, S. Fahy, and G. Ingold, Acta Crystallogr. A **66**, 157 (2010).
[3] T. Elsaesser and M. Woerner, Acta Crystallogr. A **66**, 168 (2010).
[4] P. Beaud, S. L. Johnson, E. Vorobeva, U. Staub, R. A.D. Souza, C. J. Milne, Q. X. Jia, and G. Ingold, Phys. Rev. Lett. **103**, 155702 (2009).
[5] F. Schotte, M. Lim, T. Jackson, A. Smirnov, J. Soman, J. Olson, G. Phillips, M. Wulff, and P. A. Anfinrud, Science **300**, 1944 (2003).
[6] S. Bratos and M. Wulff, Adv. Chem. Phys. **137**, 1 (2008).
[7] T. K. Kim, J. H. Lee, M. Wulff, Q. Kong, and H. Ihee, ChemPhysChem **10**, 1958 (2009).
[8] C. Bressler and M. Chergui, Chem. Rev. **104**, 1781 (2004).
[9] L. Chen, Angew. Chem., Int. Ed. **43**, 2886 (2004).
[10] L. X. Chen, X. Zhang, J. V. Lockard, A. B. Stickrath, K. Attenkofer, G. Jennings, and D.-J. Liu, Acta Crystallogr. A **66**, 240 (2010).
[11] C. Bressler, R. Abela, and M. Chergui, Z Kristallogr. **223**, 307 (2008).
[12] C. Bressler and M. Chergui, Annu. Rev. Phys. Chem. **61**, 263 (2010).
[13] M. Chergui, Acta Crystallogr. A **66**, 229 (2010).
[14] L. X. Chen, J. Electron Spectrosc. **119**, 161 (2001).
[15] L. X. Chen, G. Jennings, T. Liu, D. Gosztola, J. Hessler, D. Scaltrito, and G. Meyer, J. Am. Chem. Soc. **124**, 10861 (2002).
[16] M. Saes, C. Bressler, R. Abela, D. Grolimund, S. L. Johnson, P. A. Heimann, and M. Chergui, Phys. Rev. Lett. **90**, 047403 (2003).
[17] M. Saes, F. van Mourik, W. Gawelda, M. Kaiser, M. Chergui, C. Bressler, D. Grolimund, R. Abela, T. E. Glover, P. A. Heimann, R. W. Schoenlein, S. L. Johnson, A. M. Lindenberg, and R. W. Falcone, Rev. Sci. Instrum. **75**, 24 (2004).
[18] W. Gawelda, C. Bressler, M. Saes, M. Kaiser, A. N. Tarnovsky, D. Grolimund, S. L. Johnson, R. Abela, and M. Chergui, Phys. Scr. **T115**, 102 (2005).
[19] M. Khalil, M. A. Marcus, A. L. Smeigh, J. K. McCusker, H. H.W. Chong, and R. W. Schoenlein, J. Phys. Chem. A **110**, 38 (2006).
[20] W. Gawelda, V.-T. Pham, M. Benfatto, Y. Zaushitsyn, M. Kaiser, D. Grolimund, S. L. Johnson, R. Abela, A. Hauser, C. Bressler, and M. Chergui, Phys. Rev. Lett. **98**, 4 (2007).
[21] V.-T. Pham, W. Gawelda, Y. Zaushitsyn, M. Kaiser, D. Grolimund, S. L. Johnson, R. Abela, C. Bressler, and M. Chergui, J. Am. Chem. Soc. **129**, 1530 (2007).
[22] L. X. Chen, X. Zhang, E. C. Wasinger, K. Attenkofer, G. Jennings, A. Z. Muresan, and J. S. Lindsey, J. Am. Chem. Soc. **129**, 9616 (2007).
[23] C. G. Elles, I. A. Shkrob, R. A. Crowell, D. A. Arms, and E. C. Landahl, J. Chem. Phys. **128**, 061102 (2008).
[24] R. M. van der Veen, C. J. Milne, A. E. Nahhas, F. Lima, V.-T. Pham, J. Best, J. A. Weinstein, C. N. Borca, R. Abela, C. Bressler, and M. Chergui, Angew. Chem., Int. Ed. **48**, 2711 (2009).
[25] N. Huse, H. Wen, D. Nordlund, E. Szilagyi, D. Daranciang, T. A. Miller, A. Nilsson, R. W. Schoenlein, and A. M. Lindenberg, Phys. Chem. Chem. Phys. **11**, 3951 (2009).
[26] H. Wen, N. Huse, R. W. Schoenlein, and A. M. Lindenberg, J. Chem. Phys. **131**, 234505 (2009).
[27] N. Huse, T. K. Kim, L. Jamula, J. K. McCusker, F. M.F. de Groot, and R. W. Schoenlein, J. Am. Chem. Soc. **132**, 6809 (2010).
[28] N. Huse, H. Cho, K. Hong, L. Jamula, F. M.F. de Groot, T. K. Kim, J. K. McCusker, and R. W. Schoenlein, J. Phys. Chem. Lett. **2**, 880 (2011).
[29] W. Widdra, D. Brocker, T. Giessel, I. Hertel, W. Kruger, A. Liero, F. Noack, V. Petrov, D. Pop, P. Schmidt, R. Weber, I. Will, and B. Winter, Surf. Sci. **543**, 87 (2003).
[30] T. Giessel, D. Brocker, P. Schmidt, and W. Widdra, Rev. Sci. Instrum. **74**, 4620 (2003).
[31] E. Stern and D. Brewe, AIP Conf. Proc. **882**, 24 (2007).
[32] D. Brewe, S. Heald, E. Stern, K. Beck, and Y. Feng, AIP Conf. Proc. **705**, 1399 (2004).
[33] A. Cannizzo, C. J. Milne, C. Consani, W. Gawelda, C. Bressler, F. van Mourik, and M. Chergui, Coord. Chem. Rev. **254**, 2677 (2009).
[34] A. Cannizzo, F. van Mourik, W. Gawelda, G. Zgrablic, C. Bressler, and M. Chergui, Angew. Chem. Int. Ed. **45**, 3174 (2006).
[35] P. Beaud, S. L. Johnson, A. Streun, R. Abela, D. Abramsohn, D. Grolimund, F. S. Krasniqi, T. Schmidt, V. Schlott, and G. Ingold, Phys. Rev. Lett. **99**, 174801 (2007).
[36] C. Borca, D. Grolimund, M. Willimann, B. Meyer, K. Jefimovs, J. Comamala, and C. David, J. Phys.: Conf. Ser. **186**, 012003 (2009).
[37] C. Bressler, M. Saes, M. Chergui, D. Grolimund, R. Abela, and P. Pattison, J. Chem. Phys. **116**, 2955 (2002).
[38] M. Saes, Picosecond X-ray absorption spectroscopy: application to coordination chemistry compounds in solution, Ph.D. thesis, (Ecole Polytechnique Fédérale de Lausanne, 2004).
[39] W. Gawelda, Time-resolved x-ray absorption spectroscopy of transition metal complexes, Ph.D. thesis, (Ecole Polytechnique Fédérale de Lausanne, 2006).
[40] E. Antonini and M. Brunori, *Hemoglobin and Myoglobin in Their Reactions With Ligands*, edited by N.-H. P. Company (North-Holland:London, 1971).
[41] M. Lim, T. Jackson, and P. A. Anfinrud, J. Am. Chem. Soc. **126**, 7946 (2004).

[42]W. Gawelda, A. Cannizzo, V.-T. Pham, F. van Mourik, C. Bressler, and M. Chergui, J. Am. Chem. Soc. **129**, 8199 (2007).
[43]W. Gawelda, V.-T. Pham, R. M. van der Veen, D. Grolimund, R. Abela, M. Chergui, and C. Bressler, J. Chem. Phys. **130**, 124520 (2009).
[44]C. Bressler, C. J. Milne, V.-T. Pham, A. E. Nahhas, R. M. van der Veen, W. Gawelda, S. L. Johnson, P. Beaud, D. Grolimund, M. Kaiser, C. N. Borca, G. Ingold, R. Abela, and M. Chergui, Science **323**, 489 (2009).
[45]C. Consani, M. Prémont-Schwarz, A. E. Nahhas, C. Bressler, F. van Mourik, A. Cannizzo, and M. Chergui, Angew. Chem., Int. Ed. **48**, 7184 (2009).
[46]A factor of two from tighter x-ray focussing, a factor of two from monochromator changes and a factor of two from the air path.
[47]T. Westre, P. Kennepohl, J. DeWitt, B. Hedman, K. Hodgson, and E. Solomon, J. Am. Chem. Soc. **119**, 6297 (1997).
[48]S. Nozawa, T. Sato, M. Chollet, K. Ichiyanagi, A. Tomita, H. Fujii, S.-i. Adachi, and S. ya Koshihara, J. Am. Chem. Soc. **132**, 61 (2010).
[49]W. Gawelda, M. Johnson, F. M.F. de Groot, R. Abela, C. Bressler, and M. Chergui, J. Am. Chem. Soc. **128**, 5001 (2006).
[50]A. N. Tarnovsky, W. Gawelda, M. Johnson, C. Bressler, and M. Chergui, J. Phys. Chem. B **110**, 26497 (2006).
[51]M.-E. Moret, I. Tavernelli, M. Chergui, and U. Rothlisberger, Chem. Eur. J. **16**, 5889 (2010).
[52]M. Benfatto, S. D. Longa, K. Hatada, K. Hayakawa, W. Gawelda, C. Bressler, and M. Chergui, J. Phys. Chem. B **110**, 14035 (2006).
[53]J. Martin and M. H. Vos, Annu. Rev. Biophys. Biomol. **21**, 199 (1992).
[54]M. H. Vos, Bba-Bioenergetics **1777**, 15 (2008).
[55]E. Henry, J. Sommer, J. Hofrichter, and W. Eaton, J. Mol. Biol. **166**, 443 (1983).
[56]W. Tian, J. Sage, V. Srajer, and P. Champion, Phys. Rev. Lett. **68**, 408 (1992).
[57]M. Walther, V. Raicu, J. Ogilvie, R. Phillips, R. Kluger, and R. J. D. Miller, J. Phys. Chem. B **109**, 20605 (2005).
[58]D. M. Mills, A. Lewis, A. Harootunian, J. Huang, and B. Smith, Science **223**, 811 (1984).
[59]B. Chance, R. Fischetti, and L. Powers, Biochemistry **22**, 3820 (1983).
[60]L. Powers, B. Chance, M. Chance, B. Campbell, J. Friedman, S. Khalid, C. Kumar, A. Naqui, K. Reddy, and Y. Zhou, Biochemistry-Us **26**, 4785 (1987).
[61]T. Teng, H. Huang, and G. Olah, Biochemistry-Us **26**, 8066 (1987).
[62]A. Clozza, A. Castellano, S. D. Longa, A. Giovannelli, and A. Bianconi, Rev. Sci. Instrum. **60**, 2519 (1989).
[63]M. Chance, M. Wirt, E. Scheuring, L. Miller, A. Xie, and D. Sidelinger, Rev. Sci. Instrum. **64**, 2035 (1993).
[64]M. Chance, L. Miller, R. Fischetti, E. Scheuring, W. Huang, B. Sclavi, Y. Hai, and M. Sullivan, Biochemistry-Us **35**, 9014 (1996).
[65]A. Arcovito, C. Ardiccioni, M. Cianci, P. D'Angelo, B. Vallone, and S. D. Longa, J. Phys. Chem. B **114**, 13223 (2010).
[66]S. D. Longa, A. Arcovito, B. Vallone, A. Castellano, R. Kahn, J. Vicat, Y. Soldo, and J. Hazemann, J. Synchrotron Radiat. **6**, 1138 (1999).
[67]S. D. Longa, A. Arcovito, M. Girasole, J. Hazemann, and M. Benfatto, Phys. Rev. Lett. **87**, 155501 (2001).
[68]A. Arcovito, D. Lamb, G. U. Nienhaus, J. Hazemann, M. Benfatto, and S. D. Longa, Biophys. J. **88**, 2954 (2005).
[69]S. D. Longa, A. Arcovito, M. Benfatto, A. Congiu-Castellano, M. Girasole, J. Hazemann, and A. L. Bosco, Biophys. J. **85**, 549 (2003).
[70]M. Benfatto, S. D. Longa, and C. Natoli, J. Synchrotron Radiat. **10**, 51 (2003).
[71]D. Robin, R. Alvis, A. Jackson, and R. Holtzapplet, Micro Bunches: A Workshop on the Production, Measurement and Applications of Short Bunches of Electrons and Positrons in Linacs and Storage Rings, Upton, L.I., New York, 1995.
[72]M. Abo-Bakr, J. Feikes, K. Holldack, P. Kuske, W. Peatman, U. Schade, G. Wustefeld, and H. Hubers, Phys. Rev. Lett. **90**, 094801 (2003).
[73]X. Huang, J. Safranek, J. Corbett, Y. Nosochkov, J. Sebek, and A. Terebilo, *Proceedings of the 2007 IEEE Particle Accelerator Conference (PAC 07). 25-29 Jun 2007, Albuquerque, New Mexico. 22nd IEEE Particle Accelerator Conference*, p. 1308.
[74]R. W. Schoenlein, S. Chattopadhyay, H. H.W. Chong, T. E. Glover, P. A. Heimann, C. Shank, A. Zholents, and M. S. Zolotorev, Science **287**, 2237 (2000).

C

Diamond window flow cell design

This Appendix provides a description of the flow cell used on the time-resolved XAS experiments which needed an oxygen-free atmosphere, as well as a copy of the technical design used for the manufacturing it.

The flow-cell design is very simple on its conception and provides a robust and flexible environment for XAS experiments using liquid samples, allowing both transmission and fluorescence measurements to be taken simultaneously. It is made by a single block of stainless steel on which the several holes, grooves, channels and threads are etched. It is composed by two main parts: the sample-flowing region and the pinhole support.

The liquid flows through channels of 1 mm diameter, and are sealed with o-rings having 14 mm cross section. The aperture in which the x-rays and laser hit the sample consist of an opening of 6 mm in the front section which opens to a maximum of 12 mm in the back section of the cell to maximize the solid angle for fluorescence measurements. Teflon sheets are used to control the path length in the cell, that can be varied between 100 up to 500 μm. The pinhole support area pinhole support area was design such that the set pinhole plus its holder sits at the same plane as the sample so to allow laser/x-rays overlap during the experiments without any disconnecting the flow cell from its support. Even in the case of measurements detecting the fluorescence yield, the cell can be rotate along an axis passing through the sample plane. Figures C.1a and C.1b illustrate the mounting scheme and the assembled diamond window flow cell, respectively.

To assemble the flow cell, one should start with the placement of the two Viton rubber o-rings into the rectangular grooves in the main body of the cell. Once the o-rings are in place one has to carefully place the first diamond window in place, watching so that the holes for liquid inlet and outlet are not covered. The next step is to place the Teflon spacers leaving a space of about 1 mm between them so the liquid can be guided through. The second diamond window is then placed on top, closing the path on which the sample will flow. Finally, the top piece is screwed into place with gentle tightening of the 4 screws. To ensure the proper mounting, water is flown though as the screws on

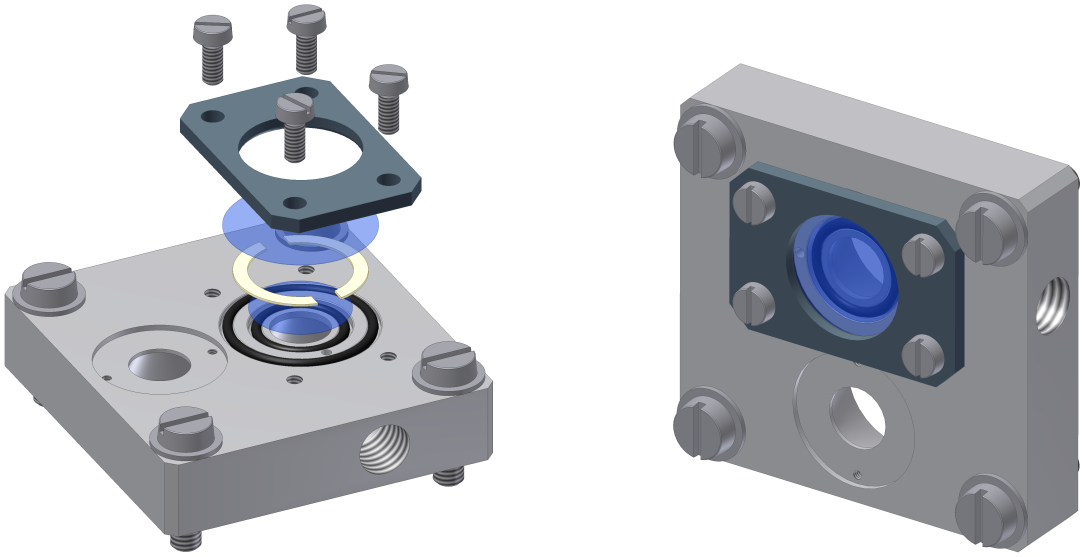

(a) Mounting diagram of the diamond flow cell

(b) Illustration of a completely mounted diamond-window flow cell.

Figure C.1.: Illustration of the diamond window flow cell.

the top piece are tightened until no leak is observed. The liquid enters and exits the cell by the side apertures in which a cone-shaped part is attached to allow flexible tubes of different diameters to be attached.

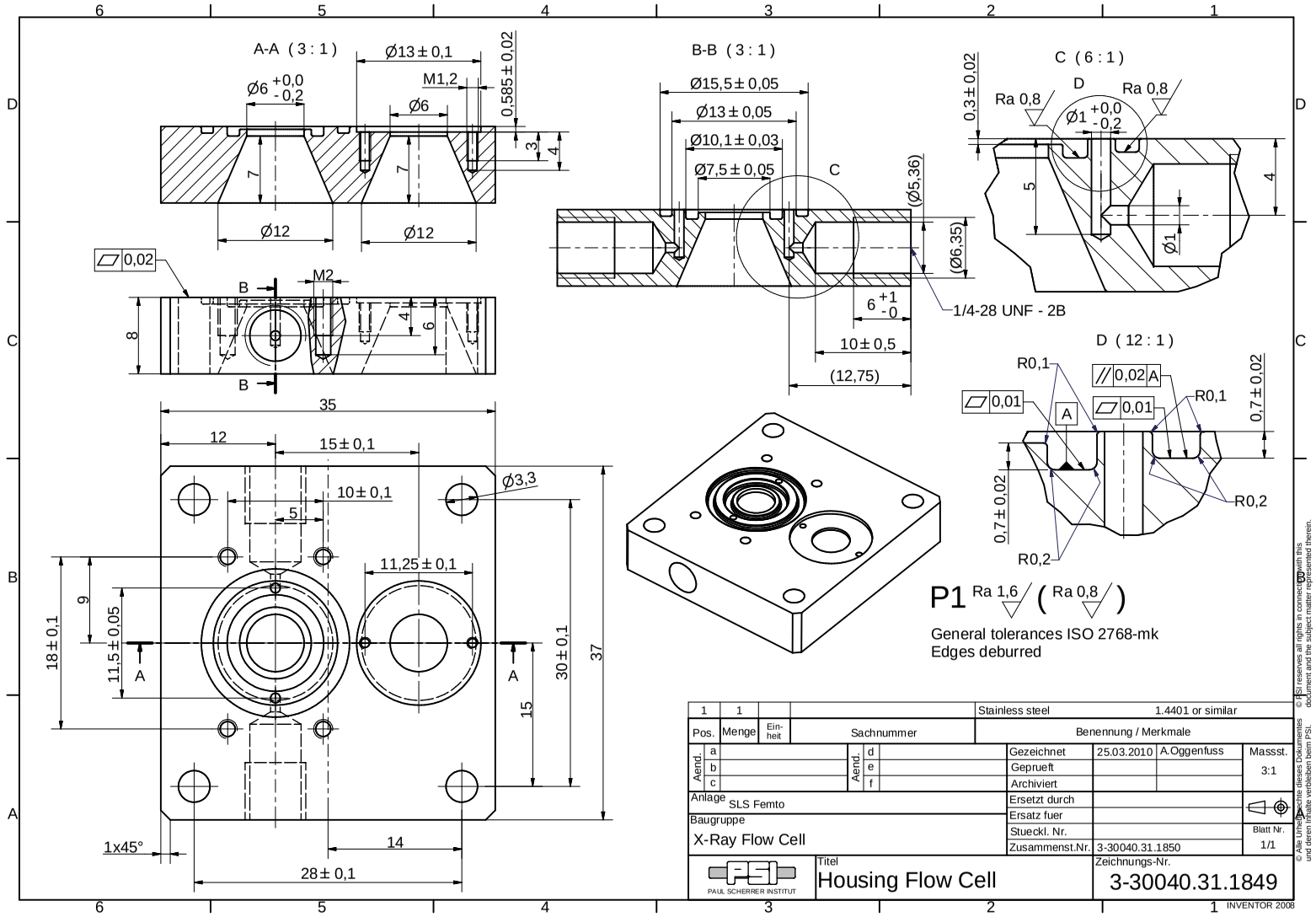

Figure C.2.: Technical design of the housing part of diamond window flow cell.

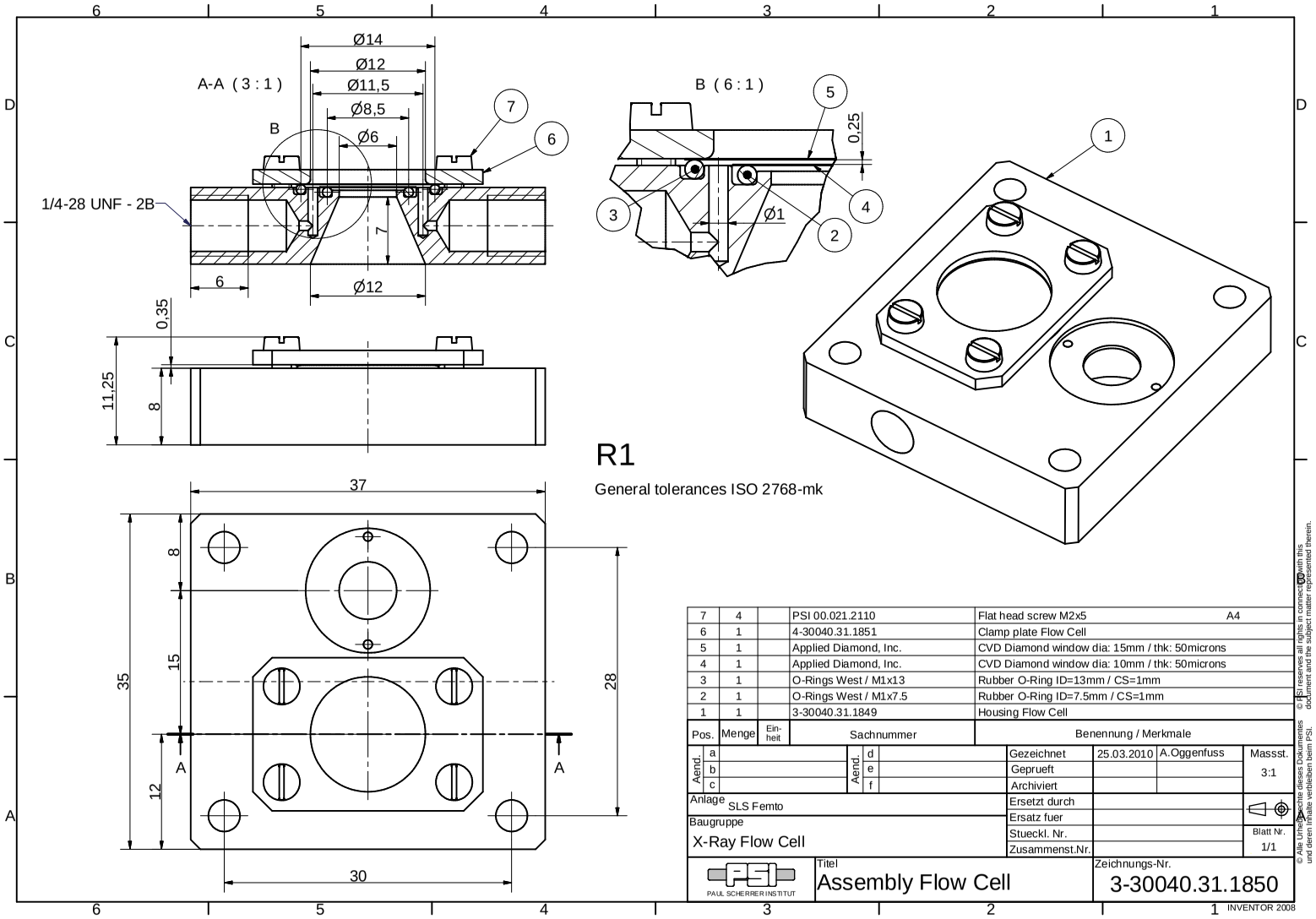

Pos.	Menge	Einheit	Sachnummer	Benennung / Merkmale
7	4		PSI 00.021.2110	Flat head screw M2x5 A4
6	1		4-30040.31.1851	Clamp plate Flow Cell
5	1		Applied Diamond, Inc.	CVD Diamond window dia: 15mm / thk: 50microns
4	1		Applied Diamond, Inc.	CVD Diamond window dia: 10mm / thk: 50microns
3	1		O-Rings West / M1x13	Rubber O-Ring ID=13mm / CS=1mm
2	1		O-Rings West / M1x7.5	Rubber O-Ring ID=7.5mm / CS=1mm
1	1		3-30040.31.1849	Housing Flow Cell

Aend. a	Aend. d	Gezeichnet	25.03.2010	A.Oggenfuss	Massst. 3:1
Aend. b	Aend. e	Geprueft			
Aend. c	Aend. f	Archiviert			
Anlage SLS Femto		Ersetzt durch			
Baugruppe X-Ray Flow Cell		Ersatz fuer			
		Stueckl. Nr.			Blatt Nr. 1/1
		Zusammenst.Nr.			

PAUL SCHERRER INSTITUT

Titel: Assembly Flow Cell

Zeichnungs-Nr.: 3-30040.31.1850

INVENTOR 2008

Figure C.3.: Technical design of the diamond window flow cell assembly.

D

Input files for the MXAN calculations of Myoglobin - steady-state case

This appendix includes examples of the input files needed to execute a fit procedure of a XAS spectrum by `MXAN`. The program needs three input files: the `experimental` file, the file `COMMAND.MIN` and the `coordinates` file. The `experimental` file is a text file containing one line of comments followed by the experimental data on a two-column format. The `COMMAND.MIN` file contains most of the instructions for the optimization procedure, including the initial guesses and limits on the fit parameters, and exact names of the `experimental` and `coordinates` files. The `coordinates` file include the energy range for the XAS spectrum, instructions on the calculation of the muffin-tin radii, the type of potential to be used and finally a list with the atomic coordinates.

Bellow it is shown examples of the instruction files used on the `MXAN` fit of the static XAS spectrum of nitrosyl-Myogloboin (MbNO). The input structure was taken from the PDB data bank, file 2FRJ.pdb. Exclamation mark (!) represents a comment.

D.1 Comands file: COMMAND.MIN

MbNO solution - from 2FRJ.pdb

2FRJ	parameter	in.deviat.	init.err.	phys. limits +/-	
1	Core	0.000	0.000	-0.050	0.050
2	Displ	0.000	0.000	-0.000	0.000
3	Dom_1	0.000	0.000	-0.100	0.100
4	Dom_2	0.000	0.000	-0.100	0.100
5	Fe-L_1	0.000	0.000	-0.200	0.200
6	Tilt	0.000	0.000	-15.000	15.000
7	Azim	0.000	0.000	-20.000	20.000
8	Bend	0.000	1.000	-30.000	50.000
9	Fe-Hi	0.000	0.000	-0.250	0.250
10	HiT1	0.000	0.000	-25.000	25.000
11	HiT2	0.000	0.000	-15.000	15.000
12	L_1-L_2	0.000	0.000	-0.150	0.150
13	Fe-N_p	0.000	0.000	-0.000	0.000
⋮	⋮	⋮	⋮	⋮	⋮
37	Ovlp	0.0500	0.0200	-0.2000	0.2000
38	V_{0imp}	-12.0000	0.5000	-17.0000	-5.0000

Control options

```
38                          ! numb.  of parameters (fixed + variable)
NORM    1SHE                ! Mode (NORM, EXTE, RECO)
                            ! Search (1SHE, CXYZ, OPTN)
U                           ! U (Unpol) XY (PolarXY) Z (Pol.z) P (Pol.)
1                           ! not active
```

INPUT files

```
MbNO_forMXAN.dat                        ! Exp.  file to fit
0.0100                                  ! Exp.  error
DATA.2FRJ                               ! Coord.  file
N                   1                   ! Other theor.  calc.
                                        ! sites [Y/N] How many?
0.0                 XXXX.BEST   0.0     ! Fract, Input file
                                        ! calc.othersite, Shift?
```

INTERMEDIATE files

```
2FRJ.PARM                               ! params for MS
2FRJ.SYMM                               ! File with symmetry info and l_max
2FRJ.XALP                               ! X-alpha potential
2FRJ.COUL                               ! Coulomb potential
2FRJ.RHOD                               ! Charge densities
```

```
                        OUTPUT PREFIX

  2FRJ_001                              ! Output files prefix (MAX 8 CHAR)

        PARAMETERS - ALIGNMENT, NORMALIZATION AND BROADENING

   0.035    0.02     -3.000    5.00      ! norm +/-  Exp.shift +/-
     Y      30000                        ! Broad [Y/N] Tot trials
  -10.000   5.000                        ! E.Fermi +/-
   1.250    0.200                        ! Broad +/-
   0.700    0.100                        ! Broad_exp +/-
     Y                                   ! mf ?
     1                                   ! # plasmons
  17.000   10.000   10.000   5.000       ! En.  +/- , Ampl.  +/-
     N      0.02     70.0     0.02       ! Extra Exc [Y/N] ampl, energy, width

                        OTHER OPTIONS

N      2                                ! Correlation links [Y/N] How many?
       4      7
       4      10                        ! between which params?
       ⋮      ⋮
Y      N                                ! Slope [Y/N],Concerted motions [Y/N]
N   30.000   10.000                      ! weight?  (N,A,T,G) xcentr, width

SET PRINT      3                        ! MINUIT printout level
SEEK         100                        ! Montecarlo search (stop after 100
                                        ! unsuccessful trials)
! SCAN         1   4     -.1   .1       ! scan parameter 1, 4 times from −.1 to +.1
! FIX          2                        ! fix parameter 2 to its best value
! FIX         37                        ! fix parameter 37 to its best value
! FIX         38                        ! fix parameter 38 to its best value
SIMPLEX      100   0.03                 ! minimization with simplex
                                        ! num.  of calls, tolerance
CALL FCN      -2                        ! fix the non-structural parameters during
                                        ! the calculation of the statistical error
MIGRAD                                  ! gradient search of minimum
SET OUT 70                              ! prepare file 70 to record results
HESSE                                   ! print results and correlation matrix
SET OUT 8
SAVE                                    ! save internal MINUIT data for a new search
CALL FCN       3                        ! end of minimum search
! CALL FCN     -1
! CONTOUR      1   4       3           ! contour plot - variables 1 and 4 until 3σ
```

D.2 Coordinates file: DATA.2FRJ

```
&job
fname = '2FRJ'      ! comment:  memo for user (4 characters)
nsca = 36           ! number of scattering atoms
lmax = 3            ! l_max for scattering waves
absorber = 1        ! absorbing atom on the list (should always be 1)
outersph=.false.    ! outer sphere caulculation (should aways be .false.)
edge = 'k'          ! atom x-ray abs.  edge (k, l1, l2, l3)
emin = -15,         ! minimum energy of the spectrum (0 at the vacuum level)
emax = 200.0        ! maximum energy of the spectrum
delta = 0.01        ! initial energy step
xscale = 2.0        ! increasing energy step as e_i = emin + delta(i-1)^xscale
gamma = 0.0
typot = 'hlrel'     ! potential type:  'hlcmp' complex Hedin-Lundqvist
                    !                  'hlrel' real Hedin-Lundqvist
                    !                  'xalph' X-alpha
charelx = 'ex'      ! channel relaxation:  'gs' = no-core-hole,
                    !                      'ex' = with core-hole
norman = 'stdcrm'   ! criterion for MT radii choice:Norman criterion
                    ! with an overlapping factor given by ovlpfac
ovlpfac = 0.1       ! overlap factor of MT spheres
coor = 'angs'       ! coordinates of the atoms:  'angs' or 'au'
potcalc = 'Y'       ! 'N':a fixed external potential is read
                    ! 'Y':potential calculated at every step of the
                    !     minimization procedure
                    ! '1':potential is calculated at the first step of the
                         minimization procedure, then kept fixed
v0imp = 0.0         ! imposed MT limit of potential (calculated if =0.0)
rhoimp = 0.0        ! imposed rho density limit (calculated if =0.0)
&end

! HEADER    Oxygen Storage/Transport 19-JAN-06 2FRJ
! TITLE     Nitrosyl horse-heart Myoglobin, Nitrite/Dithionite method
! AUTHOR    D.M.COPELAND,A.S.SOARES,A.H.WEST,G.B.RICHTER-ADDO
! REMARK    Resolution 1.30 Å.
```

iz	x	y	z	ilig	— comments —	
26	0.00000	0.00000	0.00000	0	0.00000	FE_HEM_154
7	0.37900	-0.86100	1.61900	1	1.87246	N_LIG_155
7	-1.40700	1.32000	0.66200	2	2.03968	NA_HEM_154
7	1.37800	-1.37000	-0.66400	3	2.05346	NC_HEM_154
7	-1.49900	-1.32700	-0.42900	4	2.04743	NB_HEM_154
7	1.50500	1.35600	0.41900	5	2.06865	ND_HEM_154
7	-0.18100	0.76100	-1.92700	6	2.07971	NE2_HIS_93
8	0.62800	-1.92100	2.12000	-1	2.92900	O_LIG_155
6	-1.10100	1.62400	-2.33300	-6	3.04835	CE1_HIS_93
6	2.73500	-1.19900	-0.56900	-5	3.04000	C4C_HEM_154
6	-1.15000	2.60300	1.11800	-5	3.05746	C1A_HEM_154
6	1.11600	-2.64800	-1.06500	-5	3.06457	C1C_HEM_154
6	1.30100	2.59400	1.01300	-5	3.07370	C4D_HEM_154
6	-1.34400	-2.60800	-0.91400	-5	3.07301	C4B_HEM_154
6	2.86000	1.09600	0.28600	-5	3.07614	C1D_HEM_154
6	-2.84500	-1.13800	-0.21100	-5	3.07141	C1B_HEM_154
6	0.60200	0.41600	-3.00300	-6	3.09087	CD2_HIS_93
6	-2.77800	1.16600	0.67100	-5	3.08660	C4A_HEM_154
6	3.38300	-0.04600	-0.23000	-5	3.39112	CHD_HEM_154
6	-0.13700	-3.17900	-1.24000	-5	3.41503	CHC_HEM_154
6	0.08700	3.17400	1.28900	-5	3.42686	CHA_HEM_154
6	-3.41400	0.02300	0.26500	-5	3.42435	CHB_HEM_154
⋮	⋮	⋮	⋮	⋮	⋮	⋮
8	-2.42100	2.50400	-6.03100	0	6.96450	O_LEU_89
6	-5.79600	1.88300	-3.35400	0	6.95619	CG_LEU_89
7	0.32100	3.58300	-5.98200	-6	6.98035	N_HIS_93
7	-4.73600	-0.79400	5.06600	0	6.98029	N_VAL_68
0	0.00000	0.00000	0.00000	0	0.00000	000000000000

E

Input file for the MXAN calculations of Myoglobin - time-resolved case

This appendix includes examples of the input files needed to execute a fit procedure of a transient XAS spectrum by `MXAN`. Similarly as in the calculations of static spectrum, the program needs three input files: the `experimental` file, the file `COMMAND.MIN` and the `coordinates` file, with one additional file corresponding to the best fit of the static case previously calculated. This is a `.BEST` file, which is one of the outputs of `MXAN`. The `experimental` file is a text file containing one line of comments followed by the experimental transient data on a two-column format. The experimental error in the data is considered constant and can be set (as fractional values) in the `COMMAND.MIN` file. The `.BEST` file contain all the results of a complete calculation, including the final fit structure and the calculated XAS spectrum (total cross-section and normalized). The `COMMAND.MIN` file contains most of the instructions for the optimization procedure, including the initial guesses and limits on the fit parameters, and exact names of the `experimental` and `coordinates` files. It is on this file that the initial distortion of the structure is set. The `coordinates` file include the energy range for the XAS spectrum, instructions on the calculation of the muffin-tin radii, the type of potential to be used and finally a list with the atomic coordinates.

Bellow it is shown examples of the instruction files used on the `MXAN` fit of the transient XAS spectrum of nitrosyl-Myogloboin (MbNO). The input structure was taken as the best fit obtained by `MXAN`. Exclamation mark (!) represents a comment.

E.1 Comands file: COMMAND.MIN

MbNO solution - from 2FRJ.pdb

2FRJ	parameter	in.deviat.	init.err.	phys. limits +/-	
1	Core	0.000	0.000	-0.050	0.050
2	Displ	-0.200	0.000	-0.000	0.000
3	Dom_1	0.050	0.000	-0.100	0.100
4	Dom_2	0.050	0.000	-0.100	0.100
5	Fe-L_1	1.000	0.000	-0.200	0.200
6	Tilt	0.000	0.000	-15.000	15.000
7	Azim	0.000	0.000	-20.000	20.000
8	Bend	0.000	1.000	-30.000	50.000
9	Fe-Hi	0.000	0.000	-0.250	0.250
10	HiT1	0.000	0.000	-25.000	25.000
11	HiT2	0.000	0.000	-15.000	15.000
12	L_1-L_2	0.000	0.000	-0.150	0.150
13	Fe-N_p	0.000	0.000	-0.000	0.000
⋮	⋮	⋮	⋮	⋮	⋮
37	Ovlp	0.0500	0.0200	-0.2000	0.2000
38	V_{0imp}	-12.0000	0.5000	-17.0000	-5.0000

Control options

```
38                          ! numb.  of parameters (fixed + variable)
NORM    1SHE                ! Mode (NORM, EXTE, RECO)
                            ! Search (1SHE, CXYZ, OPTN)
U                           ! U (Unpol) XY (PolarXY) Z (Pol.z) P (Pol.)
1                           ! not active
```

INPUT files

```
MbNO_transient.dat                  ! Exp.  file to fit
0.0150                              ! Exp.  error
2FRJ_DATA.BEST                      ! Coord.  file
Y                   1               ! Other theor.  calc.
                                    ! sites [Y/N] How many?
-1                  2FRJ.BEST  0.75 ! Fract, Input file
                                    ! calc.othersite, Shift?
```

INTERMEDIATE files

```
2FRJ.PARM                           ! params for MS
2FRJ.SYMM                           ! File with symmetry info and l_max
2FRJ.XALP                           ! X-alpha potential
2FRJ.COUL                           ! Coulomb potential
2FRJ.RHOD                           ! Charge densities
```

```
                        OUTPUT PREFIX

  MbNOtr01                              ! Output files prefix (MAX 8 CHAR)

        PARAMETERS - ALIGNMENT, NORMALIZATION AND BROADENING

  0.400   0.015   1.13    3.00          ! norm +/-  Exp.shift +/-
    Y     30000                         ! Broad [Y/N] Tot trials
 -5.140   1.000                         ! E.Fermi +/-
  1.590   0.100                         ! Broad +/-
  0.650   0.050                         ! Broad_exp +/-
    Y                                   ! mf ?
    1                                   ! # plasmons
  8.250   1.000   9.430   1.000         ! En.  +/- , Ampl.  +/-
    N     0.02    70.0    0.02          ! Extra Exc [Y/N] ampl, energy, width

                        OTHER OPTIONS

N     2                                 ! Correlation links [Y/N] How many?
      4     7
      4     10                          ! between which params?
      ⋮     ⋮
Y     N                                 ! Slope [Y/N],Concerted motions [Y/N]
N   30.000  10.000                      ! weight?  (N,A,T,G) xcentr, width

SET PRINT      3                        ! MINUIT printout level
SEEK         100                        ! Montecarlo search (stop after 100
                                        ! unsuccessful trials)
! SCAN         1   4     -.1   .1       ! scan parameter 1, 4 times from −.1 to +.1
! FIX          2                        ! fix parameter 2 to its best value
! FIX         37                        ! fix parameter 37 to its best value
! FIX         38                        ! fix parameter 38 to its best value
SIMPLEX      100   0.03                 ! minimization with simplex
                                        ! num.  of calls, tolerance
CALL FCN      -2                        ! fix the non-structural parameters during
                                        ! the calculation of the statistical error
MIGRAD                                  ! gradient search of minimum
SET OUT 70                              ! prepare file 70 to record results
HESSE                                   ! print results and correlation matrix
SET OUT 8
SAVE                                    ! save internal MINUIT data for a new search
CALL FCN       3                        ! end of minimum search
! CALL FCN     -1
! CONTOUR      1   4       3           ! contour plot - variables 1 and 4 until 3σ
```

E.2 Coordinates file: DATA.2FRJ

```
&job
fname = '2FRJ'      ! comment:  memo for user (4 characters)
nsca = 36           ! number of scattering atoms
lmax = 3            ! l_max for scattering waves
absorber = 1        ! absorbing atom on the list (should always be 1)
outersph=.false.    ! outer sphere caulculation (should aways be .false.)
edge = 'k'          ! atom x-ray abs.  edge (k, l1, l2, l3)
emin = -15,         ! minimum energy of the spectrum (0 at the vacuum level)
emax = 200.0        ! maximum energy of the spectrum
delta = 0.01        ! initial energy step
xscale = 2.0        ! increasing energy step as e_i = emin + delta(i-1)^xscale
gamma = 0.0
typot = 'hlrel'     ! potential type:  'hlcmp' complex Hedin-Lundqvist
                    !                  'hlrel' real Hedin-Lundqvist
                    !                  'xalph' X-alpha
charelx = 'ex'      ! channel relaxation:  'gs' = no-core-hole,
                    !                      'ex' = with core-hole
norman = 'stdcrm'   ! criterion for MT radii choice:Norman criterion
                    ! with an overlapping factor given by ovlpfac
ovlpfac = 0.1       ! overlap factor of MT spheres
coor = 'angs'       ! coordinates of the atoms:  'angs' or 'au'
potcalc = 'Y'       ! 'N':a fixed external potential is read
                    ! 'Y':potential calculated at every step of the
                    !     minimization procedure
                    ! '1':potential is calculated at the first step of the
                         minimization procedure, then kept fixed
v0imp = 0.0         ! imposed MT limit of potential (calculated if =0.0)
rhoimp = 0.0        ! imposed rho density limit (calculated if =0.0)
&end

! HEADER    Oxygen Storage/Transport 19-JAN-06 2FRJ
! TITLE     Nitrosyl horse-heart Myoglobin, Nitrite/Dithionite method
! AUTHOR    D.M.COPELAND,A.S.SOARES,A.H.WEST,G.B.RICHTER-ADDO
! REMARK    Resolution 1.30 Å.
```

iz	x	y	z	ilig	— comments —	
26	0.00000	0.00000	0.00000	0	0.00000	FE_HEM_154
7	0.37900	-0.86100	1.61900	1	1.87246	N_LIG_155
7	-1.40700	1.32000	0.66200	2	2.03968	NA_HEM_154
7	1.37800	-1.37000	-0.66400	3	2.05346	NC_HEM_154
7	-1.49900	-1.32700	-0.42900	4	2.04743	NB_HEM_154
7	1.50500	1.35600	0.41900	5	2.06865	ND_HEM_154
7	-0.18100	0.76100	-1.92700	6	2.07971	NE2_HIS_93
8	0.62800	-1.92100	2.12000	-1	2.92900	O_LIG_155
6	-1.10100	1.62400	-2.33300	-6	3.04835	CE1_HIS_93
6	2.73500	-1.19900	-0.56900	-5	3.04000	C4C_HEM_154
6	-1.15000	2.60300	1.11800	-5	3.05746	C1A_HEM_154
6	1.11600	-2.64800	-1.06500	-5	3.06457	C1C_HEM_154
6	1.30100	2.59400	1.01300	-5	3.07370	C4D_HEM_154
6	-1.34400	-2.60800	-0.91400	-5	3.07301	C4B_HEM_154
6	2.86000	1.09600	0.28600	-5	3.07614	C1D_HEM_154
6	-2.84500	-1.13800	-0.21100	-5	3.07141	C1B_HEM_154
6	0.60200	0.41600	-3.00300	-6	3.09087	CD2_HIS_93
6	-2.77800	1.16600	0.67100	-5	3.08660	C4A_HEM_154
6	3.38300	-0.04600	-0.23000	-5	3.39112	CHD_HEM_154
6	-0.13700	-3.17900	-1.24000	-5	3.41503	CHC_HEM_154
6	0.08700	3.17400	1.28900	-5	3.42686	CHA_HEM_154
6	-3.41400	0.02300	0.26500	-5	3.42435	CHB_HEM_154
⋮	⋮	⋮	⋮	⋮	⋮	⋮
8	-2.42100	2.50400	-6.03100	0	6.96450	O_LEU_89
6	-5.79600	1.88300	-3.35400	0	6.95619	CG_LEU_89
7	0.32100	3.58300	-5.98200	-6	6.98035	N_HIS_93
7	-4.73600	-0.79400	5.06600	0	6.98029	N_VAL_68
0	0.00000	0.00000	0.00000	0	0.00000	000000000000

F

Input file for the FEFF calculations of Myoglobin

```
* file name:  feff.inp (* represents a comment)
TITLE MbNO_2FRJ.pdb - 1.30 A
* MbNO K edge structure from 2FRJ.pdb (taken from MXAN input)
EDGE K
S02 1.0
CONTROL 1 1 1 1 1 1
PRINT 1 0 0 0 0 0
EXCHANGE 0 1.4 0 2
SCF 8 1 30 0.2 1
COREHOLE None
LDOS -20 0 0.2
XANES 8 0.08 0.9
FMS 10 0
POTENTIALS
 0   26   Fe   3   4
 1   7    N    2   3
 2   6    C    2   3
 3   8    O    2   3
 4   7    N    2   3    * Nitrogen of NO ligand
 5   8    O    2   3    * Oxygen of NO ligand
ATOMS
```

```
  0.00000   0.00000   0.00000  0  1.0  0.00000    FE_HEM_154
  0.37900  -0.86100   1.61900  4  1.0  1.87246     N_LIG_155
 -1.40700   1.32000   0.66200  1  1.0  2.03968    NA_HEM_154
  1.37800  -1.37000  -0.66400  1  1.0  2.05346    NC_HEM_154
 -1.49900  -1.32700  -0.42900  1  1.0  2.04743    NB_HEM_154
  1.50500   1.35600   0.41900  1  1.0  2.06865    ND_HEM_154
 -0.18100   0.76100  -1.92700  1  1.0  2.07971   NE2_HIS_93
  0.62800  -1.92100   2.12000  5  1.0  2.92900     O_LIG_155
 -1.10100   1.62400  -2.33300  2  1.0  3.04835   CE1_HIS_93
  2.73500  -1.19900  -0.56900  2  1.0  3.04000   C4C_HEM_154
 -1.15000   2.60300   1.11800  2  1.0  3.05746   C1A_HEM_154
  1.11600  -2.64800  -1.06500  2  1.0  3.06457   C1C_HEM_154
  1.30100   2.59400   1.01300  2  1.0  3.07370   C4D_HEM_154
 -1.34400  -2.60800  -0.91400  2  1.0  3.07301   C4B_HEM_154
  2.86000   1.09600   0.28600  2  1.0  3.07614   C1D_HEM_154
 -2.84500  -1.13800  -0.21100  2  1.0  3.07141   C1B_HEM_154
  0.60200   0.41600  -3.00300  2  1.0  3.09087   CD2_HIS_93
 -2.77800   1.16600   0.67100  2  1.0  3.08660   C4A_HEM_154
  3.38300  -0.04600  -0.23000  2  1.0  3.39112   CHD_HEM_154
 -0.13700  -3.17900  -1.24000  2  1.0  3.41503   CHC_HEM_154
  0.08700   3.17400   1.28900  2  1.0  3.42686   CHA_HEM_154
 -3.41400   0.02300   0.26500  2  1.0  3.42435   CHB_HEM_154
      ⋮         ⋮         ⋮    ⋮    ⋮     ⋮            ⋮
 -2.42100   2.50400  -6.03100  3  1.0  6.96450     O_LEU_89
 -5.79600   1.88300  -3.35400  2  1.0  6.95619    CG_LEU_89
  0.32100   3.58300  -5.98200  1  1.0  6.98035     N_HIS_93
 -4.73600  -0.79400   5.06600  1  1.0  6.98029     N_VAL_68
END
```

G

Non-planar bound MbNO

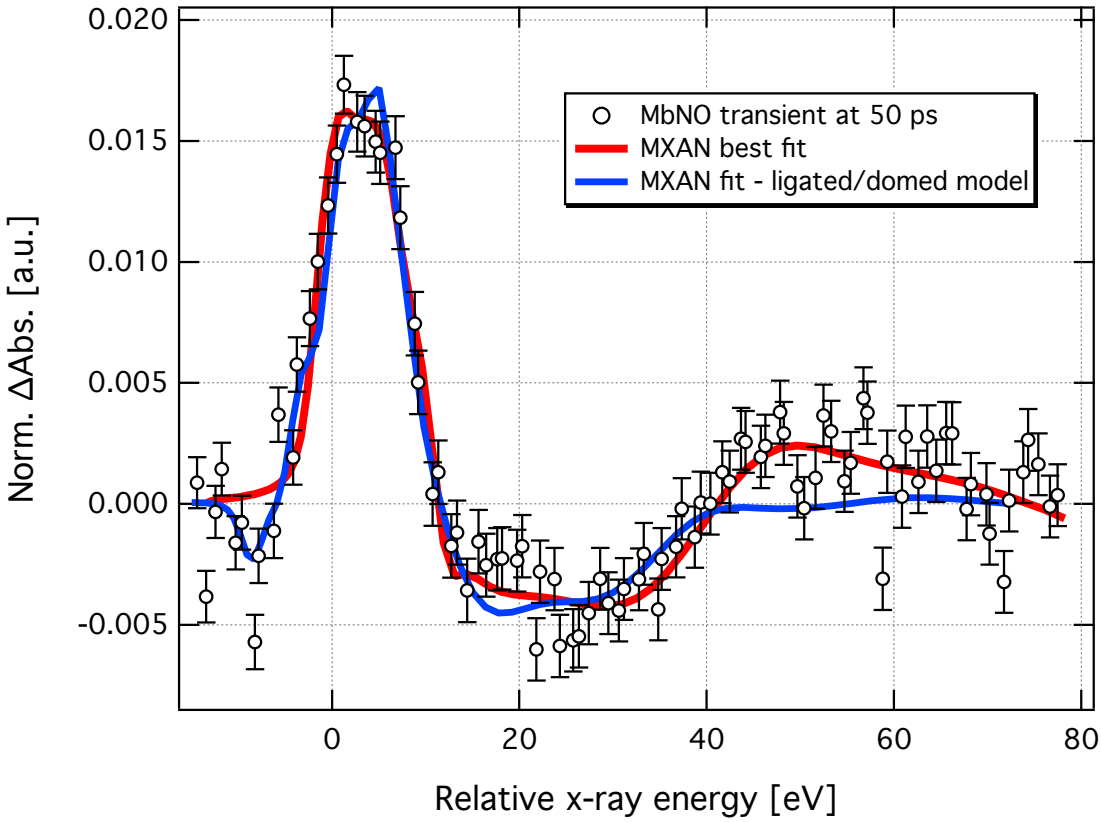

Figure G.1.: Structural fit of the transient XAS using a non-planar bound MbNO species.

Bibliography

[1] Hans Frauenfelder, Peter G Wolynes, and Robert H Austin. Biological physics. *Rev. Mod. Phys.*, 71:S419–S430, 1999. 1

[2] M Brunori, D Bourgeois, and B Vallone. The structural dynamics of myoglobin. *Journal of Structural Biology*, 147(3):223–234, Jan 2004. 1, 12, 94, 95, 96

[3] Eraldo Antonini and Maurizio Brunori. *Hemoglobin and Myoglobin in their Reactions with Ligands*. Norht-Holland Publishing Company, 1971. 2, 3, 10, 67, 94, 95, 100

[4] JC Kendrew, RE Dickerson, BE Strandberg, RG Hart, DR Davies, DC Phillips, and VC Shore. Structure of myoglobin: A three-dimensional fourier synthesis at 2 [angst]. resolution. *Nature*, 185(4711):422–427, 1960. 2, 11

[5] D M Mills, A Lewis, A Harootunian, J Huang, and B Smith. Time-resolved x-ray absorption spectroscopy of carbon monoxide-myoglobin recombination after laser photolysis. *Science*, 223(4638):811–813, 1984. 2, 40

[6] H Wang, G Peng, L M Miller, E M Scheuring, S J George, M R Chance, and S P Cramer. Iron l-edge x-ray absorption spectroscopy of myoglobin complexes and photolysis products. *Journal of the American Chemical Society*, 119(21):4921–4928, 1997. 2, 3

[7] A Clozza, A Castellano, S Della Longa, A Giovannelli, and A Bianconi. Apparatus for time-resolved x-ray absorption spectroscopy using flash photolysis. *Review of Scientific Instruments*, 60(7):2519–2521, Jul 1989. 2, 3

[8] Mark Chance, Michael Wirt, Eva Scheuring, Lisa Miller, Aihua Xie, and Dean Sidelinger. Time-resolved x-ray absorption spectroscopy on microsecond timescales: Implications for the examination of structural motions. *Review of Scientific Instruments*, 64(7):2035–2036, 1993. 2, 3

[9] M R Chance, L M Miller, R F Fischetti, E Scheuring, W X Huang, B Sclavi, Y Hai, and M Sullivan. Global mapping of structural solutions provided by the extended x-ray absorption fine structure ab initio code feff 6.01: Structure of the cryogenic photoproduct of the myoglobin-carbon monoxide complex. *Biochemistry*, 35(28):9014–9023, 1996. 2, 3

[10] V Srajer, T Teng, T Ursby, C Pradervand, and Z Ren. Photolysis of the carbon monoxide complex of myoglobin: nanosecond time-resolved crystallography. *Science*, 274(5293):1726–1729, Jan 1996. 2, 3

[11] V Srajer, Z Ren, T Teng, M Schmidt, and T Ursby. Protein conformational relaxation and ligand migration in myoglobin: A nanosecond to millisecond molecular movie from time-resolved laue x-ray diffraction. *Biochemistry*, 40(46):13802–13815, Jan 2001. 2, 3, 12, 13, 96

[12] Dominique Bourgeois, Beatrice Vallone, Friedrich Schotte, Alessandro Arcovito, Adriana E Miele, Giuliano Sciara, Michael Wulff, Philip Anfinrud, and Maurizio Brunori. Complex landscape of protein structural dynamics unveiled by nanosecond laue crystallography. *Proceedings of the National Academy of Sciences*, 100(15):8704–8709, 2003. 2, 3, 12, 13, 96

[13] D Bourgeois, B Vallone, A Arcovito, and G Sciara. Extended subnanosecond structural dynamics of myoglobin revealed by laue crystallography. *Proceedings of the National Academy of Sciences*, 103(13):4924–4929, Jan 2006. 2, 3, 11, 12, 13, 96

[14] Friedrich Schotte, Manho Lim, Timothy A Jackson, Aleksandr V Smirnov, Jayashree Soman, John S Olson, George N Phillips Jr, Michael Wulff, and Philip A Anfinrud. Watching a protein as it functions with 150-ps time-resolved x-ray crystallography. *Science*, 300:1944–1947, 2003. 2, 3, 12, 13, 96, 100

[15] Friedrich Schotte, Jayashree Soman, John S Olson, Michael Wulff, and Philip A Anfinrud. Picosecond time-resolved x-ray crystallography: probing protein function in real time. *Journal of Structural Biology*, 147(3):235–246, 2004. 2, 3, 12, 13, 96

[16] M Cammarata, M Levantino, F Schotte, Philip A Anfinrud, Friederike Ewald, Jungkweon Choi, Antonio Cupane, Michael Wulff, and Hyotcherl Ihee. Tracking the structural dynamics of proteins in solution using time-resolved wide-angle x-ray scattering. *Nature Methods*, 5(10):881–886, Jan 2008. 2, 3, 41

[17] Kyung Kim, Key Oang, Jeongho Kim, Jae Lee, Youngmin Kim, and Hyotcherl Ihee. Direct observation of myoglobin structural dynamics from 100 picoseconds to 1 microsecond with picosecond x-ray solution scattering. *Chem. Commun.*, 47(1):289–291, 2011. 2

[18] Dominique Bourgeois, Ulrike Wagner, and Michael Wulff. Towards automated laue data processing: application to the choice of optimal x-ray spectrum. *Acta Crystallographica Section D*, 56(8):973–985, 2000. 2

[19] Maurizio Brunori. Myoglobin strikes back. *Protein Sci*, 19(2):195–201, 2010. 2, 94, 96

[20] Daniel Garry, George Ordway, John Lorenz, Nina Radford, Eva Chin, Robert Grange, Rhonda Bassel-Duby, and R Williams. Mice without myoglobin. *Nature*, 395(6705):905–908, 1998. 2

[21] M Brunori. Nitric oxide, cytochrome-c oxidase and myoglobin. *Trends in Biochemical Sciences*, 26(1):21–23, Jan 2001. 2, 10, 94

[22] M Brunori. Nitric oxide moves myoglobin centre stage. *Trends in Biochemical Sciences*, 26(4):209–210, Jan 2001. 2, 10, 94

[23] H Frauenfelder, B McMahon, and P Fenimore. Myoglobin: The hydrogen atom of biology and a paradigm of complexity. *Proceedings of the National Academy of Sciences of the United States of America*, 100(15):8615–8617, Jul 2003. 3

[24] Q Gibson. Hemoproteins, ligands, and quanta. *Journal of Biological Chemistry*, 264(34):20155–20158, Jan 1989. 3, 95

[25] S Della-Longa, A Arcovito, M Girasole, J L Hazemann, and M Benfatto. Quantitative analysis of x-ray absorption near edge structure data by a full multiple scattering procedure: The fe-co geometry in photolyzed carbonmonoxy-myoglobin single crystal. *Physical Review Letters*, 87(15):155501, 2001. 3, 4, 96, 108, 109, 126, 127, 129

[26] S Della-Longa, Alessandro Arcovito, Beatrice Vallone, Agostina Congiu Castellano, Richard Kahn, Jean Vicat, Yvonne Soldo, and Jean Louis Hazemann. Polarized x-ray absorption spectroscopy of the low-temperature photoproduct of carbonmonoxy-myoglobin. *Journal of Synchrotron Radiation*, 6(6):1138–1147, 1999. 3, 4, 96, 98

[27] Stefano Della Longa and Alessandro Arcovito. X-ray-induced lysis of the feco bond in carbonmonoxy-myoglobin. *Inorganic Chemistry*, 49(21):9958–9961, Nov 2010. 3, 4, 13, 96

[28] Alessandro Arcovito, Maurizio Benfatto, Michele Cianci, S Samar Hasnain, Karin Nienhaus, G Ulrich Nienhaus, Carmelinda Savino, Richard W Strange, Beatrice Vallone, and Stefano Della Longa. X-ray structure analysis of a metalloprotein with enhanced active-site resolution using in situ x-ray absorption near edge structure spectroscopy. *Proceedings of the National Academy of Sciences*, 104(15):6211–6216, 2007. 3, 4, 96, 109

[29] Alessandro Arcovito, Chiara Ardiccioni, Michele Cianci, Paola D'Angelo, Beatrice Vallone, and Stefano Della Longa. Polarized x-ray absorption near-edge structure spectroscopy of neuroglobin and myoglobin single crystals. *Journal of Physical Chemistry B*, 114(41):13223–13231, 2010. 3, 4, 10, 96, 97, 110, 116, 120, 126

[30] D. C. Koningsberger and R. Prins. *X-ray Absorption: Principles, Applications, Techniques of EXAFS, SEXAFS and XANES*. John Wiley & Sons, 1988. 4, 12, 13, 26, 33, 49, 51

[31] Grant Bunker. *Introduction to XAFS A Practical Guide to X-ray Absorption Fine Structure Spectroscopy*. Cambridge University Press, first edition, 2010. 4, 16, 26, 46

[32] C Bressler and M Chergui. Ultrafast x-ray absorption spectroscopy. *Chemical Reviews*, 104(4):1781–1812, 2004. 4, 76, 150

[33] Christian Bressler, Rafael Abela, and Majed Chergui. Exploiting exafs and xanes for time-resolved molecular structures in liquids. *Zeitschrift für Kristallographie*, 223:307–321, 2008. 4, 41, 55, 57, 58, 147, 150

[34] Christian Bressler and Majed Chergui. Molecular structural dynamics probed by ultrafast x-ray absorption spectroscopy. *Annual Review of Physical Chemistry*, 61(1):263–282, Mar 2010. 4, 41, 55, 57, 58, 147, 150

[35] Ch Bressler, C Milne, V.-T Pham, A ElNahhas, R van der Veen, W Gawelda, S Johnson, P Beaud, D Grolimund, M Kaiser, C Borca, G Ingold, R Abela, and M Chergui. Femtosecond xanes study of the light-induced spin crossover dynamics in an iron(ii) complex. *Science*, 323(5913):489–492, Jan 2009. 4, 40, 41, 46, 74, 75, 86, 87, 151

[36] R van der Veen, Chris J. Milne, Amal El Nahhas, Frederico A. Lima, Van-Thai Pham, Jonathan Best, Julia A. Weinstein, Camelia N. Borca, Rafael Abela, Christian Bressler, and Majed Chergui. Structural determination of a photochemically active diplatinum molecule by time-resolved exafs spectroscopy. *Angewandte Chemie International Edition*, 48(15):2711–2714, 2009. 4, 40, 84

[37] Van-Thai Pham, Thomas J Penfold, Renske M van der Veen, Frederico Lima, Amal El Nahhas, Steve L Johnson, Paul Beaud, Rafael Abela, Christian Bressler, Ivano Tavernelli, Christopher J Milne, and Majed Chergui. Probing the transition from hydrophilic to hydrophobic solvation with atomic scale resolution. *Journal of the American Chemical Society*, 133(32):12740–12748, 2011. 4, 40, 46, 151

[38] Lin X Chen, Xiaoyi Zhang, Jenny V Lockard, Andrew B Stickrath, Klaus Attenkofer, Guy Jennings, and Di-Jia Liu. Excited-state molecular structures captured by x-ray transient absorption spectroscopy: a decade and beyond. *Acta Crystallogr A*, 66:240–251, 2010. 4, 41, 55, 58, 147

[39] Wojciech Gawelda. *Time-resolved x-ray absorption spectroscopy of transition metal complexes*. Phd thesis, École Polytechnique Fédérale de Lausanne, 2006. 4, 41, 64, 72, 73, 74, 75, 76, 78, 80, 81, 84, 85, 149

[40] Wojciech Gawelda, Van-Thai Pham, Maurizio Benfatto, Yuri Zaushitsyn, Maik Kaiser, Daniel Grolimund, Steven L Johnson, Rafael Abela, Andreas Hauser, Christian Bressler, and Majed Chergui. Structural determination of a short-lived excited iron(ii) complex by picosecond x-ray absorption spectroscopy. *Physical Review Letters*, 98(057401):057401, 2007. 4, 40, 41, 73, 74, 75, 76, 80, 84, 85, 149

[41] J. S. Griffiths. *The Theory of Transition Metal Ions*. Cambridge Universtity Press, 1961. 8

[42] A Hauser, N Amstutz, S Delahaye, A Sadki, Sabine Schenker, Regula Siebe, and Mohamed Zerara. Fine tuning the electronic properties of [m(bpy)3]2 complexes by chemical pressure (m=fe 2+, ru 2+, co 2+, bpy=2,2'bipyridine). *Structure and Bonding*, 106:81–96, Jan 2004. 8

[43] Antonín Vlcek. The life and times of excited states of organometallic and coordination compounds. *Coordination Chemistry Reviews*, 200-202 IS -:933–978, 2000. 8

[44] Malcolm Gerloch, John Harding, and R Woolley. The context and application of ligand field theory. 46:1–46, 1981. 8

[45] R Woolley. Ligand-field analysis of transition-metal complexes. *International Reviews in Physical Chemistry*, 6(2):93–141, 1987. 8

[46] Theoretical activity in solid state, chemistry and material science - university of oslo. http://folk.uio.no/ravi/activity/ordering/orbitalordering.html. 8

[47] S Samar Hasnain and Keith O Hodgson. Structure of metal centres in proteins at subatomic resolution. *Journal of Synchrotron Radiation*, 6(4):852–864, 1999. 9

[48] H Frauenfelder, B H McMahon, R H Austin, K Chu, and J T Groves. The role of structure, energy landscape, dynamics, and allostery in the enzymatic function of myoglobin. *Proceedings of the National Academy of Sciences*, 98(5):2370–2374, Jan 2001. 10

[49] J Wittenberg and B Wittenberg. Myoglobin function reassessed. *Journal of Experimental Biology*, 206(12):2011–2020, Jan 2003. 10, 94, 96

[50] J Moller and L Skibsted. Nitric oxide and myoglobins. *Chem. Rev*, 102(4):1167–1178, Jan 2002. 10

[51] Thorsten Burmester, Bettina Weich, Sigrid Reinhardt, and Thomas Hankeln. A vertebrate globin expressed in the brain. *Nature*, 407(6803):520–523, 2000. 10

[52] Yunjuan Sun, Kunlin Jin, Xiao Ou Mao, Yonghua Zhu, and David A Greenberg. Neuroglobin is up-regulated by and protects neurons from hypoxic-ischemic injury. *Proceedings of the National Academy of Sciences*, 98(26):15306–15311, 2001. 10

[53] Yunjuan Sun, Kunlin Jin, Alyson Peel, Xiao Ou Mao, Lin Xie, and David A Greenberg. Neuroglobin protects the brain from experimental stroke in vivo. *Proceedings of the National Academy of Sciences*, 100(6):3497–3500, 2003. 10

[54] Paola D'Angelo, Stefano Della Longa, Alessandro Arcovito, Massimiliano Anselmi, Alfredo Di Nola, and Giovanni Chillemi. Dynamic investigation of protein metal active sites: Interplay of xanes and molecular dynamics simulations. *Journal of the American Chemical Society*, 132(42):14901–14909, 2010. 10

[55] Gerhard Hummer, Friedrich Schotte, and Philip A Anfinrud. Unveiling functional protein motions with picosecond x-ray crystallography and molecular dynamics simulations. *Proceedings of the National Academy of Sciences*, 101(43):15330–15334, 2004. 11, 12, 96

[56] Jordi Cohen, Anton Arkhipov, Rosemary Braun, and Klaus Schulten. Imaging the migration pathways for o2, co, no, and xe inside myoglobin. *Biophysical Journal*, 91(5):1844–1857, Sep 2006. 11

[57] Carmelinda Savino, Adriana Miele, Federica Draghi, Kenneth Johnson, Giuliano Sciara, Maurizio Brunori, and Beatrice Vallone. Pattern of cavities in globins: The case of human hemoglobin. *Biopolymers*, 91(12):1097–1107, 2009. 11

[58] Robert Tilton, Irwin Kuntz, and Gregory Petsko. Cavities in proteins: structure of a metmyoglobin xenon complex solved to 1.9 a. *Biochemistry*, 23(13):2849–2857, 1984. 11

[59] Maurizio Brunori, Beatrice Vallone, Francesca Cutruzzola, Carlo Travaglini-Allocatelli, Joel Berendzen, Kelvin Chu, Robert M. Sweet, and Ilme Schlichting. The role of cavities in protein dynamics: crystal structure of a photolytic intermediate of a mutant myoglobin. *Proceedings of the National Academy of Sciences*, 97(5):2058–2063, Jan 2000. 11

[60] Theoretical and computational biophysics group - university of illinois at urbanachampaign. http://www.ks.uiuc.edu/Research/myoglobin-pmf/. 11

[61] J W Petrich, C Poyart, and J L Martin. Photophysics and reactivity of heme proteins: a femtosecond absorption study of hemoglobin, myoglobin, and protoheme. *Biochemistry*, 27(11):4049–4060, 1988. 12

[62] Jean-Louis Martin and Marten Vos. Femtosecond measurements of geminate recombination in heme proteins. *Methods in Enzymology*, 232:416–430, 1994. 12

[63] X Ye, A Demidov, and PM Champion. Measurements of the photodissociation quantum yields of mbno and mbo(2) and the vibrational relaxation of the six-coordinate heme species. *Journal of the American Chemical Society*, 124(20):5914–5924, Jan 2002. 12, 95, 101, 102, 104, 105, 106

[64] Marten H Vos and Jean-Louis Martin. Femtosecond processes in proteins - review. *Biochimica et Biophysica Acta*, 1411:1–20, 1999. 12, 96

[65] W D Tian, J T Sage, V Srajer, and P M Champion. Relaxation dynamics of myoglobin in solution. *Phys. Rev. Lett.*, 68(3):408–411, 1992. 12, 79, 100, 101

[66] Isabella Ascone and Richard Strange. Biological x-ray absorption spectroscopy and metalloproteomics. *Journal of Synchrotron Radiation*, 16(3):413–421, 2009. 13

[67] G Veronesi, C Degli Esposti Boschi, L Ferrari, G Venturoli, F Boscherini, F Vila, and J Rehr. Ab initio analysis of the x-ray absorption spectrum of the myoglobin–carbon monoxide complex: Structure and vibrations. *Physical Review B*, 82(2):020101, Jul 2010. 13

[68] O Carugo and K Carugo. When x-rays modify the protein structure: radiation damage at work. *Trends in Biochemical Sciences*, 30(4):213–219, Jan 2005. 13

[69] James Holton. A beginner's guide to radiation damage. *Journal of Synchrotron Radiation*, 16(2):133–142, 2009. 13

[70] C Nave and E Garman. Towards an understanding of radiation damage in cryocooled macromolecular crystals. *Journal of Synchrotron Radiation*, 12:257–260, Jan 2005. 13

[71] Nobutaka Shimizu, Kunio Hirata, Kazuya Hasegawa, Go Ueno, and Masaki Yamamoto. Dose dependence of radiation damage for protein crystals studied at various x-ray energies. *Journal of Synchrotron Radiation*, 14(1):4–10, 2007. 13

[72] H Leiros, J Timmins, R Ravelli, and S McSweeney. Is radiation damage dependent on the dose rate used during macromolecular crystallography data collection? *Acta Crystallographica Section D*, 62:125–132, Jan 2006. 13

[73] Alke Meents, Birger Dittrich, and Sascha Gutmann. A new aspect of specific radiation damage: hydrogen abstraction from organic molecules. *Journal of Synchrotron Radiation*, 16(2):183–190, 2009. 13

[74] R Ravelli and E Garman. Radiation damage in macromolecular cryocrystallography. *Current opinion in structural biology*, 16(5):624–629, Jan 2006. 13

[75] Thorsten Beitlich, Karin Kuhnel, Clemens Schulze-Briese, Robert L Shoeman, and Ilme Schlichting. Cryoradiolytic reduction of crystalline heme proteins: analysis by uv-vis spectroscopy and x-ray crystallography. *Journal of Synchrotron Radiation*, 14(1):11–23, 2007. 13

[76] Paola D'Angelo, Andrea Lapi, Valentina Migliorati, Alessandro Arcovito, Maurizio Benfatto, Otello Roscioni, Wolfram Meyer-Klaucke, and Stefano Della-Longa. X-ray absorption spectroscopy of hemes and hemeproteins in solution: Multiple scattering analysis. *Inorganic Chemistry*, 47(21):9905–9918, 2008. 13, 96, 97, 110, 118

[77] Philip Willmott. *An Introduction to Synchrotron Radiation: Techniques and Applications*. John Wiley & Sons, Ltd, first edition, 2011. 16, 17, 24, 25, 26, 42, 46

[78] M O Krause. Atomic radiative and radiationless yields for k and l shells. *Journal of Physical and Chemical Reference Data*, 8(2):307–327, 1979. 17, 26

[79] Xop: X-ray oriented programs. http://www.esrf.eu/computing/scientific/xop2.1/. 19

[80] Roger J. Dejus and Manuel Sanchez del Rio. Xop: A graphical user interface for spectral calculations and x-ray optics utilities. *Review of Scientific Instruments*, 67(9):3356–3356, 1996. 19

[81] Jens Als-Nielsen and Des McMorrow. *Elements of Modern X-ray Physics*. John Wiley & Sons, Ltd, second edition, 2011. 20, 21, 23, 24

[82] Boon K. Teo. *EXAFS: Basic Principles and Data Analysis*. Springer-Verlag, 1986. 20, 23, 26, 33, 46

[83] J. J. Sakurai. *Modern Quantum Mechanics*. Addison-Wesley, revised edition, 1994. 20

[84] J Rehr and R Albers. Theoretical approaches to x-ray absorption fine structure. *Reviews of Modern Physics*, 72(3):621–654, 2000. 20, 26, 31, 32, 36, 109, 110

[85] M Benfatto, A Congiu-Castellano, A Daniele, and S Della Longa. Mxan : a new software procedure to perform geometrical fitting of experimental xanes spectra. *Journal of Synchrotron Radiation*, 8(2):267–269, 2001. 22, 36, 80, 108

[86] M Benfatto, S Della Longa, and C Natoli. The mxan procedure: a new method for analysing the xanes spectra of metalloproteins to obtain structural quantitative information. *Journal of Synchrotron Radiation*, 10(1):51–57, Jan 2003. 22, 36, 80, 108, 109, 110, 111

[87] M Benfatto and S Della Longa. Mxan: New improvements for potential and structural refinement. *Journal of Physics: Conference Series*, 190(012031):1–4, Jan 2009. 22, 36, 80, 108

[88] G Smolentsev and A Soldatov. Fitit: New software to extract structural information on the basis of xanes fitting. *Computational Materials Science*, 39(3):569–574, Jan 2007. 22

[89] John Rehr, Joshua Kas, Micah Prange, Adam Sorini, Yoshinari Takimoto, and Fernando Vila. Ab initio theory and calculations of x-ray spectra. *Comptes Rendus Physique*, 10(6):548–559, 2009. 22, 29, 35, 80, 112

[90] John Rehr, Joshua Kas, Fernando Vila, Micah Prange, and Kevin Jorissen. Parameter-free calculations of x-ray spectra with feff9. *Phys. Chem. Chem. Phys.*, 12(21):5503–5513, 2010. 22, 29, 30, 35, 80, 112

[91] K Hatada, K Hayakawa, M Benfatto, and C Natoli. Full-potential multiple scattering theory with space-filling cells for bound and continuum states. *Journal of Physics: Condensed Matter*, 22(18):185501, 2010. 22, 31

[92] X-ray data booklet. http://xdb.lbl.gov/. 24

[93] Pieter Glatzel, Marcin Sikora, Grigory Smolentsev, and Marcos Fernández-García. Hard x-ray photon-in photon-out spectroscopy. *Catalysis Today*, 145(3-4):294–299, 2009. 25, 50

[94] M O Krause and J H Oliver. Natural widths of atomic k and l levels, k-α x-ray lines and several kll auger lines. *Journal of Physical and Chemical Reference Data*, 8(2):329–338, 1979. 26, 115

[95] K Hämäläinen, D P Siddons, J B Hastings, and L E Berman. Elimination of the inner-shell lifetime broadening in x-ray-absorption spectroscopy. *Phys. Rev. Lett.*, 67:2850–2853, Nov 1991. 26, 50

[96] Frank de Groot. High-resolution x-ray emission and x-ray absorption spectroscopy. *Chemical Reviews*, 101(6):1779–1808, Jun 2001. 26

[97] Dale E Sayers, Edward A Stern, and Farrel W Lytle. New technique for investigating noncrystalline structures: Fourier analysis of the extended x-ray–absorption fine structure. *Phys. Rev. Lett.*, 27:1204–1207, 1971. 26

[98] Edward A Stern. Theory of the extended x-ray-absorption fine structure. *Physical Review B*, 10(8):3027–3037, 1974. 26

[99] E A Stern, D E Sayers, and F W Lytle. Extended x-ray-absorption fine-structure technique. iii. determination of physical parameters. *Phys. Rev. B*, 11:4836–4846, 1975. 26

[100] DC Koningsberger, BL Mojet, GE van Dorssen, and DE Ramaker. Xafs spectroscopy; fundamental principles and data analysis. *Topics in Catalysis*, 10:143–155, 2000. 26

[101] A L Ankudinov, B Ravel, J J Rehr, and S D Conradson. Real-space multiple-scattering calculation and interpretation of x-ray-absorption near-edge structure. *Phys. Rev. B*, 58(12):7565–7576, Sep 1998. 29, 30

[102] J Rehr and R Albers. Scattering-matrix formulation of curved-wave multiple-scattering theory: Application to x-ray-absorption fine structure. *Physical Review B*, 41(12):8139, 1990. 30

[103] S I Zabinsky, J J Rehr, A Ankudinov, R C Albers, and M J Eller. Multiple-scattering calculations of x-ray-absorption spectra. *Physical Review B*, 52(4):2995–3009, 1995. 30

[104] J Rehr. Theory and calculations of x-ray spectra: Xas, xes, xrs, and nrixs. *Radiation Physics and Chemistry*, 75(11):1547–1558, Jan 2006. 30, 36, 110

[105] Joe Norman. Non-empirical versus empirical choices for overlapping-sphere radii ratios in scf-xα-sw calculations on clo4- and so2. *Molecular Physics: An International Journal at the Interface Between Chemistry and Physics*, 31(4):1191–1198, 1976. 30, 110

[106] C Natoli, M Benfatto, S Della Longa, and K Hatada. X-ray absorption spectroscopy: state-of-the-art analysis. *Journal of Synchrotron Radiation*, 10:26–42, Jan 2003. 30, 31, 36, 110

[107] Y Joly. X-ray absorption near-edge structure calculations beyond the muffin-tin approximation. *Phys. Rev. B*, 63(12):125120, Mar 2001. 31

[108] Bruce Ravel and Mathew Newville. Athena, artemis, hephaestus: data analysis for x-ray absorption spectroscopy using ifeffit. *Journal of Synchrotron Radiation*, 12:537–541, 2005. 33, 34, 48

[109] M Newville, P Līviņš, Y Yacoby, J Rehr, and E Stern. Near-edge x-ray-absorption fine structure of pb: A comparison of theory and experiment. *Physical Review B*, 47(21):14126, Jun 1993. 34

[110] Feff. http://leonardo.phys.washington.edu/feff. 35, 80, 88

[111] Renske van der Veen. *Ultrafast x-ray and optical spectroscopy of binuclear molecular complexes*. Phd thesis, École Polytechnique Fédérale de Lausanne, 2010. 35, 74, 84, 111

[112] M Benfatto and S Della Longa. Geometrical fitting of experimental xanes spectra by a full multiple-scattering procedure. *Journal of Synchrotron Radiation*, 8(4):1087–1094, 2001. 36, 80, 108, 110, 111

[113] T Tyson, K Hodgson, C Natoli, and M Benfatto. General multiple-scattering scheme for the computation and interpretation of x-ray-absorption fine structure in atomic clusters with applications to sf_6, $gecl_4$, and br_2 molecules. *Physical Review B*, 46(10):5997, Sep 1992. 36

[114] L Hedin and B I Lundqvist. Explicit local exchange-correlation potentials. *Journal of Physics C: Solid State Physics*, 4(14):2064–283, 1971. 36, 110

[115] M Benfatto, J Solera, J Chaboy, M Proietti, and J García. Theoretical analysis of x-ray absorption near-edge structure of transition-metal aqueous complexes in solution at the metal k edge. *Physical Review B*, 56(5):2447, Aug 1997. 36, 110

[116] D M Mills. Synchrotron radiation research .2. time-resolution experiments using x-ray synchrotron radiation. *Physics Today*, 37(4):22–30, 1984. 40

[117] Dennis Mills, Victor Pollock, Aaron Lewis, Alec Harootunian, and John Huang. Electronics and sample cell for the collection of time-resolved x-ray absorption spectra. *Nuclear Instruments and Methods in Physics Research*, 222(1-2):351–354, May 1984. 40

[118] Lin X Chen, Wighard J H Jager, Guy Jennings, David J Gosztola, Anneli Munkholm, and Jan P Hessler. Capturing a photoexcited molecular structure through time-domain x-ray absorption fine structure. *Science*, 292(5515):262–264, 2001. 40, 150

[119] L X Chen, G Jennings, T Liu, D J Gosztola, J P Hessler, D V Scaltrito, and G J Meyer. Rapid excited-state structural reorganization captured by pulsed x-rays. *Journal of the American Chemical Society*, 124(36):10861–10867, 2002. 40, 41

[120] Melanie Saes, Christian Bressler, Rafael Abela, Daniel Grolimund, Steven L Johnson, Philip A Heimann, and Majed Chergui. Observing photochemical transients by ultrafast x-ray absorption spectroscopy. *Physical Review Letters*, 90(4):047403, 2003. 40, 41, 74

[121] W Gawelda, M Johnson, F M F deGroot, R Abela, C Bressler, and M Chergui. Electronic and molecular structure of photoexcited [ruii(bpy)3]2+ probed by picosecond x-ray absorption spectroscopy. *Journal of the American Chemical Society*, 128(15):5001–5009, 2006. 40

[122] W Gawelda, V Pham, R van der Veen, D Grolimund, R Abela, M Chergui, and C Bressler. Structural analysis of ultrafast extended x-ray absorption fine structure with subpicometer spatial resolution: Application to spin crossover complexes. *The Journal of Chemical Physics*, 130(124520):124520, Jan 2009. 40, 61, 73, 74, 76, 80, 84, 85, 149

[123] Amal El Nahhas. *Time-Resolved Optical and X-Ray Spectroscopy of Rhenium Based Molecular Complexes*. Phd thesis, École Polytechnique Fédérale de Lausanne, 2010. 40, 74

[124] Renske van der Veen, Joshua Kas, Christopher Milne, Van-Thai Pham, Amal Nahhas, Frederico Lima, Dimali Vithanage, John Rehr, Rafael Abela, and Majed Chergui. L-edge xanes analysis of photoexcited metal complexes in solution. *Phys. Chem. Chem. Phys.*, 12(21):5551–5561, 2010. 40, 84, 111

[125] Majed Chergui and Ahmed H Zewail. Electron and x-ray methods of ultrafast structural dynamics: Advances and applications. *ChemPhysChem*, 10(1):28–43, 2009. 41, 150

[126] Majed Chergui. Picosecond and femtosecond x-ray absorption spectroscopy of molecular systems. *Acta Crystallogr A*, 66:229–239, 2010. 41, 55, 147, 150

[127] Melanie Saes, Frank van Mourik, Wojciech Gawelda, Maik Kaiser, Majed Chergui, Christian Bressler, Daniel Grolimund, Rafael Abela, Thornton E Glover, Philip A Heimann, Robert W Schoenlein, Steven L Johnson, Aaron M Lindenberg, and Roger W Falcone. A setup for ultrafast time-resolved x-ray absorption spectroscopy. *Review of Scientific Instruments*, 75(1):24–30, 2004. 41, 56, 57, 58, 59, 64, 74

[128] L X Chen. Probing transient molecular structures with time-resolved pump/probe xafs using synchrotron x-ray sources. *Journal of Electron Spectroscopy and Related Phenomena*, 119(2-3):161–174, 2001. 41, 58, 150

[129] Lin X Chen. Taking snapshots of photoexcited molecules in disordered media by using pulsed synchrotron x-rays. *Angewandte Chemie International Edition*, 43(22):2886–2905, 2004. 41

[130] Lin Chen, Xiaoyi Zhang, Erik Wasinger, Jenny Lockard, Andrew Stickrath, Michael Mara, Klaus Attenkofer, Guy Jennings, Grigory Smolentsev, and Alexander Soldatov. X-ray snapshots for metalloporphyrin axial ligation. *Chem. Sci.*, 1(5):642–650, 2010. 41

[131] W Gawelda, C Bressler, M Saes, M Kaiser, A N Tarnovsky, D Grolimund, S L Johnson, R Abela, and M Chergui. Picosecond time-resolved x-ray absorption spectroscopy of solvated organometallic complexes. *Physica Scripta*, T115:102, 2005. 41, 56, 59, 74

[132] M Gembicky, D Oss, R Fuchs, and P Coppens. A fast mechanical shutter for submicrosecond time-resolved synchrotron experiments. *Journal of Synchrotron Radiation*, 12:665–669, Jan 2005. 41, 61

[133] M Gembicky and P Coppens. On the design of ultrafast shutters for time-resolved synchrotron experiments. *Journal of Synchrotron Radiation*, 14:133–137, Jan 2006. 41, 61

[134] M Gembicky, S Adachi, and P Coppens. A khz heat-load shutter for white-beam experiments at synchrotron sources. *Journal of Synchrotron Radiation*, 14:295–296, Jan 2007. 41, 61

[135] M Cammarata, L Eybert, F Ewald, and W Reichenbach. Chopper system for time resolved experiments with synchrotron radiation. *Review of Scientific Instruments*, 80(015101), Jan 2009. 41, 61

[136] Linac coherent light source. http://lcls.slac.stanford.edu/. 42, 145, 148, 151

[137] Spring-8 compact sase source. http://www-xfel.spring8.or.jp/. 42, 148

[138] Swiss free-electron laser. http://www.psi.ch/swissfel/. 42

[139] European xfel. http://www.xfel.eu/en/. 42, 148

[140] Diamond light source. http://www.diamond.ac.uk/. 42, 43

[141] Swiss light source. http://www.psi.ch/sls/. 43

[142] P Beaud, S L Johnson, A Streun, R Abela, D Abramsohn, D Grolimund, F Krasniqi, T Schmidt, V Schlott, and G Ingold. Spatiotemporal stability of a femtosecond hard–x-ray undulator source studied by control of coherent optical phonons. *Physical Review Letters*, 99(174801):174801, 2007. 45, 53

[143] R W Schoenlein, S Chattopadhyay, H H W Chong, T E Glover, P A Heimann, C V Shank, A A Zholents, and M S Zolotorev. Generation of femtosecond pulses of synchrotron radiation. *Science*, 287:2237–2240, 2000. 45, 53

[144] N P Abreu, M Boge, F Muller, V Schlott, H C Sigg, A Streun, G Amatuni, DGishyan, K Manukyan, and A Sargsyan. Low-alpha operation of the sls storage ring. *Proceedings of PAC09*, 2009. 45, 46, 53, 155

[145] X Huang, J Safranek, J Corbett, Y Nosochkov, J Sebek, and A Terebilo. Low-alpha mode for spear3. *Proceedings of PAC07*, pages 1308–1310, 2007. 46

[146] S Johnson, P Beaud, C Milne, F Krasniqi, ES Zijlstra, ME Garcia, M Kaiser, D Grolimund, R Abela, and G Ingold. Nanoscale depth-resolved coherent femtosecond motion in laser-excited bismuth. *Physical Review Letters*, 100(155501):155501, Jan 2008. 46

[147] S Johnson, P Beaud, E Vorobeva, C Milne, ED Morray, S Fahy, and G Ingold. Directly observing squeezed phonon states with femtosecond x-ray diffraction. *Physical Review Letters*, 102(175503):175503, Jan 2009. 46

[148] S L Johnson, E Vorobeva, P Beaud, C J Milne, and G Ingold. Full reconstruction of a crystal unit cell structure during coherent femtosecond motion. *Phys. Rev. Lett.*, 103(20):205501, Nov 2009. 46

[149] P Beaud, S L Johnson, E Vorobeva, U Staub, R A De Souza, C J Milne, Q X Jia, and G Ingold. Ultrafast structural phase transition driven by photoinduced melting of charge and orbital order. *Phys. Rev. Lett.*, 103(15):155702, Oct 2009. 46

[150] G Bunker. Estimating photon flux from ion chamber currents. *BioCAT: Basic Techniques for EXAFS*, 1988. 48

[151] Mathew Newville. Ifeffit: interactive xafs analysis and feff ifeffit. *Journal of Synchrotron Radiation*, 8:322–324, 2001. 48

[152] Fundamentals of xafs. http://xafs.org/Tutorials. 49, 51

[153] Pieter Glatzel and Uwe Bergmann. High resolution 1s core hole x-ray spectroscopy in 3d transition metal complexes–electronic and structural information. *Coordination Chemistry Reviews*, 249(1-2):65–95, 2005. 50

[154] P Glatzel, M Sikora, and M Fernandez-Garcia. Resonant x-ray spectroscopy to study k absorption pre-edges in 3d transition metal compounds. *Eur. Phys. J. Special Topics*, 169:207–214, 2009. 50

[155] Uwe Bergmann and Pieter Glatzel. X-ray emission spectroscopy. *Photosynthesis Research*, 102(2-3):255–266, 2009. 50

[156] G Vankó, P Glatzel, V.-T Pham, R Abela, D Grolimund, C Borca, S Johnson, C Milne, and C Bressler. Picosecond time-resolved x-ray emission spectroscopy: Ultrafast spin-state determination in an iron complex. *Angewandte Chemie*, 122(34):6046–6048, 2010. 50, 151

[157] Xanes dactyloscope - a program for quick and rigorous xanes analysis for windows. http://www.cells.es/Beamlines/CLAESS/software/xanda.html. 51, 52

[158] W Widdra, D Brocker, T Gießel, I V Hertel, W Kruger, A Liero, F Noack, V Petrov, D Pop, P M Schmidt, R Weber, I Will, and B Winter. Time-resolved core level photoemission: surface photovoltage dynamics of the sio2/si(1 0 0) interface. *Surface Science*, 543:87–94, 2003. 52

[159] T Gießel, D Bröcker, P Schmidt, and W Widdra. Time-resolving and energy-dispersive photoelectron detector for combined laser and synchrotron radiation experiments. *Review of Scientific Instruments*, 74(11):4620–4624, 2003. 52

[160] D Brewe, S Heald, E Stern, K Beck, and Y Feng. High efficiency xafs data collection with sub-nanosecond time resolution. *AIP Conf. Proc.*, 705(1):1399–1402, May 2004. 52

[161] Edward Stern and Dale Brewe. Ultrafast xafs measurements on laser excited ge films. *AIP Conf. Proc.*, 882(1):24–28, Feb 2007. 52

[162] J Feikes, P Kuske, and G Wustefeld. Towards sub-picosecond electron bunches: upgrading ideas for bessy ii. *Proceedings of the EPAC 2006*, pages 157–159, 2006. 53

[163] T Quast, K Holldack, S Khan, and R Mitzner. Femtoslicing at bessy-detecting more photons. *Proceedings of the EPAC 2008*, pages 172–174, 2008. 53

[164] Natalia Prado de Abreu, Paul Beaud, Gerhard Ingold, and Andreas Streun. New filling pattern for sls-femto. Technical report, SLS Internal report, 2009. http://slsbd/pub/slsnotes/tmeta090317.pdf. 53

[165] Brian Ahr, Matthieu Chollet, Bernhard Adams, Elizabeth M Lunny, Christopher M Laperle, and Christoph Rose-Petruck. Picosecond x-ray absorption measurements of the ligand substitution dynamics of fe(co)5 in ethanol. *Phys. Chem. Chem. Phys.*, 13:5590–5599, 2011. 53

[166] A Streun, G Ingold, A Al-Adwan, P Beaud, M Boge, S Johnson, A Keller, T Schilcher, V Schlott, T Schmidt, L Schulz, and D Zimoch. Sub-picosecond x-ray source femto at sls. *Proceedings of the EPAC 2006*, 2006. 53

[167] G Ingold, R Abela, P Beaud, and S Johnson. Towards pump-probe resonant x-ray diffraction at femtosecond undulator sources. *Zeitschrift fur Kristallographie*, 223:292–306, Jan 2008. 53

[168] C Borca, D Grolimund, M Willimann, B Meyer, K Jefimovs, J Vila-Comamala, and C David. The microxas beamline at the swiss light source: Towards nano-scale imaging. *Journal of Physics: Conference Series*, 186(012003):1–3, Jan 2009. 54

[169] Melanie Saes. *Picosecond x-ray absorption spectroscopy: application to coordination chemistry compounds in solution.* Phd thesis, École Polytechnique Fédérale de Lausanne, 2004. 57, 58, 74

[170] Christian Bressler, Melanie Saes, Majed Chergui, Daniel Grolimund, Rafael Abela, and Philip Pattison. Towards structural dynamics in condensed chemical systems exploiting ultrafast time-resolved x-ray absorption spectroscopy. *J. Chem. Phys.*, 116(7):2955–2966, 2002. 59, 76, 150

[171] W Gawelda, V T Pham, A El Nahhas, M Kaiser, Y Zaushitsyn, S L Johnson, D Grolimund, R Abela, A Hauser, C Bressler, and M Chergui. Capturing transient electronic and molecular structures in liquids by picosecond x-ray absorption spectroscopy. *AIP Conference Proceedings - XAFS13*, 882:31–36, 2007. 64

[172] Diamond materials. http://www.diamond-materials.com/EN/index.htm. 65, 102

[173] The center of x-ray optics: X-ray interactions with matter. http://henke.lbl.gov/optical_constants/. 65

[174] International whaling commission. http://iwcoffice.org/. 67

[175] Lawrence J. kagen. *Myoglobin: Biochemical, Physiological, and Clinical Aspects.* Columbia University Press, 1973. 67, 94

[176] Seongheun Kim, Geunyeong Jin, and Manho Lim. Dynamics of geminate recombination of no with myoglobin in aqueous solution probed by femtosecond mid-ir spectroscopy. *Journal of Physical Chemistry B*, 108(52):20366–20375, 2004. 68, 102, 105, 106

[177] M Lim, T A Jackson, and P A Anfinrud. Orientational distribution of co before and after photolysis of mbco and hbco: A determination using time-resolved polarized mid-ir spectroscopy. *Journal of the American Chemical Society*, 126(25):7946–7957, 2004. 69, 100

[178] W Gawelda, A Cannizzo, V T Pham, F vanMourik, C Bressler, and M Chergui. Ultrafast nonadiabatic dynamics of [feII(bpy)3]2+ in solution. *Journal of the American Chemical Society*, 129(26):8199–8206, 2007. 73, 75

[179] Wojciech Gawelda, Andrea Cannizzo, Van-Thai Pham, Amal El Nahhas, Christopher J Milne, Renske van der Veen, Christian Bressler, and Majed Chergui. Light-induced spin crossover probed by ultrafast optical and x-ray spectroscopies. *Chimia*, 61(4):179–183, 2007. 74

[180] A Cannizzo, C.J Milne, C Consani, W Gawelda, Ch Bressler, F van Mourik, and M Chergui. Light-induced spin crossover in fe(ii)-based complexes: The full photocycle unraveled by ultrafast optical and x-ray spectroscopies. *Coordination Chemistry Reviews*, 254(21-22):2677–2686, 2010. 74, 75

[181] Cristina Consani, Mirabelle Prémont-Schwarz, Amal ElNahhas, Christian Bressler, Frank van Mourik, Andrea Cannizzo, and Majed Chergui. Vibrational coherences and relaxation in the high-spin state of aqueous [fe(bpy)]. *Angewandte Chemie International Edition*, 48(39):7184–7187, 2009. 75

[182] Christian Bressler, Melanie Saes, Majed Chergui, Rafael Abela, and Philip Pattison. Optimizing a time-resolved x-ray absorption experiment. *Nuclear Instruments and Methods in Physics Research Section A: Accelerators, Spectrometers, Detectors and Associated Equipment*, 467-468(Part 2):1444–1446, 2001. 76

[183] M Benfatto, S DellaLonga, K Hatada, K Hayakawa, W Gawelda, C Bressler, and M Chergui. A full multiple scattering model for the analysis of time-resolved x-ray difference absorption spectra. *Journal of Physical Chemistry B*, 110(29):14035–14039, 2006. 80

[184] T. Penfold. Tddft calculations of the xas spectra of fe-based complexes. private communication, 2011. 80, 87, 88, 89, 91, 111, 148

[185] S Dick. Crystal structure of tris(2,2'-bipyridine)iron(ii) bis(hexafluorophosphate), (c10h8n2)3fe(pf6)2. *Zeitschrift für Kristallographie*, 213:356–, 1998. 81

[186] Max Lawson Daku, Alfredo Vargas, Andreas Hauser, Antony Fouqueau, and Mark Earl Casida. Assessment of density functionals for the high-spin/low-spin energy difference in the low-spin iron(ii) tris(2,2-bipyridine) complex. *ChemPhysChem*, 6(7):1393–1410, 2005. 81

[187] Latévi Lawson Daku and Andreas Hauser. Ab initio molecular dynamics study of an aqueous solution of [fe(bpy)3](cl)2 in the low-spin and in the high-spin states. *The Journal of Physical Chemistry Letters*, 1(12):1830–1835, Jun 2010. 81

[188] I. Lindgren. Chemical shifts in x-ray and photo-electron spectroscopy: a historical review. *Journal of Electron Spectroscopy and Related Phenomena*, 137-140:59–71, 2004. 84

[189] Tami Westre, Pierre Kennepohl, Jane DeWitt, Britt Hedman, Keith Hodgson, and Edward Solomon. A multiplet analysis of fe k-edge 1s 3d pre-edge features of iron complexes. *Journal of the American Chemical Society*, 119(27):6297–6314, Jul 1997. 85, 86

[190] Shunsuke Nozawa, Tokushi Sato, Matthieu Chollet, Kouhei Ichiyanagi, Ayana Tomita, Hiroshi Fujii, Shin ichi Adachi, and Shin ya Koshihara. Direct probing of spin state dynamics coupled with electronic and structural modifications by picosecond time-resolved xafs. *Journal of the American Chemical Society*, 132(1):61–63, Jan 2010. 85, 86

[191] Lin X Chen, Zhiyu Wang, Jeremy K Burdett, Pedro A Montano, and James R Norris. X-ray absorption studies on electronic spin state transitions of fe(ii) complexes in different media. *The Journal of Physical Chemistry*, 99(20):7958–7964, 1995. 86

[192] G R Shulman, Y Yafet, P Eisenberger, and W E Blumberg. Observations and interpretation of x-ray absorption edges in iron compounds and proteins. *Proceedings of the National Academy of Sciences*, 73(5):1384–1388, 1976. 86, 97

[193] V Briois, Ch Cartier dit Moulin, Ph Sainctavit, Ch Brouder, and A-M Flank. Full multiple scattering and crystal field multiplet calculations performed on the spin transition feii(phen)2(ncs)2 complex at the iron k and l2,3 x-ray absorption edges. *Journal of the American Chemical Society*, 117(3):1019–1026, 1995. 86, 87

[194] V Briois, Ph Sainctavit, Gary J Long, and Fernande Grandjean. Importance of photoelectron multiple scattering in the iron k-edge x-ray absorption spectra of spin-crossover complexes: full multiple scattering calculations for several iron(ii) trispyrazolylborate and trispyrazolylmethane complexes. *Inorganic Chemistry*, 40(5):912–918, 2001. 86, 87

[195] Frank Neese. The orca program system. *Wiley Interdisciplinary Reviews: Computational Molecular Science*, 2011. 88, 138

[196] Serena DeBeer George, Taras Petrenko, and Frank Neese. Time-dependent density functional calculations of ligand k-edge x-ray absorption spectra. *Inorganica Chimica Acta*, 361(4):965 – 972, 2008. 88, 138

[197] Q Gibson and S Ainsworth. Photosensitivity of haem compounds. *Nature*, 180(4599):1416–1417, 1957. 95

[198] Barry A Springer, Stephen G Sligar, John S Olson, and George N Jr Phillips. Mechanisms of ligand recognition in myoglobin. *Chemical Reviews*, 94(3):699–714, 1994. 95

[199] S Della-Longa, A Arcovito, M Benfatto, A Congiu-Castellano, M Girasole, J L Hazemann, and A Lo Bosco. Redox-induced structural dynamics of fe-heme ligand in myoglobin by x-ray absorption spectroscopy. *Biophysical Journal*, 85(1):549–558, 2003. 96

[200] Galina S Kachalova, Alexander N Popov, and Hans D Bartunik. A steric mechanism for inhibition of co binding to heme proteins. *Science*, 284(5413):473–476, 1999. 96, 97

[201] Jaroslav Vojtchovsky, Kelvin Chu, Joel Berendzen, Robert Sweet, and Ilme Schlichting. Crystal structures of myoglobin-ligand complexes at near-atomic resolution. *Biophysical Journal*, 77(4):2153–2174, 1999. 96

[202] Daniel Copeland, Alexei Soares, Ann West, and George Richter-Addo. Crystal structures of the nitrite and nitric oxide complexes of horse heart myoglobin. *Journal of inorganic biochemistry*, 100(8):1413–1425, 2006. 96, 97, 107, 120

[203] DM Copeland, AH West, and GB Richter-Addo. Crystal structures of ferrous horse heart myoglobin complexed with nitric oxide and nitrosoethane. *Proteins*, 53(2):182–192, Jan 2003. 96, 120

[204] Alessandro Arcovito, Maurizio Benfatto, Paola D'Angelo, and Stefano Della Longa. Hemeproteins: Recent advances in quantitative xanes analysis. *AIP Conference Proceedings - XAFS13*, 882(1):306–310, 2007. 97

[205] David R Nutt and Markus Meuwly. Theoretical investigation of infrared spectra and pocket dynamics of photodissociated carbonmonoxy myoglobin. *Biophysical Journal*, 85(6):3612–3623, 2003. 98

[206] Nuria Plattner and Markus Meuwly. The role of higher co-multipole moments in understanding the dynamics of photodissociated carbonmonoxide in myoglobin. *Biophysical Journal*, 94(7):2505–2515, Apr 2008. 98

[207] S Della-Longa, I Ascone, A Fontaine, A Congiu Castellano, and A Bianconi. Intermediate states in ligand photodissociation of carboxymyoglobin studied by dispersive x-ray absorption. *European Biophysics Journal*, 23(5):361–368, 1994. 98

[208] E Henry, J Sommer, J Hofrichter, W Eaton, and M Gellert. Geminate recombination of carbon monoxide to myoglobin. *Journal of Molecular Biology*, 166(3):443–451, 1983. 100

[209] D Ionascu, F Gruia, X Ye, A Yu, F Rosca, C Beck, A Demidov, J S Olson, and P M Champion. Temperature-dependent studies of no recombination to heme and heme proteins. *Journal of the American Chemical Society*, 127(48):16921–16934, 2005. 101, 102, 104, 105, 106

[210] S Kruglik, B Yoo, and S Franzen. Picosecond primary structural transition of the heme is retarded after nitric oxide binding to heme proteins. *PNAS*, 107(31):13678–13683, Jan 2010. 101, 103, 105, 106, 128, 150

[211] Tomasz Zemojtel, Matteo Rini, Karsten Heyne, Thomas Dandekar, Erik Nibbering, and Pawel Kozlowski. No-bound myoglobin: structural diversity and dynamics of the no ligand. *Journal of the American Chemical Society*, 126(7):1930–1931, Feb 2004. 102, 105, 106

[212] J W Petrich, J C Lambry, K Kuczera, Martin Karplus, C Poyart, and J L Martin. Ligand binding and protein relaxation in heme proteins: a room temperature analysis of nitric oxide geminate recombination. *Biochemistry*, 30(16):3975–3987, 1991. 102, 105, 106

[213] J Petrich, J Lambry, Sriram Balasubramanian, David Lambright, Steven Boxer, and J Martin. Ultrafast measurements of geminate recombination of no with site-specific mutants of human myoglobin. *Journal of Molecular Biology*, 238(3):437–444, May 1994. 102, 105, 106

[214] Y Kholodenko, EA Gooding, Y Dou, M Ikeda-Saito, and RM Hochstrasser. Heme protein dynamics revealed by geminate nitric oxide recombination in mutants of iron and cobalt myoglobin. *Biochemistry*, 38(18):5918–5924, Jan 1999. 105, 106

[215] Protein data bank. http://www.pdb.org/. 107, 118, 125, 130

[216] A Arcovito, D C Lamb, G U Nienhaus, J L Hazemann, M Benfatto, and S Della Longa. Light-induced relaxation of photolyzed carbonmonoxy myoglobin: A temperature-dependent x-ray absorption near-edge structure (xanes) study. *Biophysical Journal*, 88(4):2954–2964, 2005. 109, 129

[217] J Müller, O Jepsen, and J Wilkins. X-ray absorption spectra: K-edges of 3d transition metals, l-edges of 3d and 4d metals, and m-edges of palladium. *Solid State Communications*, 42(5):365–368, 1982. 111

[218] K Hayakawa, K Hatada, S Longa, and P Angelo. Progresses in the mxan fitting procedure. *AIP Conference Proceedings - XAFS 13*, Jan 2007. 111

[219] D R Nutt, M Karplus, and M Meuwly. Potential energy surface and molecular dynamics of mbno: Existence of an unsuspected feon minimum. *Journal of Physical Chemistry B*, 109(44):21118–21125, 2005. 120

[220] David R Nutt and Markus Meuwly. Studying reactive processes with classical dynamics: Rebinding dynamics in mbno. *Biophysical Journal*, 90(4):1191–1201, 2006. 120

[221] S Roy, D Parks, K A Seu, R Su, J J Turner, W Chao, E H Anderson, S Cabrini, and S D Kevan. Lensless x-ray imaging in reflection geometry. *Nature Photonics*, 5(4):243–245, 2011. 148

[222] Brian Abbey, Lachlan Whitehead, Harry Quiney, David Vine, Guido Cadenazzi, Clare Henderson, Keith Nugent, Eugeniu Balaur, Corey Putkunz, Andrew Peele, WilliamsG. J., and McNultyI. Lensless imaging using broadband x-ray sources. *Nature Photonics*, 5(7):420–424, 2011. 148

[223] A.V. Martin *et al.* Single particle imaging with soft x-rays at the linac coherent light source. *Proc. SPIE*, 8078(1):807809, 2011. 148

[224] H. Chapman *et al.* Femtosecond x-ray protein nanocrystallography. *Nature*, 470(7332):73–77, 2011. 148

[225] Richard A Kirian, Thomas A White, James M Holton, Henry N Chapman, Petra Fromme, Anton Barty, Lukas Lomb, Andrew Aquila, Filipe R N C Maia, Andrew V Martin, Raimund Fromme, Xiaoyu Wang, Mark S Hunter, Kevin E Schmidt, and John C H Spence. Structure-factor analysis of femtosecond microdiffraction patterns from protein nanocrystals. *Acta Crystallogr A*, 67(2):131–140, 2011. 148

[226] G Doumy, C Roedig, S-K Son, C I Blaga, A D DiChiara, R Santra, N Berrah, C Bostedt, J D Bozek, P H Bucksbaum, J P Cryan, L Fang, S Ghimire, J M Glownia, M Hoener, E P Kanter, B Krässig, M Kuebel, M Messerschmidt, G G Paulus, D A Reis, N Rohringer, L Young, P Agostini, and L F DiMauro. Nonlinear atomic response to intense ultrashort x rays. *Phys. Rev. Lett.*, 106:083002, 2011. 148

[227] S.L Johnson and C.J Milne. Ultrafast x-ray science: structural transients in solution. *TrAC Trends in Analytical Chemistry*, 29(6):497–507, 2010. 150

[228] Frederico Lima, Christopher Milne, Dimali Amarasinghe, Mercedes Rittmann-Frank, Renske van der Veen, Marco Reinhard, Van-Thai Pham, Susanne Karlsson, Steven Johnson, Daniel Grolimund, Camelia Borca, Thomas Huthwelker, Markus Janousch, Frank van Mourik, Rafael Abela, and Majed Chergui. A high-repetition rate scheme for synchrotron-based picosecond laser pump/x-ray probe experiments on chemical and biological systems in solution. *Review of Scientific Instruments*, 82(6):063111–16, Jun 2011. 144, 151

[229] Nils Huse, Haidan Wen, Dennis Nordlund, Erzsi Szilagyi, Dan Daranciang, Timothy A Miller, Anders Nilsson, Robert W Schoenlein, and Aaron M Lindenberg. Probing the hydrogen-bond network of water via time-resolved soft x-ray spectroscopy. *Phys. Chem. Chem. Phys.*, 11:3951–3957, 2009. 151

[230] Nils Huse, Munira Khalil, Tae Kyu Kim, Amanda L Smeigh, Lindsey Jamula, James K McCusker, and Robert W Schoenlein. Probing reaction dynamics of transition-metal complexes in solution via time-resolved x-ray spectroscopy. *Journal of Physics: Conference Series*, 148(1):012043, 2009. 151

[231] Nils Huse, Tae Kim, Lindsey Jamula, James McCusker, Frank de Groot, and Robert Schoenlein. Photo-induced spin-state conversion in solvated transition metal complexes probed via time-resolved soft x-ray spectroscopy. *Journal of the American Chemical Society*, 132(19):6809–6816, 2010. 151

[232] C. Bressler and W. Gawelda. Time-resolved xes and rixs of fe-centered complexes. in preparation, 2011. 151

[233] C. J. Milne, M. H. Rittmann-Frank, M. Reinhard, J. Rittmann, de Paiva J, J. Szlachetko, M. Narchtegal, and M. Chergui. Ultrafast time-resolved xes and rixs at mhz repetition rate. in preparation, 2011. 151

Swiss Light Source
WLSA/209
Paul Scherrer Institut
Villigen AG
Switzerland
+41 79 396 0468
+41 56 426 2353
frederico.lima@epfl.ch
http://people.epfl.ch/frederico.lima

Frederico A. Lima

Physicist

Education

2007 – 2011 **Ph.D. in Physics**, *Ecole Polytechnique Fédérale de Lausanne*, Lausanne, Switzerland, Department of Chemistry.
EPFL Switzerland.
http://lsu.epfl.ch

PhD Thesis

Title *Investigation of physiological solutions of metalloproteins using a high repetition rate picosecond x-ray absorption experiment*

Supervisor Professor Majed Chergui

Description My project involved the extention of the existing capabilities of the time-resolved optical pump/X-ray probe X-ray absorption spectroscopy (XAS) experiments carried out at the Swiss Light Source (SLS) towards data collection at MHz repetition rates. The implementation of such methodology made possible the investigation of the structural and electronic changes related to the photoinduced dissociation and rebinding of small molecules to the iron atom in myoglobin.

2005 – 2007 **MSc. in Physics**, *Physics Department*, Universidade Federal de Minas Gerais, Belo Horizonte.
Belo Horizonte, Brazil
http://www13.fisica.ufmg.br/posgrad

Master Thesis

Title *Study of the Incommensurated Modulated phases of $K_2Mo_xW_{(1-x)}O_4$ by X-ray powder diffraction*

Supervisors Professors Nivaldo Lúcio Speziali and Carlos Basílio Pinheiro

Description Different normal and modulated phases of potassium molybdate, potassium tungstate and the mixed compound $K_2Mo_{0.5}W_{0.5}O4$ were studied by X-ray powder diffraction. The Rietveld method for structural refinement was widely used on the analysis process. A new interpretation for an intermediate modulated phase was proposed based on a structural model which describe the crystal as being composed by three orthorhombic domains, rotated by 120^0 with respect to each other.

2001 – 2004 **Bachelor degree in Physics**, *Physics Department, Universidade Federal de Minas Gerais*, Belo Horizonte, Brazil,
http://www.fisica.ufmg.br.

Complementary education

Courses and Workshops

2010 **Jyväskylä Summer School - Dynamics of (bio)molecules**, *Jyväskylä University*, Jyväskylä, Finland.

2009 **PSI Summer School - Functional Materials**, Zuoz, Switzerland.

2009 **Ultrafast X-ray Summer School**, *PULSE - SLAC National Accelerator Laboratory*, Stanford – USA.

2008 **Workshop on X-ray absorption spectroscopy and advanced XAS techniques**, *PSI - Paul Shcerrer Institut*, Villigen, Switzerland.

2008 **VII. Research Course on New X-Ray Sciences: New Materials in New Light**, *DESY - Deutsches Elektronen-Synchrotron*, Hamburg – Germany.

2008 **Advanced School on Synchrotron and Free Electron Laser Sources and their Multidisciplinary Applications**, *ICTP International Centre for Theoretical Physics*, Trieste - Italy.

2007 **Methods of Powder Difraction**, *LNLS - Laboratório Nacional de Luz Síncrotron*, Campinas, Brazil.

2007 **Latin American Workshop on Applications of Powder Diffraction**, *LNLS - Laboratório Nacional de Luz Síncrotron*, Campinas, Brazil.

2006 **Introduction to the Methods of Structural Characterization of Proteins (Introdução aos Métodos de Caracterização Estrutural de Proteínas)**, *LNLS - Laboratório Nacional de Luz Síncrotron*, Campinas, Brazil.

2004 **Practical Course in Diffraction Methods**, *Laboratory of Crystallography, EPFL*, Lausanne, Switzerland.

Internship

2004 **Study of the thermotropic phase transitions of the $K_2Mo_xW_{(1-x)}O_4$ compounds**, *EPFL*, Laboratory of Crystallography, Lausanne, Switzerland.

Supervisors Professors Gervais Chapuis and Carlos Basílio Pinheiro

Scientific Conferences

2011 **SSRL / LCLS Annual Users' Meeting & Workshops**, *Menlo Park, United States*.

2011 **SLS Sympositum - Measurements in Solution**, *Villigen, Switzerland*, (invited talk).

2011 **Fall Meeting of the Swiss Chemical Society**, *Lausanne, Switzerland*.

2011 **MUST (Molecular Ultrafast Science and Technology) Assembly Meeting**, *Lenk, Switzerland*.

2010 **First International Conference on Ultrafast Structural Dynamics**, *Ecole Polytechnique Fédérale de Lausanne*, Lausanne, Switzerland.

2008 **Swiss Physical Society Annual Meeting**, *Université de Genève*, Geneva, Switzerland.

2005 **Brazillian Crystallography Society Meeting**, *LNLS - Laboratório Nacional de Luz Síncrotron*, Campinas, Brazil.

2003 **Aperiodic 2003 - International Conference on Aperiodic Crystals**, *UFMG - Universidade Federal de Minas Gerais*, Belo Horizonte, Brazil.

Scholarships

Doctoral studies My doctoral studies have been sponsored by EPFL, PSI and the Swiss National Science Foundation.

Master studies I fulfilled my Master degree studies under scholarship of the Brazilian foundation CAPES - Coordenação de Aperfeiçoamento de Pessoal de Nível Superior

Undergraduate I fulfilled my undergraduate studies under scholarship of the Brazilian foundation CNPq - Conselho Nacional de Desenvolvimento Científico e Tecnológico

Languages

Portuguese Fluent (native)

English Fluent

French basic (A2 - Common European Framework of Reference for Languages)

Spanish basic (A1 - Common European Framework of Reference for Languages)

Scientific Interests

- Time-resolved X-ray techniques
- Time-resolved XAS, XES, RIXS
- Time-resolved and conventional Crystallography
- X-ray Free Electron Lasers

Computer Skills

General purpose	All Microsoft™ operating systems, MacOS
	TEX, LATEX, Microsoft Office™, Adobe Illustrator™
Scientific	Igor Pro™, Origin™, GNUPlot, basics of Mathematica™and Matlab™
XAS Data analysis	FEFF9, MXAN, IFEFFIT

Publications

2011 *A high-repetition rate scheme for synchrotron-based picosecond laser pump/x-ray probe experiments on chemical and biological systems in solution*, **F. A. Lima**, C. J. Milne, D. C. V. Amarasinghe, M. H. Rittmann-Frank, R. M. van der Veen, M. Reinhard,V-T. Vam, S. Karlsson, S. Johnson, D. Grolimund, C. Borca, T. Huthwelker, M. Janousch, R. Abela, F. van Mourik, and M. Chergui, Review of Scientific Instruments, **82**, 063111 (2011)
http://rsi.aip.org/resource/1/rsinak/v82/i6/p063111_s1

Determination of the electronic and molecular structure of the Bis(diimine)copper(I) complex by the copper K-edge spectrum, T. J. Penfold, S. Karlsson, **F. A. Lima**, M. Reinhard, M. H. Rittmann-Frank, J. Rittmann, R. Abela, E. Baranoff, I. Tavernelli, U. Rothlisberger, C. Milne and M. Chergui, *submitted to Angewandte Chemie*

Electronic and geometric structure of physiological solutions of myoglobin using x-ray absorption spectroscopy, **F. A. Lima**, C. Milne, T. Penfold, D. C. V. Amarasinghe, M. Reinhard, M. H. Rittmann-Frank, S. Karlsson, D. Grolimund, C. Borca, R. Abela, M. Benfatto and M. Chergui, *in preparation*

X-ray absorption studies of the photo-induced structural changes of nitrosyl-myoglobin in physiological media, **F. A. Lima**, C. Milne, T. Penfold, M. Reinhard, M. H. Rittmann-Frank, D. Grolimund, C. Borca, R. Abela, M. Benfatto and M. Chergui, *in preparation*

Probing the transition from hydrophilic to hydrophobic solvation with atomic scale resolution, V-T. Pham, T. Penfold, R. van der Veen, **F. A. Lima**, A. El Nahhas, S. Johnson, P. Beaud, R. Abela, C. Bressler, I. Tavernelli, C. Milne and M. Chergui, Journal of the American Chemical Society, **133** (32), pp 12740–12748 (2011)
http://pubs.acs.org/doi/abs/10.1021/ja203882y

Ultrafast X-ray Absorption Studies of the Structural Dynamics of Molecular and Biological Systems in Solution, C. J. Milne, R. M. Van der Veen, V-T. Pham, **F. A. Lima**, H. Rittmann-Frank, M. Reinhard, F. van Mourik, S. Karlsson, T. J. Penfold, and Majed Chergui, CHIMIA International Journal for Chemistry, **65** (5), pp. 303-307 (2011)
http://id22079462.library.ingentaconnect.com/content/scs/chimia/2011/00000065/00000005/art00004

2010 *L-edge XANES analysis of photoexcited metal complexes in solution*; R. M. van der Veen, J. J. Kas, C. J. Milne, V.-T. Pham, A. El Nahhas, **F. A. Lima**, D. A. Vithanage, J. J. Rehr, R. Abela and M. Chergui, Physical Chemistry Chemical Physics, **12**, 5551-5561 (2010)
http://pubs.rsc.org/en/Content/ArticleLanding/2010/CP/b927033g

2009 *Modulated phase of $K_2Mo_xW_{(1-x)}O_4$ mixed compounds using orthorhombic symmetry: A powder diffraction study*; **F. A. Lima**, A. A. Guarnieri, C. B. Pinheiro, and N. L. Speziali, Physical Review **B** 79 (174103) (2009)
http://prb.aps.org/abstract/PRB/v79/i17/e174103

Time-resolved x-ray absorption spectroscopy: Watching atoms dance; C. J. Milne, V-T. Pham, W. Gawelda, R. M. van der Veen, A. El Nahhas, S. L. Johnson, P. Beaud, G. Ingold, **F. Lima**, D. A. Vithanage, M. Benfatto, D. Grolimund, C. Borca, M. Kaiser, A. Hauser, R. Abela, C. Bressler and M. Chergui,Journal of Physics: Conference Series 190, 012052 (2009)
http://iopscience.iop.org/1742-6596/190/1/012052

Structural Determination of a Photochemically Active Diplatinum Molecule by Time-Resolved EXAFS Spectroscopy; R. M. van der Veen, C. J. Milne, A. El Nahhas, **F. A. Lima**, V-T. Pham, J. Best, J. A. Weinstein, C. N. Borca, R. Abela, C. Bressler and M. Chergui., Angewandte Chemie International Edition, 48 (15), 2711-2714 (2009)
http://dx.doi.org/10.1002/anie.200805946

Retrieving photochemically active structures by time-resolved EXAFS spectroscopy.; R. M. van der Veen, C. Bressler, C. J. Milne, V-T. Pham, A. El Nahhas, **F. A. Lima**, W. Gawelda, C. N. Borca, R. Abela and M. Chergui, Journal of Physics: Conference Series 190, 012054 (2009).
http://www.iop.org/EJ/abstract/1742-6596/190/1/012054

References

Professor Majed Chergui
PhD thesis supervisor
Laboratory of Ultrafast Spectroscopy
EPFL-SB-ISIC-LSU
Station 6
CH-1015 Lausanne, Switzerland
Phone:+41 21 693 0457
Fax: +41 21 693 0365
Email: majed.chergui@epfl.ch

Dr. Christopher J. Milne
Swiss Light Source
Paul Scherrer Institut
Villigen PSI
CH-5232 Villigen, Switzerland
Phone:+41 56 310 5477
Fax: +41 56 310 4413
Email: chris.milne@psi.ch

Dr. Maurizio Benfatto
Istituto Nazionale di Fisica Nucleare
Laboratori Nazionali di Frascati
Frascati, Italy
Email: Maurizio.Benfatto@lnf.infn.it

Professor Nivaldo L. Speziali
MSc. supervisor
Departamento de Física - UFMG
Belo Horizonte, MG
30161-970 - Brasil
Phone:+55 31 3409 5672
Fax: +55 31 3409 5600
Email: nspezial@fisica.ufmg.br

Professor Carlos B. Pinheiro
MSc. co-advisor
Departamento de Física - UFMG
Belo Horizonte, MG
30161-970 - Brasil
Phone:+55 31 3409 6600
Fax: +55 31 3409 5600
Email: basilio@fisica.ufmg.br

Acknowledgements

"At times our own light goes out and is rekindled by a spark from another person. Each of us has cause to think with deep gratitude to those who have lighted the flame with us"

Albert Schweitzer - Nobel Peace Prize in 1952

It is of general consensus that a PhD thesis is not the result of the work of a single person. Many people have contributed to the work presented in my thesis and I feel deeply thankful to all of them. In first place I would like to express my deepest gratitude to my thesis supervisor *Professor Majed Chergui*. Over the course of the last four and half years he was a constant source of motivation, encouragement and scientific knowledge; managing an extremely successful team of researchers and guiding us all over the frontiers of ultrafast science.

I am thankful to the PhD thesis committee members, *Professor Stefano Della Longa*, *Professor Petr Leiman*, *Professor Michel Négrerie* and *Professor Romuald Houdré* for their acceptance to become part of the jury, for the general interest in my work, and especially for the recognition, criticism and valuable comments during the exam.

I have still not found the appropriate words to acknowledge my 'direct boss' *Dr. Chris Milne*. With his friendly and easygoing way he managed to successfully accomplish several beamtimes, which in the end resulted not only on my own thesis, but on some already finished and many more still to come. Thanks for the inspiration, for the example of successful scientist, for the several discussions, for teaching me how to plan and do a time-resolved XAS experiment, for the tips on the Apple© world, for correcting my manuscript until the last minute and for the perfectionism with I see you proceeding with any work you are involved.

I would like to acknowledge every single person that helped me making my experiments, and consequently my PhD possible, but I am sure I will not succeed due to the immense number of people involved. I am very grateful to the expertise of the microXAS staff. Thanks *Dr. Daniel Grolimund*, *Dra. Camelia Borca*, *Mr. Markus Willimann* and *Mr. Beat Meyer*. Thanks for setting up the beamline so many times, to promptly answer my several questions, to always be ready to help and squeeze out every single photon, to attend my request of material and poisonous gases. Thank you very much the whole FEMTO team at PSI. Thanks for opening the roads of the time-resolved world at SLS, thanks for the inspiration and guidance. Thank you *Dr. Gerhard Ingold* for the numerous pleasant discussions over lunch, for the motivation and to look at me (and to the others from my generation) as 'the future of science'. Thanks for posing

questions and perspectives for 'the future'. Thanks *Dr. Paul Beaud* for sharing your expertise on lasers and ultrafast science, for slowly believing on me and for helping us to bring the tools back to the lab. Thank you *Professor Steve Johnson* for the example of ideal scientist, for your intelligence, for the scientific discussions, for the great mood during beamtimes and for the inspiration. Thanks *Dr. Rafael Abela* for the support of my project and all the ultrafast science field. Thank you all the administrative staff that have so efficiently taken care of the bureaucracy involved in the EPFL-PSI common projects. Thanks *Mme. Monique Grin Celka*, *Mme. Esther von Arx*, *Mme. Monique Bassin*, *Mme. Charlotte Herr*, *Mme. Daniela Jahns* and *Mme. Silvia Bacher* for all organization, travel tickets, hotel rooms, seminars, paperwork, etc that you have organized. Thank you very much *Mr. Erich De Boni* for the support with the safety and gas handling during the experiments, and *Dr. Maarten Nachtegaal* for providing access to the labs and to the 'gas läger'. Thank you *Dr. Gaudenz Jud*, the whole Controls group at PSI, and the EPFL electronics workshop for the help on the data acquisition hardware.

A very special acknowledgement goes to *Dr. Maurizio Benfatto*. Thank you very much for having hosted me at the Laboratori Nazionali di Frascati (LNF) at Istituto Nazionale di Fisica Nucleare (INFN), for the great help with the `MXAN` code and specially for making available the computer cluster facility of LNF on which I performed a great part of the calculations presented on this thesis. Also, thanks for all the discussions, the tips for the calculation and for providing the `MXAN` code to the scientific community, which is of great relevance. Thank you very much *Professor John J. Rehr* for making the `FEFF9` code available to the scientific community, representing a unique set of theoretical tools that have greatly impacted the interpretation of x-ray absorption spectroscopy.

A list of acknowledgements cannot be complete without mentioning *Dra. Melanie Johnson* and Dr. *Wojciech Gawelda*. Those who were the 'Eve and Adam' of the ultrafast time-resolved XAS in the LSU group. Thank you very much for making the first steps on this amazing field of science; for providing valuable inspiration, example, experience and even data. Thanks for the valuable discussions and for taking the time to answer my several questions. A special thanks to Melanie for being so friendly and full of energy, for being so sociable and for the great discussions about the most variable subjects imaginable.

The pleasant atmosphere in my office was definitely a key factor for my (mental and physical) health over those four years and three months of work. Thank you very much all my office colleagues and all the other PSI fellows from several distinct groups. Thanks *Dr. Renske van der Veen* for the example of an impeccable PhD work, for the help with `FEFF9`, for the discussions, for the *töggli* matches and pizzas over the nights of beamtime. Thanks *Mme. Hannelore Rittmann-Frank* for the nice time, for the great beamtimes, for the energetic mood and motivation, for sharing the passion with science, music, arts, colors; for the beers and mutual support. Thanks *Dr. Maik Kaiser* for sharing the office for a little while, for listening my complains since the beginning and

for the nice discussions after work. Thanks *Dra. Ekaterina Möhr-Vorobeva* for the help with `MXAN`, for asking difficult questions and for the Russian cakes. Thank you very much *Dra. Dimali V. Amarasinghe* for the help with the Myoglobin preparation, for discovering together how to do it right, for the assistance and insight on the experiments, and for being so kind. Many thanks to *Mr. Alex Oggenfuss* for the unmeasurable help on technical aspects of my experiments, for the flow-cell design, for the funny times, for the curiosity about Brazilian culture and habits, for the evenings at Pickwick's and for the parties in your flat. Thank you *Mr. Andrin Caviezel* for the company on the office, for the great mood (even on times of stress and enormous amounts of work we can always find you laughing!), for the inspiring photos of the Alps that I looked every day to distract my mind and to inspire me with the exotic sports you do. Thanks *Dr. Simon Mariager* for the great trips, barbecues, and especially for the support in the last moments of writing. Thanks *Mr. Bartosz Slomski* for the funny talks at SLS and for the several beers and wine we shared. I am also thankful to the new members of the FEMTO and LSU group at PSI. Thanks *Dr. Jochen Rittmann*, *Dr. Jeremy Johnson* and *Mr. Sebastian Grübel* for the (unfortunately few) time we spent together, for the pleasant atmosphere during lunches and coffee breaks, and for the knowledge passed along. Every day is a constant learning.

I would like to acknowledge all the members of the LSU group in Lausanne. The lively atmosphere present in the labs, offices and coffee room was always one more excuse for the three-hours train ride. Thanks *Mme. Cristina Consani* and *Dr. Olivier Bräm* for the productive discussions about protein functionality and the shared knowledge about Myoglobin. Thank you *Professor Frank van Mourik* for the classes, assistance with detectors and electronics, and for the very direct and efficient way of dealing with scientific questions. Thanks *Dr. Andrea Cannizzo* for being so kind and always motivates us all. Many thanks for my colleagues of the x-ray division of the LSU, *Dr. Thai Pham*, *Dra. Amal El Nahhas*, *Mr. Marco Reinhard* and *Dra. Susanne Karlsson*, for their assistance during beamtimes, for the good company and even for sharing the moments of stress, frustration and fatigue. Thanks also for the lessons, fun and especially the cultural exchange. Thanks *Mr. Luca Piazza*, *Mr. Roberto Monni*, *Mr. Andre Al Haddad* and *Dr. Fabrizio Messina* for all the fun, support, and good moments at EPFL. Another very special acknowledgement goes to *Dr. Tom Penfold* for the great help with the calculations, for the useful theoretical discussions, and the general kindness which serves as an inspiration, not only to me, but for all the students around.

I would like to express my gratitude to my MSc. advisors and good friends *Prof. Nivaldo Speziali* and *Prof. Carlos Pinheiro*. All the knowledge you passed me over the course of my Master were deeply appreciated and certainly used. Thanks also for the constant introduction to the Swiss lifestyle as seen by Brazilians, the discussions about life in general, the motivational words, the projects and to believe on my potential. A big thanks to the Brazilian team of PSI: *Dra. Natália Milas*, *Dra. Cínthia Piamonteze*, *Dr. Ezequiel Panepucci*, *Dra. Raquel de Souza* (now in USA) and *Mr. Marcelo Rechulski*. Thanks for the shared time in the cafeterias, for the nice Brazilian cooking sessions and

for the nice words in my moments of desperation. Thanks *Dr. Pierre Louis* for sharing the doubts and moments of stress, *Mmes. Juliana Bolzan* and *Sílvia Drummond* for the encouragement and care. Special thanks to my cousins *Mme. Patrícia Pêgo* for the uncountable laughs and chats, and *Mme. Flavia Alves* for the great visit and travel. Thanks *Mr. Rafael Alves*, another great cousin, for the visit and for understanding exactly how it is to live far from the family. Thanks *Mme. Dearbhla Kehir*, for being such a sweet person, a proud Irish girl, and a source of infinite fun. I hope you will join the family soon.

A very special acknowledge to all the friends I made in Switzerland over all these years. My nice flatmates, who soon turned into very dear friends. Thanks *Mr. Philipp Bott*, *Mr. René Birrer*, *Mr. Sören Lange*, *Mr. Oliver Fini* and *Mr. Stefan Dreilich*. I am profoundly grateful for the company, the support during the stressing moments, for all the amazing ski trips, bike weekends, kart racings, beer evenings, life-in-general discussions, barbecue afternoons, fondue dinners, wine tasting, *Weißwurst Frühstück*, lessons of German and Swiss behaviour and culture, amongst many other special occasions. *Muchas gracias Mr. David Lazaro* and *Mr. Carlos Garrido* for being such good listeners, for the encouragement, for the sincere criticism and to always support me. *Merci beacoup Mr. Arnaud Praplan* for the true and sincere friendship and for not hesitating one second to answer my desperate demands for help. *Danke vilimal Mr. Fabian Cavin* and family for being always so nice and supportive; *dankzij Mr. Rubem Pool* for the nice and funny times. *Muito obrigado Mr. Gabriel Wickrowski*, thanks for everything. I will not forget the nice words and the support since my early times in Switzerland. Thanks *Dr. Vitaliy Goryashko*, *Mme. Juliana Nunes*, *Dr. Daniel Valesin*, *Dr. Augusto Quadros*, *Mme. Milena Castagna*, *Dr. Mirko Milas*, *Mme. Sarah Charlier*, *Mr. Victor Charlier*, *Mme. Ana* and *Mr. Leon Charlier*. Thanks you all for the company, support and friendship.

I would like to thank above all, my mother, *Ana Maria*, who was always a source of patience, an inspiration to overcome the difficulties of life and an example of character, ethics, dedication and perseverance. Thanks mom, to believe and support me in all ways it is humanly possible! To my grandmother, *Benvinda*, I leave a big muito obrigado! Thanks granny for your jokes, for your kindness, for your example of life, for the recipes, for the patience and to show us everyday that life is still worth living. To my brother *Fernando* and sister *Mariana*, I will express once again my deepest feelings and gratitude for the devoted attention and comprehension, for the admiration and example you were (and still are) for me. Thanks for taking part in my life, even from far, and to all the love sent via email, sms, phone, Skype©, postcard, letters, thoughts or any other means. Thanks to my nephew *Arthur*, who arrived in the world when I was not present, but immediately became an infinite source of joy and happiness! Thanks to all the members of my family, for the long-distance support and curiosity about my thesis.

Thanks a lot *Mme. Mirelle Rocha* for understanding myself better than anybody else. Thanks to all my good old friends back in Brazil, *Evandro Martins*, *Júlio Lana*, *Bia*

Monteiro, *Carol Carneiro*, *Fabi*, *Maurício Vieira*; and to my new friends scattered all over the world. Thanks *Mme. Paula Bauer* for the inspiring photos, poems, musics and citations that so many times inspired the grey Monday mornings and enlightened the Sunday afternoons. Thanks *Mme. Maria Clara Ferreira* for the paintings, photographs, music, books, the little sculpture, company, enthusiasm, support and above all the visit. My deepest gratitude to *Mr. Andrea Bianchi*; who I met accidentally, but immediately became irreplaceable. *Grazie mille* for the company, support, comprehension and infinite incentive. I could not find proper words, just thank you very much.

Por fim, agradeço àqueles que fizeram minha vida e meu trabalho mais prazerosos. Muito obrigado a todos, não teria conseguido chegar até aqui sem vocês!

"Tu es responsable de ce que tu as apprivois"

Antoine de Saint-Exupéry